



**A Study of Vehicle Regenerative Shock Absorber**

A thesis submitted in fulfilment of the requirements for the degree of Doctor of  
Philosophy

**Ran Zhang**

Bachelor of Mechanical Engineering and Automotive Engineering, RMIT University

School of Engineering

College of Science, Engineering and Health

RMIT University

January 2019

# Declaration

I, Ran Zhang, certify that except where due acknowledgement has been made, the work is that of the author alone; the work has not been submitted previously, in whole or in part, to qualify for any other academic award; the content of the thesis is the result of work which has been carried out since the official commencement date of the approved research program; any editorial work, paid or unpaid, carried out by a third party is acknowledged; ethics procedures and guidelines have been followed; and, the support I have received for my research through the provision of an Australian Government Research Training Program Scholarship has been acknowledged.

Ran Zhang

January 2019

# Acknowledgements

First of all, I am deeply grateful to my supervisor Associate professor Xu Wang for the faith and patience he had in me for all these years. He has contributed to this thesis with a major impact and has guided me and encouraged me to carry on through the up and downs. Thank you as well for those wise advices, for both my research life and personal life.

I also would like to thank my second supervisor Professor Sabu John for his support and suggestions.

This thesis includes research that was supported by DMTC Limited (Australia). I have prepared this thesis in accordance with the intellectual property rights granted to partners from the original DMTC project. I would also like to thank industry partner Thales Australia for their ongoing support, advice and expertise.

To all the research staffs who have taken some time to discuss research ideas and build the prototypes, I want to thank them for making things happen.

I would like to thank all my PhD colleagues, with whom I have shared moments of anxiety but also of excitement. Their presence and the moments of leisure we shared together is invaluable.

A very special word of gratitude goes to my parents who have been loving me and supporting me for what I do. I would not have come this far without them.

Finally I would like to thank my wife and the love of my life, Wanru, for always being strong by my side and showing how proud she is of me. I love you and I thank you for all the wonderful things you did for me and the family. I am so grateful to have you in my life.

The last word goes to Raymond, my baby boy, who has been the light of my life for the past 18 months and who has given me the extra strength and motivation to get things done. This thesis is dedicated to him.



# Table of Contents

|   |    |
|---|----|
| Abstract.....   | 1  |
| Chapter 1 .....   | 3  |
| 1.1 Background.....   | 3  |
| 1.2 Research motivation.....  | 6  |
| 1.3 Research scopes and objectives .....  | 7  |
| 1.4 Outline of thesis .....   | 8  |
| 1.5 List of publications .....  | 10 |
| Chapter 2 .....   | 13 |
| 2.1 Introduction.....   | 14 |
| 2.2 Direct drive regenerative shock absorber systems and their technologies.....        | 17 |
| 2.2.1 Magnet arrangement pattern design .....   | 17 |
| 2.2.2 Coil design .....   | 23 |
| 2.3 In-direct drive regenerative shock absorber systems and their technologies .....    | 26 |
| 2.3.1 Mechanical motion rectifier .....   | 26 |
| 2.3.2 Fluid motion rectifier .....  | 31 |
| 2.4 Comparison between the direct drive system and the indirect drive system .....      | 36 |
| 2.5 Hybrid systems and their technologies .....   | 41 |
| 2.6 Damping and vehicle dynamic performance.....  | 45 |
| 2.6.1 Damping performance of the direct drive system.....                               | 45 |
| 2.6.2 Damping performance of the indirect drive systems. ....                           | 48 |
| 2.7 Circuit and control algorithms for enhancing power output and vehicle dynamics..... | 53 |
| 2.7.1 Power maximization .....  | 53 |
| 2.7.2 Vehicle dynamic control .....   | 57 |
| 2.7.3 Balance between the energy harvesting and vehicle dynamic performance .....       | 59 |
| 2.8 Road excitation input .....   | 64 |
| 2.8.1 Sinusoidal displacement excitation input.....                                     | 64 |
| 2.8.2 Step input .....  | 64 |
| 2.8.3 Road displacement profile .....   | 65 |
| 2.8.4 Road test.....  | 68 |
| 2.9 Nonlinearity .....  | 72 |
| Chapter 3 .....   | 77 |

|   |     |
|---|-----|
| 3.1 Introduction.....   | 78  |
| 3.2 Analytical models .....   | 82  |
| 3.3 Validation of the analytical model .....  | 85  |
| 3.4 Experiment design .....   | 87  |
| 3.5 Experiment setup .....  | 88  |
| 3.6 Identification of the parameters .....  | 89  |
| 3.7 Results and discussions.....  | 96  |
| 3.7.1 Measurement of the harvested power values versus the excitation frequencies .....   | 97  |
| 3.7.2 Measurement of the harvested power versus the input excitation displacement amplitude at 7 Hz – the amplitude sensitivity at 7 Hz. .... | 101 |
| 3.7.3 Measurement of the harvested power versus the external resistance at 12 Hz – the external resistance sensitivity at 12 Hz. ....         | 102 |
| 3.8 Sensitivity analysis.....   | 103 |
| 3.8.1 Coil profile.....   | 103 |
| 3.8.2 Electro-mechanical coupling.....  | 105 |
| 3.9 Conclusions.....  | 112 |
| Chapter 4 .....   | 115 |
| 4.1 Background.....   | 116 |
| 4.2 Double speed regenerative shock absorber design.....  | 119 |
| 4.2.1 Concept design.....   | 119 |
| 4.2.2 System simulation of the double speed regenerative shock absorber and the direct-drive regenerative shock absorber.....                 | 120 |
| 4.2.3 Experimentation on the double speed regenerative shock absorber and the direct-drive regenerative shock absorber.....                   | 130 |
| 4.2.4 Parameter identification and the simulation validation.....   | 134 |
| 4.2.5 Integration of the double speed regenerative shock absorber and the direct-drive regenerative shock absorber.....                       | 140 |
| 4.2.6 Optimization of the double speed regenerative shock absorber.....   | 147 |
| 4.3 Indirect drive regenerative shock absorber design and its comparison with the direct-drive regenerative shock absorber.....               | 153 |
| 4.3.1 Concept design.....   | 153 |
| 4.3.2 Modeling of the indirect-drive system .....   | 156 |
| 4.3.3 Parameter identification and the experimental validation.....   | 163 |
| 4.3.4 Performance analysis .....  | 167 |
| 4.3.5 Parametrical Sensitivity Analysis using Monte Carlo simulation.....   | 171 |
| 4.3.6 Results and discussion .....  | 189 |
| 4.3.7 Future perspective and recommendations .....  | 190 |

|   |     |
|---|-----|
| 4.4 Conclusion: .....   | 192 |
| Chapter 5 .....   | 194 |
| 5.1 Introduction.....   | 195 |
| 5.2 Half vehicle modelling with the integrated indirect-drive regenerative shock absorber. ....                               | 197 |
| 5.3 Taguchi method .....  | 206 |
| 5.4 Optimization .....  | 216 |
| 5.5 Conclusion .....  | 222 |
| Chapter 6 .....   | 224 |
| 6.1 Introduction.....   | 225 |
| 6.2 The modelling of the full vehicle suspension system integrated with the indirect-drive regenerative shock absorbers. .... | 226 |
| 6.3 Results and discussions.....  | 233 |
| 6.4 Conclusion .....  | 239 |
| Chapter 7 .....   | 240 |
| 7.1 Research contribution .....   | 240 |
| 7.2 Future work.....  | 241 |
| Reference.....  | 242 |
| Appendix: .....   | 249 |

# List of Figures

|  |    |
|--|----|
| Figure 1.1: Generating electrical energy through piezoelectric material element (top) and generating electrical energy through electromagnetic device (bottom). .....    | 5  |
| Figure 2.1: Design of the electromagnetic damper with two layers of magnets .....  | 18 |
| Figure 2.2: Captured energy versus the dimension of a spacer between two magnets .....   | 19 |
| Figure 2.3: Halbach array magnet stack.....  | 20 |
| Figure 2.4: Magnetic flux plots of (a) longitudinal pattern with spacer, (b) transverse pattern with spacer, (c) transverse pattern, (d) Halbach array .....             | 21 |
| Figure 2.5: Different number of magnets in the transverse array for comparison with the Halbach array.....   | 22 |
| Figure 2.6: Four-phase coil design.....  | 23 |
| Figure 2.7: Normalized power vs number of coil phases.....   | 23 |
| Figure 2.8: Mechanical motion rectifier proposed by Li, Zuo [41] .....   | 28 |
| Figure 2.9: Dual overrunning clutch transmission system.....   | 29 |
| Figure 2.10: Ball screw indirect drive regenerative shock absorber system.....   | 30 |
| Figure 2.11: The design of a mechanical motion rectifier based the energy-harvesting shock absorber using a ball-screw mechanism.....                                    | 31 |
| Figure 2.12: The hydraulic shock absorber prototype .....  | 32 |
| Figure 2.13: Working principle of the hydraulic regenerative shock absorber system without a mechanical motion rectifier.....  | 33 |
| Figure 2.14: (a) Direct drive regenerative shock absorber system. (b) Indirect drive regenerative shock absorber system. ....  | 38 |
| Figure 2.15: Direct drive linear regenerative shock absorber (Mark 1) and indirect drive ball screw regenerative shock absorber (Mark 2) installed on the same ATV ..... | 39 |
| Figure 2.16: Hybrid dual cylinder regenerative suspension system and its prototype.....  | 42 |

|   |    |
|---|----|
| Figure 2.17: The conceptual design of a hybrid regenerative shock absorber .....  | 43 |
| Figure 2.18: The cross-section of the hybrid regenerative shock absorber and its experimental setup                                   | 43 |
| Figure 2.19: A parallel hydraulic EM damper.....  | 47 |
| Figure 2.20: The cross section of the MR regenerative damper and its damping force against the displacement for applied currents..... | 48 |
| Figure 2.21: Continuous damping provided by the dual clutches system.....   | 49 |
| Figure 2.22: Damping force versus shock absorber displacement for different excitation frequencies                                    | 50 |
| Figure 2.23: Damping force- displacement loops of the regenerative shock absorber .....   | 51 |
| Figure 2.24: Single bridge rectifier (top) [39], two bridge rectifiers in series (bottom) [22].....                                   | 54 |
| Figure 2.25: The SMFE circuit (top) [86] and energy extraction for different circuits (bottom) [87]..                                 | 55 |
| Figure 2.26: Direct AC-DC step-up converter [89] .....  | 56 |
| Figure 2.27: Electrical circuit of a hydraulic indirect drive regenerative shock absorber [74].....                                   | 57 |
| Figure 2.28: Independent tunable electromagnetic damper system .....  | 58 |
| Figure 2.29: Regenerative suspension dynamic model and configuration of SMR.....  | 59 |
| Figure 2.30: The H bridge for the mode switching between regeneration and actuation .....   | 61 |
| Figure 2.31: Control electric circuits of the proposed regenerative shock absorber system with relay switches .....                   | 61 |
| Figure 2.32: PSD of input displacement excitation profile of the C level road on which the vehicle is travelling at 80 km/h.....      | 67 |
| Figure 2.33: The output power versus road class and vehicle velocity.....   | 68 |
| Figure 2.34: Road test of the ball-screw-based MMR shock absorber and its electrical outputs .....                                    | 70 |
| Figure 2.35: The road test of MMR shock absorber and recorded displacement and power output.....                                      | 71 |
| Figure 2.36: Road test set up of AERS and its body acceleration in the frequency domain at 20km/h on Class B road. ....               | 72 |
| Figure 2.37: Frequency spectrum of the power generation in a quarter vehicle regenerative suspension system.....                      | 73 |

|  |     |
|--|-----|
| Figure 2.38: Nonlinear magnetic levitation energy harvesting system and its frequency spectrum of oscillator velocity. ....  | 74  |
| Figure 2.39: Schematic of a MEMS energy harvester with the nonlinear softened springs and its force displacement curve. ....   | 74  |
| Figure 2.40: Experimental setup of the Mazda CX-7 nonlinear shock absorber and its force velocity curve. ....  | 75  |
| Figure 3.1: A quarter vehicle suspension model with the regenerative shock absorber. ....  | 82  |
| Figure 3.2: Harvesting circuit of the regenerative shock absorber. ....  | 83  |
| Figure 3.3: Simulation schematic for Equations (3.5-3.6) for calculation of the output power using the integration method from the Matlab SIMULINK software. ....  | 87  |
| Figure 3.4: Schematic view of the 2DOF electromagnetic vibration energy harvesting system. ....  | 88  |
| Figure 3.5: Experimental setup of the 2DOF electromagnetic vibration energy harvesting system on the MTS Landmark servo hydraulic test system (hydraulic shaker). ....   | 89  |
| Figure 3.6: Experiment setup for hammer impact modal analysis tests. ....  | 90  |
| Figure 3.7: Frequency response function amplitudes of the single degree of freedom top mass spring oscillator system (a) the single degree of freedom bottom mass spring oscillator system (b) the two degree of freedom mass spring oscillator system (c). .... | 92  |
| Figure 3.8: Magnet holder and the magnetic field intensity contour of the magnets in the Halbach array around the coil using the ANSYS Maxwell software. ....  | 94  |
| Figure 3.9: Comparison of the output power values versus the excitation frequencies obtained from the analysis model, simulation model and experiments. ....   | 99  |
| Figure 3.10: Harvested power versus the displacement excitation amplitude at 7 Hz. ....  | 102 |
| Figure 3.11: Harvested power versus the external resistance at 12 Hz. ....   | 103 |
| Figure 3.12: Power frequency response amplitude curves versus the winding number of the coil. ...  | 104 |
| Figure 3.13: 2D magnetic field intensity contour of magnets arranged in the patterns of the Halbach array, longitudinal and transverse arrays. ....  | 105 |
| Figure 3.14: Magnetic field intensity versus the coil width $H$ . ....   | 106 |

|  |     |
|--|-----|
| Figure 3.15: Harvested power versus the displacement excitation frequencies for the three magnet arrangement patterns. ....  | 107 |
| Figure 3.16: Harvested power versus the excitation frequencies for different $B$ values.....   | 108 |
| Figure 3.17: Contour map of power output versus the coil length and magnetic field intensity. ....   | 111 |
| Figure 3.18: Power output versus the coil length and magnetic field intensity. ....  | 112 |
| Figure 4.1: The working principle of the double speed RSA. ....  | 120 |
| Figure 4.2: Two degrees of freedom (2DOF) mass-spring-dashpot quarter vehicle suspension system model.....   | 121 |
| Figure 4.3: Simulation model of a quarter vehicle suspension system with (a) direct-drive RSA and (b) double speed RSA.....  | 123 |
| Figure 4.4: (a) positive cycle of the rectification process, (b) negative cycle of the rectification process, (c) the output voltage.....  | 124 |
| Figure 4.5: Schematic of the double speed RSA system. ....   | 126 |
| Figure 4.6: (a) Isometric view, (b) sectional view and (c) composition of the double speed RSA. ...  | 131 |
| Figure 4.7: (a) Top mounts with pinion gears, (b) coil carrier with rack gears, (c) longitudinally stacked magnets with their polarities being opposite to each other in the double speed RSA. ... | 132 |
| Figure 4.8: The experimental setup of the double speed RSA on the hydraulic MTS machine. ....  | 133 |
| Figure 4.9: Experiment setup of the double speed RSA and direct-drive RSA.....   | 134 |
| Figure 4.10: Damping coefficient of the double speed RSA measured in 50 seconds. ....  | 135 |
| Figure 4.11: Magnetic field intensity analysis of the magnets using ANSYS Maxwell software module.....   | 136 |
| Figure 4.12: The simulation and experiment results of the output power of the double speed RSA increasing with the excitation displacement amplitude.....  | 137 |
| Figure 4.13: Comparison of the simulated and measured voltage outputs of the direct-drive and double speed RSA under displacement excitation of 2 mm over the frequency range from 0 to 25Hz..     | 139 |

|  |     |
|--|-----|
| Figure 4.14: Comparison of the simulated voltage outputs of the double speed RSA with direct-drive RSA under the sinusoidal wave road profile excitation with a displacement amplitude of 0.035m. ....     | 140 |
| Figure 4.15: Comparison of the power outputs of the double speed RSA with those of the direct-drive RSA under the sinusoidal wave road profile excitation displacement amplitude of 0.035m. ....           | 141 |
| Figure 4.16: Shock absorber (suspension) velocity on the double speed RSA. ....  | 142 |
| Figure 4.17: Comparison of the energy harvesting efficiency of the double speed RSA and direct-drive RSA. ....   | 143 |
| Figure 4.18: Random road excitation time history with a peak displacement amplitude of 0.035 m. ....   | 144 |
| Figure 4.19: RMS Power output time trace of the double speed RSA and the direct-drive RSA in the quarter vehicle suspension system under the random excitation shown in Figure 4.18. ....                  | 145 |
| Figure 4.20: Voltage output of the double speed RSA with random road excitation amplitude varying with standard deviation of 20% of the mean value. ....   | 146 |
| Figure 4.21: Voltage output of the direct-drive RSA with random road excitation amplitude varying with standard deviation of 20% of the mean value. ....   | 147 |
| Figure 4.22: Amplification factor $n$ on the double speed RSA. ....  | 149 |
| Figure 4.23: Harvested power versus the increased amplification factor $n$ at the second modal resonant frequency of 9.94Hz. ....  | 150 |
| Figure 4.24: Shock absorber displacement versus the increased amplification factor $n$ at the second modal resonant frequency of 9.94Hz. ....  | 150 |
| Figure 4.25: Harvested power at the second resonant frequency of 9.94 Hz versus the reciprocating coil mass and amplification factor. ....   | 151 |
| Figure 4.26: Harvested power at the second resonant frequency of 9.94 Hz versus the coil mass and amplification factor $n$ . ....  | 152 |
| Figure 4.27: The composition and dimensions of (a) direct-drive regenerative shock absorber, (b) indirect-drive regenerative shock absorber and (c) the working principle of the arm-teeth mechanism. .... | 156 |



|   |     |
|---|-----|
| Figure 4.28: Schematic of a two degrees of freedom quarter vehicle suspension system integrated with the indirect-drive regenerative shock absorber.....  | 156 |
| Figure 4.29: The composition of the indirect-drive regenerative shock absorber and its equivalent reciprocating mass $m_s$ .....  | 158 |
| Figure 4.30: The prototype of indirect-drive regenerative shock absorber.....   | 164 |
| Figure 4.31: The experiment set up of the indirect-drive regenerative shock absorber.....   | 165 |
| Figure 4.32: The comparison between simulation and experimental output voltage results for the indirect-drive regenerative shock absorber with 10 mm excitation displacement amplitude at 1 Hz. ....  | 165 |
| Figure 4.33: The comparison of the quarter vehicle suspension system integrated with the direct-drive and the indirect-drive regenerative shock absorbers for (a) the ratio of the output voltage over excitation displacement amplitude, (b) the ratio of power over squared excitation displacement amplitude, (c) the ratio of the electromagnetic damping force over excitation displacement amplitude, (d) the ratio of the vehicle body acceleration over excitation displacement amplitude and (e) the total conversion efficiency of both the direct and indirect drive systems. .... | 171 |
| Figure 4.34: Ratio of the output power to squared excitation displacement amplitude for variation of $m_2$ using its original value as the mean value and a standard deviation of 20% of the original value for (a) the direct-drive system and (b) the indirect-drive system.....  | 174 |
| Figure 4.35: Ratio of the output power to squared excitation displacement amplitude for variation of $k_2$ using its original value as the mean value and a standard deviation of 20% of the original value for (a) the direct-drive system and (b) the indirect-drive system. ....   | 175 |
| Figure 4.36: Ratio of the output power to squared excitation displacement amplitude for variation of $m_1$ using its original value as the mean value and a standard deviation of 20% of the original value for (a) the direct-drive system and (b) the indirect-drive system.....  | 177 |
| Figure 4.37: Ratio of the output power to squared excitation displacement amplitude for variation of $k_1$ using its original value as the mean value and a standard deviation of 20% of the mean value for (a) the direct-drive system and (b) the indirect-drive system. ....   | 179 |

|   |     |
|---|-----|
| Figure 4.38: Ratio of the output power to squared excitation displacement amplitude for variation of $c_2$ using its original value as the mean value and a standard deviation of 20% of the mean value for (a) the direct-drive system and (b) the indirect-drive system. .... | 181 |
| Figure 4.39: Ratio of the power output to squared excitation displacement amplitude for variation of $c_1$ using its original value as the mean value and a standard deviation of 20% of the mean value for (a) the direct-drive system and (b) the indirect-drive system. .... | 181 |
| Figure 4.40: Ratio of the power output to squared excitation displacement amplitude for variation of $B_l$ using its original value as the mean value and a standard deviation of 20% of the mean value for (a) the direct-drive system and (b) the indirect-drive system. .... | 184 |
| Figure 4.41: Ratio of the power output to squared excitation displacement amplitude for variation of $L_e$ using its original value as the mean value and a standard deviation of 20% of the mean value for (a) the direct-drive system and (b) the indirect-drive system. .... | 184 |
| Figure 4.42: Ratio of the output voltage to excitation displacement amplitude and ratio of power output to squared excitation displacement amplitude for increasing $R$ in (a) the direct-drive system and (b) the indirect-drive system.....                                   | 186 |
| Figure 4.43: Ratio of the power output to squared excitation displacement amplitude for variation of $R_e$ using its original value as the mean value and a standard deviation of 20% of the mean value for (a) the direct-drive system and (b) the indirect-drive system. .... | 187 |
| Figure 4.44: Ratio of the power output to squared excitation displacement amplitude for variation of the gear ratio $j$ using its original value as the mean value and a standard deviation of 20% of the mean value in the indirect-drive system.....                          | 189 |
| Figure 4.45: The future design of the indirect-drive regenerative shock absorber. ....  | 192 |
| Figure 5.1: The working principle of the indirect-drive RSA.....  | 197 |
| Figure 5.3: The composition of the equivalent reciprocating mass $m_s$ . ....   | 201 |
| Figure 5.4: The ratio of total power output to the squared input excitation displacement amplitude in the frequency range of 0-30 Hz.....   | 204 |

|   |     |
|---|-----|
| Figure 5.5: Time domain simulation model of the half vehicle suspension system integrated with the indirect-drive RSA. ....   | 205 |
| Figure 5.6: The ratio of the total power output to the squared displacement input excitation amplitude for 8 systems.....   | 210 |
| Figure 5.7: The effect of each parameter on the total power output ratio and the energy harvesting bandwidth.....   | 216 |
| Figure 5.8: The ratio of the total power output to the squared input displacement excitation amplitude for System 8 and the optimized System 8 in the frequency of 0-30 Hz. ....  | 218 |
| Figure 5.9: The modelling of the road profiles of Classes A, C and E in the time domain when the vehicle is travelling at 5.556 m/s (20 km/h). ....   | 221 |
| Figure 5.10: The total power output of the original System 8 and the optimized System 8 at a vehicle speed of 20 km/h on the road profiles of (a) Class A, (b) Class C and (c) Class E.....   | 222 |
| Figure 6.1: The schematic of the 7 DOF full vehicle suspension system. ....   | 227 |
| Figure 6.2: The ratios of power output to the squared input excitation displacement amplitude of the (a) front right RSA, (b) the rear left RSA, (c) front left RSA and (d) rear right RSA.....   | 235 |
| Figure 6.3: The comparison of the power output ratios between (a) front shock absorber in half vehicle suspension system and front right shock absorber in full vehicle suspension system and (b) shock absorber in quarter vehicle suspension system and front right shock absorber in full vehicle suspension system..... | 237 |
| Figure 6.4: The modelling of 7 DOF full vehicle suspension system in time domain.....   | 238 |
| Figure 6.5: The comparison of the power output ratios of the front right shock absorber simulated in the frequency domain and the time domain. ....   | 239 |

# List of Tables

|   |     |
|---|-----|
| Table 1.1 Comparison of the piezoelectric system with the electromagnetic system .....  | 5   |
| Table 2.1: Summary of the direct drive regenerative shock absorber.....   | 24  |
| Table 2.2: Summary of the indirect drive regenerative shock absorbers .....   | 34  |
| Table 2.3: Summary of the hybrid system .....   | 44  |
| Table 2.4: The summary of the damping performance of the regenerative shock absorbers.....  | 51  |
| Table 2.5: The summary of the control algorithms of the regenerative shock absorbers. ....  | 61  |
| Table 2.6: ISO 8608 values of $G_d(n_0)$ and $G_d(\Omega_0)$ [127].....   | 66  |
| Table 3.1: Parameters identified for the 2DOF mass-spring-damping oscillator system. ....   | 95  |
| Table 3.2: The input excitation displacement amplitudes, frequencies and external resistances for the experiments. ....                               | 97  |
| Table 3.3: comparison of the natural frequencies of the 2DOF electromagnetic vibration energy harvesting system obtained from different methods. .... | 100 |
| Table 4.1: Parameters of the 2DOF mass-spring-dashpot simulation model of the quarter vehicle suspension system .....                                 | 121 |
| Table 4.2: Parameters of the quarter vehicle suspension system integrated with the single or double speed RSAs. ....                                  | 137 |
| Table 4.3: Parameters of the indirect-drive regenerative shock absorber. ....   | 166 |
| Table 5.1: Parameters of Taguchi method in two levels. ....   | 207 |
| Table 5.2: Taguchi matrix with 8 test run systems. ....   | 208 |
| Table 5.3: The results of the total power output ratio and energy harvesting bandwidth for the 8 test run systems. ....                               | 210 |
| Table 5.4: The detailed Taguchi calculation.....  | 212 |
| Table 5.5: The effect of each parameter on the peak power output. ....  | 215 |
| Table 5.6: The effect of each parameter on the energy harvesting bandwidth. ....  | 215 |

|  |     |
|--|-----|
| Table 5.7: The selected parameters in the original System 8 and the optimized System 8 ..... | 218 |
| Table 5.8: The road roughness of the different road class. ....                              | 219 |
| Table 6.1: The parameters of the 7 DOF full vehicle suspensions system. ....                 | 227 |
| Table 6.2: Natural frequencies of the 7 DOF vehicle suspension system. ....                  | 233 |

# Nomenclature

|                     |  |
|---------------------|--|
| $\Omega$            | Angular spatial frequency                  |
| $x_c$               | Coil displacement                          |
| $v_{coil\_magnets}$ | Coil speed with respect to the magnets     |
| $m_c$               | Coil mass                                  |
| $R_e$               | Coil resistance                            |
| $L_e$               | Coil inductance                            |
| $H$                 | Coil width                                 |
| $T_c$               | Coil kinetic energy                        |
| $P_{input}$         | Damping power                              |
| $F_{Wi}$            | Damping force of the $i^{th}$ oscillator   |
| $\eta_{tp}$         | Efficiency of top plate                    |
| $\eta_{pg}$         | Efficiency of planetary gear               |
| $\eta_g$            | Efficiency of generator                    |
| $m_s$               | Equivalent reciprocating mass              |
| $c_L$               | Equivalent suspension damping              |
| $r_e$               | Equivalent radius                          |
| $Bl$                | Electromechanical coupling                 |
| $r$                 | Equivalent radius                          |
| $P_E$               | Electrical power                           |
| $R$                 | External resistance                        |
| $j\omega$           | Excitation frequency                       |
| $m_{1f}$            | Front wheel assembly mass                  |
| $k_{1f}$            | Front tyre stiffness                       |
| $c_{1f}$            | Front tyre damping                         |
| $k_{2f}$            | Front suspension stiffness                 |
| $c_{2f}$            | Front shock absorber damping               |
| $k_{tfr}$           | Front right tyre stiffness                 |
| $k_{tfl}$           | Front left tyre stiffness                  |
| $K_{sfr}$           | Front right suspension stiffness           |
| $K_{sfl}$           | Front left suspension stiffness            |
| $C_{tfr}$           | Front right tyre damping coefficient       |
| $C_{tfl}$           | Front left tyre damping coefficient        |
| $C_{sfr}$           | Front right suspension damping coefficient |
| $C_{sfl}$           | Front left suspension damping coefficient  |
| $m_b$               | Full vehicle mass                          |
| $j$                 | Gear ratio                                 |
| $r_g$               | Generator rotor radius                     |
| $U_{generated}$     | Generated voltage                          |
| $k_e$               | Generator constant                         |
| $\omega_g$          | Generator angular velocity                 |
| $\theta$            | Half vehicle body rotational angle         |
| $F_{Gi}$            | Inertia force of the $i^{th}$ oscillator   |
| $F_{LR}$            | Lorentz force                              |
| $m_m$               | Magnets mass                               |

|           |   |
|-----------|---|
| $B$       | Magnetic field intensity  |
| $c_s$     | Mechanical damping  |
| $n$       | Multiplication factor   |
| $K_i$     | Motor constant  |
| $J_W$     | Moment of the rotational inertia of the pinion gears                      |
| $m_{fr}$  | Mass of front right wheel assembly  |
| $m_{fl}$  | Mass of front left wheel assembly   |
| $m_{rl}$  | Mass of rear left wheel assembly  |
| $m_{rr}$  | Mass of rear right assembly   |
| $I_a$     | Pitching moment of inertia  |
| $\alpha$  | Pitching angle  |
| $m_p$     | Planetary gear mass   |
| $r_p$     | Planetary gear radius   |
| $P_{ob}$  | Power spectral density of bounce  |
| $P_{op}$  | Power spectral density of pitch   |
| $m_2$     | Upper vehicle body mass   |
| $x_2$     | Quarter vehicle body displacement   |
| $r$       | Radius of the pinion gear   |
| $m_{1r}$  | Rear wheel assembly mass  |
| $k_{1r}$  | Rear tyre stiffness   |
| $k_{2r}$  | Rear suspension stiffness   |
| $c_{1r}$  | Rear tyre damping   |
| $c_{2r}$  | Rear shock absorber damping   |
| $k_{trl}$ | Rear left tyre stiffness  |
| $k_{trr}$ | Rear right tyre stiffness   |
| $K_{srl}$ | Rear left suspension stiffness  |
| $K_{srr}$ | Rear right suspension stiffness   |
| $C_{srr}$ | Rear right suspension damping coefficient                                 |
| $C_{srl}$ | Rear left suspension damping coefficient                                  |
| $c_R$     | Rotary damping coefficient  |
| $y$       | Road excitation displacement amplitude                                    |
| $J_{FW}$  | Rotational inertia of the flywheel  |
| $J_{am}$  | Rotational inertia of the driving arm                                     |
| $J_{pcr}$ | Rotational inertia of the planetary gear carrier                          |
| $J_P$     | Rotational inertia of the planetary gear                                  |
| $J_g$     | Rotational inertia of the generator                                       |
| $J_s$     | Rotational inertia of the sun gear  |
| $J$       | Rotational inertia of the half vehicle                                    |
| $I_b$     | Rolling moment of inertia   |
| $\beta$   | Rolling angle   |
| $C_{trr}$ | Rear right tyre damping coefficient                                       |
| $C_{trl}$ | Rear left tyre damping coefficient  |
| $k_2$     | Suspension stiffness  |
| $c_2$     | Shock absorber damping  |
| $F_{Ki}$  | Spring restoring force of the $i^{\text{th}}$ oscillator                  |
| $f_s$     | Spatial frequency   |
| $l_f$     | The distance between center of gravity of the vehicle and the front axial |

|                         |  |
|-------------------------|--|
| $l_r$                   | The distance between center of gravity of the vehicle and the rear axial         |
| $G_d(\Omega)$           | The vertical displacement with respect to the angular spatial frequency $\Omega$ |
| $G_d(\Omega)$           | The vertical displacement with respect to the angular spatial frequency $\Omega$ |
| $G_d(\Omega_0)$         | The vertical displacement when $\Omega_0=1$ rad/m                                |
| $a$                     | The distance between center of gravity of the vehicle and the front tyre         |
| $b$                     | The distance between center of gravity of the vehicle and the rear tyre          |
| $m_{tp}$                | Top plate mass   |
| $\eta_{direct-drive}$   | Total conversion efficiency of the direct-drive system                           |
| $\eta_{indirect-drive}$ | Total conversion efficiency of the indirect-drive system                         |
| $l$                     | Total coil length of the electromagnetic generator                               |
| $T$                     | Total kinetic energy   |
| $W$                     | Total damping energy   |
| $V$                     | Total spring potential energy  |
| $k_l$                   | Tyre stiffness   |
| $c_l$                   | Tyre damping   |
| $x_l$                   | Tyre displacement  |
| $U$                     | Voltage output   |
| $m_l$                   | Wheel assembly mass  |





# Abstract

The technology of energy harvesting from shock absorber has become more promising over the years with a potential for implementation. The aim of the research is to improve the energy harvesting ability of the regenerative shock absorber and evaluate its feasibility operating in the real road condition on the vehicle.

This thesis consists of 7 chapters to address the research questions raised from the existing research gaps based on the literature reviews: 1. How can the performance of the electromagnetic energy harvester in 2DOF system be improved? 2. For the direct drive and indirect drive regenerative shock absorbers, which one has better performance? 3. How can the half vehicle model with regenerative shock absorbers be modelled for the premium energy harvesting performance?

In order to answer the research questions, firstly a 2 degrees of freedom oscillating system resembling the quarter vehicle suspension system is constructed with the electromagnetic harvester and validated by the simulation model. It is found that the peak power output occurs at natural frequency. Base excitation amplitude and external resistance can also affect the system power output. As for the energy harvester, better energy harvesting performance can be achieved through two factors: coil speed with respect to the magnets and the electro-mechanical coupling constant. The double speed mechanism can increase the coil speed with respect to the magnets and is applied on a design of novel regenerative shock absorber. It is found that increasing the coil speed with respect to the magnets for 2 times can result in increasing the power output by 4 times. A novel indirect drive regenerative shock absorber with the arm-teeth system is also designed and fabricated to answer the second research

question. The results show that the power output can be substantially increased compared with the traditional direct drive regenerative shock absorber. It is also found that the arm-teeth system makes the regenerative shock absorber more sensible to parameter optimization and has the potentials to increase the energy harvesting bandwidth.

As the response to research question three, a half vehicle suspension system model is established with two indirect drive regenerative shock absorbers. The Taguchi method is unitized for the parameter optimization. With the application of the random road excitation displacement amplitude, the optimized model can harvest more energy than the non-optimized model when the vehicle is driving on the Class A, Class C and Class E road. Lastly a full vehicle suspension system model is developed as an extension to the half vehicle suspension system model. It is found that at high frequency range, the peak power output ratio of full vehicle suspension system is same as that of the half and quarter vehicle suspension system. The advantages of the full vehicle suspension system are more obvious at low frequency range or when the vehicle is driving on the off-road condition.

# Chapter 1

## *Introduction*

### 1.1 Background

Shock absorbers are equipped on most of the vehicles to dampen the vibrations due to the road irregularities for the purpose of the ride comfort. During this process the conventional hydraulic shock absorber dissipates the kinetic energy into heat. The regenerative shock absorber can harvest this energy and convert it into electrical energy which can be stored in

batteries or capacitors. However due to the low energy conversion efficiency and the negative effect on the ride and handling performance it has not been widely realized. Therefore, a systematic research aiming at improving the conversion efficiency of the regenerative shock absorber while maintaining the overall ride and handling performance of the vehicle is needed.

The feasibility of the regenerative shock absorber depends on:

1. High power output to weight ratio
2. Better mechanical-electrical energy conversion efficiency
3. High compatibility with the vehicle.

Among the methods in which the kinetic energy can be converted into electrical energy, as shown in Figure 1.1, the methods through use of the piezoelectric material and electromagnetic generator were frequently discussed because of their outstanding compatibilities and high efficiencies. Poulin, Sarraute [1] constructed the equivalent impedance models to compare two electromechanical systems. It was also concluded in the study that the piezoelectric system has higher power density than the electromagnetic system and thus is more suitable to microsystems. The comparison results are listed in Table 1.1 below.

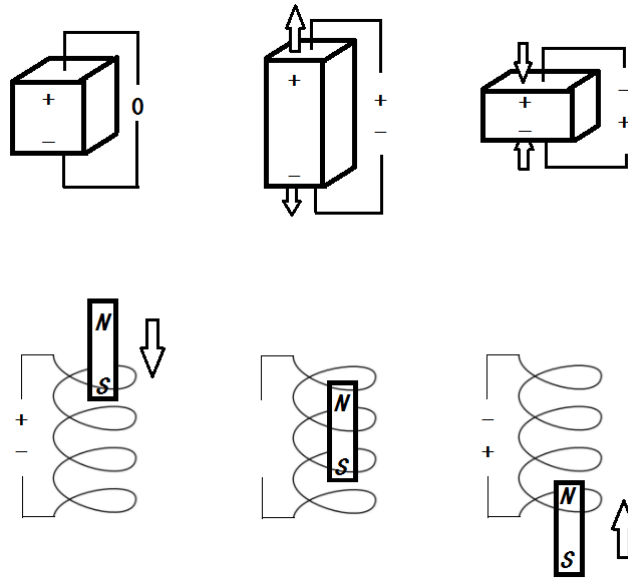


**Figure 1.1: Generating electrical energy through piezoelectric material element (top) and generating electrical energy through electromagnetic device (bottom).**

**Table 1.1 Comparison of the piezoelectric system with the electromagnetic system[1].**

| Comparison Elements between the Two Systems | Electromagnetic System | Piezoelectric System |
|---|------------------------|----------------------|
| Strain                                      | Low                    | High                 |
| Displacement                                | High                   | Low                  |
| Voltage                                     | Variable               | High                 |
| Current                                     | Variable               | Low                  |
| Resonant frequency                          | Variable               | High                 |
| Output impedance                            | Resistive              | Capacitive           |
| Adapted load                                | Variable               | High                 |

A typical shock absorber on a commercial vehicle needs to be reliable and able to operate in the frequency range of 1–30 Hz and with a maximum shock displacement of 0.1 m. It can be seen from Table 1.1 that in a regenerative shock absorber the electromagnetic transducer can outperform the piezoelectric transducer due to the lower strain, low resonant frequency and

higher displacement of the suspension system. As a result, the research is focused on the electromagnetic regenerative shock absorber for its high feasibility.

## 1.2 Research motivation

The kinetic energy of the shock absorber is dissipated into the ambient environment in the form of heat. The amount of dissipated power can be calculated through Equation (1.1).

$$P = c \cdot v^2 \quad (1.1)$$

According to Ref [2], the dissipated power is more than 80 W per shock absorber for a commercial vehicle driving at 90 km/h, which indicates a huge potential in improving the fuel efficiency of the vehicle. A rougher terrain or higher vehicle speed can generally result in more dissipated energy. Harvesting the kinetic energy through the shock absorber does not require any additional energy source, as the kinetic energy is always available to be harvested regardless of the vehicle types, road conditions and driving habits, as long as the vehicle is on the move. The energy harvested from the shock absorber can be used to charge the battery to increase the energy utilization efficiency, or to extend the traveling distance of an electric vehicle. With a proper design, there is possibility to completely replace the alternator of the vehicle with a set of regenerative shock absorbers. The ultimate motivation of this research is to reduce energy waste and to reduce the greenhouse gas emission through adopting the electromagnetic regenerative shock absorbers in the vehicles.

## 1.3 Research scopes and objectives

The main aim of the thesis is to design new mechanisms for the regenerative shock absorber to harvest the kinetic energy induced by the road elevation while vehicle is driving. The scope of this research is presented as the following.

1. A 2DOF (two degrees of the freedom) oscillating system representing the quarter car suspension system will be fabricated and modelled.
2. A regenerative shock absorbers with new concepts will be built and compared with the conventional regenerative shock absorber.
3. A regenerative shock absorber with a different drive mode will be fabricated for the system comparison of the energy harvesting performance.
4. A half car suspension system with two shock absorbers will be investigated targeting at increasing the power output and broadening the energy harvesting bandwidth.

The objective of this PhD thesis are:

1. To investigate performance of an electromagnetic transducer in a 2DOF oscillating system.
2. To adopt and evaluate new design concepts of electromagnetic regenerative shock absorbers
3. To improve energy harvesting performance of a set of regenerative shock absorbers integrated in the vehicle model.



## 1.4 Outline of thesis

### Chapter 2

A comprehensive review of the technologies on the electromagnetic regenerative shock absorber will be conducted. The regenerative shock absorbers will be categorized and evaluated in three drive modes: direct-drive mode, indirect-drive mode and hybrid drive mode in terms of mechanisms and damping performances. The effect of the electrical circuit, control algorithm and different road excitations will be discussed as well.

### Chapter 3

A 2DOF (two degrees of the freedom) oscillating system simulating the quarter vehicle suspension system will be designed and fabricated. The parameter sensitivity analysis will be conducted based on the validated simulation model. The magnetic pattern of the Halbach array will be studied for its effects on the electromechanical coupling. The effect of the coil length and the magnetic field intensity will also be investigated for the premium power output.

### Chapter 4

Two novel designs of regenerative shock absorber are to be developed considering the contributing factors investigated previously and the new designs will be compared with the

conventional design in terms of its feasibility, peak power output and energy harvesting efficiency. How the output power can be affected by different mechanisms will be investigated as well.

## Chapter 5

A half vehicle model with two indirect-drive regenerative shock absorbers at each end (4 DOF) will be established to investigate the effect of varying parameters on the peak power output and the energy harvesting bandwidth. An optimized half vehicle model integrated with the regenerative shock absorber will be presented with the premium combination of the parameters.

## Chapter 6

The energy harvesting from the regenerative shock absorber based on the full vehicle model (7 DOF) will be studied to obtain the more accurate assessment of the system performance in achieving the best overall power output considering the pitching mode and rolling mode of the vehicle.

## Chapter 7

A conclusion will be drawn in regards to how the research questions are addressed and to give recommendation to the future research directions.

## 1.5 List of publications

1. **Zhang, R.**, Wang, X. and Liu, Z., 2018. *A novel regenerative shock absorber with a speed doubling mechanism and its Monte Carlo simulation*. Journal of Sound and Vibration, 417, pp.260-276 [SCImago JCR rank 37/689 in Engineering/Mechanical Engineering; Q1–SJR: 1.462, H-index: 138, Impact factor: 2.593] [3].
2. **Zhang, R.**, Wang, X. and John, S., 2018. *A Comprehensive Review of the Techniques on Regenerative Shock Absorber Systems*. Energies, 11(5), p.1167 [SCImago JCR rank 59/731 in Energy/Energy Engineering and Power Technology; Q2–SJR: 0.67, H-index: 56, Impact factor: 2.89] [4].
3. Al Shamia, E., Wang, X., **Zhang, R.**, Zuo, L. (2018) *A parameter study and optimisation of two body wave energy converters*, accepted by Renewable Energy on 30 June 2018 [SCImago JCR rank 18/395 in Energy/ Renewable Energy, Sustainability and the Environment; JCR rank 18/317 in Material Science/ Materials Chemistry; Q1–SJR: 1.847, H-index: 143, Impact factor: 5.4] [5].

4. Liu, Z. W., Wang, X., **Zhang, R.** and Wang, L. P. (2018), *A Dimensionless Parameter Analysis of a Cylindrical Tube Electromagnetic Vibration Energy Harvester and Its Oscillator Nonlinearity Effect*, *Energies*, 2018, 11, 1653; doi:10.3390/en11071653 [SCImago JCR rank 59/731 in Energy/Energy Engineering and Power Technology; Q2–SJR: 0.67, H-index:56, Impact factor: 2.89] [6].
  
5. Al Shamia, E., **Zhang, R.**, Wang, X. (2019), *Point Absorber Wave Energy Harvesters: A Review of Recent Developments*, *Energies*. [SCImago JCR rank 59/731 in Energy/Energy Engineering and Power Technology; Q2–SJR: 0.67, H-index:56, Impact factor: 2.89] [7].
  
6. **Zhang, R.**, Wang, X., Shu, H. L., John, S. (2018), *The effects of the electro-mechanical coupling and Halbach magnet pattern on energy harvesting performance of a two degree of freedom electromagnetic vibration energy harvester* , *International Journal of Vehicle Noise and Vibration*, 12 April 2018 . [SCImago JCR rank 52/225 in Engineering/Automotive Engineering; JCR rank 334/950 in Engineering/Mechanical Engineering; Q3–SJR: 0.297, H-index:14, Impact factor: 0.62] [8].
  
7. **Zhang, R.**, Wang, X., Al Shamia, E., John, S., Zuo, L., Wang, C. (2018). *A novel indirect-drive regenerative shock absorber for energy harvesting and comparison with a conventional direct-drive regenerative shock absorber*. *Journal of Applied Energy*, 229, pp.111-127 [SCImago JCR rank 5/731 in Energy Engineering and Power Technology; Q1–SJR: 3.16, H-index:140, Impact factor: 7.9] [9].

8. **Zhang, R.** and Wang, X., (2019). *Parameter study and optimization of a half-vehicle suspension system model integrated with an arm-teeth regenerative shock absorber using Taguchi method*. Mechanical Systems and Signal Processing, 126, pp.65-81. [SCImago JCR rank 19/101 in Mechanical Engineering; Q1–SJR: 2.067, H-index: 121, Impact factor: 4.37] [10].

9. Liu, Z., Wang, X., Ding, S., **Zhang, R.**, & McNabb, L. (2019). *A new concept of speed amplified nonlinear electromagnetic vibration energy harvester through fixed pulley wheel mechanisms and magnetic springs*. Mechanical Systems and Signal Processing, 126, 305-325. [SCImago JCR rank 19/101 in Mechanical Engineering; Q1–SJR: 2.067, H-index: 121, Impact factor: 4.37] [11].

## Chapter 2

### *Literature review on regenerative shock absorbers*

*In this chapter, the current technologies of the electromagnetic regenerative shock absorber systems have been categorized and evaluated. Three drive modes of the regenerative shock absorber systems, namely the direct drive mode, the indirect drive mode and hybrid drive mode are reviewed for their readiness to be implemented. The damping performances of the three different modes are listed and compared. Electrical circuit and control algorithms have also been evaluated to maximize the power output and to deliver the premium ride comfort*

*and handling performance. Different types of parameterized road excitations have been applied to vehicle suspension systems to investigate the performance of the regenerative shock absorbers. The potential of incorporating nonlinearity into the regenerative shock absorber design analysis is discussed. The research gaps for the comparison of the different drive modes and the nonlinearity analysis of the regenerative shock absorbers are identified and, the corresponding research questions have been proposed for future work.*

## 2.1 Introduction

The power output of the electromagnetic energy harvesting system depends on total resistance and voltage output which, according to Faraday's law of induction, can be expressed by:

$$U = Bl \cdot v \quad (2.1)$$

Where B is the magnetic field intensity, l is the total coil length and v is the coil speed with respect to magnets.

Therefore, the increase of the system power output can be realized through the improvement of the coil and magnet arrangement and configuration or amplification of the coil speed with respect to magnets. These are two main focuses of the recent development innovations for the electromagnetic regenerative shock absorbers.

The direct drive system has the magnets and coils directly attached to the vehicle body and wheel assembly, respectively. When subjected to the reciprocating movement due to the road unevenness, the relative motion between the magnets and coil generates electricity as a result of the direct attachment to the oscillators. Therefore, the coil speed with respect to the magnets strictly depends on the relative speed between the vehicle cabin and wheel. The relative speed depends on the driving speeds of the vehicle and road profiles. As a result, only the electromagnetic constant  $Bl$  can be designed, changed and optimized to increase the power output.

Instead of increasing the electromagnetic constant  $Bl$  of the direct drive system, an indirect drive system relies on the speed amplifying mechanism which can increase the coil speed with respect to the magnets. Most of the regenerative shock absorber can be categorized into these two drive modes for adaption with the requirements of energy harvesting and vibration control.

For the direct drive system, the efforts were most focused on finding the optimum magnet arrangement with a higher flux gradient per unit mass [12-14], as well as the optimum coil profile [15] and the optimum mass distribution of the transducer [16]. However their feasibility for the application of the shock absorber is still undetermined. Whereas for the indirect drive system, questions have been raised on maintaining the ride comfort and road handling ability since it is the main function of the shock absorber, therefore the



compatibility of the indirect drive regenerative shock absorber onto the vehicle would also be focused in the future.

Many innovative designs including different types of the transducers had been proposed, such as piezoelectric, electromagnetic, magnetorheological, hydraulic and pneumatic transducers [17-21]. Each of these types had its own advantages and disadvantages and was only applicable in certain applications. Due to the packaging size and mass restrictions of the shock absorber, the transducers are hard to be fairly compared to determine which type is most suitable for the application of the shock absorbers.

In order to maximize the energy harvesting efficiency, further investigations have been conducted on the electrical circuits and control algorithms. Because of the variation of the transducers utilized in the harvester, different electrical circuits and control algorithms may not work equally well, what is the combination of the transducer and the electrical circuit and control algorithm for the highest energy harvesting efficiency taking into account the input and output requirements of the shock absorber? The question has not been answered yet.

This chapter will review the regenerative shock absorbers based on their drive modes, the studies of the damping performance, efficiency analysis as well as the electrical circuit and control algorithm will be presented. The excitation input of the regenerative shock absorber will be applied as sinusoidal, step and random inputs. Lastly, the possibility and potential of the nonlinear regenerative shock absorber will be discussed.

## 2.2 Direct drive regenerative shock absorber systems and their technologies

A direct drive system has attracted substantial amount of interests due to its compact design and simple manufacturing. Zuo, Scully [22] proposed a 1:2 scale linear regenerative shock absorber system with longitudinal magnet arrangement patterns. Also, an aluminium centre rod and steel outer shell was added to increase the magnetic field intensity. This prototype was able to produce 2-8 W power and it was found that more power can be harvested at the modal resonant frequencies.

### *2.2.1 Magnet arrangement pattern design*

In order to further increase the magnetic field intensity for high output power, different magnet patterns were proposed. One of the easiest ways is to double the number of the magnets, resulting in more magnetic flux lines that can be trapped in between two layers of magnets where the coils are wired, thus increasing the output voltage. Many researchers have adopted this way in their designs as it is efficient and simple to build [23-25].

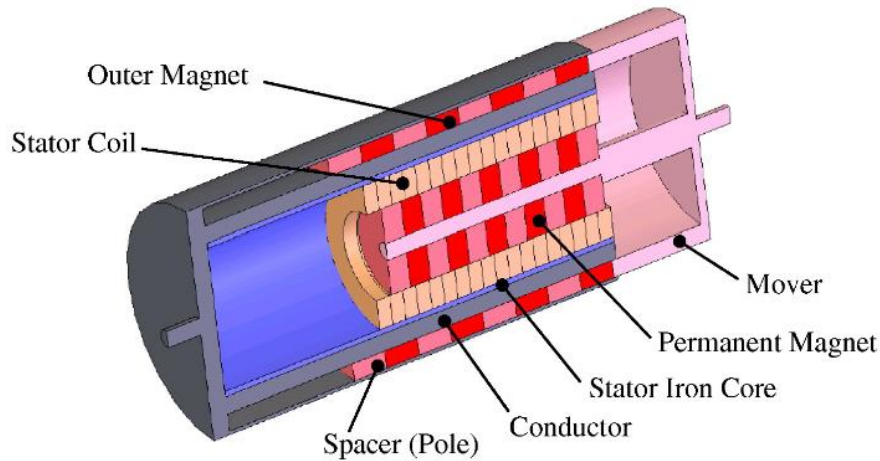


**Figure 2.1: Design of the electromagnetic damper with two layers of magnets [24].**

It is also shown in Figure 2.1 that in a magnet stack, the magnets are not placed right next to each other, instead they are separated by spacers. The same layout was adopted by Cheung [26] who proposed a magnet sliding tube designed for harvesting wave energy where the net flux density in the spacer area between two opposing polarity magnets is zero due to the complete flux cancellation as shown in Figure 2.2 where Case A represents the separation, in this case, flux cancellation did not take place due to the short ranged magnetic potential, the behaviour was just the sum of two isolated single magnets. Cases B and C represent the separation decreased, in these cases, the flux cancellation effect became more prominent and the amount of captured energy increased accordingly to reach a maximum at a gap of about  $\frac{1}{3}$  of the magnet length. The captured energy in this case increased by 60%. However, the two side peaks remained nearly unchanged because of the end effect. As the thickness of the spacer gradually decreases (from A to C), the effect of the flux cancellation decreases and the captured energy reaches the maximum when the spacer had the same thickness of a magnet. As a result, the captured energy can be increased by 60%. The same result was obtained by

Ebrahimi, Bolandhemmat [24] who concluded that magnet stack can yield the highest output power with spacers of equal thickness.

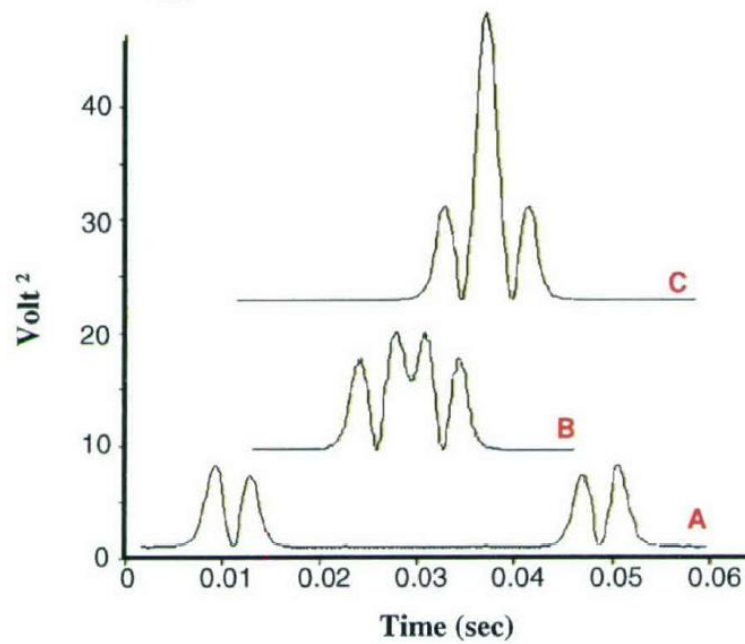


Figure 2.2: Captured energy versus the dimension of a spacer between two magnets [26].

The main limit involved in using two layers of magnets or spaced magnets is the problem of the extra weight. The excessive weight will result in more fuel consumption, which is contradictory to the original purpose of the regenerative shock absorber.

The magnetic arrangement pattern of the Halbach array was studied by many researchers for its high weighted magnetic flux density compared with other magnet arrangement patterns. As shown in Figure 2.3, by turning the polarity orientation of the magnets 90 degree each time to form a Halbach array, the magnetic flux lines can be accumulated on one side of the Halbach array that is close to the coils, leaving nearly zero magnetic field intensity on the other side of the Halbach array. The effects of Halbach array on the energy harvesting

performance of a regenerative shock absorber system was investigated by Zhang [2]. He discovered that the Halbach array has the highest magnetic flux density compared to the conventional longitudinal and transverse magnet polarity orientation layouts with or without the spacer shown in Figure 2.4, because the radial magnets in Halbach array arrangement perform better than the other magnet arrangement in achieving the high magnetic flux density.

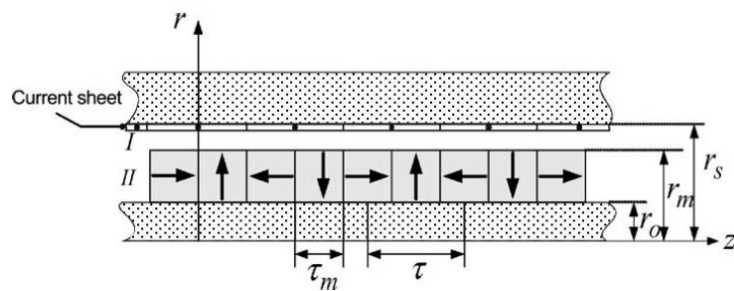
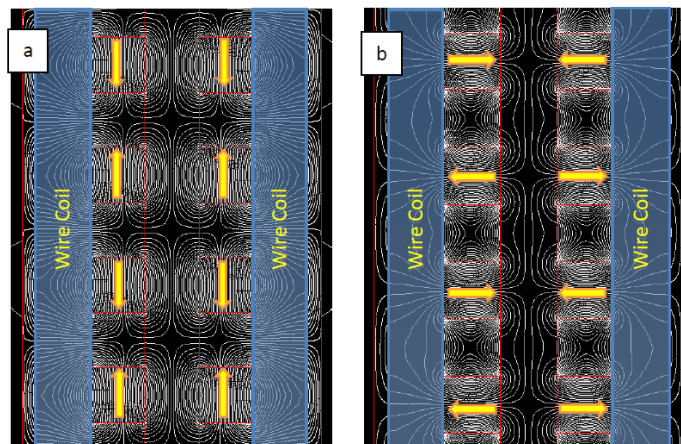
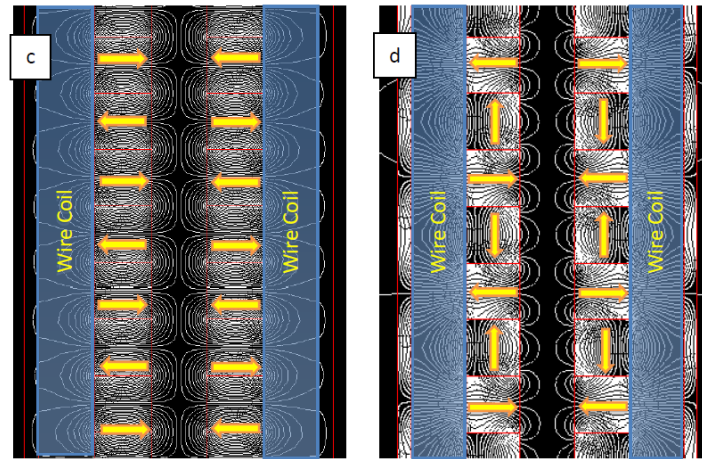


Figure 2.3: Halbach array magnet stack [27].





**Figure 2.4: Magnetic flux plots of (a) longitudinal pattern with spacer, (b) transverse pattern with spacer, (c) transverse pattern, (d) Halbach array[2].**

Zhu, Beeby [28] designed a vibrational energy harvester using the magnet arrangement pattern of the Halbach array and compare the Halbach array with 4 other different magnet arrangement patterns shown in Figure 2.5. It was found that the magnetic field strength in the Halbach array is highest among all the magnet arrangement patterns. However, the voltage output of the Halbach array pattern with spacers is greater than that of layout (a) and (b) but almost 10 times smaller than layout (c) and (d). This is because although the Halbach array has a stronger magnetic field, its magnetic flux gradient is lower than that in (c) and (d). Therefore, it should be realized that the Halbach array may not be the solution for all the problems in question and reducing the thickness of magnets can lead to better results. But in the research, longitudinally arranged polarity orientation of the magnets was not taken into consideration, thus the most efficient magnetic arrangement was still unclear.

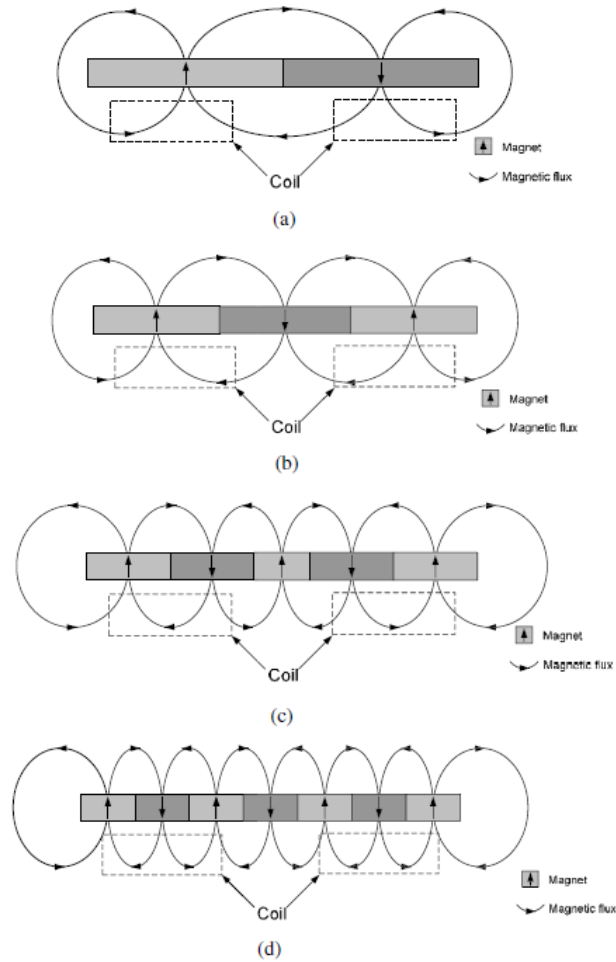


**Figure 2.5: Different number of magnets in the transverse array for comparison with the Halbach array [28].**

The use of the Halbach array magnet arrangement pattern can also be helpful in obtaining the enhanced dynamics. Long, He [29] designed a suspension system utilizing the magnets arranged in Halbach array to obtain a good damping performance. It has been experimentally validated that the Halbach array with a controller can improve the system stability. Some researchers combined the two above-mentioned methods and proposed the double layers of the Halbach array magnet arrangement [25, 28, 30-33].

### 2.2.2 Coil design

Regardless of which magnetic pattern is being used in the regenerative shock absorber, some studies suggested designing the coil based on the magnet arrangement. Tang, Lin [25] proposed to use a four phase coil in one magnetic cycle, as shown in Figure 2.6. The reason for that is shown in Figure 2.7 where higher normalized power can be obtained with higher coil phase number. More electromotive potential would be cancelled out if less coil phases are adopted.

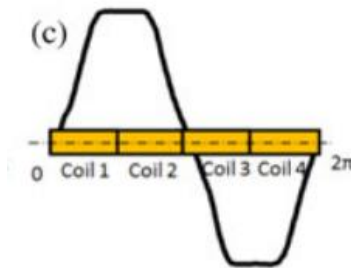


Figure 2.6: Four-phase coil design [25].

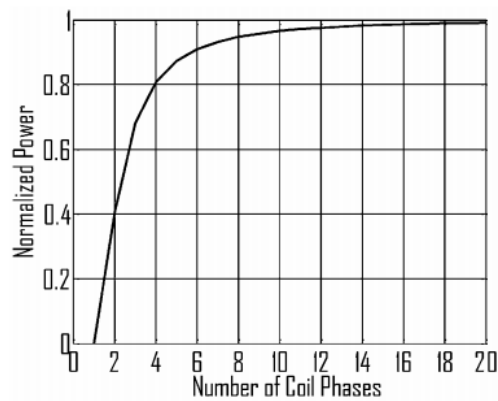


Figure 2.7: Normalized power vs number of coil phases [25].



The coil profile was investigated by Elvin and Elvin [34] on the effect of the number of coil layers, coil resistance and gauge numbers. The results showed that with more number of layers more energy can be generated until it reaches its limit where too much energy begins to be dissipated due to the resistance of the extensive coil. Also the use of a coil with less gauge number will not yield higher voltage but it has the commercial benefits and takes up less space. Different regenerative shock absorbers with the direct drive systems have been summarized below in Table 2.1.

**Table 2.1: Summary of the direct drive regenerative shock absorber**

| Presenter                | Mechanism                                 | Voltage output (V) | Power output(W) | vehicle(km/h) or road excitation amplitude and frequency (Hz) | Energy harvesting efficiency |
|--------------------------|---|--------------------|-----------------|---|------------------------------|
| Zuo, Scully [22]         | Electromagnetic system                    | 10V                | 8W              | 4Hz   | N/A                          |
| Goldner, Zerigian [35]   | Electromagnetic system                    | 1.3V               | N/A             | 2mm at 20Hz   | N/A                          |
| Gupta, Jendrzejczyk [23] | Electromagnetic system with two layers of | 2.52V              | 54W             | N/A   | N/A                          |

|                      |   |      |        |                         |       |
|----------------------|---|------|--------|-------------------------|-------|
|                      | magnets   |      |        |                         |       |
| Xie and Wang [36]    | Piezoelectric material                              | N/A  | 738W   | 126Km/h on class D road | N/A   |
| Sapiński, Rosół [37] | Electromagnetic system                              | 10V  | N/A    | 4.5mm at 10Hz           | N/A   |
| Tang, Lin [38]       | Electromagnetic system                              | N/A  | 2.8W   | 5mm at 10Hz             | N/A   |
| Wang, Ding [39]      | Electromagnetic system                              | N/A  | 24.78W | N/A                     | 20.1% |
| Asadi, Ribeiro [40]  | Electromagnetic system                              | N/A  | N/A    | 4.03mm at 10Hz          | N/A   |
| Chen and Liao [17]   | Combination of MR damper and electromagnetic system | 1.9V | N/A    | 3mm at 1Hz              | N/A   |
| Sapiński, Rosół [37] | Combination of MR damper and electromagnetic system | 2V   | 0.4W   | 4.5mm at 4Hz            | N/A   |

## 2.3 In-direct drive regenerative shock absorber systems and their technologies

Due to the weight limit of the magnets and coils, many attempts have been made to increase the coil speed with respect to the magnets.

The in-direct drive regenerative shock absorber system does not transfer the road excitation directly into the linear motion between the translator and the stator. Instead, it amplifies the input excitation through a variety of mechanisms and converts the linear motion mostly into a rotational motion. Many types of mechanisms that have been proposed include: the ball screw mechanism, rack and pinion mechanism, hydraulic mechanism, pneumatic mechanism and their variants. Among these mechanisms, the ball screw, rack and pinion and their variants can be regarded as mechanical motion rectifier due to the mechanical mechanism related working principle. The devices that utilize the hydraulic system or pneumatic system to deliver motion conversion and velocity amplification can be regarded as a fluid motion rectifier.

### *2.3.1 Mechanical motion rectifier*

Li, Zuo [41] proposed an innovative motion rectifier system, which can convert the up and down movement of the shock absorber into unidirectional rotation of the generator, shown in Figure 2.8. The rack and pinion mechanism helps to convert and amplify the excitation displacement. The bidirectional linear motion to unidirectional rotation rectification is accomplished with the bevel gear and clutch. The experiments and simulations were carried out by the researchers and it showed that the prototype achieved over a high efficiency of 60% and 15 W power output was obtained when the vehicle is driven at a speed of 15 mph. Further investigation was conducted by Li and Zuo [42] to evaluate the performance of the prototype. A quarter car suspension model was constructed to simulate the situation where vehicle was driven on the ISO Class C road. It was found that the motion rectifier can achieve the road comfort and the road handling on a conventional vehicle. 60-84 W can be harvested from a quarter car regenerative suspension with the motion rectifier when travelling at 67.5 mph, which is more than that from the quarter car regenerative suspension without the motion rectifier.

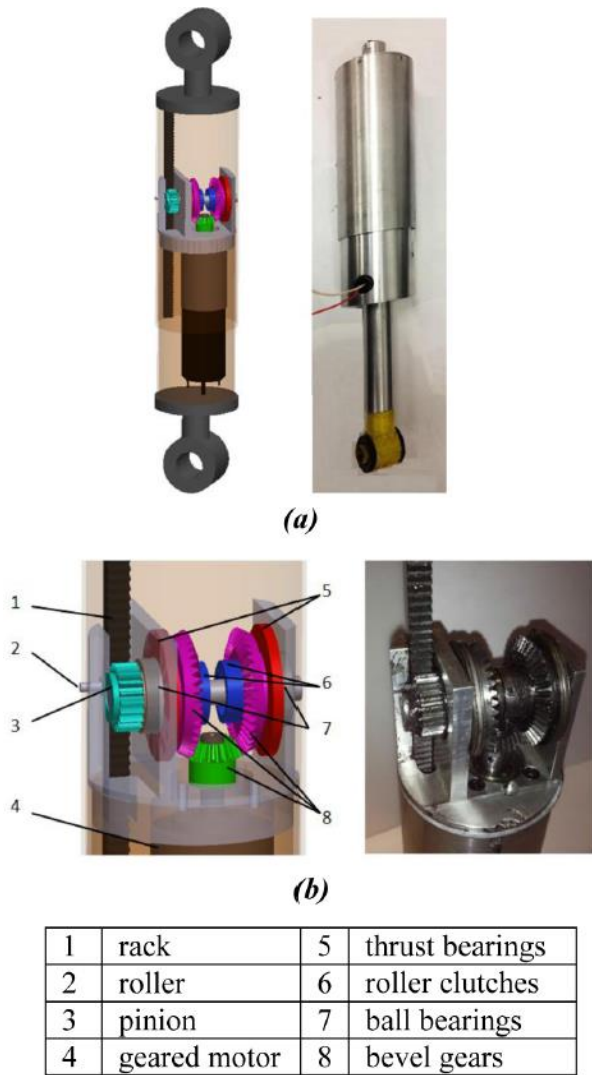


**Figure 2.8: Mechanical motion rectifier proposed by Li, Zuo [41]**

Zhang, Zhang [43] and Guo, Liu [44] optimized the mechanical motion rectifier by proposing the dual overrunning clutch system. Two sets of racks and pinions and the 2 overrunning clutches attached allow the excitation amplification and motion rectification to occur simultaneously with limited space provided. The shaft rotates in one direction and drives the DC generator for power generation. The working principle is shown in Figure 2.9. The generated power was stored in the capacitor for other application. The fabricated prototype

generated 4.302 W at 2.5 Hz with the excitation displacement amplitude of 7.5 mm. Additionally, the damping performance can be changed by adjusting the external load electric resistance.

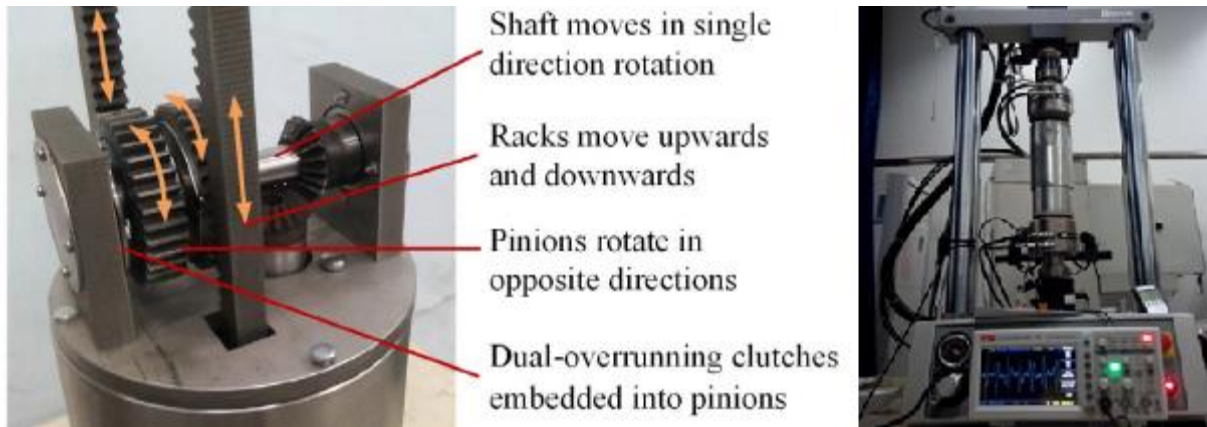


**Figure 2.9: Dual overrunning clutch transmission system [43].**

Another interesting design was proposed by Xie, Li [45]. Unlike other rack pinion system where the electrical generator provides the damping force, this design utilizes the traditional viscous damper in parallel with the secondary rack and pinions at the bottom, to provide damping and harvest energy. Considering the packaging size, however, this layout may not be feasible in a real application.

Ball screw mechanism was introduced as an alternative by many researchers [46-50], the schematic is shown in Figure 2.10. Similar to the rack and pinion system, it also converts the up and down motion into a rotational motion through a ball screw spinning along the thread. Due to the up and down movement of the shock absorber, the converted rotational motion is

bidirectional and needs rectification as well. Zhang, Huang [51] incorporated the ball-screw mechanism and DC brushless motor into a regenerative shock absorber system. The experiment result showed that the maximum voltage of 17.5V can be generated under the sine wave road input. Because of the low voltage, a condenser is needed to charge the battery. It was also pointed out by the author that the ride and comfort performance cannot be guaranteed under a high frequency road excitation.

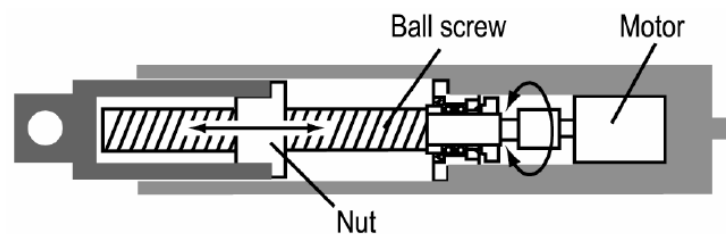


**Figure 2.10: Ball screw indirect drive regenerative shock absorber system [52]**

Another combined innovation on regenerative shock absorber was proposed by Liu, Xu [53] where a ball screw was installed for the conversion from the linear to rotary motion and two overrunning clutches were used for the rectification from the bidirectional to unidirectional motion, as shown in Figure 2.11. The input velocity amplification factor can be adjusted through a ball screw mechanism and kinetic energy can be harvested throughout the whole reciprocating motion of the shock body. The experimental results indicate that an average power output of 24.7 W can be harvested over an 8 s period, and the adjustable damping coefficient can be maintained close to the damping coefficient of the passenger vehicle shock absorbers.

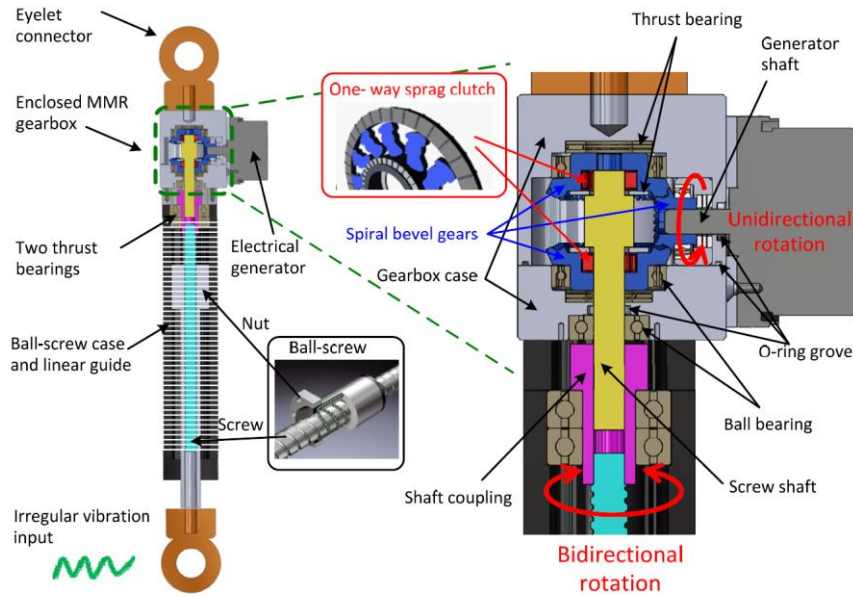


**Figure 2.11: The design of a mechanical motion rectifier based the energy-harvesting shock absorber using a ball-screw mechanism [53]**

### 2.3.2 Fluid motion rectifier

Instead of converting the axial motion into rotational motion mechanically, the hydraulic/pneumatic systems were introduced in many energy harvester designs for smoother operation and less mechanical friction energy dissipation [20, 54-60]. Like the other indirect drive regenerative shock absorber systems where the stroke velocity is amplified mechanically, the smoother operation and the motion rectification can be delivered simultaneously in the hydraulic system. Among all these innovations, Fang, Guo [61] developed an actively controlled hydraulic suspension system by using an oil pump to generate hydraulic pressure in the shock absorbers, as shown in Figure 2.12. The system had one-way check valves to control the direction of fluid flow, accelerometers in all four



corners, and actuators and accumulators, to reduce the response time in the system and ensure that sufficient pressure is maintained in the system. Wang, Gu [62] proposed the similar hydraulic system with four check valves for flow rectification and found that the accumulators can be optimized to increase the power efficiency up to 40%.

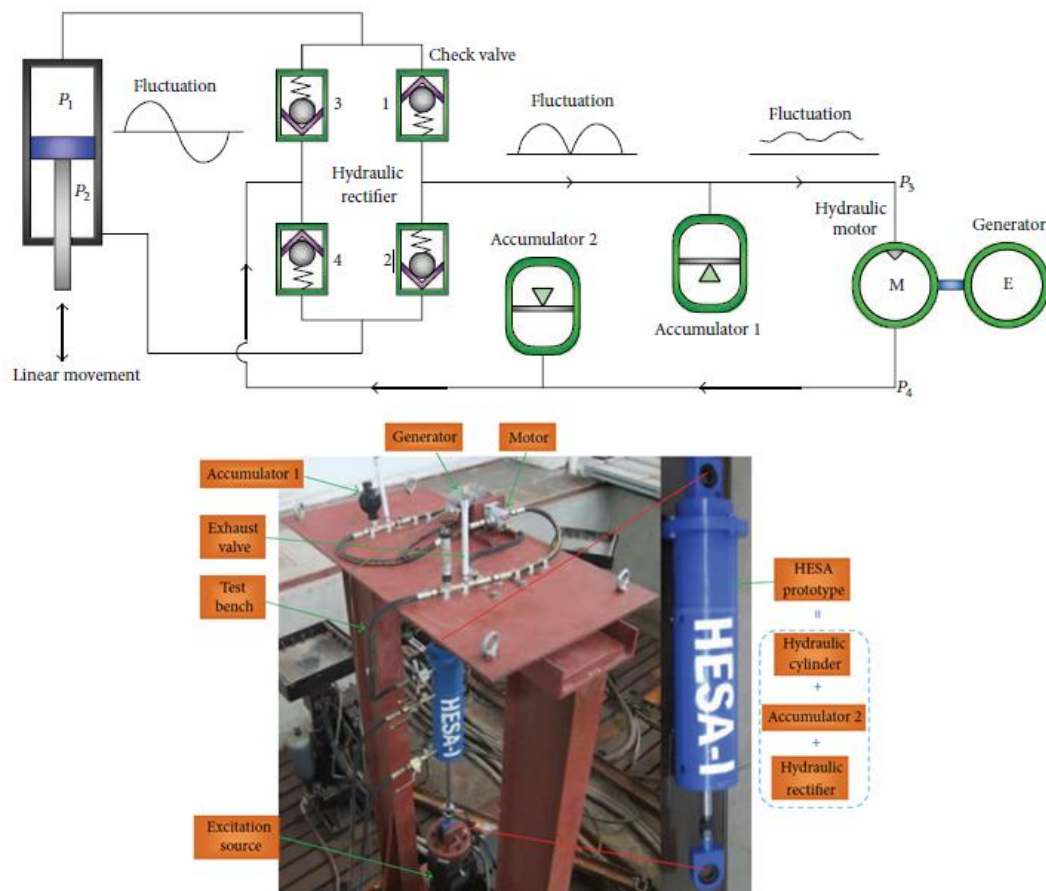
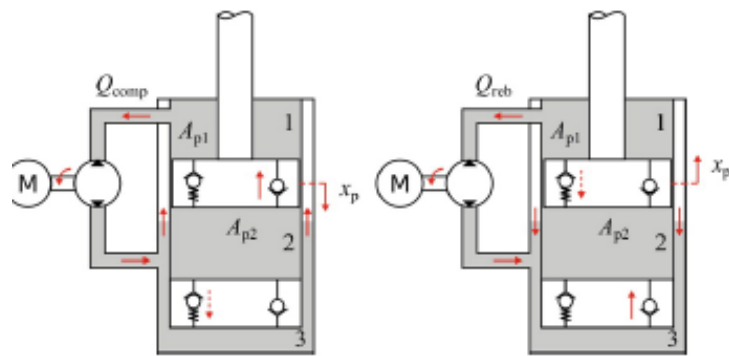


Figure 2.12: The hydraulic shock absorber prototype [61]

The drawback of the hydraulic/pneumatic energy harvesting system is that the response time is delayed due to the flow rate and fluid compressibility, also, the rupture may lead to potential failure, resulting in an unreliable system that can cause accidents. To simplify the

system, Galluzzi, Tonoli [63] developed a hydraulic regeneration system where check valves are placed inside the hydraulic piston to reduce the mechanical difficulty while amplifying the stroke velocity, as shown in Figure 2.13. The results show a 12% increase in harvested power over the regenerative shock absorber system without the proposed mechanical motion rectifier.



**Figure 2.13: Working principle of the hydraulic regenerative shock absorber system without a mechanical motion rectifier [63]**

Pneumatic suspension system was adopted by many vehicles especially in off road applications [64] due to its high energy density which meets the space limitation [65], and its comfort and changeable damping performance [66]. It can be converted into a regenerative system with the additional energy converting elements[67]. Shaiju and Mitra [68] proposed the idea where the oscillating motion energy of the vehicle sprung mass could be captured and stored in the form of compressed air energy. The theoretical results also showed that the vehicle dynamics could be improved by the pneumatic suspension system through being integrated with the braking system. The pneumatic system operates in a similar way as the

hydraulic system due to the similar flow property, many authors regarded them as the same system [24, 69]. Due to the compressible nature of air, however to some extent, the pneumatic system performs differently from the hydraulic system. Therefore, evaluation of the energy harvesting performance of the pneumatic regenerative shock absorber is identified as a research gap because few people have worked on it. Different indirect drive regenerative shock absorber systems have been summarized below in Table 2.2.

**Table 2.2: Summary of the indirect drive regenerative shock absorbers**

| Presenter                | Mechanism  | Voltage output (V) | Power output(W) | vehicle(km/h) or excitation frequency (Hz) | Energy harvesting efficiency |
|--------------------------|--|--------------------|-----------------|--|------------------------------|
| Li and Zuo [42]          | Rack and pinion  | N/A                | 60-84W          | 108km/h on class C road                    | N/A                          |
| Gupta, Jendrzejczyk [23] | Rack and pinion  | 1.1V               | 88.8W           | N/A  | 21%                          |
| Nakano [70]              | Ball-screw   | N/A                | 55.39W          | N/A  | 36%                          |
| Fang, Guo [61]           | Hydraulic system with 4 check valves for rectification | N/A                | 6.2W            | 0.48Hz                                     | 16.6%                        |

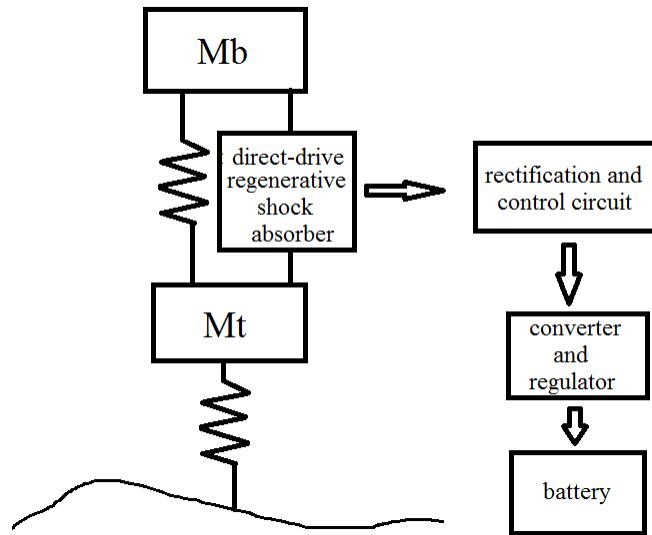
|                                 |  |       |        |                           |        |
|---------------------------------|--|-------|--------|---------------------------|--------|
| Choi, Seong<br>[71]             | Rack and<br>pinion                                 | 15V   | 40W    | 20mm at 3Hz               | N/A    |
| Zhang,<br>Zhang [43]            | Rack and<br>pinion, two<br>overrunning<br>clutches | 3V    | 4.302W | 7.5mm at<br>2.5Hz         | 54.98% |
| Zhang,<br>Huang [51]            | Ball screw   | 15V   | 11.73W | 5mm at 15Hz               | N/A    |
| Chu, Zou<br>[72]                | Rod and<br>helical slot                            | 3.31V | 11.3W  | 0.94mm at<br>11Hz         | 77%    |
| Wang, Gu<br>[62]                | Hydraulic<br>system                                | 20V   | 260W   | 25mm at 1Hz               | 40%    |
| Sabzehgar,<br>Maravandi<br>[73] | Algebraic<br>screw                                 | N/A   | 0.54W  | 3.05mm at<br>5.6Hz        | 56%    |
| Liu, Xu [53]                    | Ball screw<br>with two<br>one way<br>clutches      | N/A   | 24.7W  | 2mm at 4Hz                | 51.9%  |
| Kawamoto,<br>Suda [49]          | Ball screw   | N/A   | 44W    | 80km/h on<br>class C road | N/A    |
| Zhang,<br>Zhang [74]            | DC<br>generator<br>connected                       | N/A   | 33.4W  | 50mm at<br>1.67Hz         | N/A    |

|                       |                                    |     |     |     |     |
|-----------------------|------------------------------------|-----|-----|-----|-----|
|                       | to the hydraulic actuator          |     |     |     |     |
| Shaiju and Mitra [68] | Pump powered by the compressed air | N/A | N/A | N/A | N/A |

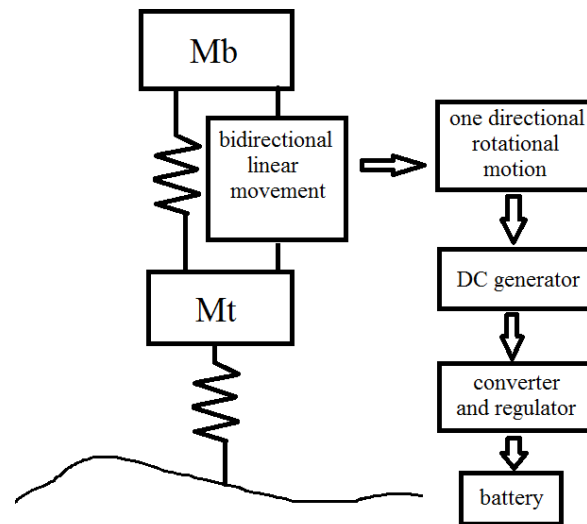
## 2.4 Comparison between the direct drive system and the indirect drive system

The regenerative shock absorber system can be divided into two main categories based on the drive mode. If the energy can be regenerated directly as a result of the linear movement between the two oscillators, namely the wheel assembly and the vehicle body, it can be categorized as the direct-drive regenerative shock absorber system. The other type, which is the indirect drive regenerative shock absorber system, relies on a certain mechanism to achieve the conversion between the linear motion of the shock absorber and the rotary motion of the generator. During this process the input speed can be amplified by the mechanism. The 2DOF lumped mass spring systems can be applied to represent the quarter car suspension

systems with these two categories of the regenerative shock absorber systems, as shown in Figure 2.14.



(a)



(b)

**Figure 2.14: (a) Direct drive regenerative shock absorber system. (b) Indirect drive regenerative shock absorber system.**

Compared with the direct drive system, the indirect drive system has the following advantages:

1. The frequency, displacement and velocity amplitudes of the input excitation can be changed through the installed mechanism to achieve better energy harvesting and vehicle dynamics
2. The increase of the input excitation speed through the speed amplifying mechanism can eliminate the need for a strong magnetic field, therefore the amount of magnets can be reduced and undesired additional weight can be minimized.
3. The layout of the system is more flexible as the mechanism of the indirect drive does not have to be inside the shock absorber

In Figure 2.14, another noticeable difference between these two drive modes is that the direct drive system has the AC output and the indirect drive has the DC output. As a result, the voltage output of the direct drive system needs rectification before charging the battery whereas in the indirect drive system, the unidirectional rotation of the DC motor have a constant DC output thus the rectification process is not required. Regulation or dc-dc inverter is needed for both systems to maintain a steady constant voltage for effectively charging a battery.

To compare the energy harvesting performance of the regenerative shock absorbers with different drive modes, Gupta, Jendrzejczyk [23] have both direct drive and indirect drive regenerative shock absorbers installed on an all-terrain vehicle (ATV) passing a wooden beam, shown in Figure 2.15. Mark 1 shock absorber is a direct drive linear electromagnetic generator with two layers of magnets and mark 2 is an indirect drive system with a lever arm that can convert the linear motion into rotary motion where the input speed is amplified 6 times. The results showed that when running over the wooden beam, direct drive system can generate 7.4W while the indirect drive system can generate 88.8W.

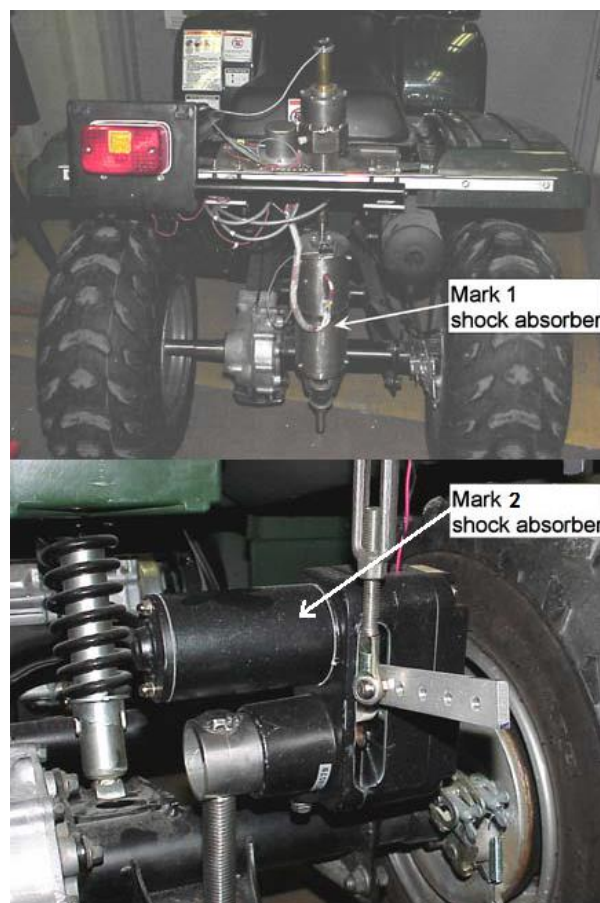


**Figure 2.15: Direct drive linear regenerative shock absorber (Mark 1) and indirect drive ball screw regenerative shock absorber (Mark 2) installed on the same ATV [23].**



Even though the results indicated a considerable difference between the amounts of the harvested power, it cannot be concluded that the indirect drive system is more efficient than the direct drive system. In most of the studies that compare the drive modes, the generator configurations differ as the direct drive system has a linear generator and the indirect drive system has a rotary generator, hence the difference of the generator configurations results in the difference of the energy output. In addition, the damping coefficients of the regenerative shock absorbers and their effects on the vehicle dynamics should also be evaluated.

For the indirect drive system with the fluid motion rectifier, Ebrahimi, Bolandhemmat [24] believed that the fluid motion rectifier is heavy, expensive, and consumes too much energy. More disadvantages were addressed by Crolla [67] who pointed out that not only will the fluid leakages and raptures decrease the reliability, but also will they degrade the suspension performance which is limited by the narrow excitation frequency bandwidth of the hydraulic/pneumatic system. Additionally, more energy is dissipated with the increased temperature of the fluid.

Ultimately, considering the difference of the transducers of the different drive modes, it is suggested in future studies to use the same generator constant or electromechanical coupling constant so that the energy generating ability and the motor resistance force can be compared.

## 2.5 Hybrid systems and their technologies

In addition to the direct drive system and indirect drive system, many innovations have been proposed to combine the multiple drive modes together for improving both the reliability and damping performance.

As shown in Figure 2.16, Singh and Satpute [75, 76] proposed a dual cylinder system where the main cylinder works as a shock absorber dampening the vibration through the vehicle suspension and also providing the drive to the secondary cylinder for the velocity amplification. When the secondary cylinder fails, the main cylinder will continue to operate as a passive damper. Considerable amount of energy can be generated without compromising the ride comfort and the road handling performance.

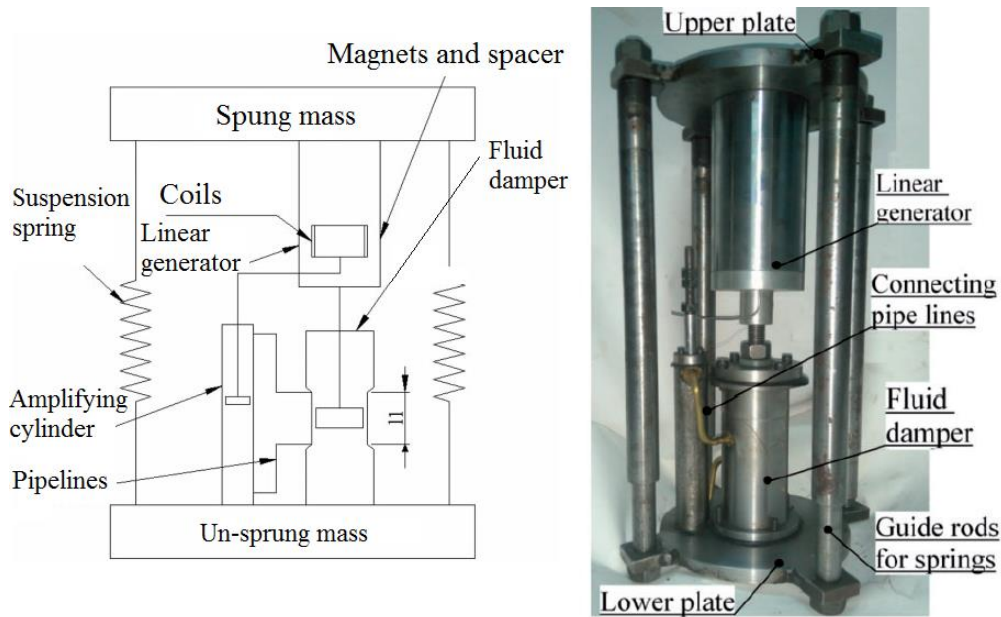


**Figure 2.16: Hybrid dual cylinder regenerative suspension system and its prototype [76].**

A more complex design was proposed by Xie, Li [45] shown in Figure 2.17. The secondary piston driven by the main viscous piston has the rack and pinion mechanism. The DC generator is attached at the bottom of the secondary piston to harvest energy. This layout improves the system reliability with the fail safe mode.

To further reduce the amount of dissipated energy due to the viscosity of the piston liquid, as shown in Figure 2.18, Demetgul and Guney [77] developed a hydraulic regenerative shock absorber that scavenges energy from both hydraulic fluid motion and shock body motion. Both the power generated from the hydraulic piston generator and the linear generator can be used to charge the energy storing devices.

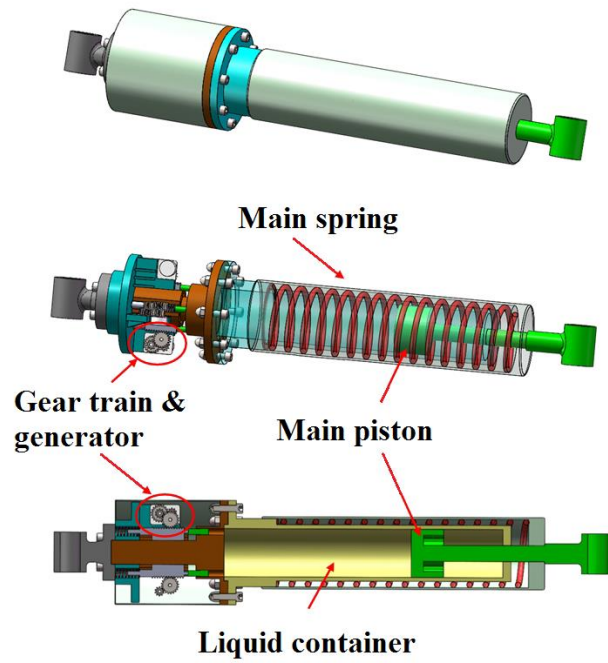


Figure 2.17: The conceptual design of a hybrid regenerative shock absorber [45].

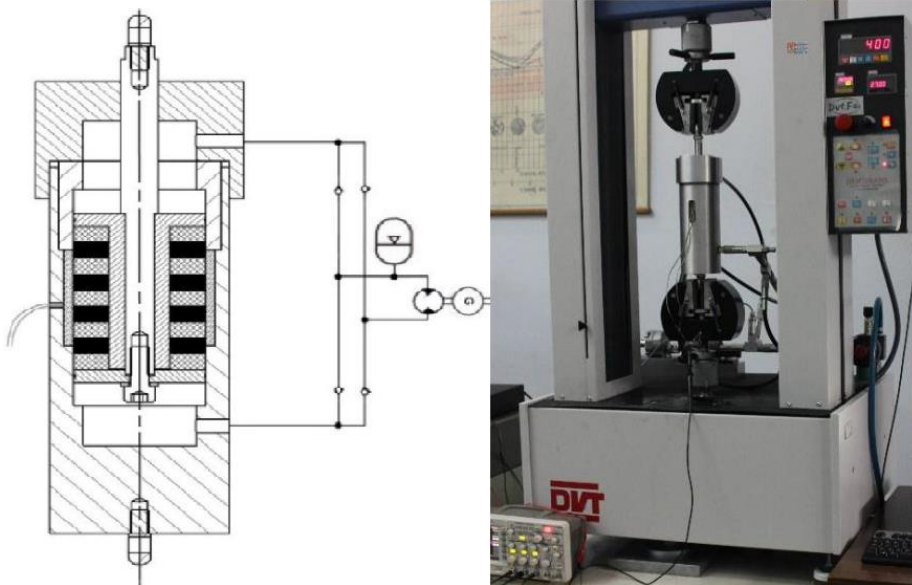


Figure 2.18: The cross-section of the hybrid regenerative shock absorber and its experimental setup [77].

Although most of the hybrid systems have the fail safe mode, the main drawback of the hybrid systems is the low reliability brought by the complexity of the design that can potentially increase the chance of failure. A large number of components can also dissipate additional amount of energy, resulting in lower power output in comparison with the direct drive system and indirect drive system. In addition, the space constraint of the shock absorber makes the hybrid system less plausible. The hybrid systems are summarized in Table 2.3 below.

**Table 2.3: Summary of the hybrid system**

| Presenter              | Mechanism   | Voltage output (V) | Power output(W)  | vehicle(km/h) or excitation frequency (Hz) | Efficiency |
|------------------------|---|--------------------|------------------|--|------------|
| Singh and Satpute [75] | Hydraulic piston with linear electromagnetic generator    | N/A                | 15W              | 35km/h on class C road                     | 13%        |
| Xie, Li [45]           | Secondary piston with rack and pinion to drive the rotary | N/A                | 130W (simulated) | 120km/h on class C road                    | N/A        |

|                               |  |    |  |                     |     |  |
|-------------------------------|--|----|--|---------------------|-----|--|
|                               | generator  |    |  |                     |     |  |
| Demetgul<br>and Guney<br>[77] | Combined<br>linear<br>electromagnetic<br>generator and<br>hydraulic<br>rotary<br>generator | 6V | 0.003W for<br>electromagnetic<br>generator,<br>0.56W for<br>hydraulic<br>generator | 15mm at<br>0.005m/s | N/A |  |

## 2.6 Damping and vehicle dynamic performance

Traditional shock absorbers utilize the viscosity of the fluid inside the cylinder to dampen the vehicle suspension vibration, and the damping coefficient of the shock absorber can be changed by tuning the size of the orifice. Whereas in the regenerative shock absorber where the kinetic energy is converted into electrical energy, the damping effect is entirely or partially contributed by the energy harvesting devices such as a generator.

### *2.6.1 Damping performance of the direct drive system*

The damping coefficient of a passenger vehicle quarter suspension is approximately 1500Ns/m [78] and 8000-10000Ns/m for heavy duty vehicles [79]. According to Yan and Sun [80], equivalent damping coefficient of the electromagnetic generator in the regenerative shock absorber can be expressed by Equation (2.2) if the damping performance is entirely provided by the electromagnetic generator.

$$c_{eq} = \frac{k_i^2}{R} \quad (2.2)$$

where  $k_i$  is the product of the magnetic field intensity and coil length;  $R$  is the total electrical resistance. Therefore for a regenerative shock absorber with a damping coefficient of 1500Ns/m on a passenger vehicle suspension and a  $10\Omega$  electrical resistance, the electromagnetic coupling coefficient is calculated by Equation (2.2) and given by  $k_i = 122.5\text{Tm}$  which is a large value, meaning that it can only be realized using multiple strong magnet arrays and a coil that has sufficient length. The packaging space of a shock absorber is limited, thus making it difficult to provide enough damping performance with only a direct drive system.

In order to meet the damping requirement of the shock absorber for vehicle dynamics, many innovations have been proposed with an additional damper in parallel with the direct drive energy harvester. Asadi, Ribeiro [40] proposed to have a viscous damper and a direct drive linear motor fused together, shown in Figure 2.19. This design enables the regenerative shock absorber to have additional damping performance provided by a hydraulic piston. Experimental results showed that a damping coefficient of 1302-1520Ns/m can be obtained for the regenerative shock absorber.

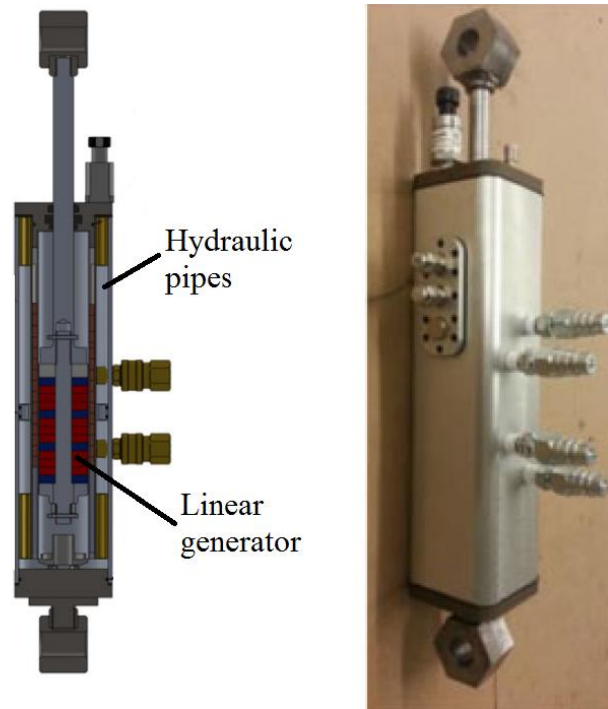


**Figure 2.19: A parallel hydraulic EM damper.**

To further improve the damping performance of the shock absorber, Magnetorheological (MR) fluids are applied to achieve variable damping control. Chen and Liao [17] developed a parallel damper consisting of MR damper and electromagnetic generator, shown in Figure 2.20. The generated power can then be utilized as the power supply for the MR current driver and sensors. A damping force of 700N can be achieved under 11mm excitation at 1Hz and simultaneously a maximum of 2V can be harvested. Damping force control algorithm can also be integrated in the MR energy harvesting damper for optimum vibration control [37, 81].



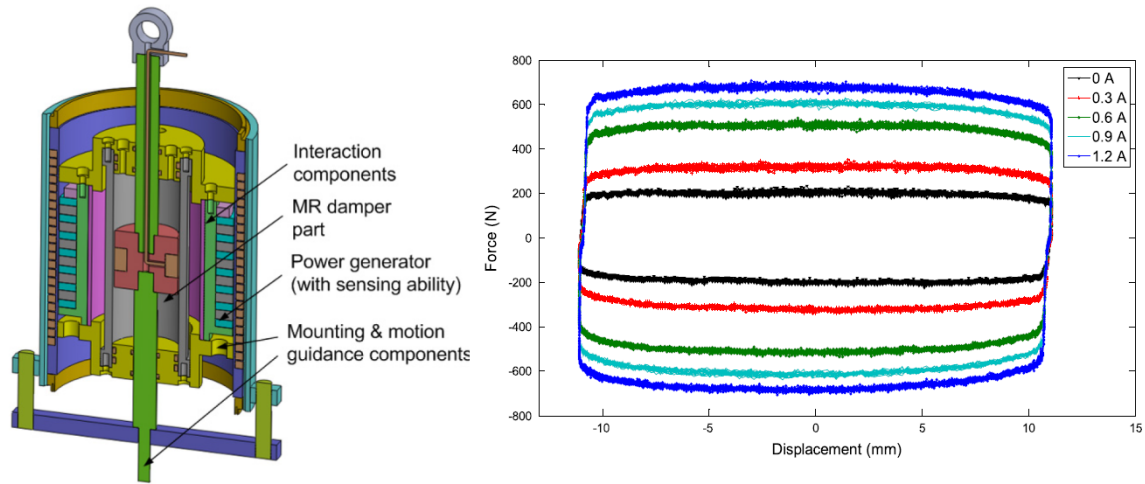


**Figure 2.20: The cross section of the MR regenerative damper and its damping force against the displacement for applied currents.**

### 2.6.2 Damping performance of the indirect drive systems.

For the indirect drive systems, because of the presence of the speed amplifying mechanism, the back electromagnetic force of the generator can be amplified to obtain larger damping. However, one common problem exists in most of the indirect drive systems incorporated with a motion rectifier. During half the time of the conversion from the bidirectional motion of shock body to the unidirectional rotation of the generator, the mechanism becomes disengaged and the generator continues to rotate due to inertia, resulting in the absence of the damping force in half of the motion cycle. The indirect drive systems equipped with one overrunning clutch or one way bearing tend to present such problem, as shown in [49, 51, 70, 73].

To obtain the stable damping force throughout the entire motion cycle, the designs are upgraded with two clutch systems [41, 43, 53]. These two clutches are installed facing each other on the drive shaft and both connected with same output shaft. Therefore when the drive shaft rotates in two directions, one of the clutches will always remain engaged, as shown in Figure 2.21.

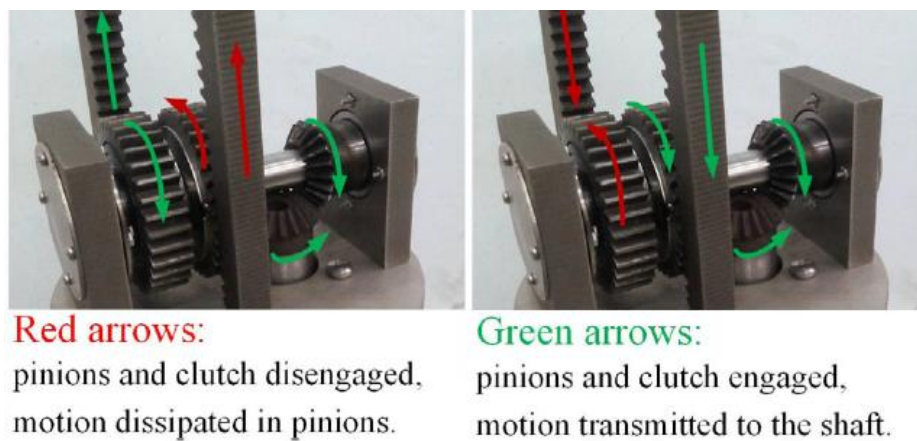


**Figure 2.21: Continuous damping provided by the dual clutches system [43].**

According to Zhang, Zhang [43], the damping force measured experimentally is shown in Figure 2.22, it can be seen that the damping force applies for both compression and recoil phase of the shock absorber with higher frequencies yielding higher damping force.

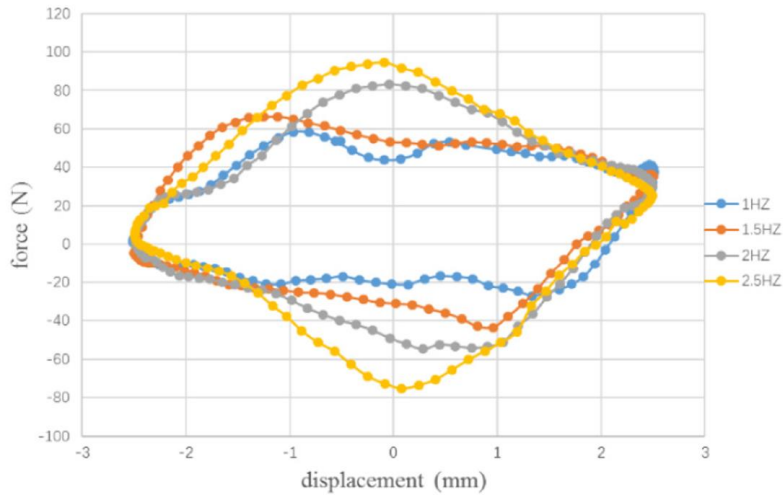


**Figure 2.22: Damping force versus shock absorber displacement for different excitation frequencies.**

In the hydraulic indirect drive systems, the damping force can also apply throughout the whole motion cycle shown in Figure 2.23, as a result of having flow resistance in both directions. Comparing the direct drive with the indirect drive system, the latter has a larger damping coefficient than the former as long as the damping is presented throughout the entire motion cycle. This damping effect is caused by the friction loss of the speed amplifying mechanism and energy loss of the complex mechanism operation. Therefore, a trade-off between the vibration control and energy harvesting need to be reached through a control algorithm. The damping coefficient and force results of the regenerative shock absorbers are compared and listed in Table 2.4 below.

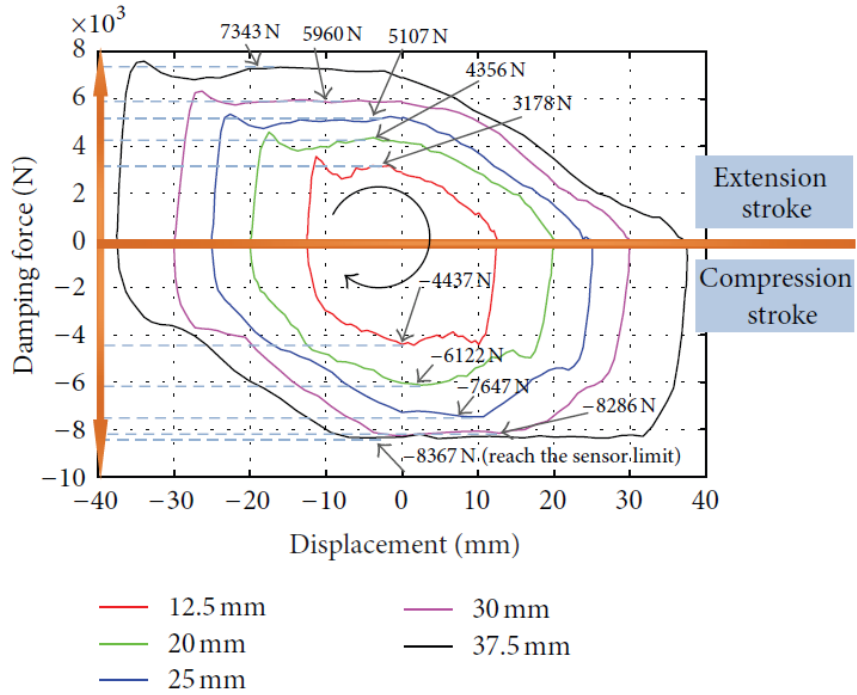


Figure 2.23: Damping force- displacement loops of the regenerative shock absorber [61]

Table 2.4: The summary of the damping performance of the regenerative shock absorbers.

| Presenter            | Mechanism              | Damping coefficient | Maximum damping force |
|----------------------|------------------------|---------------------|-----------------------|
| Direct drive system  |                        |                     |                       |
| Sapiński, Rosół [37] | Electromagnetic system | N/A                 | 520N                  |
| Tang, Lin [38]       | Electromagnetic system | 940Ns/m             | N/A                   |
| Wang, Ding [39]      | Electromagnetic system | 1320Nm/s            | N/A                   |
| Asadi, Ribeiro [40]  | Electromagnetic system | 1302-1540Ns/m       | N/A                   |

|                           |  |             |        |
|---------------------------|--|-------------|--------|
| Chen and Liao [17]        | Combination of MR damper and electromagnetic system    | N/A         | 700N   |
| Sapiński, Rosół [37]      | Combination of MR damper and electromagnetic system    | N/A         | 520N   |
| Indirect drive system     |  |             |        |
| Li and Zuo [42]           | Rack and pinion  | 1425 Ns/m   | N/A    |
| Gupta, Jendrzeczyk [23]   | Rack and pinion  | 38.5 Ns/m   | N/A    |
| Nakano [70]               | Ball-screw   | 7200 Ns/m   | N/A    |
| Fang, Guo [61]            | Hydraulic system with 4 check valves for rectification | N/A         | 7343N  |
| Choi, Seong [71]          | Rack and pinion  | N/A         | 700N   |
| Zhang, Zhang [43]         | Rack and pinion, two overrunning clutches              | 1637.2 Ns/m | N/A    |
| Chu, Zou [72]             | Rod and helical slot                                   | N/A         | 600N   |
| Wang, Gu [62]             | Hydraulic system                                       | N/A         | 10000N |
| Sabzehgar, Maravandi [73] | Algebraic screw  | 237Ns/m     | N/A    |
| Liu, Xu [53]              | Ball screw with two one way clutches                   | 15420 Ns/m  | N/A    |
| Zhang, Zhang [74]         | DC generator connected to the hydraulic actuator       | N/A         | 1450N  |
| Hybrid system             |  |             |        |

|                           |   |           |     |
|---------------------------|---|-----------|-----|
| Singh and Satpute<br>[75] | Hydraulic piston with linear<br>electromagnetic generator | 1898 Ns/m | N/A |
|---------------------------|---|-----------|-----|

## 2.7 Circuit and control algorithms for enhancing power output and vehicle dynamics

The regenerative shock absorber system can generate power for electrical applications. Due to the difference in the power requirement between the power generating element and the power receiving element, the regulation and rectification are essential for the electrical circuits of energy harvesting and storage. In addition, the control parameters may influence the dynamic performance of the vehicle suspension system and energy dissipation performance [82]. Therefore control algorithms need to be incorporated to improve vehicle dynamics and/or the energy harvesting ability by adjusting the parameters according to the input excitation levels [83].

### 2.7.1 Power maximization

Because the direct drive system has AC output and the indirect drive system has DC output, to obtain the steady DC current for charging battery, many direct drive systems incorporated the rectification bridges [22, 39, 84], as shown in Figure 2.24.

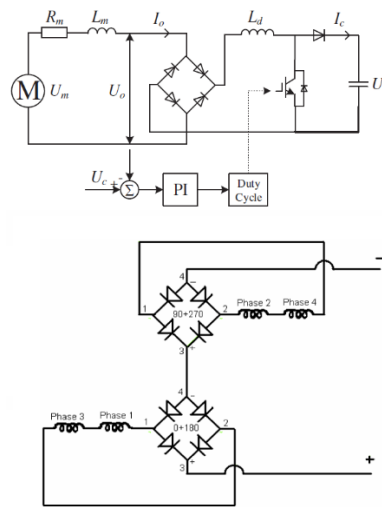


**Figure 2.24: Single bridge rectifier (top) [39], two bridge rectifiers in series (bottom) [22]**

A drawback of this layout is that a full wave rectified output is a pulsed DC and it is advisable to add a reservoir capacitor for smoothing out the variations. An excessive number of diodes would also consume electrical energy. Arroyo, Badel [85] proposed the SMFE circuits with only two diodes, shown in Figure 2.25 (top). The SMFE stands for synchronous magnetic flux extraction and it's suitable for electromagnetic vibrational energy harvesting.

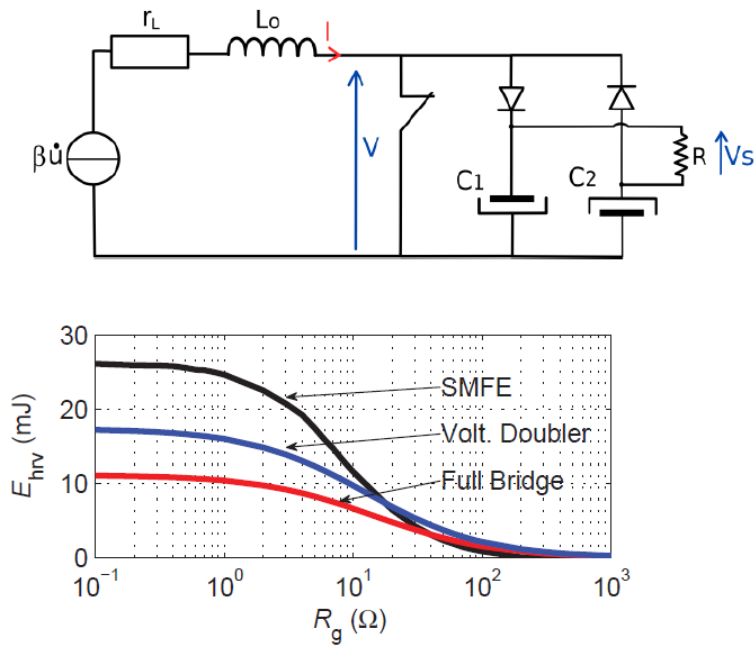


Figure 2.25: The SMFE circuit (top) [86] and energy extraction for different circuits (bottom) [87].

Based on the research conducted by Sanchez, Jodka [87] shown in Figure 2.25 (bottom), with the same generator resistance, the SMFE method can extract higher amount of energy than that with a voltage doubler circuit or full bridge rectifier. Another advantage brought by using the SMFE other than simply using shunt resistance is that it also incorporates the rectification and amplification of the voltage, thus increasing the efficiency of the electromagnetic energy harvester [88]. For the similar purpose, Dwari and Parsa [89] proposed an AC-DC step-up converter that can be applied on regenerative shock absorber to charge the battery, as shown in Figure 2.26. It consists of a boost and buck boost converter connected in parallel and achieves an efficiency of 61% which is better than that by using a conventional bridge rectifier.



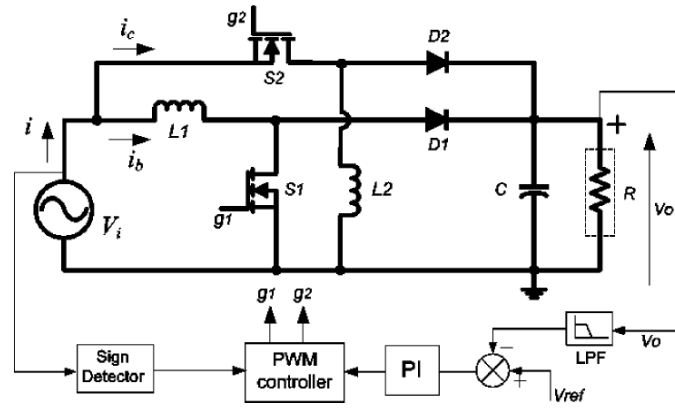


Figure 2.26: Direct AC-DC step-up converter [89].

For the indirect drive system, due to the motion rectifier, the bidirectional to unidirectional conversion of output voltage is no longer necessary. In many designs [74, 77, 90], the DC generator is characterized by an internal inductance and a resistance, and is connected to a single external resistance over which the power can be extracted, as shown in Figure 2.27. However, under the random road excitations, in order to charge the energy storing devices, a regulator needs to be included in the circuit as the generator voltage output needs to be regulated to steadily stay at a certain voltage level. Therefore, many efficient DC-DC converters are proposed in accordance with the targeted output ranges [91-93].

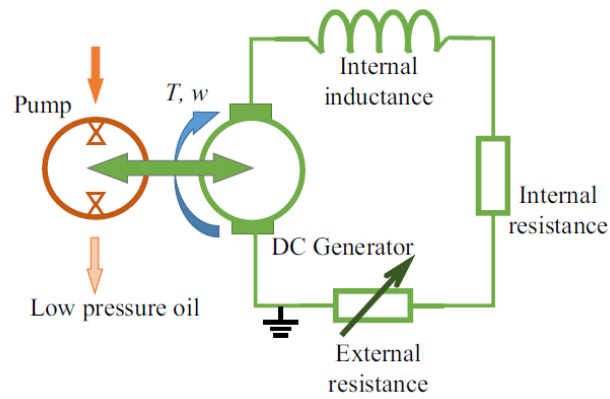
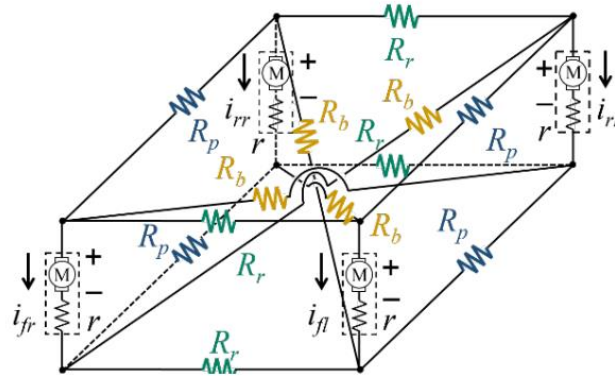


Figure 2.27: Electrical circuit of a hydraulic indirect drive regenerative shock absorber [74].

### 2.7.2 Vehicle dynamic control

In addition to energy harvesting, most of the regenerative shock absorber systems operate inversely as a part of the active suspension system or semi-active suspension system when the external power is applied [94]. Many studies have been done on how to improve vehicle dynamics with the electromagnetic shock absorber [95-103].

Fukumori, Hayashi [46] [104] conducted the experiments using coupled electromagnetic dampers that can tune the bouncing and rolling modal frequencies of the vehicle independently through a variable external resistor, the schematic of which is shown in Figure 2.28. However, the voice coil motor was used in the experiment instead of the originally proposed ball-screw regenerative shock absorber system, therefore the energy harvesting performance was not able to be evaluated under the condition where the ride comfort was optimized.



**Figure 2.28: Independent tunable electromagnetic damper system [104]**

Skyhook control strategy assumes that there is a dashpot of damping  $C_{sky}$  on the top of the sprung mass to dampen the vehicle body vibration from the road unevenness excitation [105]. Choi, Seong [71] designed a suspension system based on the electrorheological fluid damper with skyhook controller, the model of which is simulated to compare its simulation results with the experimental results in terms of attenuating vibration. It was found that the skyhook controller powered by the regenerative shock absorber system can significantly reduce the vibration. Ding, Wang [84] implemented Skyhook controller in the active control mode for vibration isolation. Hsieh, Huang [106] proposed the concept where a switched-mode rectifier (SMR) was used to provide positive or negative damping by implementing a skyhook control strategy, as shown in Figure 2.29. The results showed that the SMR can provide electrical damping based on the skyhook response outcome to achieve the balance between the passive control and the active control. His later research also indicated that the SMR can improve the harvesting efficiency for up to 14% [107].

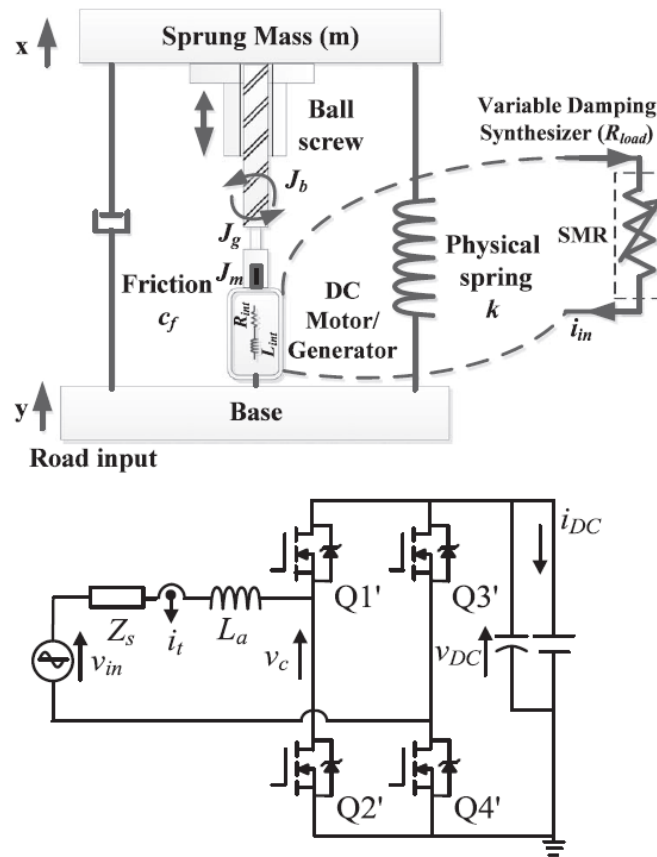


Figure 2.29: Regenerative suspension dynamic model and configuration of SMR.

### 2.7.3 Balance between the energy harvesting and vehicle dynamic performance

Due to the contradiction between the energy harvesting and ride comfort, compromises have been made for the balance of the ride comfort, road holding and power generation. Ataei, Asadi [108] provide all the possible solutions as Pareto front by prioritizing one of the three objectives. It is shown that the optimized system can deliver better comfort and handling than the non-optimized system. Similar method was adopted by Clemen, Anubi [109] for obtaining the best trade-off between the objectives. For the same purpose of finding the best

trade-off between vehicle dynamic performance and energy harvesting, Casavola, Di Iorio [110] proposed the maximum induced power control (MIPC) algorithm that can improve the energy harvesting ability without sacrificing the other objectives.

The concept of mode switching was also introduced to harvest the energy without compromising the ride and comfort performance. Zheng, Yu [47] proposed a system featuring the mode switching operation, namely, the electric motor mode and regenerative braking mode. In the electric motor mode, the optimal ride and comfort performance can be achieved through the active control by tuning the external circuit; in regenerative braking mode, the system can harvest energy while improving the ride and comfort performance. This operation can be achieved through the H bridge switching between the regeneration/actuation mode, one example of the operation is shown in Figure 2.30 [111]. Nakano [70] and Nakano, Suda [112] proposed another mode switching system featuring regeneration mode, drive mode and brake mode, allowing the system to respond instantly to the stroke velocity, as shown in Figure 2.31. The possibility of powering the actuator in the motor mode utilizing the power generated in the regenerative mode was also discussed and it was concluded that this self-power operation is somewhat achievable even though the actuation force is slightly insufficient. This combination of vibration control and energy harvesting is called regenerative vibration control, which can be used in regenerative building vibration controls [113-117] and vehicle regenerative shock absorber systems [118, 119]. The control algorithms are summarized in Table 2.5 below.

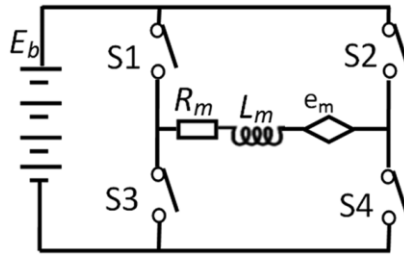


Figure 2.30: The H bridge for the mode switching between regeneration and actuation.

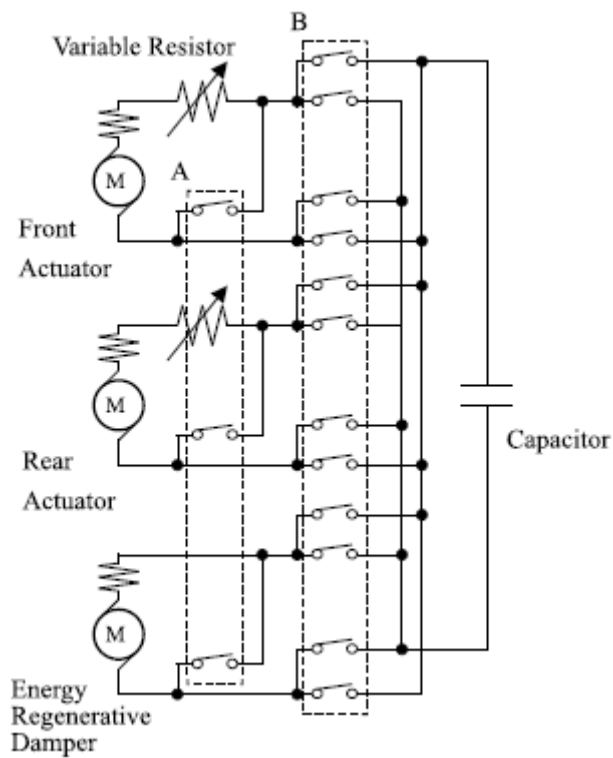


Figure 2.31: Control electric circuits of the proposed regenerative shock absorber system with relay switches [70].

Table 2.5: The summary of the control algorithms of the regenerative shock absorbers.

| Presenter | Drive | Electrical circuit and | Results |
|-----------|-------|------------------------|---------|
|           |       |                        |         |

|                           | mode              | control algorithm   |  |
|---------------------------|-------------------|---|--|
| Fukumori,<br>Hayashi [46] | Indirect<br>drive | Independent damping<br>control circuit  | Reduced pitch angle  |
| Yu, Huo [120]             | Indirect<br>drive | PI controller   | Reduced suspension<br>acceleration, pitch angle,<br>normal force and increased<br>power output |
| Nakano [70]               | Indirect<br>drive | Regeneration mode and<br>drive mode   | Active control and self-<br>power  |
| Choi, Seong [71]          | Indirect<br>drive | Skyhook controller  | Reduced suspension travel<br>and settling time   |
| Zheng, Yu [121]           | Indirect<br>drive | Electrical motor mode<br>and regenerative braking<br>mode controlled by<br>PWM        | Optimum ride comfort   |
| Kawamoto, Suda<br>[48]    | Indirect<br>drive | PI controller   | Reduced sprung mass<br>acceleration and tire<br>deflection                                     |
| Wang, Ding [39]           | Direct<br>drive   | active comfort mode,<br>active safety mode and<br>regeneration mode, PI<br>controller | Reduced cabin acceleration<br>and dynamic tire load in<br>active mode                          |
| Singh and Satpute<br>[75] | Hybrid            | Harvesting mode and<br>shunt mode controlled by                                       | Energy can be either<br>harvested or dissipated as   |

|                           |                |  |  |
|---------------------------|----------------|--|--|
|                           |                | two switches and a resistance  | heat   |
| Huang, Hsieh [122]        | Indirect drive | Switch-mode rectifier  | Tuneable damping coefficient   |
| Zhang, Li [105]           | Indirect drive | Skyhook controller   | Reduced sprung mass acceleration, suspension deflection and tire dynamic                         |
| Sapiński, Rosół [37]      | Direct drive   | On-off algorithm or skyhook controller                               | Less force and less transmissibility obtained with skyhook controller than with on-off algorithm |
| Liu, Li [94]              | Direct drive   | Fuzzy control  | Reduced amplitude of suspension dynamic flexibility, tire dynamic displacement                   |
| Ding, Wang [84]           | Direct drive   | Passive generation mode, active control mode with skyhook controller | Better vibration isolation in the active control mode  |
| Sabzehgar, Maravandi [73] | Indirect drive | PWM control  | Conversion of three phase power output for charging the battery                                  |



## 2.8 Road excitation input

In order to evaluate the regenerative shock absorber, a certain road excitation input needs to be applied so that the output response of the system can be analysed. Sinusoidal signal, step signal and random signal have been utilized by many researchers to simulate the road displacement excitation input.

### *2.8.1 Sinusoidal displacement excitation input*

Sinusoidal displacement excitation input has been widely applied to simulate the excitation input because it presents a certain excitation frequency. For a linear regenerative suspension system, its natural resonant frequencies can be targeted to maximize power output and the harvesting efficiency. According to Wang, Liang [123], given the input excitation frequency, the power input and output can be calculated to give system energy harvesting efficiency. With the sinusoidal road displacement excitation input, the voltage output appears to be sinusoidal, which can be rectified into DC voltage.

### *2.8.2 Step input*

The use of a step signal as the road displacement excitation input can evaluate the regenerative shock absorber's vibration response time and attenuation ability, thus giving the idea of how the vehicle responds to a single road bump. In their researches, Li and Zuo [124]

compared the vehicle responses to a 10 mm step road displacement excitation for the vehicle suspension fitted with three regenerative shock absorbers in terms of weighted acceleration, dynamic/static tire force ratio, suspension deflection, harvested power and damping force.

### 2.8.3 Road displacement profile

In addition to the sinusoidal and step input, the road class model has also been applied to the regenerative shock absorber based on its roughness classification since the road roughness has a significant impact on the power dissipated in the shock absorber [125]. Goldner, Zerigian [35] included the road profile in the experiment by using a rotating wheel with a bump. However, this setup cannot fully resemble the real road condition which has a more random displacement profile. In order to evaluate the performance of the regenerative shock absorber on different road conditions, the road model and its classification were introduced to conduct the simulation accurately. According to ISO-8608, A to H are used to classify the roads [126]. Many authors have incorporated road models with the classifications in the simulation as the input excitation [44, 122, 127, 128].

The PSD functions of the road displacement input are given by:

$$\begin{cases} G_d(n) = G_d(n_0) \cdot \left(\frac{n}{n_0}\right)^{-2} \\ G_d(\Omega) = G_d(\Omega_0) \cdot \left(\frac{\Omega}{\Omega_0}\right)^{-2} \end{cases} \quad (2.3)$$

where  $G_d(n)$  and  $G_d(\Omega)$  are the PSD functions of the vertical displacements which are functions of spatial frequency  $n$  and of angular spatial frequency  $\Omega$ .  $G_d(n_0)$  and  $G_d(\Omega_0)$  are given in Table 2.6 below corresponding to the road classifications.

**Table 2.6: ISO 8608 values of  $G_d(n_0)$  and  $G_d(\Omega_0)$  [127].**

| Road class | $G_d(n_0)$ (10 <sup>-6</sup> m <sup>3</sup> ) |             | $G_d(\Omega_0)$ (10 <sup>-6</sup> m <sup>3</sup> ) |             |
|------------|---|-------------|--|-------------|
|            | Lower limit                                   | Upper limit | Lower limit  | Upper limit |
| A          | ---   | 32          | ---  | 2           |
| B          | 32  | 128         | 2  | 8           |
| C          | 128   | 512         | 8  | 32          |
| D          | 512   | 2048        | 32   | 128         |
| E          | 2048  | 8192        | 128  | 512         |
| F          | 8192  | 32768       | 512  | 2048        |
| G          | 32768   | 131072      | 2048   | 8192        |
| H          | 131072  | ---         | 8192   | ---         |
|            | n <sub>0</sub> =0.1 cycles/m                  |             | Ω <sub>0</sub> =1 rad/m                            |             |

Guo, Liu [44] developed the PSD of the road elevation profile shown in Figure 2.32. The road profile equivalent to level C was generated with random roughness and used in the simulation as an input source. The PSD functions of the bounce and pitch road displacement input profiles were developed by Nakano [70], taking into consideration of the time delay between the wheels due to the vehicle travelling, as shown below:

$$\begin{cases} P_{ob}(f_t) = \frac{vR}{f_t^2} \cos^2\left(\frac{f_t}{v} \pi(l_f + l_r)\right) \\ P_{op}(f_t) = \frac{4vR}{(l_f + l_r)^2 f_t^2} \sin^2\left(\frac{f_t}{v} \pi(l_f + l_r)\right) \end{cases} \quad (2.4)$$

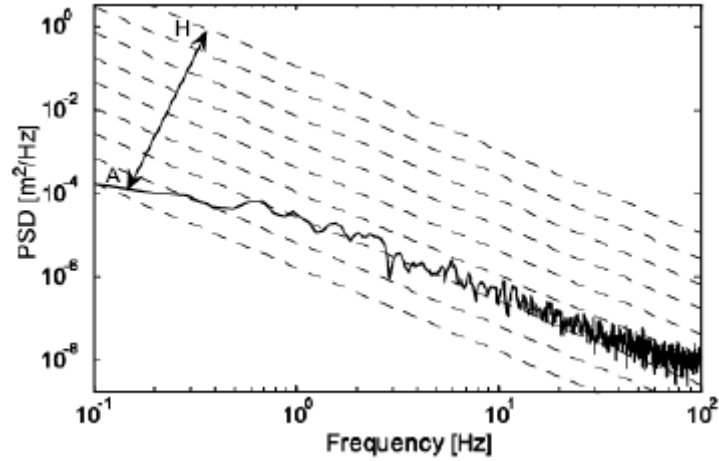


**Figure 2.32: PSD of input displacement excitation profile of the C level road on which the vehicle is travelling at 80 km/h.**

Xie, Li [45] compared the output power of the regenerative shock absorber under the different road classes, shown in Figure 2.33. The result showed that the more pronounced the road roughness is, the more the power output at certain vehicle velocities.

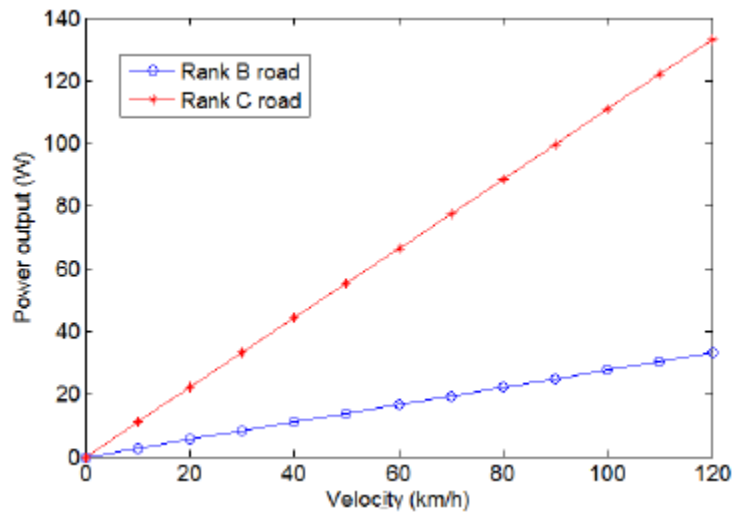


Figure 2.33: The output power versus road class and vehicle velocity [45].

#### 2.8.4 Road test

Road test is the most straightforward and simplest way to demonstrate the performance of the shock absorber in the real world. The accelerometers were mounted on the sprung mass and unsprung to pick up the acceleration signals and data acquisition device was placed in the vehicle cabin to record the test data. A double clutch ball screw based regenerative shock absorber designed by Liu, Xu [53] was tested on a Ford F250 in place of the traditional oil damper, as shown in Figure 2.34. The vehicle was driven at 64 km/h on the paved road, it is shown that with a 10  $\Omega$  external resistance, the total power output was in phase with the voltage output and an average of 13.3 W could be harvested over 8 seconds. As shown in Figure 2.35, a similar test was conducted by Li, Zuo [129] to assess the feasibility of the proposed regenerative shock absorber, an average of 15.4 W could be harvested over 8 seconds with a 20  $\Omega$  external resistance, when the vehicle was driven at 24 km/h on a circled

campus road. It is also indicated that the power output was out of phase with the road displacement, which means that in addition to the excitation displacement amplitude, the excitation displacement phase could also affect the power output.

In order to evaluate the results in the frequency domain, Liu, Li [94] proposed to have the regenerative shock absorber installed on a self-made electric vehicle driven at 20 km/h on a Class B road, as shown in Figure 2.36. In the road test, the comfort levels of the passive damper and the proposed regenerative damper with the Variable Universe Fuzzy (VUF) control were compared and the results are shown in the frequency domain. It can be seen that the VUF control lowered the vehicle body acceleration and such reduction was more obvious at the resonant frequencies.

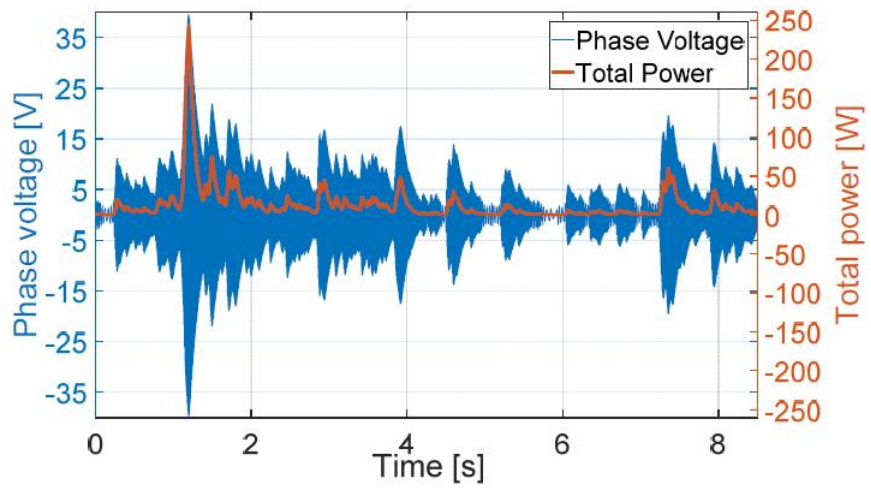
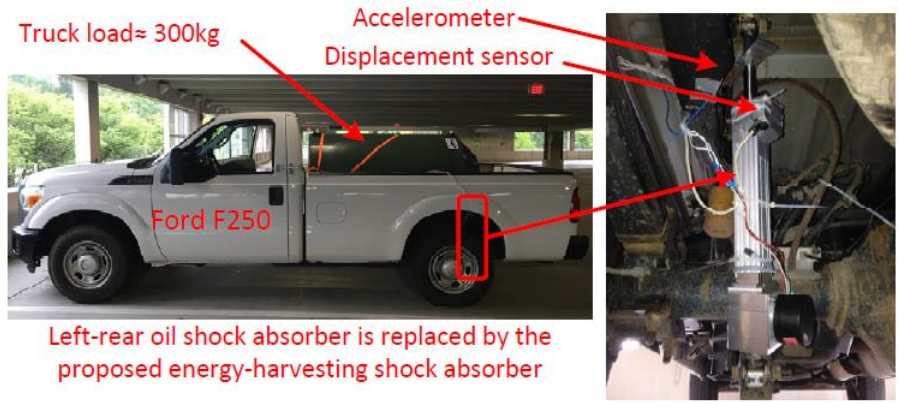


Figure 2.34: Road test of the ball-screw-based MMR shock absorber and its electrical outputs.

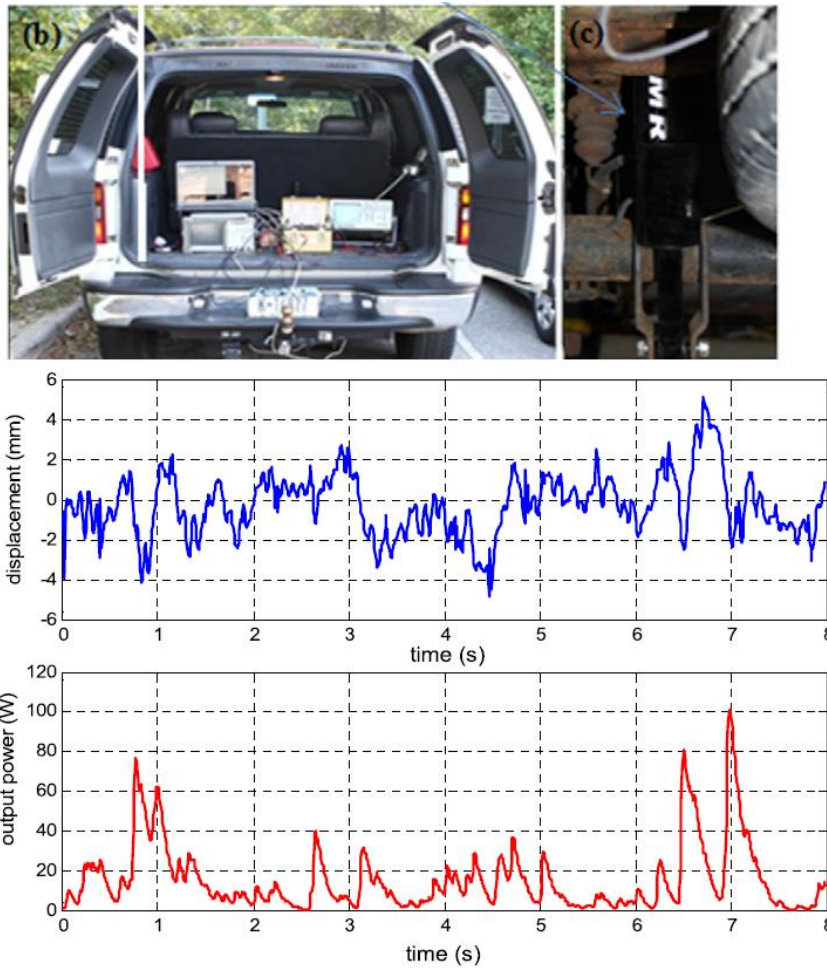
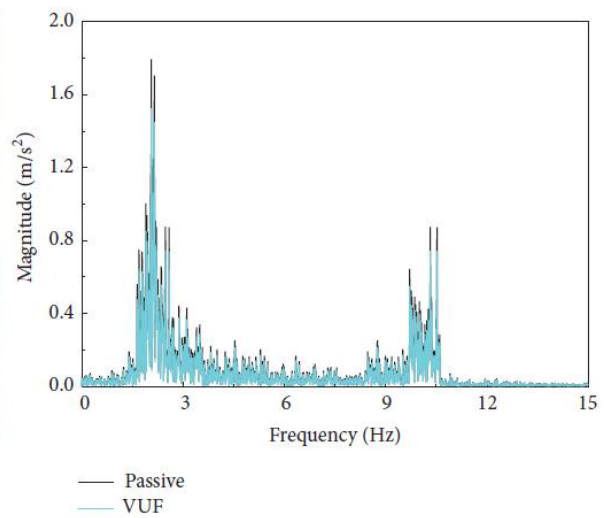


Figure 2.35: The road test of MMR shock absorber and recorded displacement and power output.





**Figure 2.36: Road test set up of AERS and its body acceleration in the frequency domain at 20km/h on Class B road.**

## 2.9 Nonlinearity

Due to the nature of the linear regenerative vehicle suspension, more energy can be harvested at the resonant natural frequencies. Figure 2.37 is an example of the frequency spectrum of the power generation in a quarter vehicle regenerative suspension system. One of the drawbacks of the linear regenerative vehicle suspension is that the resonant peak frequency bandwidth is really narrow, resulting in very little energy that can be regenerated [130]. Therefore in order to achieve high power output, many researchers have adopted a nonlinear model for the regenerative vehicle suspension to broaden the frequency bandwidth for energy harvesting [131-135].

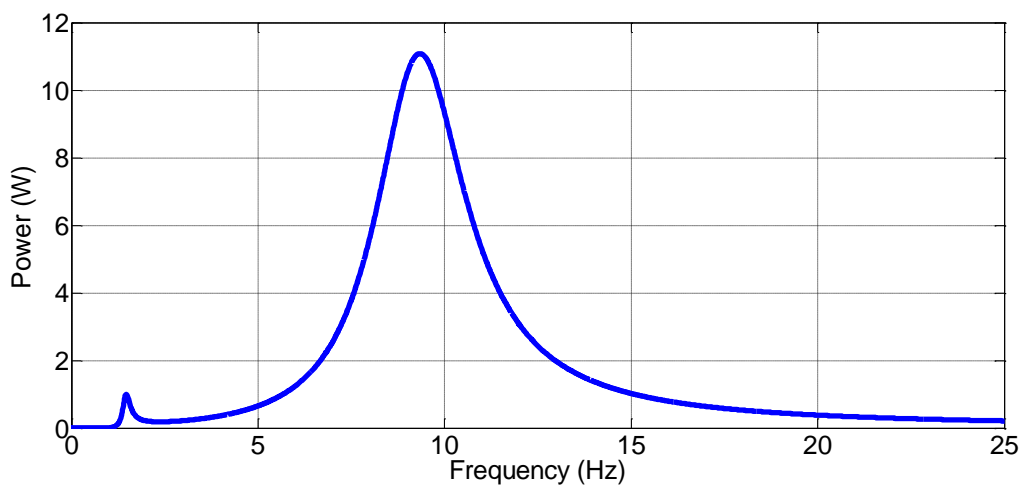


**Figure 2.37: Frequency spectrum of the power generation in a quarter vehicle regenerative suspension system**

A magnetic levitation energy harvesting device was proposed by Mann and Sims [136] and shown in Figure 2.38. The mathematical model could be obtained using the Duffing equation and it was found that the nonlinearity was applicable to larger excitation displacement amplitude, resulting in a broader harvesting frequency bandwidth. The peak power could be obtained away from the equivalent resonant frequencies. Another interesting innovation was brought by Barton, Burrow [130] who further increased the bandwidth by changing the load resistance. It was also discovered that the nonlinearity presents super-harmonic resonances well above the natural frequencies of the equivalent linear system, allowing the system to respond at a frequency higher than the excitation frequency. This up-frequency conversion could be useful for the low frequency operation such as a vehicle suspension system.

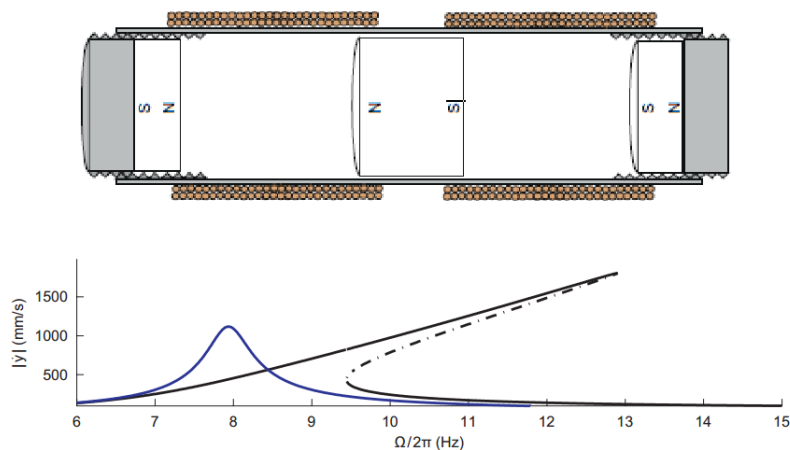


**Figure 2.38: Nonlinear magnetic levitation energy harvesting system and its frequency spectrum of oscillator velocity.**

Nonlinear soften spring, as another approach to increase the bandwidth, was applied in the MEMS harvester design by Nguyen, Halvorsen [137], as shown in Figure 2.39. The results indicated that compared with the linear model, the nonlinear model achieved an improvement of 68% in power output when subjected to the random vibration excitation. The effective bandwidth was increased for 13 times due to the softened spring.

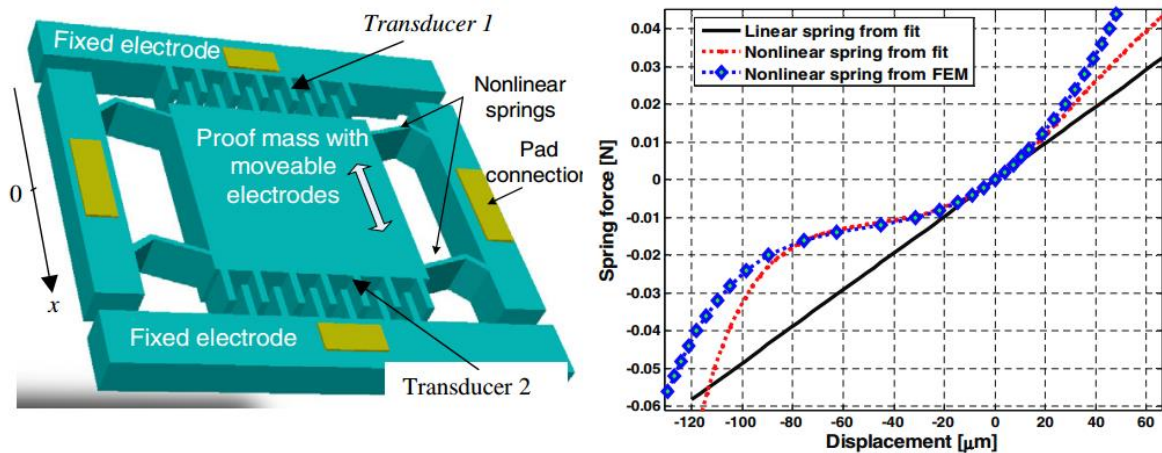


**Figure 2.39: Schematic of a MEMS energy harvester with the nonlinear softened springs and its force displacement curve.**

There have been a number of suspension system designs that incorporate the nonlinearity model due to its advantages in prediction of vehicle dynamics. Özcan, Sönmez [138] evaluated the nonlinear spring and nonlinear damper in the half car system to optimize the comfort and the handling of the light vehicle. Similar dynamic study was conducted by Cui,

Kurfess [139] on the shock absorber in a Mazda CX-7, the test result clearly showed that the nonlinearity was involved in the operation shown in Figure 2.40. The stability and comfort of the vehicle could be improved by this nonlinearity.

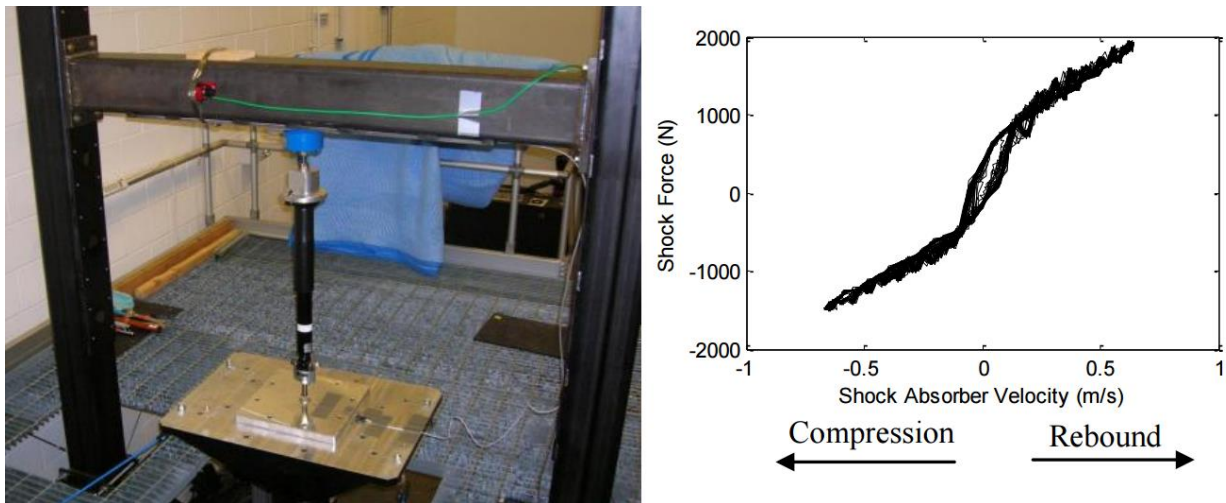


**Figure 2.40: Experimental setup of the Mazda CX-7 nonlinear shock absorber and its force velocity curve.**

Although the concept of the nonlinearity model has been largely applied on the vehicles to predict vehicle vibration response due to the road profile excitation, there have not been many investigations undertaken for the nonlinear model of the vehicle suspension system built with the regenerative shock absorber in terms of harvesting energy, which can be identified as a research gap and should draw more attention considering the potentials of the regenerative shock absorber and its readiness to be implemented. The potential advantages of the nonlinear regenerative shock absorbers are:

1. Widening the frequency bandwidth for harvesting more energy on the random road surface.
2. Shifting the harvesting frequency away from the vehicle equivalent resonant frequency for better reliability.
3. Converting the low road excitation frequency into high energy harvesting frequency.
4. Better comfort and road handling.

## Chapter 3

### *Two degrees of freedom vibration energy harvesting system*

*This chapter presents the study of two degrees of freedom electromagnetic vibration energy harvesting system with a magnet arrangement of the Halbach array. Theoretical analysis model of the system is established through frequency response analysis of the system motion equations. The simulation model is developed from time domain integration of the system motion equations using the Matlab SIMULINK software. The results of the theoretical*

*analysis and simulation models are compared and verified by the results of a series of experiments.*

*By establishing valid vibration energy harvesting system analysis and simulation models, the vehicle quarter suspension system with a regenerative shock absorber can be simulated. It is found that the magnetic pole arrangement pattern of the Halbach array can improve the harvesting performance, however, to some extent, the increase of the electro-mechanical coupling may reduce the harvested power output of the two degrees of freedom system.*

### 3.1 Introduction

Recently, there are increasing amount of research interest in vibration energy harvesting systems converting the mechanical vibration energy into electrical energy. Such systems are versatile and can be used on different types of running machineries, including the vehicle where the power train vibration [140, 141], the suspension vibration [142, 143] and seat vibration can be taken in account [144]. One good example is the linear regenerative shock absorber proposed by Li and Zuo [42]. In the paper, they believed that only 10-16% of the fuel chemical energy is utilized to drive the vehicle, meaning that 84-90% of the fuel energy is wasted most in the form of heat energy. They proposed a linear energy harvester prototype in which a high magnetic conductive steel casing was added to obtain a stronger magnetic field. Similarly, Goldner, Zerigian [35] proposed another linear electromagnetic energy harvesting shock absorber that can respond to a rotating wheel on the bump resembling the road roughness. The road roughness level was simulated and studied for the road surface

where a vehicle is driven at a speed of 20m/s. The regenerative shock absorber installed in the vehicle can generate 1.92 kW to 17.42 kW of electric power depending on the simulated road conditions. In order to incorporate more realistic road model, Singh and Satpute [75] apply the road displacement data obtained experimentally into the simulation of the proposed linear regenerative shock absorber system. This system is expected to harvest an average of 15W from each wheel. However, in these studies, the frequency response analysis of the two degrees of freedom (2DOF) mass-spring-dashpot electromagnetic harvesting system was not conducted. Therefore, there could be more potential for power extraction if the frequency response analysis of the mass-spring-dashpot electromagnetic harvesting system was considered.

In a rail car system, Ung, Moss [145] proposed an inertial-based electromagnetic generator with 2DOF coupled oscillating system that can be equipped on the train to harvest the vibrational energy. One of the two natural frequencies resulting from the mass change of the loaded and unloaded condition should be tuned to be close to the excitation frequency for better harvesting efficiency. However, in a typical 2DOF system such as a quarter vehicle suspension system, the inertial-based electromagnetic generator cannot be used as the shock absorber where the damping force is required for the vibration control. The same problem exists for some regenerative shock absorbers equipped with the ball screw mechanism where the damping force is very small or absent when the clutch is disengaged [51, 70, 146], resulting in the poor ride and handling performance. Therefore, the knowledge gap is identified as the electro-mechanical coupling analysis of the 2DOF oscillating system taking into account its damping requirement.



According to Elvin and Elvin [34], four factors that may affect the harvesting efficiency include: (a) how well the resonator's natural frequency matched with the dominant excitation frequency of the ambient environment, (b) the degree of electromechanical coupling, (c) the mechanical damping of the resonator, (d) the electrical impedance of the attached circuit.

As the part of the electromechanical system, many studies [25, 32, 33] have concluded that coil configurations also have direct effect on the power generation, based on Faraday's law of induction  $U = BLV$  where  $B$  is the magnetic field strength,  $l$  is the coil length and  $v$  is the relative velocity between the magnets and coil. Therefore,  $Bl$  stands for the electromechanical coupling between the electrical portal and mechanical portal. The generator coil profile with more layers can yield higher voltage output as a result of cutting magnetic flux lines with more coils. For every different wire gauge, there is specific premium number of layers with which the maximum power extraction can be achieved [34]. It was also found that for thinner winding coils, the maximum power output can be achieved with less coil layers. In reality, however, the main constraint of the coil design is the amount of the available space, therefore if the total volume of the coil is assumed to be constant, the potential of using thinner coils was not fully understood.

Efforts have been made to obtain a stronger electromechanical coupling for improved efficiency. Magnetic pattern of Halbach array was introduced by many authors [27, 43] for its high power density compared with other magnet patterns. Zhu, Beeby [28] investigate the vibrational energy harvesting performance using the Halbach array. It was found that with the

same magnet volume, the electromagnetic field strength of the Halbach array was stronger than that of the magnets arranged in the conventional way. However, field strength becomes weaker with low vibration amplitude, so when the displacement of the magnets is at the comparable level with coil diameter, the Halbach array can improve the power output by 40%. The double layered Halbach array magnet arrangement was also simulated [25, 30, 145] and it was claimed that the magnetic flux gradient can be improved by 37% and power output can be improved by 88%. Another advantage of the Halbach array is that the magnetic flux line is concentrated on one side of the magnets, resulting in nearly zero magnetic field zone on the other side which can significantly reduce the undesired magnetic interference and thus reduce the overall size.

Most of these studies focused on the performance study of the harvesters and did not consider the dynamic system related to the harvesters. It is important to include the dynamic mass spring dashpot oscillator system in the analysis since the electromagnetic vibration energy harvester works as a part of the dynamic system and it should not be separately treated. In addition, the use of the magnet pattern with stronger magnetic field intensity has not been discussed much in terms of its energy harvesting efficiency. How the electro-mechanical coupling can affect the performance of the 2DOF linear electromagnetic vibration energy harvester still remains unknown.

In this chapter, a 2DOF vibration energy harvesting system with the magnet pattern of the Halbach array is presented. The 2DOF system that has two mass oscillators can represent a quarter vehicle regenerative suspension system, a plane regenerative landing gear system, etc.

The model is characterized from analysis and simulation. Experiments were carried out on the system through a hydraulic shaker to validate the analysis and simulation models. The experimental results are compared with the analysis and simulation results. Sensitivity analysis of the coil profile, magnet arrangement pattern and electro-mechanical coupling is also investigated based on the validated model to optimize the performance of the 2DOF vibration energy harvesting system.

## 3.2 Analytical models

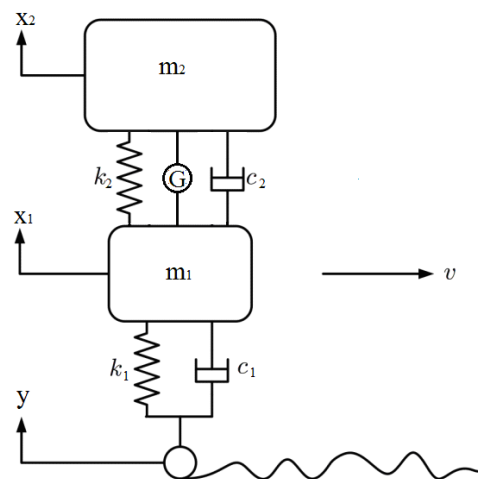


**Figure 3.1: A quarter vehicle suspension model with the regenerative shock absorber.**

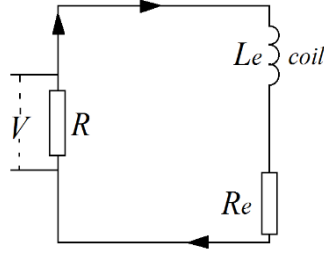


**Figure 3.2: Harvesting circuit of the regenerative shock absorber.**

This 2DOF electromagnetic vibration energy harvesting system model is developed based on the 2DOF mass-spring-dashpot oscillator system shown in Figure 3.1, which can be used to simulate the regenerative quarter vehicle suspension for the performance analysis, parameter study and optimization.  $m_2$  is the top oscillator mass;  $m_1$  is the bottom oscillator mass;  $k_2$  is the suspension spring stiffness;  $k_1$  is the tyre stiffness;  $c_2$  is the suspension damping coefficient;  $c_1$  is the tyre damping coefficient and  $G$  is the electromagnetic generator that converts the relative movement between the oscillators into electrical current,  $x_2$  is the displacement of the top oscillator and  $x_1$  is the displacement of the bottom oscillator. As a vehicle of this quarter suspension moves, the irregularities on the road will induce the excitation displacement of  $y$  which in the simulation, is expressed as a displacement excitation signal source.

Shown in Figure 3.2 is the energy harvesting electric circuit of the linear electromagnetic generator where the coil inside the generator has the inductance of  $L_e$  and the coil resistance of  $R_e$ .  $R$  is the external resistance over which the voltage  $V$  can be extracted.

The voltage over the inductor is calculated by:

$$V_{\text{inductor}} = L_e \cdot \frac{dI}{dt} = L_e \cdot \dot{V} \quad (3.1)$$

Therefore the generated voltage can be expressed as

$$V_{\text{generated}} = L_e \cdot \frac{\dot{V}}{R} + \frac{V}{R} \cdot (R + R_e) \quad (3.2)$$

Because this voltage is generated as a result of relative movement between the oscillator  $m_1$  and the oscillator  $m_2$ , the generated voltage can also be expressed as:

$$V_{\text{generated}} = Bl \cdot (\dot{x}_2 - \dot{x}_1) \quad (3.3)$$

Comparing Equations (3.2) and (3.3) yields:

$$Bl \cdot (\dot{x}_2 - \dot{x}_1) = \frac{L_e \cdot \dot{V}}{R} + \frac{V}{R} (R + R_e) \quad (3.4)$$

Rearranging Equation (3.4) gives

$$\dot{V} = \left( \frac{Bl \cdot R}{L_e} \right) \cdot \dot{x}_2 - \left( \frac{Bl \cdot R}{L_e} \right) \cdot \dot{x}_1 - \left( \frac{R + R_e}{L_e} \right) \cdot V \quad (3.4)$$

The dynamic equations of the motion of the two oscillators are given by

$$\begin{cases} m_1 \ddot{x}_1 + c_1 (\dot{x}_1 - \dot{y}) + k_1 (x_1 - y) + c_2 (\dot{x}_1 - \dot{x}_2) + k_2 (x_1 - x_2) + Bl \cdot \frac{V}{R} = 0 \\ m_2 \ddot{x}_2 + c_2 (\dot{x}_2 - \dot{x}_1) + k_2 (x_2 - x_1) - Bl \cdot \frac{V}{R} = 0 \end{cases} \quad (3.6)$$

Applying the Laplace transform to Equations (3.5-3.6) gives the matrix equation:

$$\begin{bmatrix} m_1 \cdot s^2 + (c_1 + c_2) \cdot s + (k_1 + k_2) & -c_2 \cdot s - k_2 & \frac{B \cdot l}{R} \\ -c_2 \cdot s - k_2 & (m_2 \cdot s^2 + c_2 \cdot s + k_2) & -\frac{B \cdot l}{R} \\ -B \cdot l \cdot s & B \cdot l \cdot s & -\frac{L_c}{R} \cdot s - 1 \end{bmatrix} \begin{Bmatrix} X_1(s) \\ X_2(s) \\ \bar{V}(s) \end{Bmatrix} = \begin{Bmatrix} c_1 \cdot s + k_1 \\ 0 \\ 0 \end{Bmatrix} \cdot Y(s) \quad (3.7)$$

where  $X_1(s)$ ,  $X_2(s)$  and  $\bar{V}(s)$  are the Laplace transforms of the time histories of the displacements  $x_1(t)$ ,  $x_2(t)$  and voltage  $V(t)$ .

The output voltage peak amplitude  $V_m$  and harvested power can be calculated in the frequency range of 0 to 30 Hz. With the base excitation displacement amplitude of 2 mm ( $Y_m=2$  mm), the frequency response amplitude curves of the 2DOF electromagnetic vibration energy harvesting system can be calculated from Equation (3.7) and plotted in Figure 3.9 where  $s$  is assumed to be equal to  $i\omega$ , and  $\omega=2\pi f$  is the radial frequency of the base excitation in rad/s and  $f$  is the frequency of the base excitation in Hz. The results of the analysis model are plotted in solid curves and presented in Figure 3.9 for comparison and validation.

### 3.3 Validation of the analytical model

In order to validate the analysis model presented by Equation (3.7) and verify the analysis results of harvested power presented by the solid curve as shown in Figure 3.9, a Matlab SIMULINK simulation code is developed in the time domain based on the integration method as shown in Figure 3.3 where the amplitude of the input displacement signal of a sine wave is set as 2 mm, which is same as the base input displacement excitation amplitude of the analysis model. Three round sum blocks represent equation marks in Equations (3.5-3.6). With a given input displacement excitation of a sine wave signal, the output voltage and harvested power can be calculated and plotted in the time domain to compare with the results obtained from the analysis model.

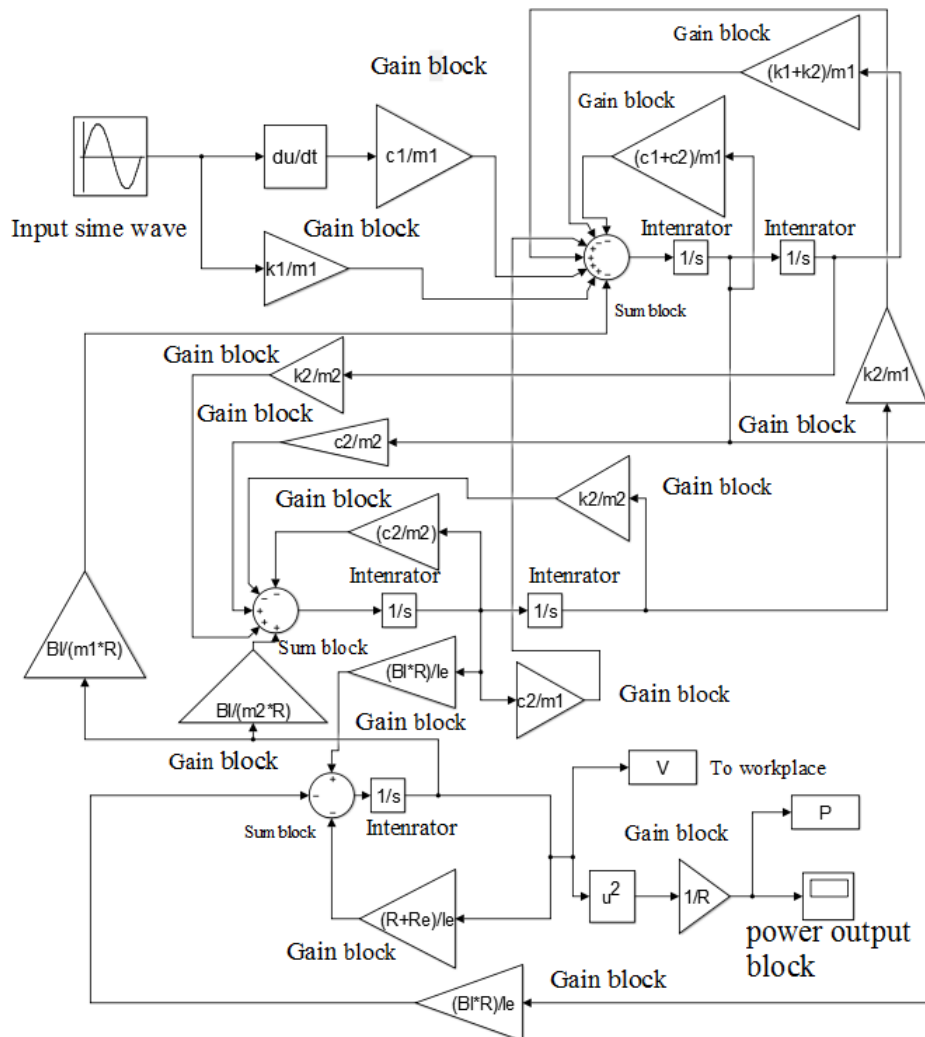


**Figure 3.3: Simulation schematic for Equations (3.5-3.6) for calculation of the output power using the integration method from the Matlab SIMULINK software.**

## 3.4 Experiment design

A two degrees of freedom mass-spring damping oscillator system was fabricated to simulate a vehicle quarter suspension system where a regenerative shock absorber was used to convert the vibration energy to the electrical energy. It is shown in Figure 3.4 where the coil assembly is fixed on the top oscillator that represents the car body. The magnets are arranged in a Halbach array pattern and mounted in a “magnet holder” on the top of the bottom oscillator that represents the wheel and tyre. The movements of both the oscillators are guided in the vertical direction by six bolts which prevent detachment. Similarly, the top and bottom springs represent the suspension spring and tyre respectively. The relative movement between the coil assembly and magnet assembly is produced by the shaker, as a result, such movement can induce the current based on Faraday’s law.



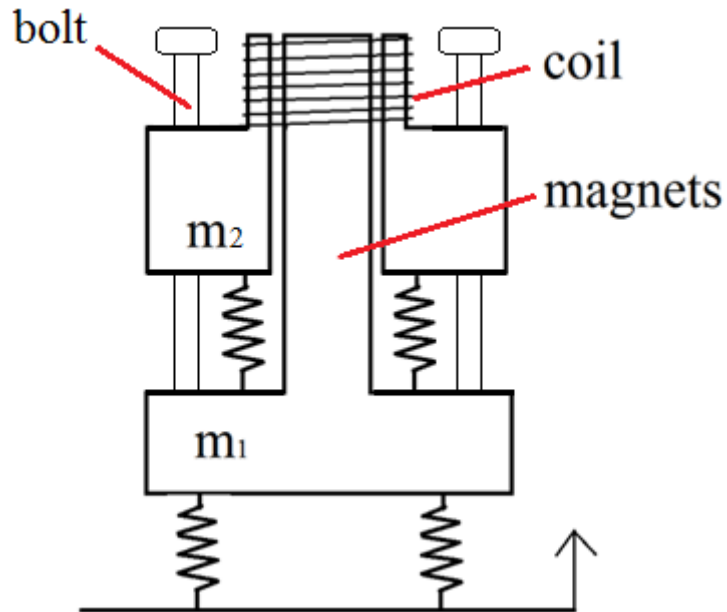


**Figure 3.4: Schematic view of the 2DOF electromagnetic vibration energy harvesting system.**

The coil consists of nine sub-coils connected in series, the representation of its overall resistance is shown in Figure 3.2. An external resistor is connected in series with all the sub-coils in the circuit for the voltage extraction. This voltage signal is then displayed by an oscilloscope where the change of the voltages can be easily monitored, recorded and compared.

### 3.5 Experiment setup

In order to further validate the analysis and simulation models, a series of experiments were conducted on the 2DOF electromagnetic vibration energy harvesting system. The experimental set up is shown in Figure 3.5.



**Figure 3.5: Experimental setup of the 2DOF electromagnetic vibration energy harvesting system on the MTS Landmark servo hydraulic test system (hydraulic shaker).**

### 3.6 Identification of the parameters

In order to identify the system parameters of the 2DOF mass spring dashpot oscillator system, the hammer impact modal analysis test is conducted on a rigid platform shown in Figure 3.6.

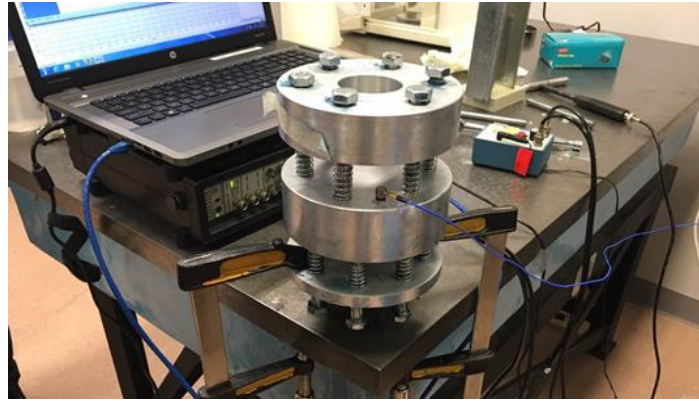
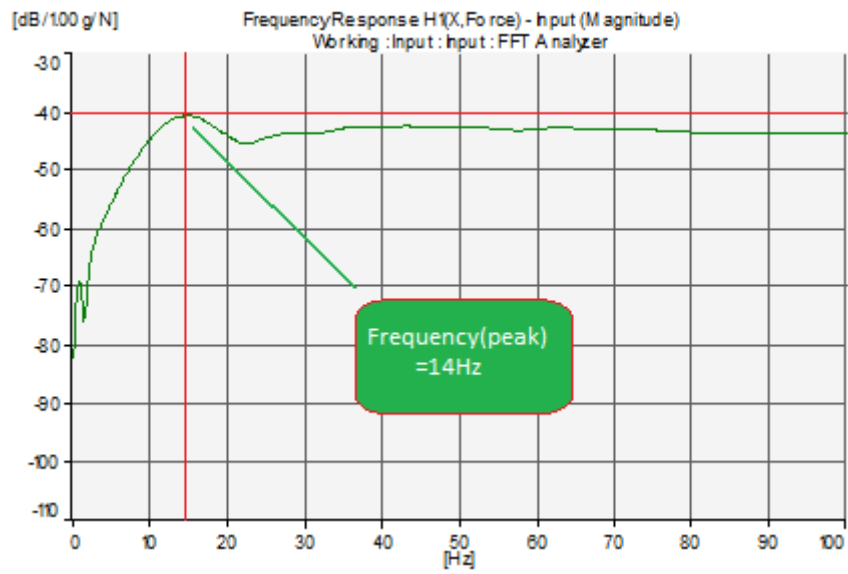


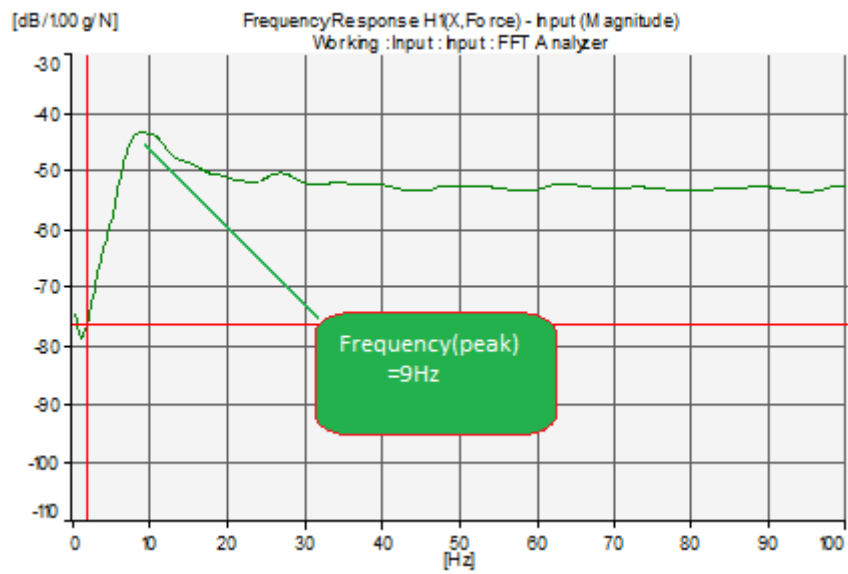
**Figure 3.6: Experiment setup for hammer impact modal analysis tests.**

A hammer mounted with a force transducer is used to impact the top mass block, a uni-axial accelerometer was mounted on the top of the mass block to measure the vertical vibration response from the hammer impact excitation. The force and acceleration signals are recorded by the Bruel & Kjaer Pulse frontend data acquisition system and processed by analysis software where the frequency response functions between the force and the response acceleration are measured.

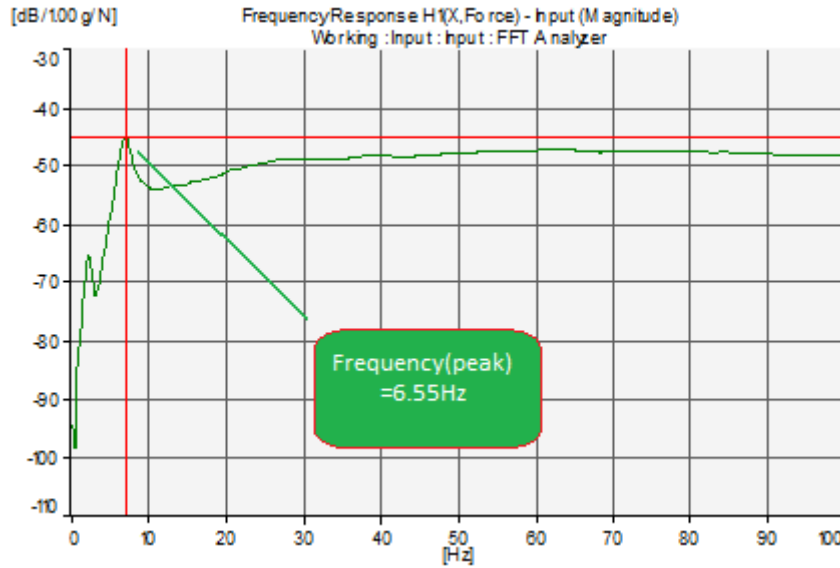
Figures 3.7(a) and 3.7(b) show the measured frequency response function amplitude curves of the separated single degree of freedom (SDOF) top mass spring oscillator system and the separated SDOF bottom mass spring oscillator system respectively. Figure 3.7(c) shows the measured frequency response function amplitude curves of the assembled whole 2DOF system.



(a)



(b)



(c)

**Figure 3.7: Frequency response function amplitudes of the single degree of freedom top mass spring oscillator system (a) the single degree of freedom bottom mass spring oscillator system (b) the two degree of freedom mass spring oscillator system (c).**

The natural resonant frequencies of the isolated SDOF top and bottom mass block systems are identified by the peak frequencies  $f_{\text{peak}}$  which are 14 Hz and 9 Hz respectively. The spring stiffness coefficient of the SDOF top or bottom oscillator system is given by

$$k = m \times (2\pi \times f_{\text{peak}})^2, \quad (3.8)$$

where the top mass  $m_2$  is weighted to be 1.59 kg and the bottom mass  $m_1$  is weighted to be 3.99 kg. The stiffness coefficients of the top and bottom spring sets can be calculated from Equation (3.8) or measured. The measured results are  $k_2=8666$  N/m and  $k_1=9188$  N/m. If the measured stiffness coefficients are adopted for the linearization model, from the eigenanalysis of Equation (3.6), the calculated natural frequencies are 6.1 Hz and 14.6 Hz which is

close to the measured natural resonant frequency of the two degree of freedom mass spring oscillator system of 14 Hz. This measured natural resonant frequency has verified the calculated natural resonant frequency.

The damping loss factor is given by

$$\eta = \frac{c}{\sqrt{m \times k}}, \quad (3.9)$$

where  $\eta$  is the damping loss factor identified from Figures 3.7(a) or 3.7(b) using the half power bandwidth method. As a result, values for the damping coefficients  $c_1, c_2$  can be determined from and the stiffness coefficients  $k_1, k_2$ , the oscillator masses,  $m_1, m_2$  and the identified damping loss factors  $\eta_1, \eta_2$  according to Equation (3.9). As a result, the values for the damping coefficients  $c_1$  and  $c_2$  are identified and calculated to be 12 Ns/m and 50 Ns/m.

The coil inductance is calculated by:

$$L_e = \frac{\mu_0 \times \mu_r \times N^2 \times A}{H}, \quad (3.10)$$

where  $N$  is the winding number of the coil,  $N=585$ ;  $\mu_0$  is the permeability of the coil with air core,  $\mu_0=4\pi \times 10^{-7} \text{ N}\cdot\text{m}^{-2}$ ;  $\mu_r$  is the permeability coefficient of the coil, for the iron core,  $\mu_r=1450$ , for the air core,  $\mu_r=1$ ;  $H$  is the coil width and given by:

$$H = d \cdot N, \quad (3.11)$$

where  $d$  is the diameter of the wire of the coil.  $A$  is the cross sectional area of the coil and given by:

$$A = \frac{\pi \times D^2}{4}, \quad (3.12)$$

where  $D$  is the diameter of the coil.  $Bl$  value stands for the electro-mechanical coupling which is the product of the magnetic field intensity  $B$  and the total coil wire length  $l$ . A 1:1 scaled simulation model of the linear electromagnetic vibration energy harvester is shown in Figure 3.8, which was developed in the ANSYS Maxwell software for simulation parameter identification of the magnetic field intensity around the coil. A cylinder shell resembling the coil profile is developed and placed 1.5 cm away from the outside of the magnets holder. As a result, the average value for the magnetic density around the coil can be calculated and given as 0.0254 T.

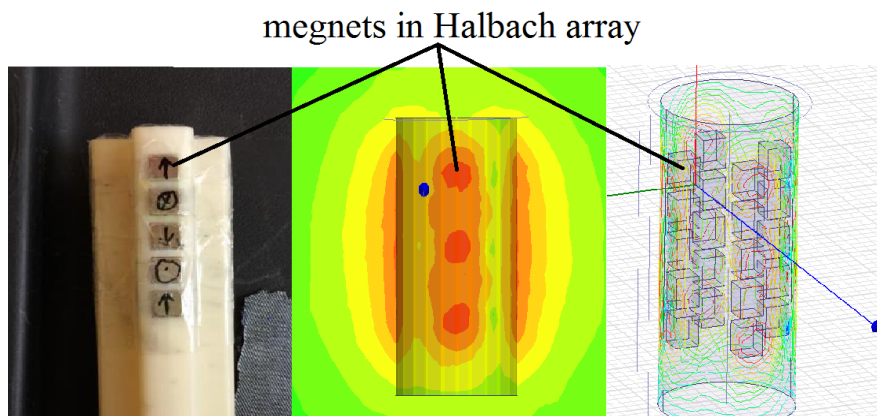


**Figure 3.8: Magnet holder and the magnetic field intensity contour of the magnets in the Halbach array around the coil using the ANSYS Maxwell software.**

Therefore  $Bl$  is calculated by:

$$Bl = B \times l = B \times \pi \times N \times D, \quad (3.13)$$

The parameters of the 2DOF mass-spring-damping oscillator system model identified by the impact modal analysis tests, experimental measurement and ANSYS Maxwell software simulation are listed in Table 3.1.

**Table 3.1: Parameters identified for the 2DOF mass-spring-damping oscillator system.**

|       |  |         |
|-------|--|---------|
| $m_1$ | the bottom mass (kg)                                     | 3.99    |
| $m_2$ | the top mass (kg)  | 1.59    |
| $k_1$ | Stiffness of the bottom spring (N/m)                     | 9188    |
| $k_2$ | Linear stiffness coefficient of the top spring (N/m)     | 8666    |
| $c_1$ | The bottom damping coefficient (Ns/m)                    | 12      |
| $c_2$ | The top damping coefficient (Ns/m)                       | 50      |
| $R_e$ | Coil resistance ( $\Omega$ )                             | 10      |
| $H$   | Coil width (m)   | 0.2925  |
| $l$   | Coil wire total length (m)                               | 110.214 |
| $Bl$  | Product of magnetic field intensity and coil length (Tm) | 2.8     |
| $L_e$ | Coil inductance (H)                                      | 0.00415 |
| $R$   | External resistance ( $\Omega$ )                         | 10      |



|                 |  |       |
|-----------------|--|-------|
| $f_1$           | Identified first natural frequency of the two degree of freedom oscillator system from the impact test (Hz)  | 6.55  |
| $f_2$           | Identified second natural frequency of the two degree of freedom oscillator system from the impact test (Hz) | 13.5  |
| $f_{top}$       | Identified the natural frequency of the isolated top oscillator system (Hz)                                  | 14    |
| $f_{bottom}$    | Identified the natural frequency of the isolated bottom oscillator system (Hz)                               | 9     |
| $\eta_{bottom}$ | Identified the damping loss factor of the isolated bottom oscillator system from the impact test             | 6.3%  |
| $\eta_{top}$    | Identified the damping loss factor of the isolated top oscillator system from the impact test                | 42.5% |
| $A$             | Excitation displacement amplitude range (mm)   | 0-5   |
| $f$             | Excitation frequency range (Hz)  | 0-20  |

### 3.7 Results and discussions

There are three experiments completed for measurement of the harvested power, they are:

1. Measurement of the harvested power values versus the excitation frequencies

2. Measurement of the harvested power versus the input excitation displacement amplitude at 7 Hz.
3. Measurement of the harvested power versus the external resistance at 12 Hz.

**Table 3.2: The input excitation displacement amplitudes, frequencies and external resistances for the experiments.**

|              | Amplitude (m) | Frequency (Hz) | External resistance ( $\Omega$ ) |
|--------------|---------------|----------------|----------------------------------|
| Experiment 1 | 0.002         | 0-30           | 10                               |
| Experiment 2 | 0.001-0.01    | 7              | 10                               |
| Experiment 3 | 0.002         | 12             | 1-50                             |

In Experiments 2 and 3, the frequencies of 7 Hz and 12 Hz were chosen as the input excitation frequencies because the oscillators vibrate vigorously at the natural resonant frequencies of 6.5 Hz and 13.5 Hz. For the purpose of harvesting the maximum amount of vibration energy without causing any mechanical damage or initiating the nonlinearity, 7 Hz and 12 Hz were set as the input excitation frequencies.

### *3.7.1 Measurement of the harvested power values versus the excitation frequencies*

Sine wave displacement excitation with the amplitude of 2 mm was set as the input of experiment, analysis and simulation models for comparison and validation purposes.

For the simulation model, the harvested voltage and power can be calculated using the code in Figure 3.3. The harvested voltage time trace curves in the individual excitation frequencies from 0 Hz to 30 Hz are plotted and displayed by the scope modules in the Matlab SIMULINK software where the peak or root mean square (RMS) values of the harvested voltage time trace curves are recorded. The harvested power results are calculated from the recorded peak or RMS values of the harvested voltage for the individual frequencies which are plotted and shown in Figure 3.9.

It is seen from Figure 3.9 that the results of the Matlab SIMULINK simulation model based on Equations (3.5-3.6) (yellow triangle marks) are very close to those of the frequency response analysis (solid line), which validates the previous frequency response analysis model of Equation (3.7).

For the simulation model, the frequency response amplitude curve of the harvested power has two peaks at 6.2 Hz and 14 Hz respectively, representing the two natural resonant frequencies of the 2DOF electromagnetic vibration energy harvesting system. It can be seen that the harvested power at the first natural resonant frequency reaches 0.025W which is significantly larger than that at the second natural resonant frequency, as a result of the weight and stiffness distribution of the oscillators.

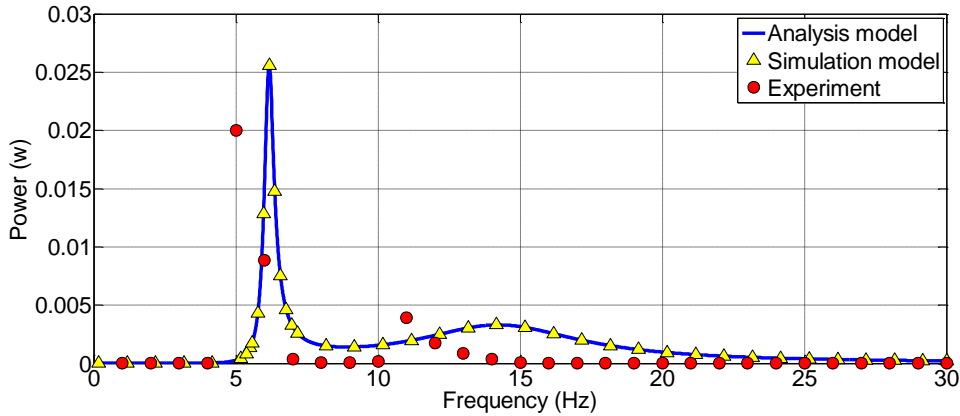


**Figure 3.9: Comparison of the output power values versus the excitation frequencies obtained from the analysis model, simulation model and experiments.**

From the experiment results, it can be seen that the two power peaks occur at the frequencies of 5 Hz and 11 Hz, which are slightly less than those of the predicted natural resonant frequencies. This could be caused by the added equivalent mass of the 2DOF electromagnetic vibration energy harvesting system mounted on the hydraulic shaker test platform or by the large excitation displacement amplitude which induced nonlinearity of the springs. The analysis and simulation results obtained from Equation (3.7) and the Matlab SIMULINK code in Figure 3.3 are based on the assumption of the linear 2DOF electromagnetic vibration energy harvesting system. The actual spring stiffness decreases with the displacement, as a result, the 2DOF electromagnetic vibration energy harvesting system acts a non-linear softening system. The power curve peaks are shifted to lower frequencies. It is noted that the peak values of the experiment results are less than those of the analysis and simulation results, the reason could be that the six connecting bolts shown in Figure 3.5 were originally designed to guide the movement of the oscillators to maintain the motion stability. However, they may limit the movement of the oscillators due to the finite length of the bolts. In

particular, at the first natural frequency, the oscillators vibrate with large displacement amplitude, the limitation could occur. Therefore, the actual displacements of the oscillators are limited by the finite length of the bolts and not as large as those predicted. In addition, the bolts develop the sliding frictions, resulting in less energy that can be harvested.

**Table 3.3: comparison of the natural frequencies of the 2DOF electromagnetic vibration energy harvesting system obtained from different methods.**

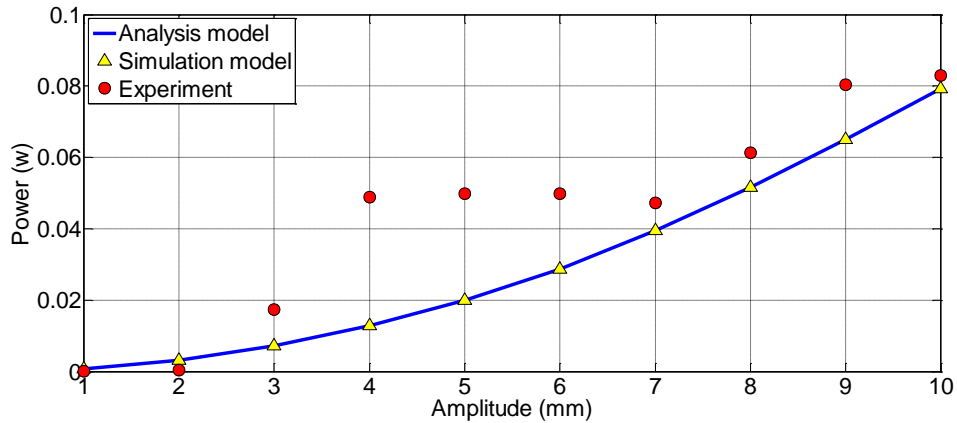
| The theoretical frequency response analysis method | Simulation from the Matlab SIMULINK software | Impact modal analysis tests | MTS dynamic hydraulic shaker tests |
|--|--|-----------------------------|------------------------------------|
| 6.2Hz, 14Hz  | 6.2Hz, 14Hz                                  | 6.55Hz, 14Hz                | 5Hz, 11Hz                          |

Table 3.3 compares the natural frequencies of the 2DOF mass spring oscillator system obtained from theoretical analysis, the Matlab Simulink simulation, impact modal analysis tests and dynamic shaker tests. It can be seen that the results of theoretical analysis, simulation and impact modal analysis tests are very close to one another, which has validated the theoretical frequency response and the Matlab Simulink simulation models. It should be pointed out that the natural resonant frequencies measured from the modal analysis impact tests are different from those measured from the MTS hydraulic shaker experiments. The reason is that the impact modal analysis test is carried out in a static condition of the 2DOF mass spring oscillator system where the system is assumed to be linear, whereas in the MTS

hydraulic shaker experiments, the components of the system are bouncing vigorously due to the shaker excitation. The large oscillator displacement might have induced the non-linearity of the 2DOF mass spring oscillator device. Overall speaking, the natural resonant frequencies measured from the hydraulic shaker tests are close to those obtained from the theoretical frequency response analysis, Matlab Simulink simulation and impact modal analysis tests with a minor difference controlled in a reasonable range.

### *3.7.2 Measurement of the harvested power versus the input excitation displacement amplitude at 7 Hz – the amplitude sensitivity at 7 Hz.*

In Figure 3.10, the theoretical frequency response analysis results from Equation (3.7) and the simulation results developed from the Matlab Simulink code are identical and both of them show the increasing trend of the power as a result of increasing input displacement excitation amplitude. This trend has been verified by the experiment results shown in Figure 3.10. The difference between the analytical results and the experimental results can be due to the nonlinearity of the oscillating system. In order to extract more energy, larger displacement excitation amplitude is preferred, meaning that the rough terrain will greatly improve the energy harvesting performance.



**Figure 3.10: Harvested power versus the displacement excitation amplitude at 7 Hz.**

### *3.7.3 Measurement of the harvested power versus the external resistance at 12 Hz – the external resistance sensitivity at 12 Hz.*

Many authors [16, 77, 147, 148] have stated in their studies that the impedance matching method can improve the efficiency of the system, meaning that by matching the external resistance of the harvesting circuit with the internal resistance, the power output can be enhanced and maximized.

In Figure 3.11, the experimental and simulation results present a similar trend. The difference of the experimental and simulation results could be caused by the nonlinearity of the two oscillators moving out of phase when their vibrating around the 2<sup>nd</sup> natural frequency. The possible direct contact between the oscillators will result in the undesired energy dissipation.

The peak power value can be obtained when the external resistance is equal to the coil internal resistance of 10  $\Omega$ , as shown in Figure 3.11.

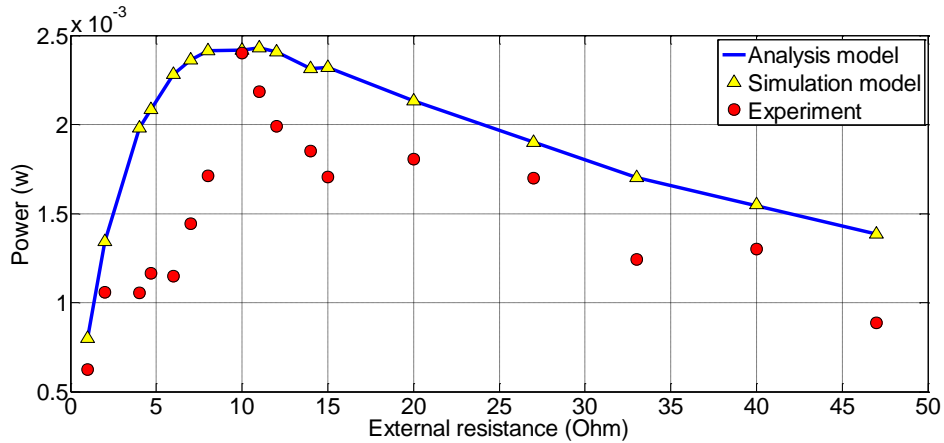


Figure 3.11: Harvested power versus the external resistance at 12 Hz.

## 3.8 Sensitivity analysis

### 3.8.1 Coil profile

The total number of coil windings was 585 in the current design of the device. As the magnets move up and down, the electricity can be generated as a result of the coil cutting through the magnetic flux based on the Faraday's Law. The generated voltage can be expressed as:

$$V_{generated} = Bl(\dot{x}_2 - \dot{x}_1), \quad (3.14)$$



Equation (3.14) shows that as the total length of the coil wire increases, the generated voltage will increase as well. Therefore it can be concluded that increasing the winding number of the coil will improve the performance of the 2DOF electromagnetic vibration energy harvesting system. Figure 3.12 shows the frequency response amplitude curves of the harvested power with different winding number of the coil where the winding number of the coil is set to be a multiplier of 585. It is shown that with the  $10 \times 585$  winding number of the coil, which is 5850 turns, the harvested power at the first natural frequency will reach 0.3 W, which is more than ten times as large as that at the same frequency with just 585 winding number of the coil. In addition, the change of the coil winding number does not affect the frequency response amplitude curve shape of the harvested power because the electromagnetic force generated by the coils is equivalent to the damping force which does not change the natural resonant frequency.

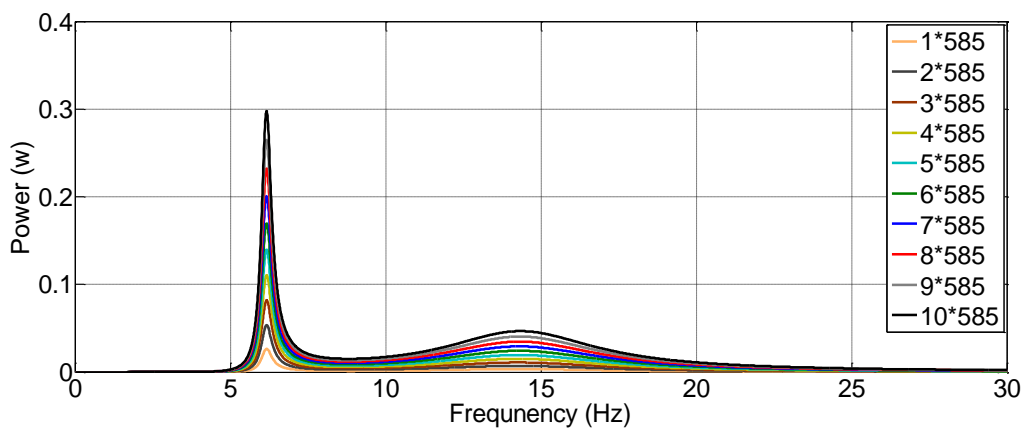


**Figure 3.12: Power frequency response amplitude curves versus the winding number of the coil.**

### 3.8.2 Electro-mechanical coupling

Based on the nature of the electromagnetic generator, the electromechanical coupling can be represented mathematically by  $Bl$  [1]. The coil length  $l$  depends on the coil profile which is discussed in the previous section and the magnetic field intensity  $B$  is dependent on the magnetic pattern. In order to better understand how the magnet pattern arrangement contributes to the harvested power, Halbach array, transversely and longitudinally arranged pole magnets are included in the simulation model in the ANSYS Maxwell software for comparison.

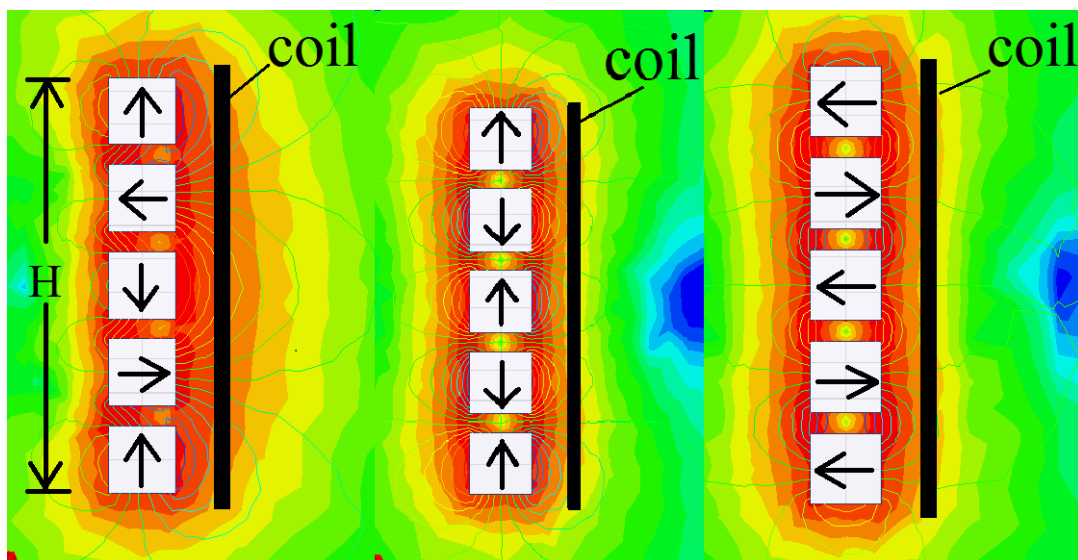


**Figure 3.13: 2D magnetic field intensity contour of magnets arranged in the patterns of the Halbach array, longitudinal and transverse arrays.**

Figure 3.13 shows that the magnetic field intensity contour and flux lines for three different magnet pole arrangement patterns. It is obvious that the flux lines for the magnet arrangement pattern of the Halbach array are more densely packed than those of the other two where the

magnets are arranged in the patterns of the transverse and longitudinal pole arrays. The magnet pattern of the Halbach array also maintains the larger area of the strong magnetic field around the coil, meaning that the harvester with the magnets arranged in the pattern of the Halbach array will still work efficiently even when the coil is placed further away from the magnets. As shown in Figure 3.13, as the coil number or the coil length increases, it will not be possible for all coil turns to have the same field intensity, unless all the coil turns are kept in the range of high magnetic flux density. This can be achieved by radially overlapping the wired coil layers so that all the coil turns are kept in the range of high magnetic intensity. Figure 3.14 shows that the curve of the magnetic field intensity versus the coil width, which is denoted by  $H$  in Figure 3.13. The larger magnetic field intensity can be expected by the pattern of the Halbach array especially in the middle section of the coil width while the other two arrangement patterns present the reduction of magnetic field intensity in the same area.

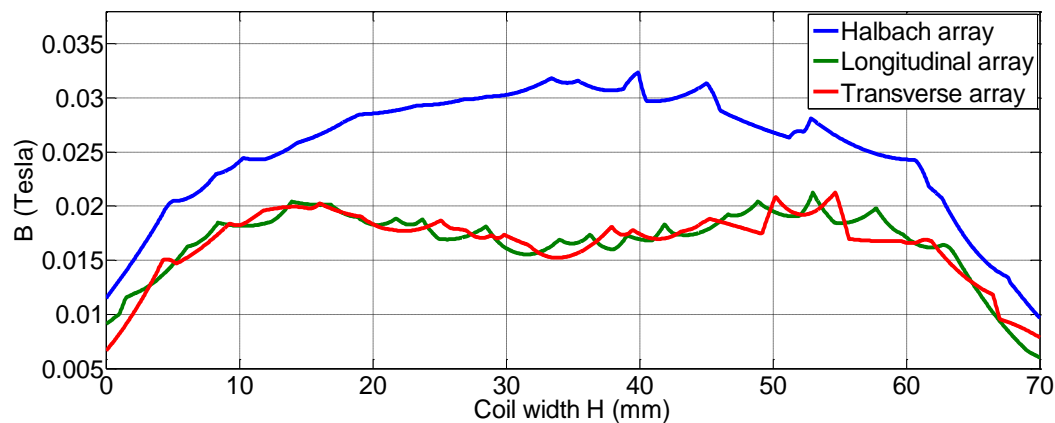


**Figure 3.14: Magnetic field intensity versus the coil width  $H$ .**

How the magnet arrangement pattern can contribute to energy harvesting is shown in Figure 3.15. Figure 3.15 shows that harvested power versus the excitation frequency for the three magnet arrangement patterns. It is seen that with the magnet pattern of the Halbach array, the harvested power is significantly larger than those with the other patterns, especially when the harvester is excited around the natural frequencies. Such difference of the harvested power is expected to be larger if a gap is presented between the coil and magnets. This is because that the magnet pattern of the Halbach array enables the magnets to produce a strong magnetic field over a larger area and longer distance away from the coil.

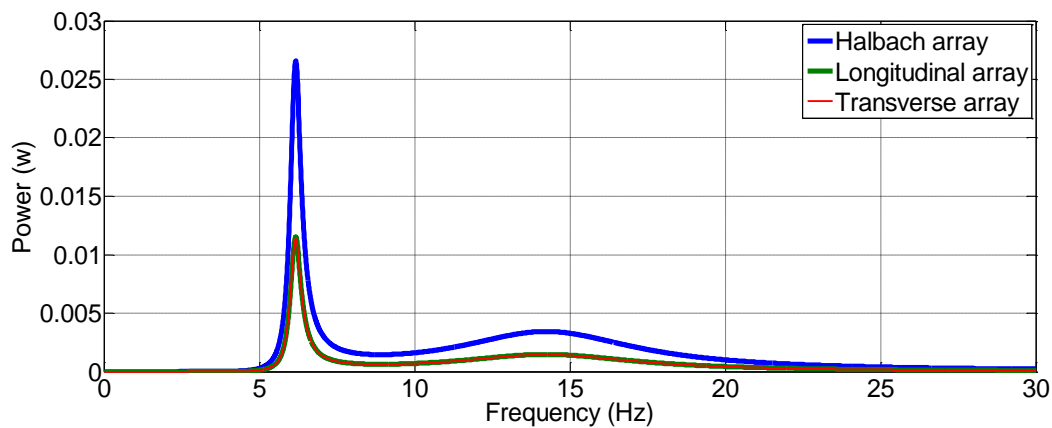


**Figure 3.15: Harvested power versus the displacement excitation frequencies for the three magnet arrangement patterns.**

As the vibration between the magnets and coils increases in amplitude, the magnetic field intensity may change during the vibration, the magnetic flux density may change around the coils, increased magnetic flux density change rate may benefit the resulting behavior of the energy harvesting system.

Increasing the magnetic field intensity using some of magnetic patterns can improve its energy harvesting performance of the harvester. Taking into account the 2DOF system that the harvester is working within, however, higher  $Bl$  value does not necessarily promise higher power output. Assuming a constant coil length  $l$ , shown in Figure 3.16 is the output power plot over the frequency range of 0 – 30 Hz for different  $B$  values.

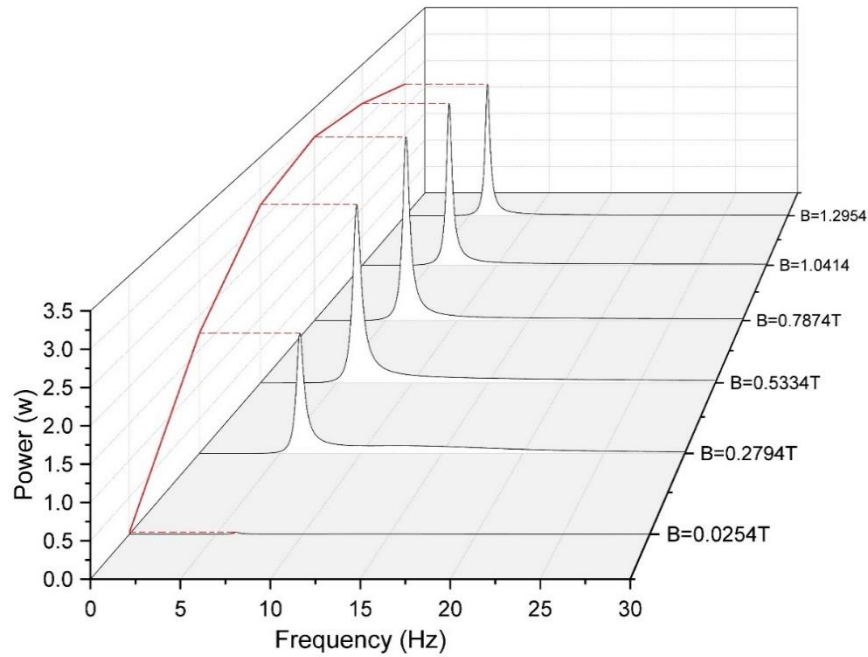


**Figure 3.16: Harvested power versus the excitation frequencies for different  $B$  values.**

It shows that with  $B$  increasing from the original value 0.0254 T to 1.2954 T, at the first natural frequency the power output increases significantly and reaches 3 W at 0.7874 T. However further increasing the magnetic field intensity can result in the drop in the output power, the reason being that strong electro-mechanical coupling reduces the displacement between the oscillators, resulting in less harvested voltage thus lower power output. This

should be taken into consideration if incorporating the harvester into any 2DOF system such as a car suspension.

In many car suspension systems, the damping behavior should be maintained as the reduced vibration or comfort is one of the major attributes prioritized by the customers [142, 143]. In order to replace the viscous damper with the electromagnetic regenerative shock absorber while maintaining the comfort level of the vehicle, the damping coefficient needs to be specified in a confined range. This electromagnetic damping coefficient can be expressed as:

$$C_e = \frac{F_{\text{electromagnetic}}}{v}, \quad (3.15)$$

where  $F_{\text{electromagnetic}}$  is the electromagnetic damping force provided by the harvester and the  $v$  is the relative velocity between the oscillators.

The  $F_{\text{electromagnetic}}$  can be obtained by Lorentz law,

$$F_{\text{electromagnetic}} = Bl \cdot I = \frac{Bl \cdot U}{R + R_e}, \quad (3.16)$$

where  $U$  is the generated voltage by the harvester which is given by,

$$U = Bl \cdot v, \quad (3.17)$$

Substituting Equation (3.16) and Equation (3.17) into Equation (3.15) gives,

$$C_e = \frac{(Bl)^2}{R + R_e}, \quad (3.18)$$

The Equation (3.18) indicates the relationship between the electromagnetic damping coefficient  $C_e$  and the electro-mechanical coupling  $Bl$ . The electromagnetic force is proportional to the input velocity with a factor of  $C_e$ , as a result, it has the similar behavior as a conventional damper. Therefore it is possible to replace the conventional damper completely with a regenerative electromagnetic shock absorber while maintaining its damping performance.

It is assumed that the proposed 2DOF electromagnetic harvester is a regenerative suspension system where the conventional damper between the oscillators  $m_1$  and  $m_2$  needs to be replaced by regenerative electromagnetic damper which is required to have the same damping coefficient for the purpose of the comfort. For example if the required damping coefficient is 6250 Ns/m, according to Equation (3.18),  $Bl$  can be calculated as 250 Tm, then the curve of Equation (3.18) can be plotted on the contour map of the harvested power versus the coil length and magnetic field intensity, as shown in Figure 3.17.

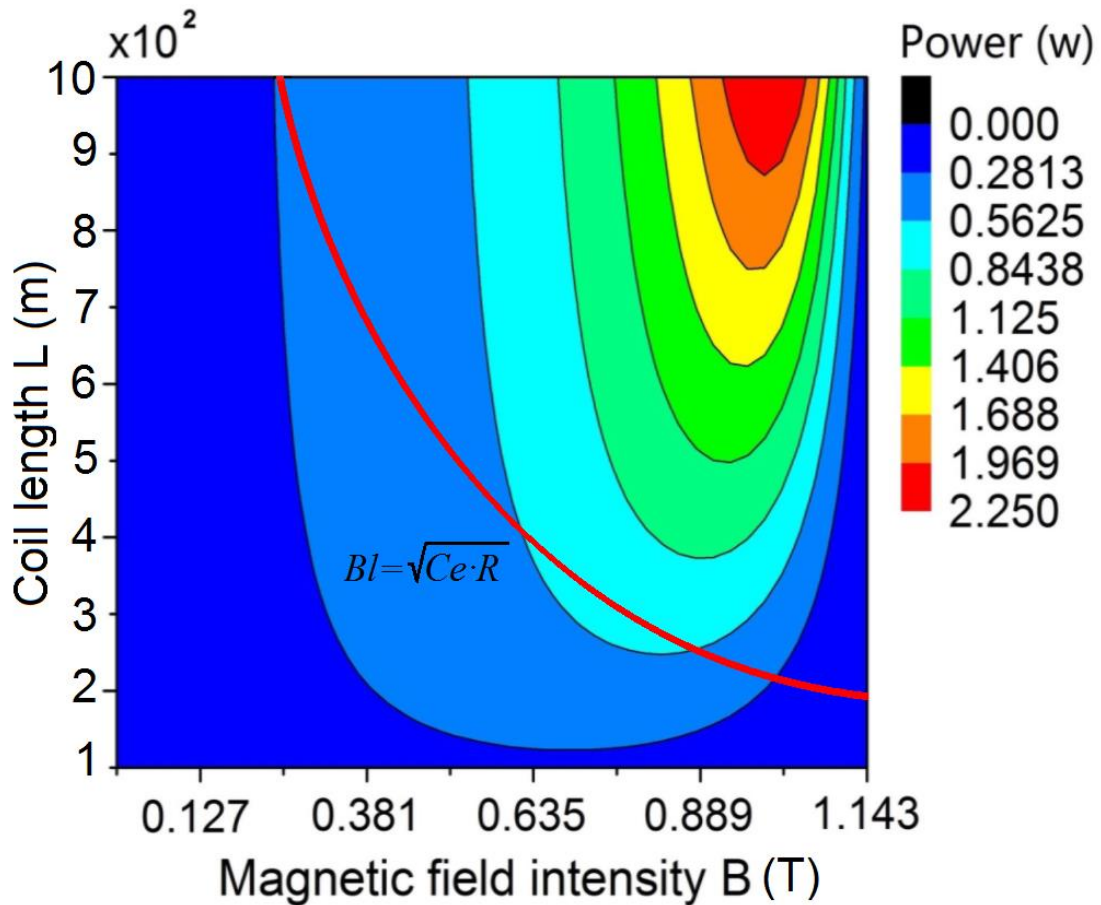


Figure 3.17: Contour map of power output versus the coil length and magnetic field intensity.

It shows that any combination of magnetic field intensity  $B$  and coil length  $l$  on the red line can satisfy the damping requirement of the vehicle, however the output power presents the difference. In order to maximize the energy harvesting ability without affecting its damping performance, only the part located in the light blue area will be utilized for its optimization. The output power plot with respect to the  $Bl$  value is shown in Figure 3.18. The maximum power occurs at  $B=0.8255$ T and  $l=300$ m indicated by the red solid line and any other  $Bl$  combination will result in lower output power. The displacement of the oscillators remains the same for the selected  $Bl$  combination, therefore it can be said the system optimization has been achieved.



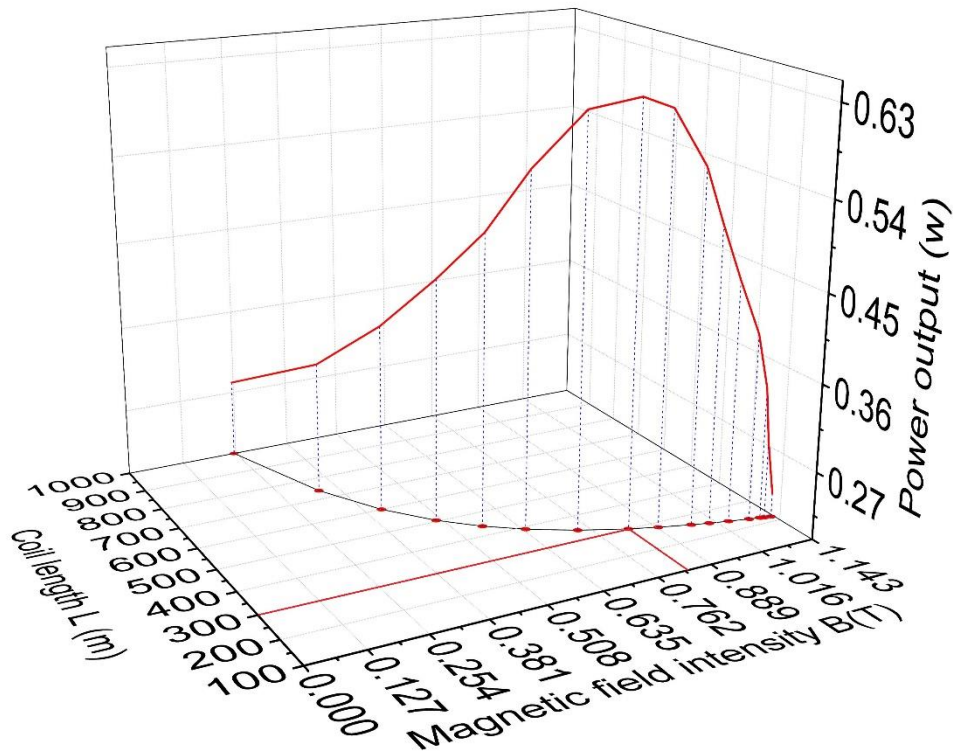


Figure 3.18: Power output versus the coil length and magnetic field intensity.

### 3.9 Conclusions

In this chapter, a 2DOF electromagnetic vibration energy harvesting system is proposed to simulate the power exploitation of any 2DOF oscillating system including the regenerative vehicle quarter suspension system. The proposed system consists of two masses, two groups of springs, and one electromagnetic vibration energy harvesting unit. The magnet arrangement pattern of the Halbach array was built into the unit. The 2DOF electromagnetic vibration energy harvesting system has been built and tested to identify the system

parameters of the damping and stiffness coefficients of the two oscillators. The input parameters of the simulation have been determined through experiment and FEA calculation analysis. Theoretical frequency response analysis and Matlab SIMULINK simulation models of this 2DOF electromagnetic vibration energy harvesting system are then developed and validated by the results of each other and the experimental results. When subjected to the same range of the excitation frequencies, amplitude and external resistance, the results obtained from three different approaches of analysis, simulation and experiment are close to one another. Therefore the frequency response analysis and simulation models have been validated to be able to represent this 2DOF electromagnetic vibration energy harvesting system. These models thus allow for the sensitivity analysis to be conducted for the system design optimization.

Currently 0.025 W can be harvested by the 2DOF electromagnetic vibration energy harvesting system with the winding number of 585 of the coil. More coil winding numbers can significantly improve the system energy harvesting performance based on Equation (3.14). It can be concluded that increasing the coil winding number will increase the harvested power in the design of the 2DOF electromagnetic vibration energy harvesting system.

It has also been shown that the different magnet pole arrangement patterns affect the amount of the harvested power. The magnet pole arrangement pattern of the Halbach array provides a much larger area of high magnetic flux density around the coil than the other patterns, which helps to improve the energy harvesting performance. However with the same coil profile, the

magnetic field intensity  $B$  has a premium value after which the harvested power will decrease. Therefore, it should be noted that in a 2DOF energy harvesting system, having the stronger magnet filed may not necessarily result in higher power output.

Considering the regenerative shock absorber inside a quarter vehicle suspension model which is a 2DOF oscillating system, for a certain type of vehicle, the regenerative shock absorber needs to have the same damping coefficient as that of the conventional shock absorber. It has been found that a range of the combinations of the magnetic field intensity  $B$  and coil length  $l$  can be applied to obtain the desired damping coefficient, and optimized power extraction only occurs when the regenerative shock absorber harvests more energy while maintaining the targeted damping response of the conventional shock absorber.

## Chapter 4

### *The design of the innovative regenerative shock absorbers*

*In this chapter, two innovative regenerative shock absorbers, namely the double speed regenerative shock absorber and the indirect-drive regenerative shock absorber, are designed and fabricated. The simulation models of both the absorbers are validated by the experimental results and both the absorbers are compared with the conventional direct-drive regenerative shock absorber to reveal their potentials in energy harvesting and vibration control. Based on the results of the sensitivity analysis, both the absorber designs are evaluated and optimised.*

## 4.1 Background

In order to reduce the dissipation of the energy in a viscous damper as the heat loss, many researches have been conducted on utilizing electromagnetic generators to convert the kinetic energy into the electrical energy. It is proposed to connect the magnets and coils to the vehicle body and wheel assembly, respectively [22]. The electric current can then be induced directly as a result of the relative movement between the vehicle body and the wheel. According to the Faraday's law  $U = Bl \cdot v$  where  $U$  is the voltage output,  $Bl$  is the electromechanical coupling constant and  $v$  is the speed of the moving conductor [149]. For the above-mentioned shock absorbers, the magnet speed with respect to the coils is limited to the relative speed between the vehicle body and wheel. The current output of the regenerative shock absorber also relies on the electromechanical coupling constant which is related to design of the combination of the coils and magnets. The large electromechanical coupling constant may bring a potential problem of large size and weight of the shock absorbers [146], which is not sustainable for the regenerative shock absorber.

To further improve the performance of the regenerative shock absorber, many studies have been focused on development of the amplifying mechanism to increase the magnet speed with respect to the coils without adding too much extra weight. Rack and pinion mechanisms [42, 43], ball-screws [43, 46, 51, 70, 121] are widely used to convert the unidirectional

reciprocating movement of the shock absorber into the rotational movement of a generator. Because of the use of the DC generator, the unidirectional reciprocating movement needs to be rectified into one directional rotation through one-way clutch [42]. The shock absorber can also be connected to the hydraulic system to achieve the motion conversion and the speed amplification. In such designs, check valves are utilized to produce one-way flow for the hydraulic motor which drives a DC generator. The rotating speed of the DC generator can then be amplified by adjusting the pipe profile [63]. Some innovative designs are also proposed that includes adding the secondary amplifying cylinder in the shock absorber to provide propulsion to a DC generator, which operates on a faster speed due to the smaller pipe line [75, 76].

The regenerative shock absorbers with the amplifying mechanism often have a higher magnet speed with respect to the coils. In order to compare the regenerative shock absorbers with and without the amplifying mechanism, a linear generator and a rotary generator with ball screws have been incorporated respectively into two shock absorbers of an ATV (all-terrain vehicle) [23]. The result indicates that in terms of the power output, the rotary generator with the speed amplifying mechanism has more advantages over the linear generator directly driven by the oscillators. However, there is not an apple to apple comparison as the generators used in the experiments are significantly different from each other in configurations, such difference can largely affect the energy generating ability and output power values. Additionally, in order to generate unidirectional rotation to drive the DC generator, the mechanical motion rectifier such as one way clutches or check valves have to be incorporated, which potentially results in more mechanical energy loss due to the friction

losses. Therefore, whether the speed amplifying mechanism is able to enhance the overall performance of the regenerative shock absorber is still unknown.

This chapter presents the design and modelling of the double speed regenerative shock absorber (or double speed RSA) that utilizes the reciprocation of the electricity-generating coils for harvesting the vibrational energy. The double speed RSA is equipped with the rack and pinion mechanism to amplify the magnet speed with respect to the coils, therefore the induced current and voltage can be increased.

The parameters of the double speed RSA and regenerative shock absorber without the double speed amplifying mechanism (or direct-drive RSA) have been identified through experimental measurements. Sinusoidal wave excitations and random signal excitations have been applied as the road profile excitation input to the simulation models to predict the voltage output, power output and efficiency of models. To further evaluate the responses of a vehicle to the random road profile displacement excitation input, the comparison based on the Monte Carlo simulation between the double speed RSA and direct-drive RSA has been conducted.

In the second part of this chapter, a novel indirect-drive regenerative shock absorber (or indirect-drive RSA) is presented to convert the reciprocating motion to the unidirectional rotational motion through an arm-teeth mechanism and the rotational speed is amplified through a gear box. The simulation models of the quarter vehicle suspension system with the

proposed indirect-drive RSA (or indirect-drive system) and with a direct-drive RSA (or direct-drive system) have both been established and experimentally validated based on the prototypes of the two designs. The generators adopted by both the direct-drive and indirect-drive systems have the same electromechanical coupling constant, coil resistance and coil inductance in order to compare the two drive systems and to evaluate their parameters in a comparable way. Parameter sensitivity analysis will be conducted using the Monte Carlo simulation where the excitation force is assumed to be evenly distributed in the excitation frequency range. Each of the system parameters is assumed to be normally distributed with its initial value as the mean value and 20% of the mean value as its standard deviation for both the direct-drive and indirect-drive systems. The parameters will be evaluated to reveal the key differences of the two systems and potentials for improving their energy harvesting performance.

## 4.2 Double speed regenerative shock absorber design

### *4.2.1 Concept design*

The working principle of the double speed RSA is shown in Figure 4.1. Two sets of rack and pinion mechanism are installed in between the magnets and coils to increase the magnet speed with respect to the coils for larger current and voltage induction while converting the kinetic energy into electricity. The magnets are connected to the wheel assembly and the rack and pinion mechanism is connected to the upper vehicle body. As a result, when going



through the compression phase, the coil moves down and the magnets move up in the same speed and vice versa, as a result the magnet speed with respect to the coils is doubled.

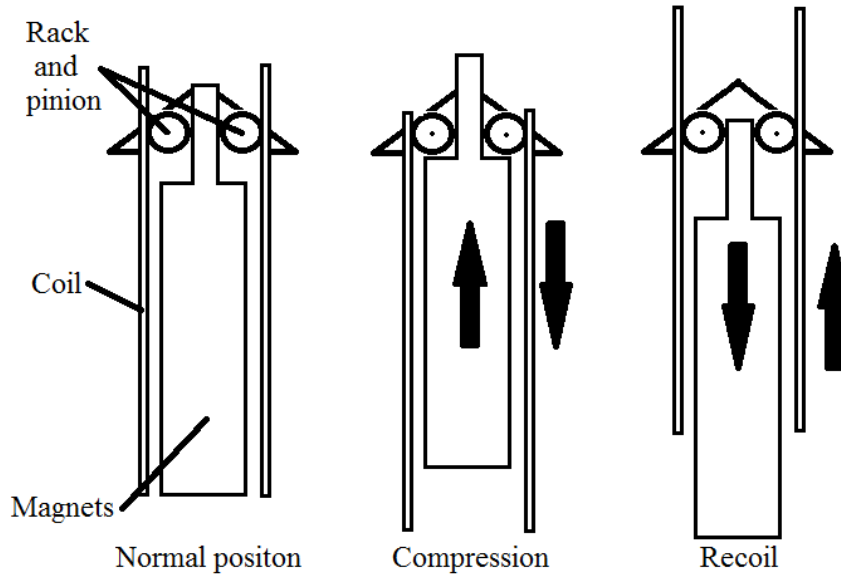


**Figure 4.1: The working principle of the double speed RSA.**

#### 4.2.2 System simulation of the double speed regenerative shock absorber and the direct-drive regenerative shock absorber

Schematic of two degrees of freedom mass-spring-dashpot model of a quarter vehicle suspension system is shown in Figure 4.2 with the parameters shown in Table 4.1.  $m_1$  is the wheel assembly mass,  $m_2$  is the quarter vehicle mass,  $x_1$  is the wheel assembly displacement,  $x_2$  is the vehicle body displacement,  $c_1$  is the tyre damping,  $c_2$  is the suspension damping and  $y$  is the road excitation displacement amplitude.

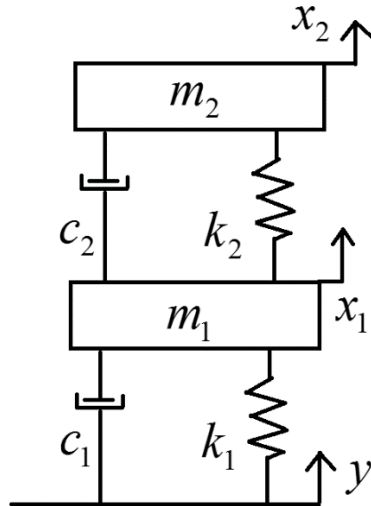


**Figure 4.2: Two degrees of freedom (2DOF) mass-spring-dashpot quarter vehicle suspension system model.**

**Table 4.1: Parameters of the 2DOF mass-spring-dashpot simulation model of the quarter vehicle suspension system**

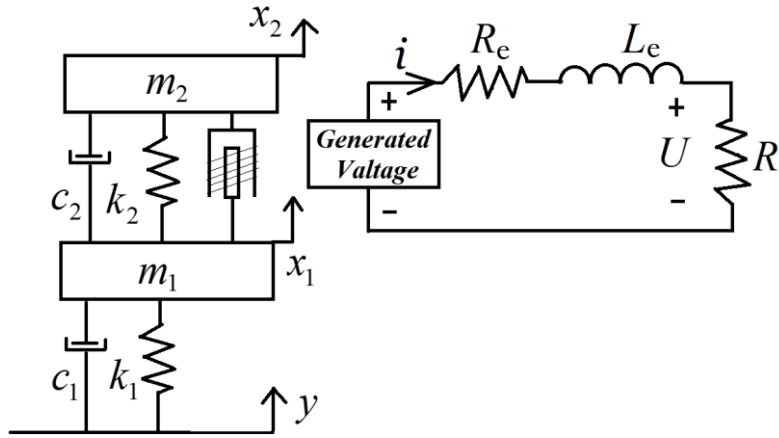
|                           | Parameter | Value      |
|---------------------------|-----------|------------|
| Wheel assembly mass       | $m_1$     | 40 kg      |
| Quarter vehicle body mass | $m_2$     | 260 kg     |
| Tyre stiffness            | $k_1$     | 130000 N/m |
| Suspension stiffness      | $k_2$     | 26000 N/m  |
| Tyre damping              | $c_1$     | 264.7 Ns/m |
| Shock absorber damping    | $c_2$     | 520 Ns/m   |

The regenerative shock absorbers are placed between the vehicle body and the wheel assembly, the relative movement between the vehicle body and the wheel assembly leads to the shock absorber movement. The road displacement excitation can be represented by different signals including the step signal, sine wave signal or white noise signal. The maximum shock absorber displacement is 0.035m. Larger shock absorber displacement

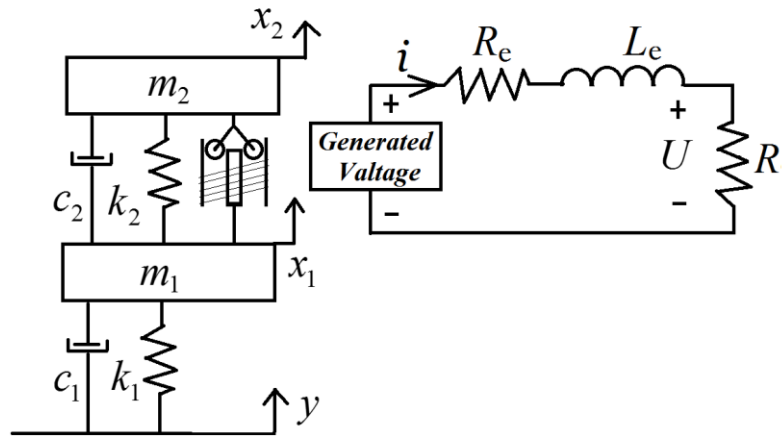
resulting in structural damage should be avoided and locked for security and will not be considered in this thesis.

The double speed RSA is placed in between the quarter vehicle mass and wheel assembly mass to provide the additional electromagnetic damping and generate electrical energy. The coil winding of the double speed RSA can be represented by the electrical circuit shown in Figure 4.3(b) where  $R_e$  is the coil resistance and  $L_e$  is the coil inductance, the power is extracted over the external resistor  $R$ . The road excitation displacement is denoted as  $y$ .

For comparison, the direct-drive regenerative shock absorber (direct-drive RSA) is introduced, shown in Figure 4.3(a). Unlike the double speed RSA that has the rack and pinion mechanism to increase the relative speed, the direct-drive RSA has coils and magnets directly connected to the quarter vehicle mass and wheel assembly mass, and as a result, the magnet speed with respect to coils is equal to the relative speed between the two masses. The configuration of the magnets and the coils are the same for the double speed RSA and direct-drive RSA, the same electrical circuit is applied for both types of RSA.



(a)



(b)

**Figure 4.3: Simulation model of a quarter vehicle suspension system with (a) direct-drive RSA and (b) double speed RSA**

In addition, rectification process such as a bridge rectifier can be added to convert AC to DC, as shown in Figure 4.4, for practical applications [123]. Alternatively, active rectifiers such as a boost converter can also be used for the AC-DC conversion and the maximization of the power extraction [89, 91, 92, 107].

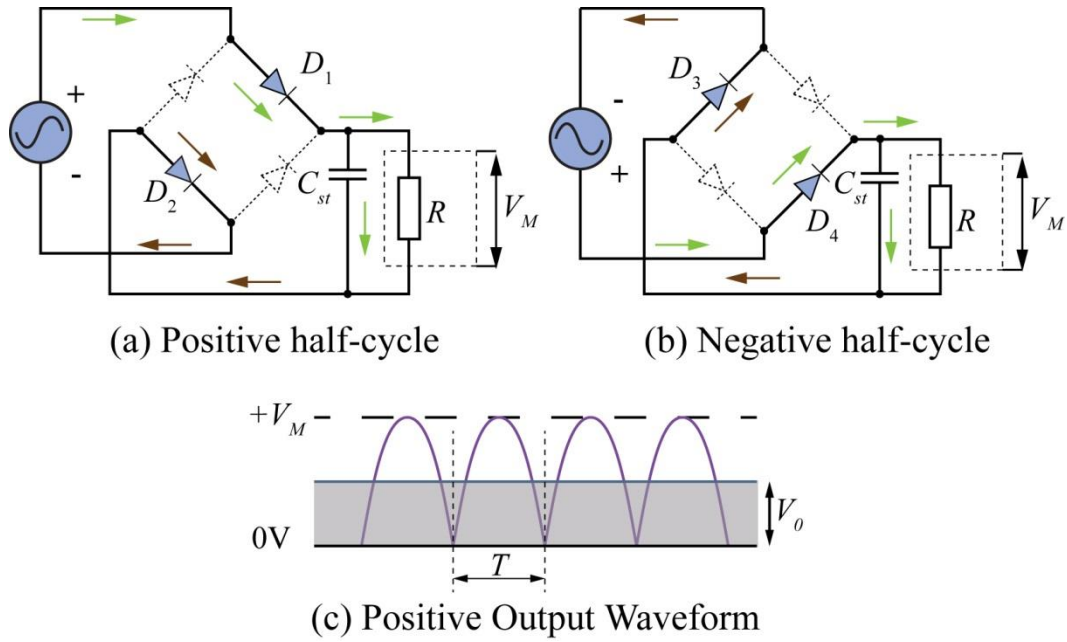


Figure 4.4: (a) positive cycle of the rectification process, (b) negative cycle of the rectification process, (c) the output voltage [123].

#### Governing equations of the double speed RSA

Based on the Lagrange's theorem, the equations of the motion of the system can be expressed as:

$$\begin{cases} \frac{d}{dt} \left( \frac{\partial T}{\partial \dot{x}_1} \right) - \left( \frac{\partial T}{\partial x_1} \right) + \left( \frac{\partial W}{\partial \dot{x}_1} \right) + \left( \frac{\partial V}{\partial x_1} \right) - Bl \cdot \frac{U}{R} = 0 \\ \frac{d}{dt} \left( \frac{\partial T}{\partial \dot{x}_2} \right) - \left( \frac{\partial T}{\partial x_2} \right) + \left( \frac{\partial W}{\partial \dot{x}_2} \right) + \left( \frac{\partial V}{\partial x_2} \right) + Bl \cdot \frac{U}{R} = 0 \end{cases} \quad (4.1)$$

where  $T$  is the total kinetic energy of the system as a result of the reciprocating masses and rotating pinion gears.  $W$  is the damping energy and  $V$  is the spring potential energy. The inertia force  $F_{Gi}$ , damping force  $F_{Wi}$ , spring restoring force  $F_{ki}$  and Lorenz force  $F_{LZ}$  of the  $i^{\text{th}}$  mass ( $i=1$  or  $2$ ) are given by

$$\left\{ \begin{array}{l} F_{Gi} = \frac{d}{dt} \frac{\partial T}{\partial \dot{x}_i} - \frac{\partial T}{\partial x_i} \\ F_{wi} = \frac{\partial W}{\partial \dot{x}_i} \\ F_{ki} = \frac{\partial V}{\partial x_i} \end{array} \right. \quad (4.2)$$

The total kinetic energy of the system can be expressed by the sum of the kinetic energy of the wheel, rack gears and the magnets moving at a speed of  $\dot{x}_1$ , the quarter vehicle body mass and two pinion gears moving at speed of  $\dot{x}_2$ , the kinetic energy of the coils and rack gears and the kinetic energy of two rotational pinion gears.

The kinetic energy of the coil is given by:

$$T_c = \frac{1}{2} \cdot m_c \cdot \dot{x}_c^2 \quad (4.3)$$

where  $\dot{x}_c$  is the absolute velocity of the coil,  $m_c$  is the sum of the coil mass, coil carrier mass and rack gear mass. As shown in Figure 4.5, two pinion gears are fixed on the quarter vehicle mass where each of the pinion gears meshes with the two rack gears that are connected to the magnet and coil respectively.

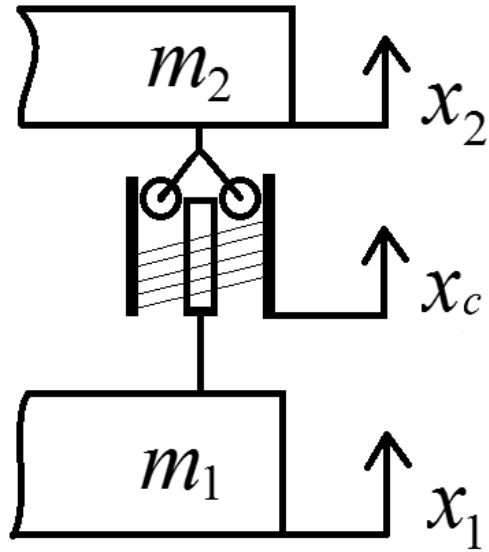


Figure 4.5: Schematic of the double speed RSA system.

If the quarter vehicle mass is stationary, which has  $\dot{x}_2 = 0$ , the coil moves in the opposite motion to the magnet, the coil speed is same as the magnet speed, which is  $-\dot{x}_1$ . When the quarter vehicle mass moves in a speed of  $\dot{x}_2$ , the absolute coil speed is then given by Equation (4.4).

$$\dot{x}_c = \dot{x}_2 - \dot{x}_1 \quad (4.4)$$

Therefore, the kinetic energy of the system can be expressed by:

$$\begin{cases} T = \frac{1}{2} \cdot (m_1 + m_m) \cdot \dot{x}_1^2 + \frac{1}{2} \cdot m_c \cdot (\dot{x}_2 - \dot{x}_1)^2 + \frac{1}{2} \cdot (m_2 + m_p) \cdot \dot{x}_2^2 + \frac{1}{2} \cdot (2 \cdot J_w) \cdot \left( \frac{\dot{x}_1 - \dot{x}_2}{r} \right)^2 \\ W = \frac{1}{2} \cdot (c_2 + c_s) \cdot (\dot{x}_1 - \dot{x}_2)^2 + \frac{1}{2} \cdot c_1 \cdot (\dot{x}_1 - \dot{y})^2 \\ V = \frac{1}{2} \cdot k_2 \cdot (x_1 - x_2)^2 + \frac{1}{2} \cdot k_1 \cdot (x_1 - y)^2 \end{cases} \quad (4.5)$$

where  $m_m$  is the mass of the magnets and rack gear,  $m_p$  is the pinion gear mass,  $J_w$  is the moment of rotational inertia of the pinion gear and  $r$  is the pinion gear radius;  $y$  is the displacement of the road profile excitation and  $c_s$  is the mechanical damping coefficient of the double speed RSA.  $m_2$  and  $m_1$  represent the quarter vehicle mass and wheel assembly mass respectively.

As the speed of the magnet is  $\dot{x}_1$  and the coil speed is given by Equation (4.4). The relative speed of the coil with respect to the magnet can be given by

$$v_{coil-magnet} = \dot{x}_2 - 2 \cdot \dot{x}_1 \quad (4.6)$$

In the electrical circuit, as shown in Figure 4.2(b), the coil of the generator has internal resistance  $R_e$  and inductance  $L_e$ . Because the power is harvested over the external resistance  $R$ , the governing equation of the electrical circuit is given by:

$$L_e \cdot \frac{\dot{U}}{R} + \frac{U}{R} \cdot (R + R_e) = Bl \cdot (\dot{x}_2 - 2\dot{x}_1) \quad (4.7)$$

Substitution of Equation (4.6) into Equation (4.1) and inclusion of Equation (4.7) give the governing equations of the mechanical and electrical system as below:



$$\left[ \begin{array}{l}
\left( m_1 + m_m + m_c + \frac{2 \cdot J_w}{r^2} \right) \cdot \ddot{x}_1 - \left( m_c + \frac{2 \cdot J_w}{r^2} \right) \cdot \ddot{x}_2 + (c_1 + c_2 + c_s) \cdot \dot{x}_1 - (c_2 + c_s) \cdot \dot{x}_2 \\
-k_2 \cdot x_2 + (k_2 + k_1) \cdot x_1 - Bl \cdot \frac{U}{R} - c_1 \cdot \dot{y} - k_1 \cdot y = 0 \\
\left( m_2 + m_p + m_c + 2 \cdot \frac{J_w}{r^2} \right) \cdot \ddot{x}_2 - \left( m_c + 2 \cdot \frac{J_w}{r^2} \right) \cdot \ddot{x}_1 + (c_2 + c_s) \cdot \dot{x}_2 - (c_2 + c_s) \cdot \dot{x}_1 + k_2 \cdot x_2 \\
-k_2 \cdot x_1 + Bl \cdot \frac{U}{R} = 0 \\
Bl \cdot (\dot{x}_2 - 2 \cdot \dot{x}_1) - L_e \cdot \frac{\dot{U}}{R} - \frac{U}{R} \cdot (R + R_e) = 0
\end{array} \right. \quad (4.8)$$

where  $Bl$  is the electromechanical coupling constant;  $B$  is the magnetic field intensity,  $l$  is the total length of the coils;  $U$  is the output voltage.

Applying the Laplace transform to the Equation (4.8) gives:

$$\left[ \begin{array}{ccc}
m_1 \cdot s^2 + m_m \cdot s^2 + m_c \cdot s^2 + \frac{2 \cdot J_w}{r^2} \cdot s^2 + c_2 \cdot s + c_s \cdot s + c_1 \cdot s + k_2 + k_1 & -m_c \cdot s^2 - \frac{2 \cdot J_w}{r^2} \cdot s^2 - c_2 \cdot s - c_s \cdot s - k_2 & -\frac{Bl}{R} \\
-m_c \cdot s^2 - \frac{2 \cdot J_w}{r^2} \cdot s^2 - c_2 \cdot s - c_s \cdot s - k_2 & m_c \cdot s^2 + m_2 \cdot s^2 + m_p \cdot s^2 + \frac{2 \cdot J_w}{r^2} \cdot s^2 + c_2 \cdot s + c_s \cdot s + k_2 & \frac{Bl}{R} \\
-2 \cdot Bl \cdot s & Bl \cdot s & -\frac{R + R_e}{R} - \frac{L_e \cdot s}{R}
\end{array} \right] \cdot \begin{bmatrix} X_1(s) \\ Y(s) \\ X_2(s) \\ Y(s) \\ U(s) \\ Y(s) \end{bmatrix} = \begin{bmatrix} c_1 \cdot s + k_1 \\ 0 \\ 0 \end{bmatrix} \quad (4.9)$$

where  $X_1(s)$ ,  $X_2(s)$ ,  $U(s)$  and  $Y(s)$  are the Laplace transforms of the time histories of the displacements  $x_1(t)$ ,  $x_2(t)$ , voltage  $u(t)$  and  $y(t)$  in the double speed RSA.

### Governing equations of the direct-drive RSA

Because of the absence of the rack and pinion mechanism, the magnets and coils are respectively added to the un-sprung and sprung masses. Based on the force equilibrium relationship, the equations of the motion of the mechanical and electric systems are given by.

$$\left\{ \begin{array}{l} (m_1 + m_m) \cdot \ddot{x}_1 + (c_1 + c_2) \cdot \dot{x}_1 - c_2 \cdot \dot{x}_2 + (k_1 + k_2)x_1 - k_2 \cdot x_2 - c_1 \cdot \dot{y} - k_1 \cdot y - 2 \cdot \frac{Bl \cdot U}{R} = 0 \\ (m_2 + m_c) \cdot \ddot{x}_2 + c_2 \cdot (\dot{x}_2 - \dot{x}_1) + k_2 \cdot (x_2 - x_1) + 2 \cdot \frac{Bl \cdot U}{R} = 0 \\ Bl(\dot{x}_1 - \dot{x}_2) - L_e \cdot \dot{U} - \frac{U}{R}(R + R_e) = 0 \end{array} \right. \quad (4.10)$$

Applying the Laplace transform yields

$$\begin{bmatrix} m_1 \cdot s^2 + m_m \cdot s^2 + c_2 \cdot s + c_1 \cdot s + k_2 + k_1 & -c_2 \cdot s - k_2 & -\frac{Bl}{R} \\ -c_2 \cdot s - k_2 & m_c \cdot s^2 + m_2 \cdot s^2 + c_2 \cdot s + k_2 & \frac{Bl}{R} \\ Bl \cdot s & -Bl \cdot s & -\frac{R + R_e}{R} - \frac{L_e \cdot s}{R} \end{bmatrix} \cdot \begin{bmatrix} \frac{X_1(s)}{Y(s)} \\ \frac{X_2(s)}{Y(s)} \\ \frac{U(s)}{Y(s)} \end{bmatrix} = \begin{bmatrix} c_1 \cdot s + k_1 \\ 0 \\ 0 \end{bmatrix} \quad (4.11)$$

where  $X_1(s)$ ,  $X_2(s)$ ,  $U(s)$  and  $Y(s)$  are the Laplace transforms of the time histories of the displacements  $x_1(t)$ ,  $x_2(t)$ , voltage  $u(t)$  and  $y(t)$  in the direct-drive RSA.

#### *4.2.3 Experimentation on the double speed regenerative shock absorber and the direct-drive regenerative shock absorber*

A prototype of the double speed RSA is designed and fabricated to identify the parameters in the simulation model for its feasibility analysis. The components of the double speed RSA and its design concepts are shown in Figure 4.6, which includes the top mount, pinion gears, rack gears, magnet stacks, shaft, coil carrier and the coils.

As shown in Figure 4.7(a) the pinion gears are installed on the 3D printed top mount which can be clamped on the MTS hydraulic machine. The coil is wound on the 3D printed coil carrier in Figure 4.7(b) where two rack gears are attached. The coil is connected in series with an external resistor that has the same resistance as the coil to maximize the power output [16, 77, 148]. The rare earth ring-shaped Neodymium magnets are axially stacked together with their polarities being opposite to each other in the longitudinal direction on a threaded aluminum shaft shown in Figure 4.7(c). The use of the aluminum shaft enables a better flux line distribution and light weight [22]. In Figure 4.7(c) through the rack and pinion gears the magnet stack and the coils can move in the opposite direction to double the relative speed of the magnets with respect to the coils. Experimental setup is shown in Figure 4.8 where the hydraulic MTS shaker machine is used as the platform to excite the double speed RSA which produces the current and voltage output. An impedance head built with both accelerometer and force transducer is placed between the bottom of RSA and the driving end of the hydraulic MTS machine to measure the base acceleration and the input excitation force.

The measured voltage output will be compared with the simulation result. Some of the parameters in the simulation model are directly identified or obtained from the Maxwell electromagnetic analysis simulation of the magnetic field around the coils. The other parameters are identified from experiments or by matching the simulated voltage output with the measured voltage output where the initial values of the parameters are assumed and then adjusted through trials and errors.

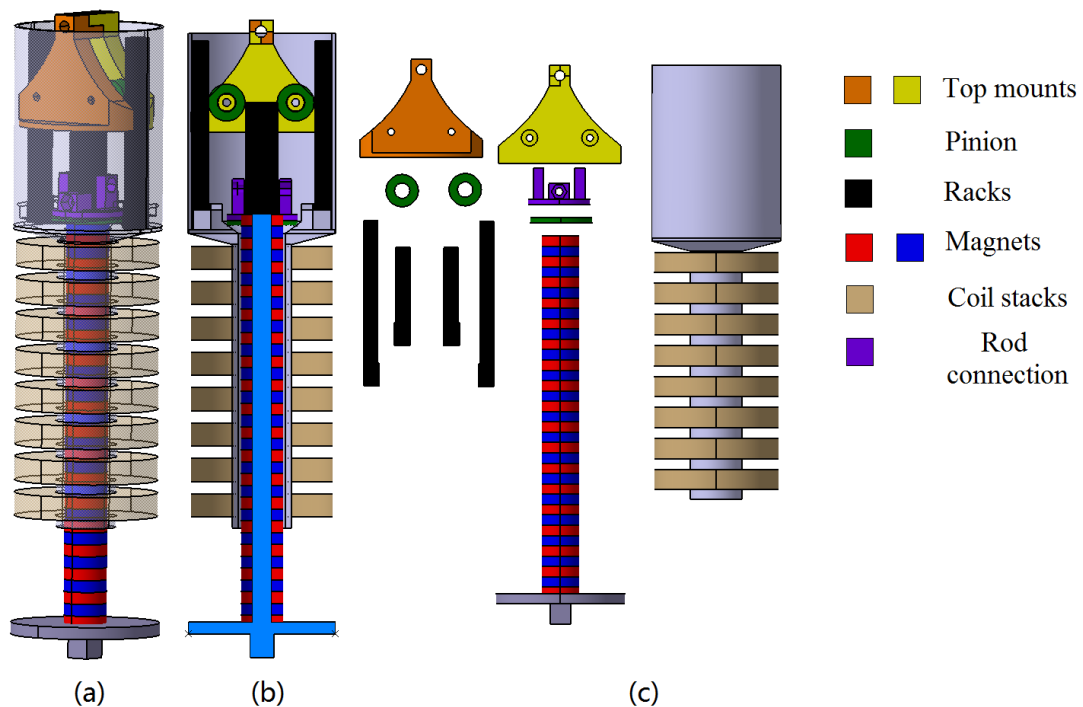


**Figure 4.6: (a) Isometric view, (b) sectional view and (c) composition of the double speed RSA.**

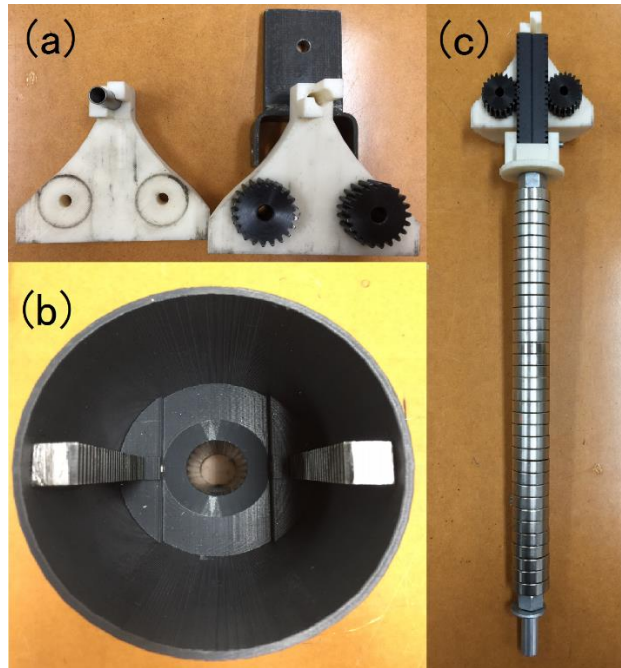


**Figure 4.7: (a) Top mounts with pinion gears, (b) coil carrier with rack gears, (c) longitudinally stacked magnets with their polarities being opposite to each other in the double speed RSA.**



**Figure 4.8: The experimental setup of the double speed RSA on the hydraulic MTS machine.**

Shown in Figure 4.9 is the comparison of experimental setup of the double speed RSA and direct-drive RSA. In order to compare the double speed RSA with the direct-drive RSA, the same coil and magnet configurations are used. During the test of the direct-drive RSA, the coil is fixed onto the top part of the hydraulic MTS shaker machine and the magnets are connected to the bottom part of the hydraulic MTS shaker machine. As a result the magnet speed with respect to the coils is equal to the input shaker excitation speed of the MTS machine.

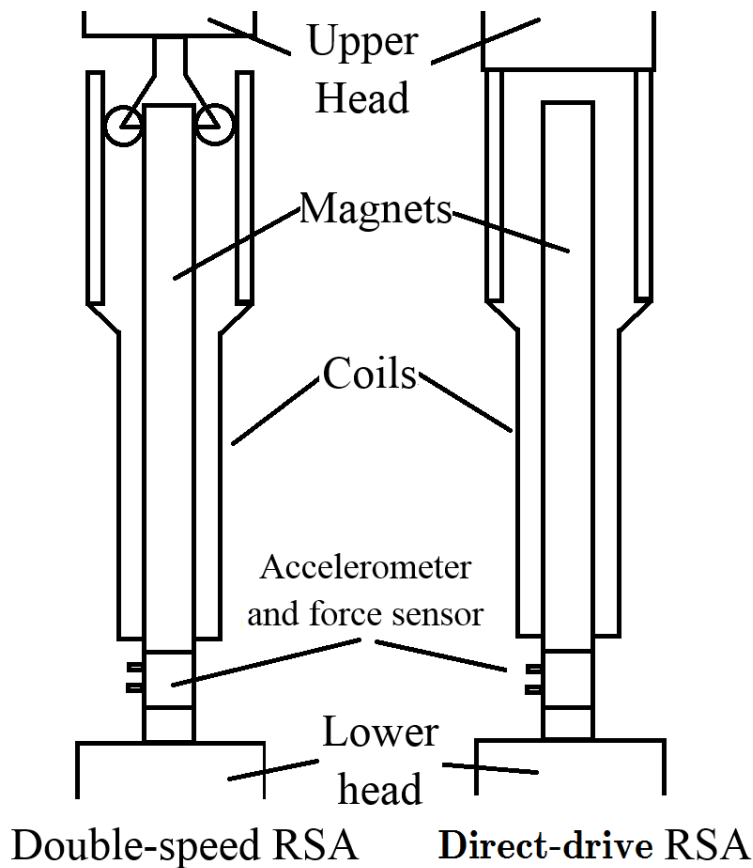


**Figure 4.9: Experiment setup of the double speed RSA and direct-drive RSA**

The prototype undergoes the testing with the frequency ranging from 1 Hz to 25 Hz, which is the operating frequency range of the shock absorber. Different displacement excitation amplitudes and different frequencies are applied to simulate the excitation displacement amplitude and frequency range of all terrains. A Bruel & Kjaer Pulse frontend and software system is used for signal conditioning and the data acquisition.

#### *4.2.4 Parameter identification and the simulation validation*

In order to identify the mechanical damping coefficient  $c_s$  of the double speed RSA, a prototype of the double speed RSA is installed on a hydraulic MTS machine with an impedance head placed between the bottom of the shock absorber and the driving end of the shaker to measure the force needed to move the shock absorber and the input speed of the shock absorber. The impedance head combines one force transducer with one accelerometer in one small cylindrical piece. Shown in Figure 4.10 is the damping coefficient measured over a time span of 50 s which is calculated from the measured force divided by the input velocity of the shock absorber. The double speed RSA is excited with the amplitude of 0.01m at a low frequency of 1Hz to minimize the effect of mass inertia force. It can be seen that the averaged damping coefficient is around 32 Ns/m indicated by a dashed line. Because the fluctuation of the damping coefficient is small under the varying velocity, it can be assumed that the double speed RSA provides the damping force in a similar way as the traditional

viscous damper. Because there is no direct contact between the magnets and coil, the mechanical friction induced damping in the direct-drive RSA is extremely low and thus can be neglected. There is also no direct contact between the magnets and coil in the double speed RSA. However, the presence of the rack and pinion mechanism in the double speed RSA could bring mechanical frictions which may result in a certain mechanical friction induced damping.

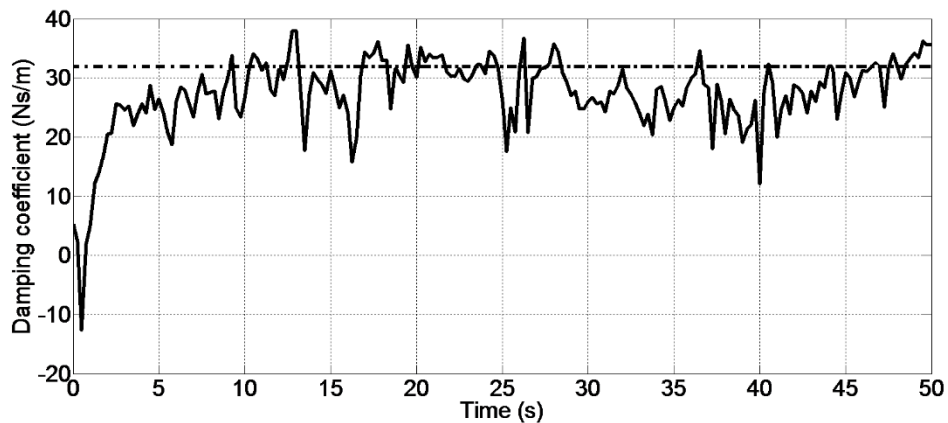


**Figure 4.10: Damping coefficient of the double speed RSA measured in 50 seconds.**

The magnetic fields around the coils used in both the double speed RSA and direct-drive RSA systems are simulated in the ANSYS Maxwell software to obtain the averaged electromagnetic field intensity from which the electromechanical coupling constant can be calculated. Shown in Figure 4.11 is the magnet stack of the prototype on the LHS and its corresponding magnetic field intensity contour plot on the RHS. It can be calculated from the plot that the magnetic intensity around the coils has an average value of 0.055T. Because the



coil length in the prototype is 117m, the estimated electromagnetic coupling constant is calculated to be  $6.5\text{T} \cdot \text{m}$ .

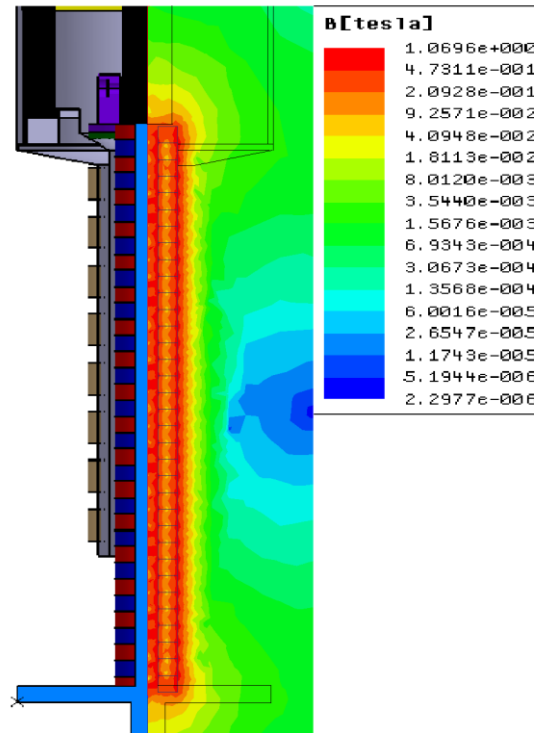


**Figure 4.11:** Magnetic field intensity analysis of the magnets using ANSYS Maxwell software module.

Figure 4.12 shows the experimental validation of the electromechanical coupling constant  $Bl$ . The double speed RSA is excited by the hydraulic MTS machine with the frequencies of 7 Hz, 8 Hz, 9 Hz, 10 Hz and 11 Hz at which the peak power output is recorded. It shows that the harvested power increases with the excitation displacement amplitude and frequency, which means that the double speed RSA harvests more energy with larger and more frequent shock absorber movement or larger input speed. With the electromechanical coupling constant being  $6.5\text{T} \cdot \text{m}$ , for every frequency and excitation displacement amplitude, the

simulation results are well matched with the experimental results. Therefore, the electromechanical coupling constant is verified to be  $6.5 \text{ T} \cdot \text{m}$  and can be directly applied to the simulation of the double speed RSA and the direct-drive RSA.

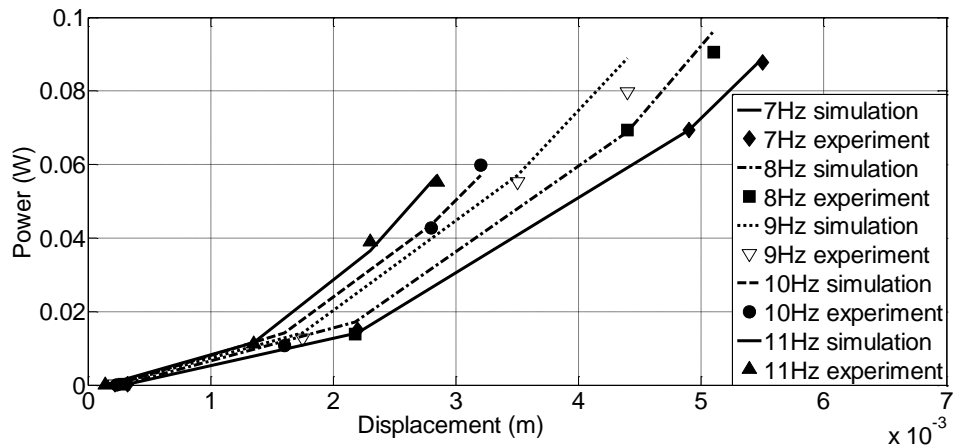


**Figure 4.12: The simulation and experiment results of the output power of the double speed RSA increasing with the excitation displacement amplitude.**

Table 4.2 shows all the parameters of the quarter vehicle suspension system that is used as the platform for evaluation and comparison of the direct-drive and double speed RSAs.

**Table 4.2: Parameters of the quarter vehicle suspension system integrated with the single or double speed RSAs.**

|                      |       |        |
|----------------------|-------|--------|
| Wheel assembly mass  | $m_1$ | 40 kg  |
| Quarter vehicle body | $m_2$ | 260 kg |

|   |       |                             |
|---|-------|-----------------------------|
| mass  |       |                             |
| Magnet mass   | $m_m$ | 2.428 kg                    |
| Coil mass   | $m_c$ | 1.256 kg                    |
| Pinion mass   | $m_p$ | 0.5 kg                      |
| Tyre stiffness  | $k_1$ | 130000 N/m                  |
| Suspension stiffness                                  | $k_2$ | 26000 N/m                   |
| Tyre damping coefficient                              | $c_1$ | 264.7 Ns/m                  |
| Suspension damping coefficient                        | $c_2$ | 520 Ns/m                    |
| Mechanical damping of the regenerative shock absorber | $c_s$ | 32 Ns/m                     |
| Electro-mechanical coupling                           | $Bl$  | 6.5T m                      |
| Coil resistance                                       | $R_e$ | 113 $\Omega$                |
| External resistance                                   | $R$   | 113 $\Omega$                |
| Coil inductance                                       | $L_e$ | 0.000094H                   |
| Moment of the rotational inertia of the pinion gears  | $J_w$ | 0.0000203 kg.m <sup>2</sup> |
| Radius of the pinion gear                             | $r$   | 0.015 m                     |

In order to compare the double speed RSA and direct-drive RSA based on the analytical frequency response analysis models (Equations (4.8) and (4.10)) and their prototypes in Figure 4.9, the road profile displacement of the quarter vehicle suspension system is utilized

as the excitation input of the double speed RSA and direct-drive RSA to predict the voltage output. As shown in Figure 4.13, under the displacement excitation amplitude of 0.002m, higher voltage can be generated at the natural resonant frequencies. The maximum voltage output of the double speed RSA reaches 2 V at the second natural resonant frequency, which is a double of the maximum voltage output 1V of the direct-drive RSA. The material used in the prototype largely deforms which may potentially decrease the energy output, resulting in the slight drop in the voltage output when the double speed RSA is excited in the frequency range larger than 20 Hz. In general, the experimental results coincide with the simulation results, thus the simulation models of the direct-drive and double speed RSA have been validated throughout the whole operating frequency range.

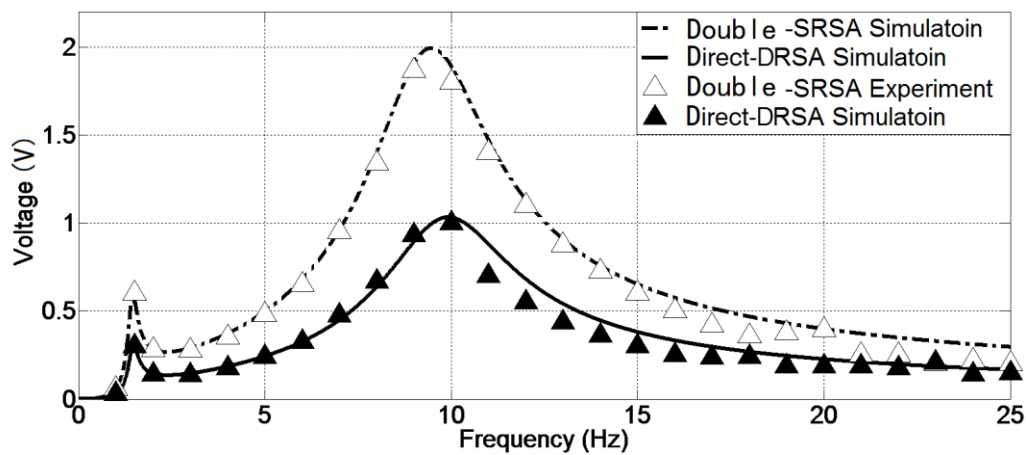


**Figure 4.13: Comparison of the simulated and measured voltage outputs of the direct-drive and double speed RSA under displacement excitation of 2 mm over the frequency range from 0 to 25Hz.**

#### 4.2.5 Integration of the double speed regenerative shock absorber and the direct-drive regenerative shock absorber

The physical difference between the double speed RSA and direct-drive RSA is mainly the rack and pinion mechanism which contributes to the speed amplification. Electrically, the electromechanical coupling constant  $Bl$  is the same for both the designs of the direct-drive and double speed RSA due to the same coil and magnet configuration in the prototype. The rack and pinion mechanism of the double speed RSA doubles the magnet speed with respect to the coils, therefore increases the output voltage and harvested power. When integrated into a quarter vehicle system, the sinusoidal wave road profile excitation displacement amplitude is assumed to be 0.035m. The output voltage and power results of the direct-drive and double speed RSA are shown in Figures 4.14 and 4.15.

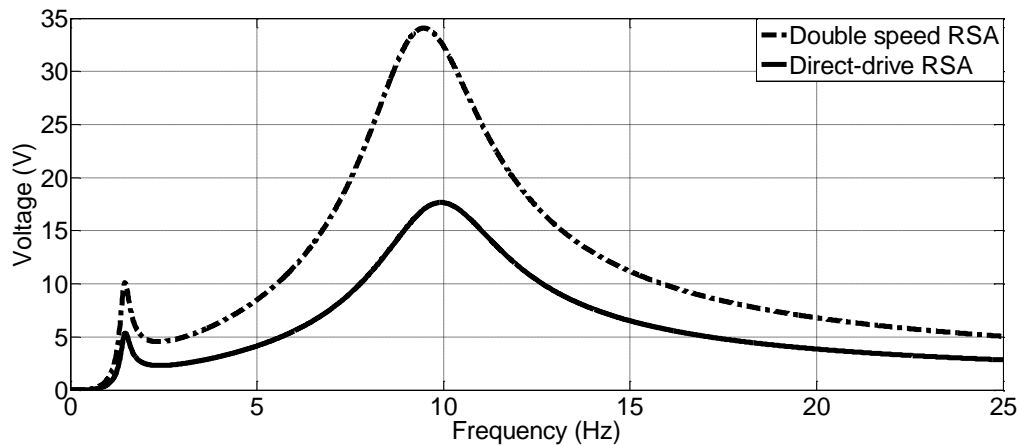


**Figure 4.14: Comparison of the simulated voltage outputs of the double speed RSA with direct-drive RSA under the sinusoidal wave road profile excitation with a displacement amplitude of 0.035m.**

Figure 4.14 is different from Figure 4.13, because Figure 4.13 is the comparison of the simulated and measured output voltage spectra of the double speed RSA under the displacement excitation of 2 mm. Figure 4.14 is the comparison of the simulated output voltage spectra of the direct-drive and double speed RSA under the displacement excitation of 35 mm.

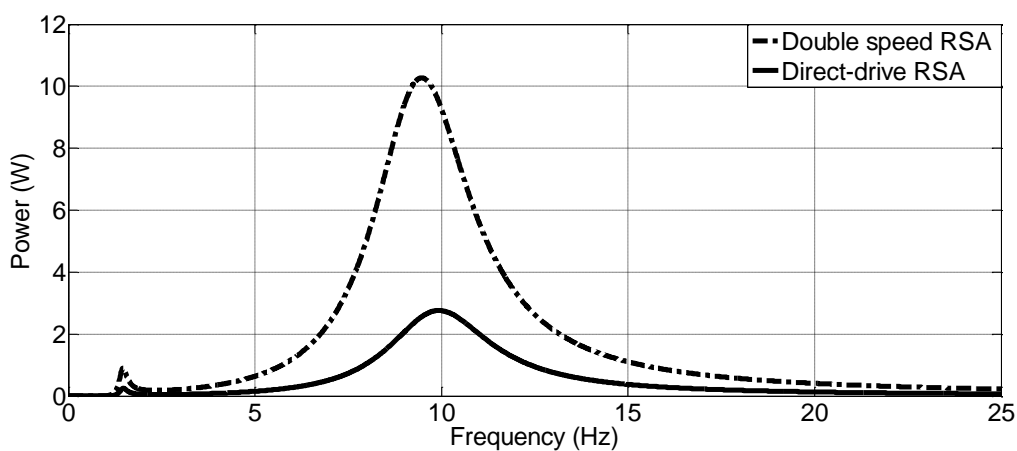


**Figure 4.15: Comparison of the power outputs of the double speed RSA with those of the direct-drive RSA under the sinusoidal wave road profile excitation displacement amplitude of 0.035m.**

Figures 4.14 and 4.15 show that in the two degrees of freedom (2DOF) regenerative vehicle quarter suspension system, the output voltage has peaks at two modal resonant frequencies and more energy can be harvested in the second hopping mode. At the same frequency, the double speed RSA with the rack and pinion mechanism is able to generate twice as much voltage or 4 times as much power as the direct-drive RSA without the rack and pinion mechanism if the same electrical circuit is connected. Therefore, the vibration control should

be focused at the first modal resonant frequency, while the vibration energy harvesting should be focused on the second modal resonant frequency.

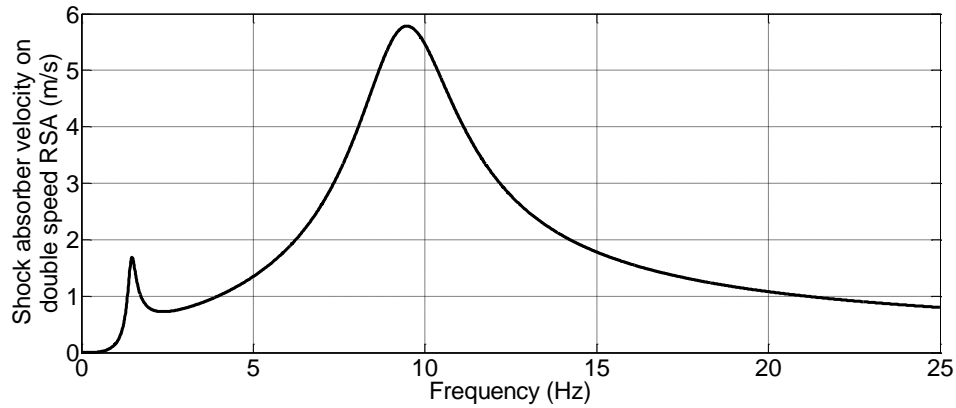


**Figure 4.16: Shock absorber (suspension) velocity on the double speed RSA.**

When the sinusoidal wave road profile excitation displacement amplitude is set at 0.035m, Figure 4.16 shows the shock absorber velocity response to the road profile excitation. The total power dissipated on the shock absorber can be expressed by:

$$P_{damping} = \frac{1}{2} \cdot c \cdot v^2 \quad (4.12)$$

where  $c$  is shock absorber damping coefficient and  $v$  is the shock absorber (suspension) velocity, it can be seen that more power can be dissipated at the second resonant frequency than at the first resonant frequency. Without the regenerative shock absorber, this dissipated power will be lost in the form of heat loss. The energy recovering efficiency can be obtained as the ratio of the harvested power to the dissipated power, shown in Figure 4.17 below. With the current design of magnets and coil, throughout the whole operating frequency range, the

direct-drive RSA has a constant efficiency of 0.034%. The efficiency of the direct-drive RSA of 0.034% is 4 times smaller than the efficiency of the double speed RSA of 0.137% which, however, needs to stay in the high frequency range to maintain the efficiency level. After 2Hz, the advantage of adopting the rack and pinion mechanism starts to outweigh the disadvantage caused by its friction loss. It can be seen that the double speed RSA has higher efficiency than the direct-drive RSA in most of the frequency range.

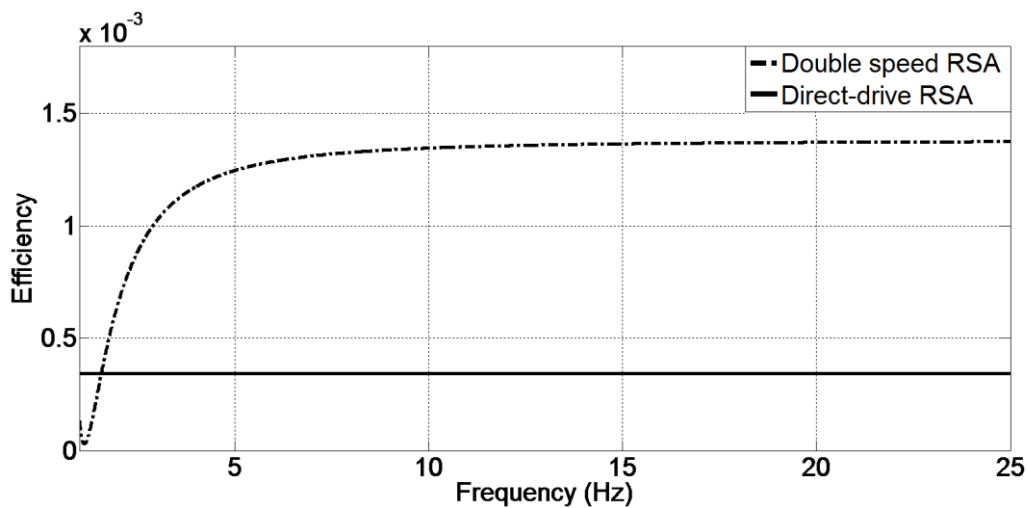


**Figure 4.17: Comparison of the energy harvesting efficiency of the double speed RSA and direct-drive RSA.**

Given that the peak road displacement amplitude is 0.035m, the actual road model can be described as a random signal within a certain amplitude range. Therefore when subjected to the random road profile excitation shown in Figure 4.18, the RMS power output time traces of the direct-drive and double speed RSA can be obtained and the results are shown in Figure 4.19. It shows that under the random road displacement excitation, the RMS value of power output of the double speed RSA still remains 4 times as large as that of the direct-drive RSA.



The results predicted with the random road displacement excitation coincide with the results predicted with a harmonic displacement excitation at modal resonant frequencies in Figure 4.15. Therefore the mathematic model of the double speed RSA is applicable to both the harmonic and random road profile displacement excitations of different frequencies or amplitudes.

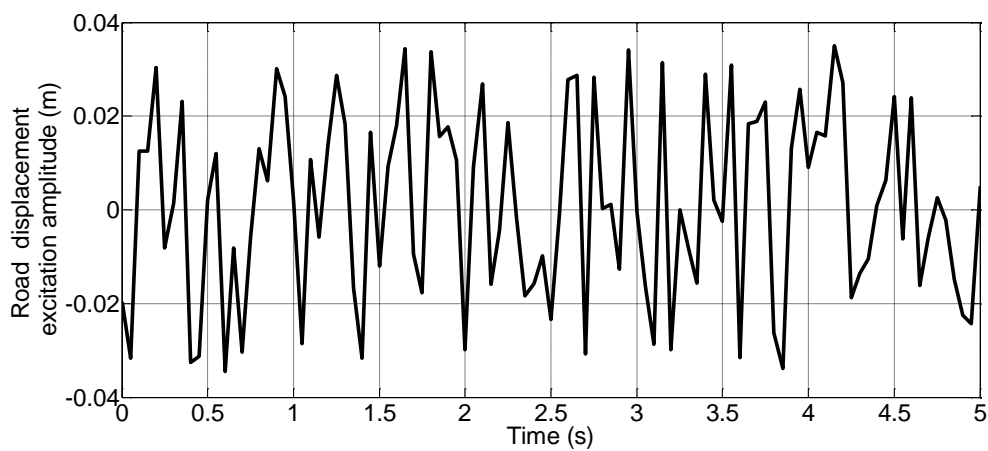
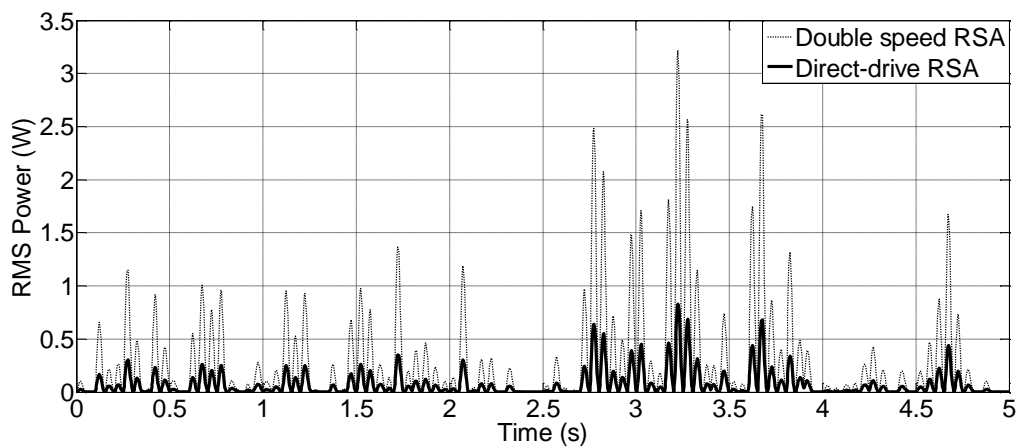


Figure 4.18: Random road excitation time history with a peak displacement amplitude of 0.035 m.



**Figure 4.19: RMS Power output time trace of the double speed RSA and the direct-drive RSA in the quarter vehicle suspension system under the random excitation shown in Figure 4.18.**

Monte Carlo simulation is conducted to further evaluate the performance of the RSA under random road excitation input, as shown in Figures 4.20 and 4.21 where 3000 samples of random road excitations are applied to both direct-drive and double speed RSAs. The mean curves of the voltage output coincide with the predicted results in Figure 4.14.

The road profile displacement excitation amplitude is randomized in the normal distribution with a mean value of 0.035m and the standard deviation of 20% of the mean value, the excitation frequency is randomized in a uniform distribution in the frequency range of 0-25 Hz. This randomization reflects the irregular and random road profile excitation well. Because the road profile excitation displacement amplitude input consists of numerous random samples, the Monte Carlo method allows the simulation to mimic the real road profile conditions in the frequency domain. Comparing the voltage outputs of the direct-drive and double speed RSAs in Figures 4.20 and 4.21. It can be seen that for both the designs, the voltage output can be more sensitive to the road profile irregularity at the second modal resonant frequency.

At the second modal resonant frequency, the voltage output varies from 18V to 52V for the double speed RSA in Figure 4.20 and 9V to 28V for the direct-drive RSA in Figure 4.21. The simulation results show that double speed RSA is more sensitive to the road profile irregularities than the direct-drive RSA and hence is able to reach higher maximum voltage

output. The advantages of the double speed RSA can only become obvious at 9.93Hz, therefore it is recommended for double speed RSA to operate in the frequency range near second modal resonate frequency to release its full potential.

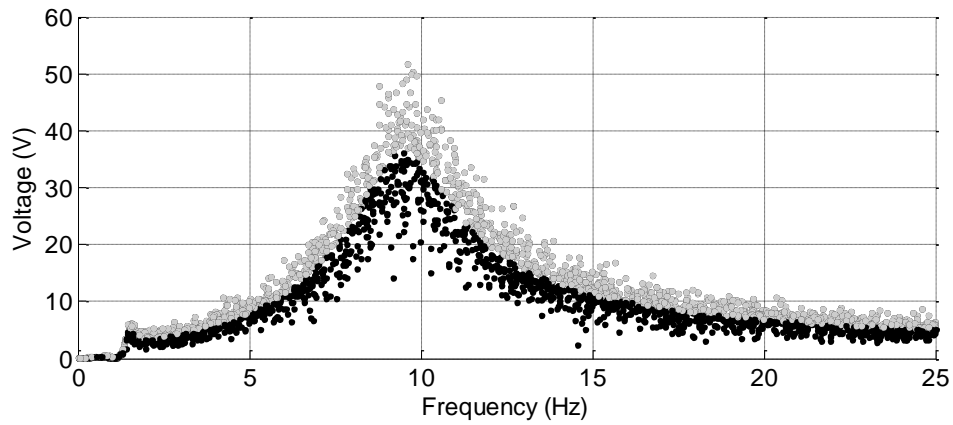


**Figure 4.20: Voltage output of the double speed RSA with random road excitation amplitude varying with standard deviation of 20% of the mean value.**

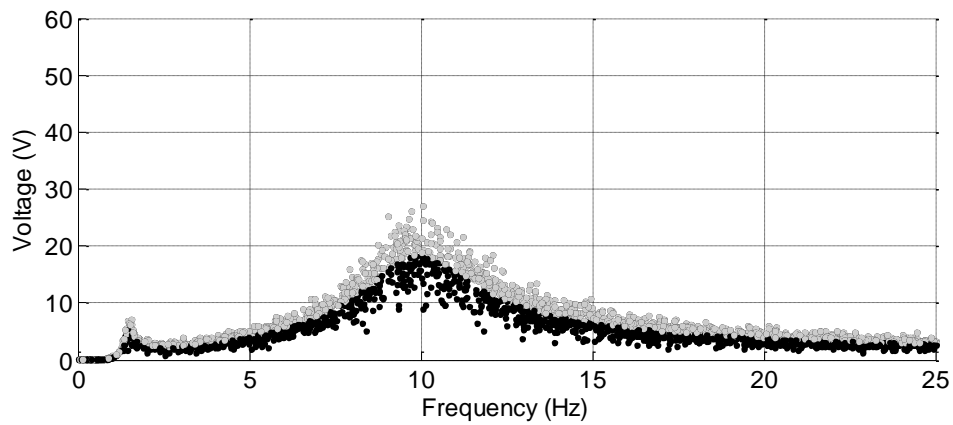


**Figure 4.21: Voltage output of the direct-drive RSA with random road excitation amplitude varying with standard deviation of 20% of the mean value.**

#### *4.2.6 Optimization of the double speed regenerative shock absorber*

The optimization of the double speed RSA focuses on the second modal resonance frequency at which the peak power output can be achieved. The road profile excitation displacement amplitude of the sinusoidal wave is set at 0.035m to be consistent with the non-optimized model.

##### *Amplification factor*

The magnet velocity with respect to the coils can be amplified by the proposed mechanism, gear box, ball screws, fixed pulleys and their variants. The amplification number is denoted as  $n$ . Due to the pinion gears in the proposed design having an even radius, the amplification factor of the double speed RSA is 1, shown in Figure 4.22. The magnet velocity with respect to the coils is doubled because the coil and magnet move in the opposite directions. Larger value of  $n$  can be realized with a lever or a gear box.

If the displacement of the coil is  $n$  times as large as that of the magnet through gear box or lever amplification, the absolute coil velocity can be obtained as:

$$v_c = n\dot{x}_2 - n\dot{x}_1 \quad (4.13)$$

Substituting Equation (4.13) into the expressions of the kinematic, potential and damping energies of both the masses similar to Equation (4.5), substituting the expressions into Equation (4.1) and inclusion of electric circuit equation gives the governing equations of the quarter vehicle suspension system with the regenerative shock absorber having the amplification factor  $n$ :

$$\left\{ \begin{array}{l} (m_1 + m_m) \cdot \ddot{x}_1 - nm_c (n\ddot{x}_2 - n\ddot{x}_1) + 2Jw \frac{1}{r} \left( \frac{\ddot{x}_1 - \ddot{x}_2}{r} \right) + (c_2 + c_s) \cdot (\dot{x}_1 - \dot{x}_2) + c_1 \cdot (\dot{x}_1 - \dot{y}) + k_2 \cdot (x_1 - x_2) + k_1 \cdot (x_1 - y) - n \cdot \frac{Bl \cdot U}{R} = 0 \\ nm_c (n\ddot{x}_2 - n\ddot{x}_1) + (m_2 + m_p) \ddot{x}_2 - 2Jw \frac{1}{r} \left( \frac{\ddot{x}_1 - \ddot{x}_2}{r} \right) - (c_2 + c_s) \cdot (\dot{x}_1 - \dot{x}_2) - k_2 \cdot (x_1 - x_2) + n \cdot \frac{Bl \cdot U}{R} = 0 \\ L_e \cdot \frac{\dot{U}}{R} + \frac{U}{R} (R + R_e) = Bl [n\dot{x}_2 - (n+1)\dot{x}_1] \end{array} \right. \quad (4.14)$$

Assuming the differences in masses or structures of the pinion gears and its variants are neglected, the effects of increasing the amplification factor are shown in Figure 4.23 where the shock absorber is excited at the second modal resonant frequencies with a sinusoidal wave road profile excitation displacement amplitude of 0.035m. The range for amplification factor is set to be no more than 3 as any value larger than that would be unpractical.

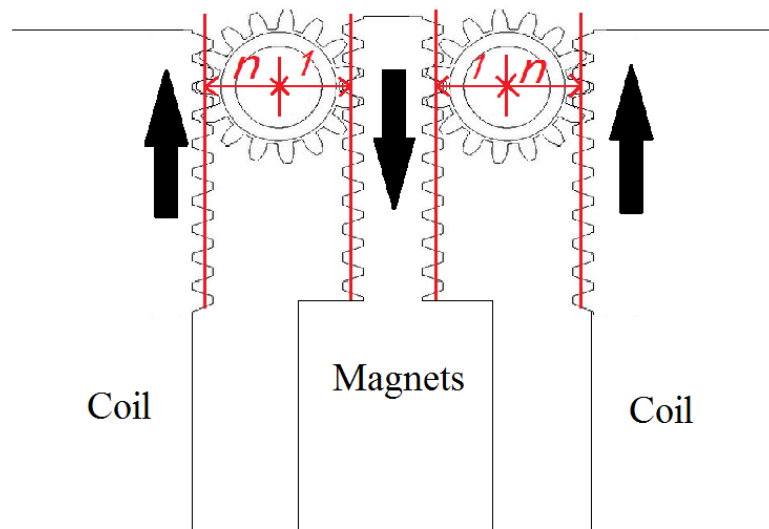


**Figure 4.22: Amplification factor  $n$  on the double speed RSA.**

It is shown in Figure 4.23 that energy harvesting ability of the regenerative shock absorber can be affected by the amplification factor, as the increased relative speed of the coils with respect to the magnets can induce higher voltage and thus higher power output. The peak power reaches 11.7 W at the amplification factor of 1.45, further increasing the amplification factor  $n$  will eventually results in the drop in the power output. The large amplification factor can increase the coil velocity with respect to the magnets, on the other hand, the increased mass inertia of the coil may result in the decreased shock absorber displacement, as shown in Figure 4.24. Therefore for reciprocating coil with speed amplifying mechanism, an optimal amplification factor can be identified to minimize its effect on the vehicle dynamics.

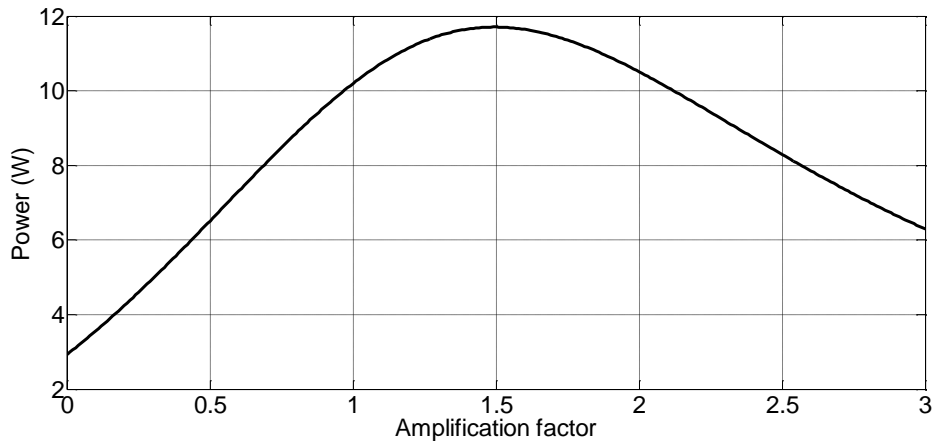


**Figure 4.23: Harvested power versus the increased amplification factor  $n$  at the second modal resonant frequency of 9.94Hz.**

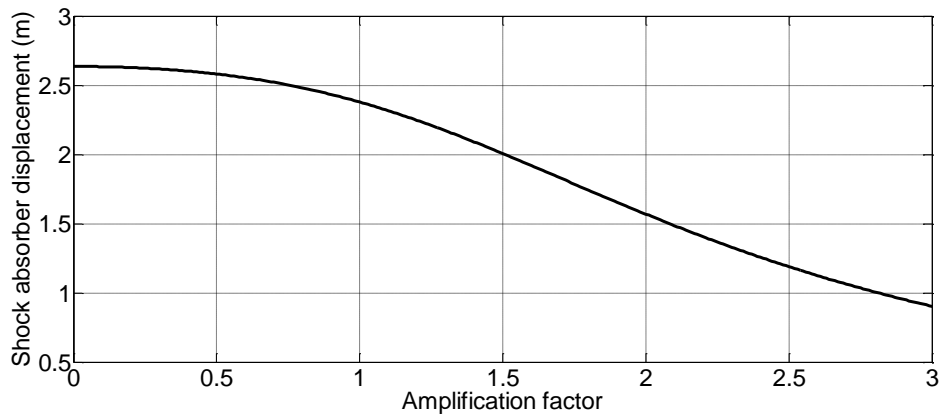


**Figure 4.24: Shock absorber displacement versus the increased amplification factor  $n$  at the second modal resonant frequency of 9.94Hz.**

### *Coil mass*

The increase of the reciprocating coil mass essentially would be caused by the increase of the coil volume and coil length, which is proportional to the voltage output according to the Faraday's law. Due to the fact that the direct-drive RSA does not have any coil mass

reciprocating with respect to the sprung mass, the increased coil mass is directly added onto the sprung mass of the quarter vehicle suspension system for comparison of the direct-drive and double speed RSA in order to keep sprung mass the same.

Increase in the coil amount can affect the electromechanical coupling, coil resistance and coil inductance etc. By taking all the effects into consideration, Figure 4.25 shows a near linear relationship between the power output and the coil mass. Higher power output can be achieved by increasing the coil mass. Any coil mass more than 5 kg is not feasible and excluded for consideration.

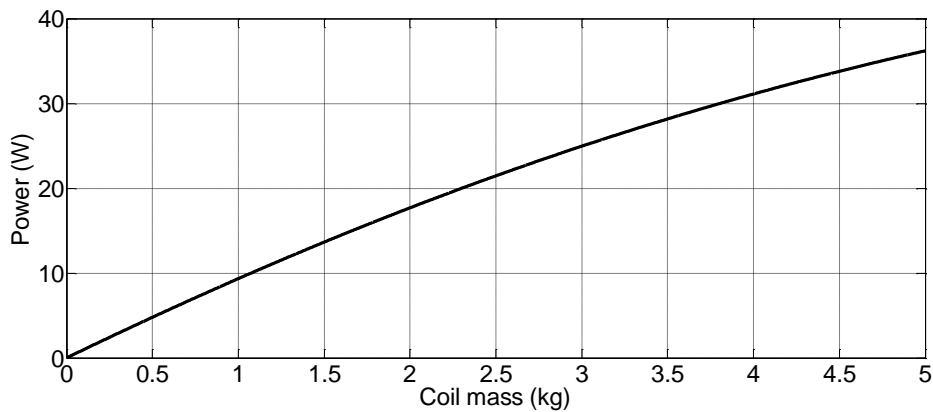


**Figure 4.25: Harvested power at the second resonant frequency of 9.94 Hz versus the reciprocating coil mass and amplification factor.**

Figure 4.26 shows the harvested power versus the coil mass and amplification factor  $n$  in the practical range. The maximum power of 54W can be harvested with a coil mass of 5kg and amplification factor of 3. The combinations of the coil mass and amplification factor for the



maximum power output is represented by solid line along with its projection on the horizontal plane. It shows that in general, when both the coil mass and amplification factor are large, the power output tends to increase with the coil mass and amplification factor. When the coil is less than 2.5 kg, however, the power output is more sensitive to the amplification factor. When the coil mass is larger than 2.5 kg, the power output is more sensitive to the coil mass. This is validated by the fact that when the coil mass is 1.256 kg, the double speed RSA has higher power output than the direct-drive RSA because of the larger amplification factor  $n$ .

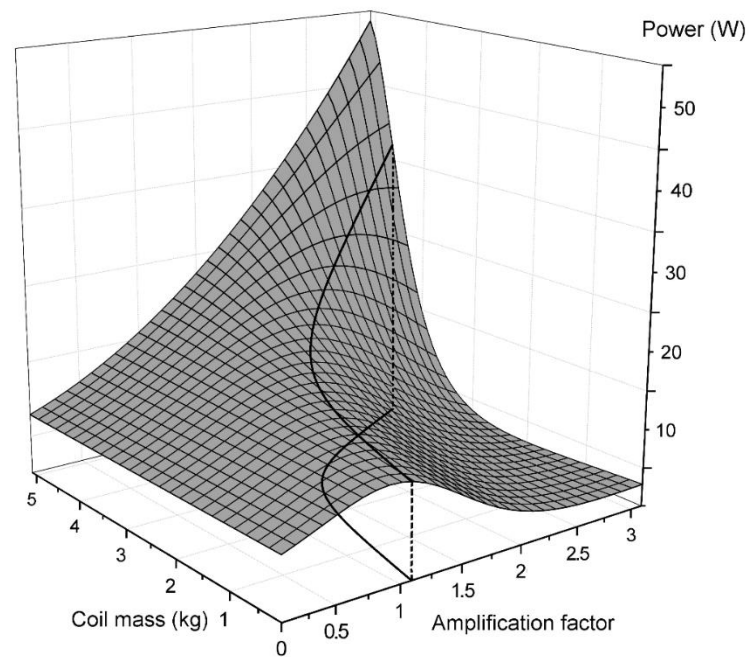


**Figure 4.26: Harvested power at the second resonant frequency of 9.94 Hz versus the coil mass and amplification factor  $n$ .**

## 4.3 Indirect drive regenerative shock absorber design and its comparison with the direct-drive regenerative shock absorber

### 4.3.1 Concept design

Both the direct-drive and indirect-drive regenerative shock absorbers are designed to be fitted on the vehicle suspension system for harvesting the vibration energy that otherwise would have been wasted as heat energy dissipated into the ambient environment. Both regenerative shock absorbers have electromagnetic generators which, according to the Faraday's law of induction, generate electrical energy from the relative motion between the magnets and coils. In the direct-drive regenerative shock absorber shown in Figure 4.27(a), the magnets and the coils are directly attached to the vehicle body and wheel assembly, respectively. Therefore, the relative speed between the vehicle body and the wheel assembly can be regarded as the magnets' speed with respect to the coil's speed. The direct-drive regenerative shock absorber has a simple structure and thus is more reliable. However, this design only allows a linear generator to be excited at a speed no larger than the relative speed between the vehicle body and wheel assembly. In order to increase the magnets' speed with respect to the coil's speed, the indirect-drive regenerative shock absorber as shown in Figure 4.27(b) is designed with an arm-teeth system that converts the reciprocating motions of the shock absorber into the unidirectional motion of the rotary generator. Figure 4.27(c) demonstrates its working

principle. During the compression phase, the driving arms on the top plate are engaged with teeth on the flywheel, as a result, the relative movement of the top plate and flywheel drives the flywheel to rotate. A gear box connected at the other end of the flywheel will amplify the angular velocity and eventually propel the rotary generator. During the recoil phase, the driving arms moves upward with the top plate, allowing the driving arms to be disengaged from the flywheel. The flywheel will continuously rotate due to its inertia and will be engaged with driving arms again in the next shock absorber motion cycle. Therefore the flywheel always rotates in one direction, so does the generator connected to it.

The different configurations of the generator used in the two designs can also have an impact on the vibration energy harvesting performance. The linear generator in the direct-drive regenerative shock absorber has the magnets stacked in an opposite direction along an aluminum shaft, the enamel copper wire is wined on the coil holder outside the magnets as shown in Figure 4.27(a) where there is reciprocating relative motion of the magnets with respect to the coils. The magnetic field intensity change around the coils generates the alternating current (also called “AC”) output. In the indirect-drive regenerative shock absorber, the integrated arm-teeth mechanism functions as a one-way clutch which rectifies the bidirectional linear motion into the unidirectional rotary motion in order to match up with the DC generator. Hence, the indirect-drive regenerative shock absorber generates DC output. These two regenerative shock absorbers are designed with similar shape and dimensions in order to be fitted within the same vehicle suspension system.

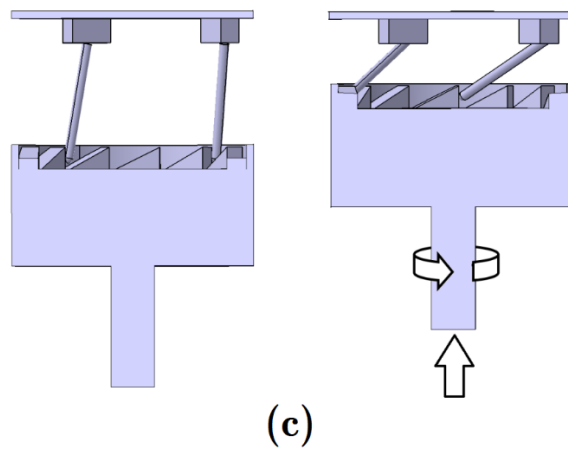
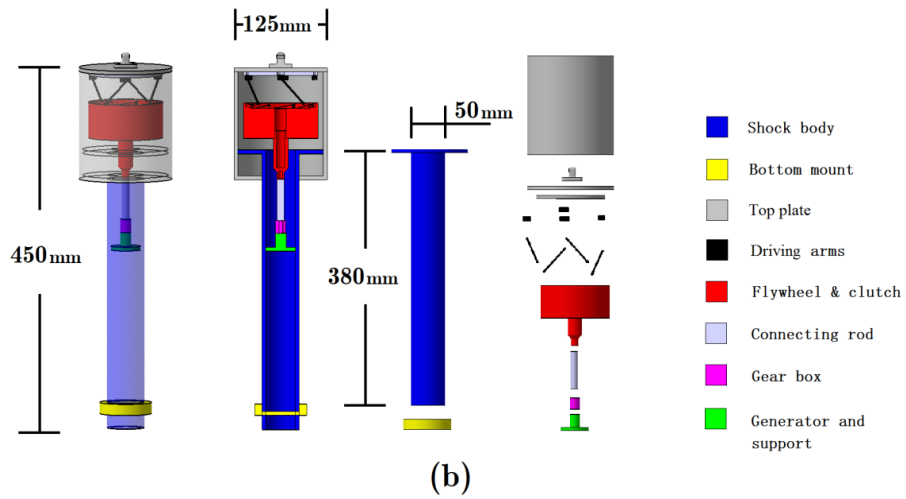
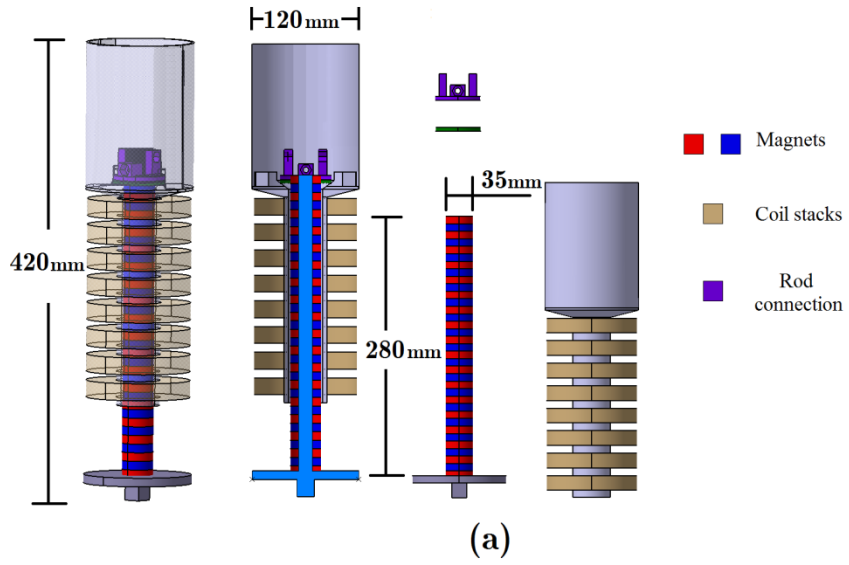


**Figure 4.27: The composition and dimensions of (a) direct-drive regenerative shock absorber, (b) indirect-drive regenerative shock absorber and (c) the working principle of the arm-teeth mechanism.**

#### 4.3.2 Modeling of the indirect-drive system

The schematic of the 2DOF mass-spring-dashpot quarter vehicle suspension system integrated with the indirect-drive regenerative shock absorber is shown in Figure 4.28. Both the direct-drive and the indirect-drive regenerative shock absorbers are integrated in the same quarter suspension system of a passenger vehicle for comparison.

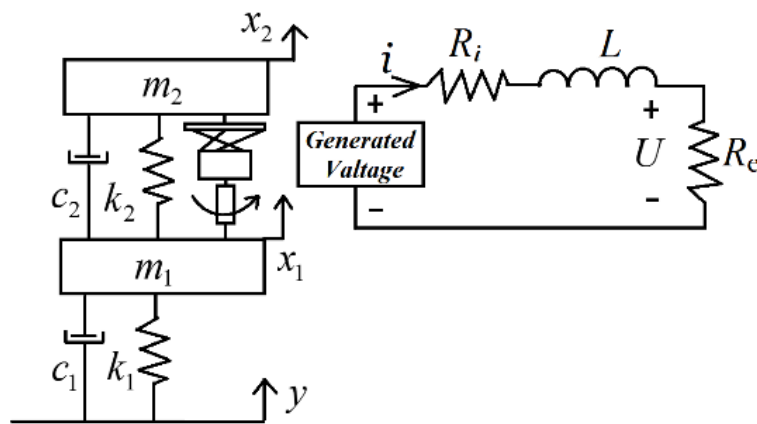


**Figure 4.28: Schematic of a two degrees of freedom quarter vehicle suspension system integrated with the indirect-drive regenerative shock absorber.**

The force equilibrium equations are given by:

$$\begin{cases} F_{LR} = Bl \cdot \frac{U}{R} \\ F_{Gi} + F_{Wi} + F_{Ki} \pm n \cdot F_{LR} = 0 \end{cases} \quad (4.15)$$

where  $F_{LR}$  is the Lorenz force as a result of moving coil in the magnetic field;  $F_{Gi}$  is the inertia force of the  $i^{\text{th}}$  oscillator ( $i=1,2$ );  $F_{Wi}$  is the damping force of the  $i^{\text{th}}$  oscillator;  $F_{Ki}$  is the spring restoring force of the  $i^{\text{th}}$  oscillator. Because of the gearbox, the Lorenz force  $F_{LR}$  is amplified when applied between the sprung mass and un-sprung mass and this multiplication factor is denoted as  $n$ .

Based on Lagrange's equation, individual forces can be expressed as:

$$\begin{cases} F_{Gi} = \frac{d}{dt} \frac{\partial T}{\partial \dot{x}_i} - \frac{\partial T}{\partial x_i} \\ F_{Wi} = \frac{\partial W}{\partial \dot{x}_i} \\ F_{Ki} = \frac{\partial V}{\partial x_i} \end{cases} \quad (4.16)$$

where  $\dot{x}_i$  and  $x_i$  are the velocity and displacement of the  $i^{\text{th}}$  oscillator;  $T$ ,  $W$  and  $V$  are the total kinetic energy, damping energy and spring potential energy, respectively, which are given by:

$$\begin{cases} T = \frac{1}{2} \cdot m_s \cdot (\dot{x}_1 - \dot{x}_2)^2 + \frac{1}{2} \cdot m_1 \cdot \dot{x}_1^2 + \frac{1}{2} \cdot m_2 \cdot \dot{x}_2^2 \\ W = \frac{1}{2} \cdot c_1 \cdot (\dot{x}_1 - \dot{y})^2 + \frac{1}{2} \cdot c_2 \cdot (\dot{x}_1 - \dot{x}_2)^2 + \frac{1}{2} \cdot c_L \cdot (\dot{x}_1 - \dot{x}_2)^2 \\ V = \frac{1}{2} \cdot k_1 \cdot (x_1 - y)^2 + \frac{1}{2} \cdot k_2 \cdot (x_1 - x_2)^2 \end{cases} \quad (4.17)$$

where  $m_s$  is the equivalent reciprocating mass of the combination of the top plate, arm teeth mechanism, differential gear box and DC generator and  $c_L$  is the equivalent reciprocating

damping of the combination of top plate, arm teeth mechanism, differential gear box and DC generator.

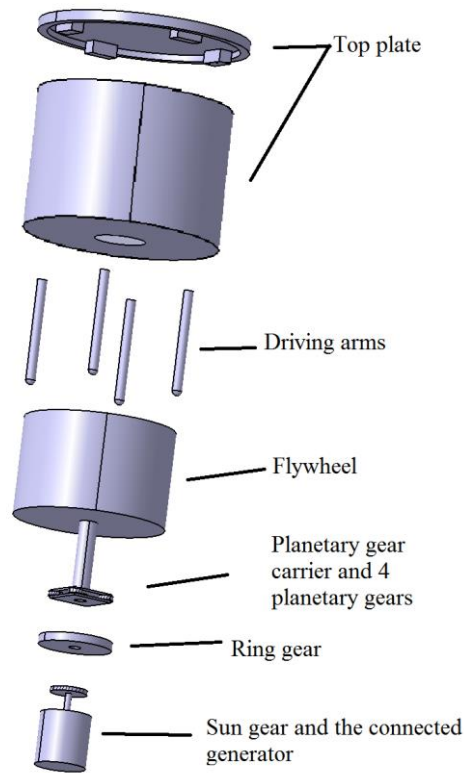


**Figure 4.29: The composition of the indirect-drive regenerative shock absorber and its equivalent reciprocating mass  $m_s$ .**

The equivalent reciprocating mass  $m_s$  includes the masses of the top plate, flywheel, driving arms, planetary gear carrier, 4 planetary gears and the combination of the sun gear and the generator after the gearbox, as shown in Figure 4.29. The flywheel, driving arms, planetary

gear carriers and 4 planetary gears are rotating at the same angular velocity; the generator and the sun gear rotate faster due to gearbox.

Therefore,  $m_s$  can be given by

$$m_s = m_{tp} + \frac{J_{FW} + J_{am} + J_{pcr} + 4 \cdot (J_p + m_p \cdot r_p^2)}{r_e^2} + \frac{J_g + J_s}{r_e^2} \cdot j^2 \quad (4.18)$$

where  $m_{tp}$  is the equivalent reciprocating mass of the top plate;  $J_{FW}$ ,  $J_{am}$ ,  $J_{pcr}$ ,  $J_p$ ,  $J_s$  and  $J_g$  are the rotational inertia of the flywheel, arm teeth, planetary gear carrier, planetary gear, sun gear and generator;  $r_p$  is the distance from the center of the sun gear to the center of a planetary gear, which is equal to a sum of the sun gear radius and planetary gear radius;  $r_e$  is the equivalent rotational inertia radius of the combination of the flywheel, arm teeth, planetary gear carrier, planetary gear, sun gear and generator;  $m_p$  is the mass of the planetary gear;  $j$  is the gear ratio of the differential gear box.

To obtain  $c_L$  in Equation (4.17), which is the damping coefficient of the differential gear box and DC generator, the conservation of energy is introduced:

$$P_{input} \cdot \eta_{tp} \cdot \eta_{pg} \cdot \eta_g = P_E \quad (4.19)$$

where  $P_{input}$  is the total damping power,  $P_E$  is the electrical power output,  $\eta_{tp}$ ,  $\eta_{pg}$  and  $\eta_g$  are the efficiencies of the top plate arm-teeth mechanism, differential gear box and DC generator, respectively.



Total damping power  $P_{input}$  and electrical power output  $P_E$  can be obtained as:

$$P_{input} = \frac{1}{2} \cdot c_L \cdot (\dot{x}_2 - \dot{x}_1)^2 \quad (4.20)$$

$$P_E = \frac{1}{2} \cdot c_R \cdot \omega_g^2 \quad (4.21)$$

where  $c_R$  is the rotary damping coefficient of the generator and  $\omega_g$  is the generator angular velocity. Substitute Equation (4.20) and Equation (4.21) into Equation (4.19),  $c_L$  can be obtained as:

$$c_L = \frac{c_R \cdot \omega_g^2}{(\dot{x}_2 - \dot{x}_1)^2 \cdot \eta_{tp} \cdot \eta_{pg} \cdot \eta_g} \quad (4.22)$$

Because the relationship between the generator angular velocity  $\omega_g$  and shock absorber velocity is given as:

$$\omega_g = j \cdot \frac{\dot{x}_2 - \dot{x}_1}{r_e} \quad (4.23)$$

Therefore by substituting Equation (4.23) into Equation (4.22),  $c_L$  is then given by.

$$c_L = \frac{c_R \cdot i^2}{r_e^2 \cdot \eta_{tp} \cdot \eta_{pg} \cdot \eta_g} \quad (4.24)$$

where  $c_R$  is the rotary damping coefficient of the generator related to the generator constant  $k_e$  and resistances (internal resistance  $R_e$  and external resistance  $R$ ) and is given by:

$$c_R = \frac{k_e^2}{R_e + R} \quad (4.25)$$

Therefore  $c_L$  can be obtained by substituting Equation (4.25) into Equation (4.24):

$$c_L = \frac{k_e^2 \cdot j^2}{r_e^2 \cdot \eta_{tp} \cdot \eta_{pg} \cdot \eta_g \cdot (R + R_e)} \quad (4.26)$$

The generated voltage is given by the product of the generator constant and angular velocity or the product of the electromechanical coupling constant and coil velocity with respect to the magnet, as shown in Equation (4.27) and Equation (4.28).

$$U_{generated} = Bl \cdot \omega_g \cdot r_g \quad (4.27)$$

$$U_{generated} = k_e \cdot \omega_g \quad (4.28)$$

where  $r_g$  is generator rotor radius.

By comparing Equation (4.27) with Equation (4.28),  $k_e$  can be obtained as:

$$k_e = Bl \cdot r_g \quad (4.29)$$

The magnetic force is amplified by a factor of  $n$  through the mechanism. Due to the conservation of energy:

$$F_{LR} \cdot v_{coil\_magnets} = n \cdot F_{LR} \cdot (\dot{x}_2 - \dot{x}_1) \quad (4.30)$$

where coil speed with respect to magnets  $v_{coil\_magnets}$  is given by:

$$v_{coil\_magnets} = \frac{(\dot{x}_2 - \dot{x}_1) \cdot j \cdot r_g}{r_e} \quad (4.31)$$

Therefore  $n$  can be obtained through comparing Equation (4.31) with Equation (4.30):

$$n = \frac{j \cdot r_g}{r_e} \quad (4.32)$$

The generated voltage can be obtained by substituting Equation (4.23) to Equation (4.28):

$$U_{generated} = k_e \cdot j \cdot \frac{\dot{x}_2 - \dot{x}_1}{r_e} \quad (4.33)$$

Equation (4.33) can be substituted into Equation (4.13) in place of  $Bl \cdot (\dot{x}_1 - \dot{x}_2)$ , as a result, the governing equation of the electrical domain is given by:

$$L_e \cdot \frac{\dot{U}}{R} + \frac{U}{R} \cdot (R + R_e) = \frac{k_e \cdot j}{r_e} \cdot (\dot{x}_1 - \dot{x}_2) \quad (4.34)$$

Therefore substitution of Equation (4.32) into Equation (4.15) and inclusion of Equation (4.34) give the dynamic equations of the two degrees of freedom mass-spring-dashpot vehicle quarter suspension system integrated with the indirect-drive regenerative shock absorber as

$$\left\{ \begin{array}{l} m_s \cdot (\ddot{x}_1 - \ddot{x}_2) + m_1 \cdot \ddot{x}_1 + c_1 \cdot (\dot{x}_1 - \dot{y}) + c_2 \cdot (\dot{x}_1 - \dot{x}_2) + c_L \cdot (\dot{x}_1 - \dot{x}_2) + k_1 \cdot (x_1 - y) \\ + k_2 \cdot (x_1 - x_2) + Bl \cdot \frac{U}{R} \cdot \frac{j \cdot r_g}{r_e} = 0 \\ m_s \cdot (\ddot{x}_2 - \ddot{x}_1) + m_2 \cdot \ddot{x}_2 + c_2 \cdot (\dot{x}_2 - \dot{x}_1) + c_L \cdot (\dot{x}_2 - \dot{x}_1) + k_2 \cdot (x_2 - x_1) - Bl \cdot \frac{U}{R} \cdot \frac{j \cdot r_g}{r_e} = 0 \\ L_e \cdot \frac{\dot{U}}{R} + \frac{U}{R} \cdot (R + R_e) = \frac{k_e \cdot j}{r_e} \cdot (\dot{x}_1 - \dot{x}_2) \end{array} \right. \quad (4.35)$$

where

$$\left\{ \begin{array}{l} m_s = m_{tp} + \frac{J_{FW} + J_{am} + J_{pcr} + 4 \cdot (J_p + m_p \cdot r_p^2)}{r_e^2} + \frac{J_g + J_s}{r_e^2} \cdot j^2 \\ c_L = \frac{k_e^2 \cdot j^2}{r_e^2 \cdot \eta_{tp} \cdot \eta_{pg} \cdot \eta_g \cdot (R + R_e)} \\ k_e = Bl \cdot r_g \end{array} \right. \quad (4.36)$$

### 4.3.3 Parameter identification and the experimental validation

The prototype of the indirect-drive regenerative shock absorber is shown in Figure 4.30. The recoil leaf springs under the driving arms enable the driving arms to quickly return to original position when the driving arms are disengaged from the flywheel. The driving arms can only move within a certain angle, allowing for the proper engagement and disengagement. Figure 4.31 shows the experimental setup of the indirect-drive regenerative shock absorber on the MTS hydraulic machine.

Except for the parameters that can be identified by calculations and measurements, all the rotary generator constants can be obtained from the supplied specifications. The time domain simulation model of the indirect-drive system is developed based on Equation (4.35) and is shown in Appendix 1. For comparison, the time domain simulation model of the direct-drive system is presented in Appendix 2. Because of the difference in the configurations of the direct-drive and the indirect-drive regenerative shock absorbers, experiments are conducted for identification of the electromechanical coupling constant  $Bl$  of the indirect-drive regenerative shock absorber. When the indirect-drive regenerative shock absorber is excited

on the MTS hydraulic machine with 10mm displacement amplitude at 1 Hz, the simulation and experimental output voltage results are compared and shown in Figure 4.32. From Figure 4.32 it can be observed that when the lower head of MTS machine moves up, the arm-teeth mechanism starts to engage to propel the flywheel. The angular velocity of the flywheel is amplified through the gear box of the DC generator, causing the rapid increase in the voltage output. In the recoil phase, the arm-teeth mechanism becomes disengaged and voltage output gradually drops down to 0 when the flywheel stops rotating. When  $Bl$  is 1.8 Tm, the simulation output voltage curve matches up with the experimental output voltage curve, therefore  $Bl=1.8$  Tm has been identified for the indirect-drive regenerative shock absorber.

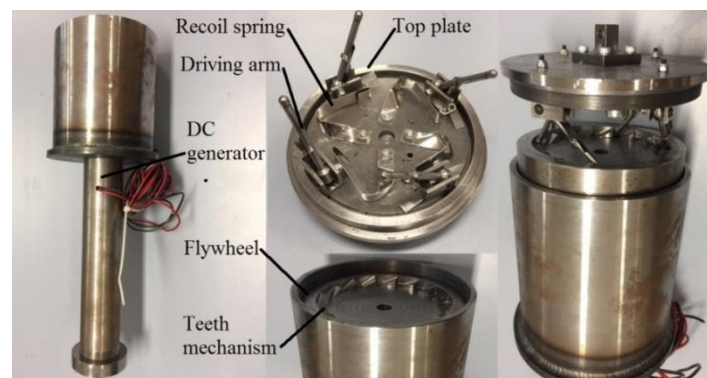


**Figure 4.30: The prototype of indirect-drive regenerative shock absorber**

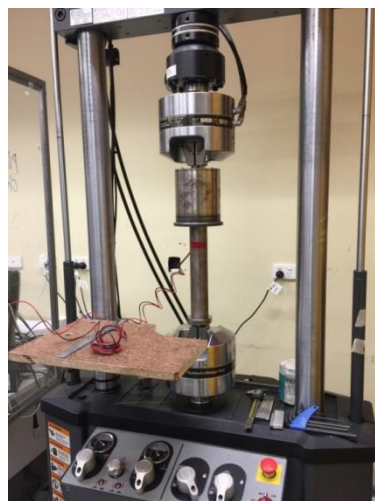


**Figure 4.31: The experiment set up of the indirect-drive regenerative shock absorber.**

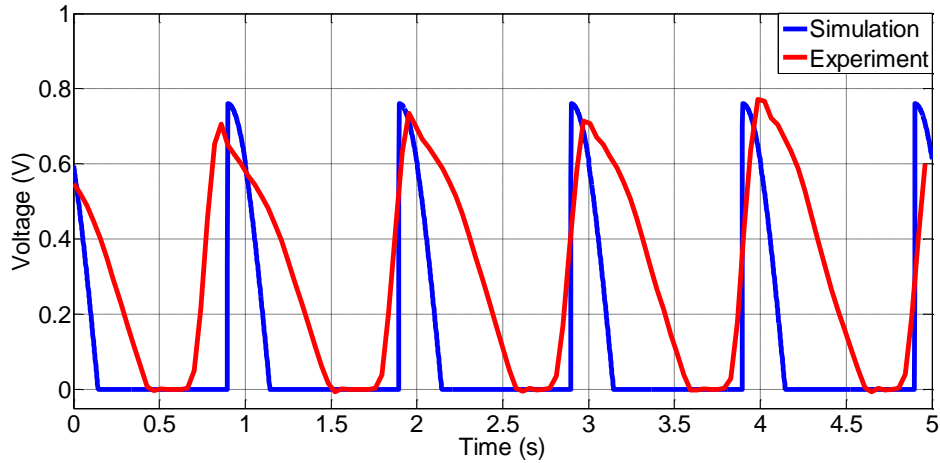


**Figure 4.32: The comparison between simulation and experimental output voltage results for the indirect-drive regenerative shock absorber with 10 mm excitation displacement amplitude at 1 Hz.**

The DC generator used in the indirect-drive regenerative shock absorber has a different configuration from the linear generator in the direct-drive regenerative shock absorber. In order to compare their performance based on the same platform, the same generator configuration should be applied to both the regenerative shock absorber systems. Electromechanical coupling constant, generator coil resistance and coil inductance are the key parameters in assessing the power generating ability of both the regenerative shock absorber systems. In the direct-drive regenerative shock absorber, the linear generator coil resistance  $R_e$  is  $113\Omega$  and the coil inductance  $L_e$  is  $0.000094$  H based on measurements. Therefore  $B_l=6.5$  Tm,  $R=113\Omega$  and  $L_e=0.000094$  H will be adopted by both the direct-drive and indirect-drive regenerative shock absorber systems. Based on Equation (4.36), the

generator constant  $k_e$  can be calculated. The parameters of the indirect-drive regenerative shock absorber have been identified and listed in Table 4.3.

**Table 4.3: Parameters of the indirect-drive regenerative shock absorber.**

|  | Parameter   | Value                                   |
|--|-------------|---|
| Top plate mass                                   | $m_{tp}$    | 3.722 kg                                |
| Planetary gear mass                              | $m_p$       | 0.049 kg                                |
| Electromechanical coupling                       | $Bl$        | 6.5 Tm                                  |
| Coil resistance                                  | $R_e$       | 113 $\Omega$                            |
| External resistance                              | $R$         | 113 $\Omega$                            |
| Coil inductance                                  | $L_e$       | $9.4 \times 10^{-5}$ H                  |
| Gear ratio                                       | $j$         | 22.6                                    |
| Rotational inertia of the flywheel               | $J_{FW}$    | $6.65 \times 10^{-2}$ kg.m <sup>2</sup> |
| Rotational inertia of the driving arm            | $J_{am}$    | $1.92 \times 10^{-4}$ kg.m <sup>2</sup> |
| Rotational inertia of the planetary gear carrier | $J_{pcr}$   | $5.64 \times 10^{-7}$ kg.m <sup>2</sup> |
| Rotational inertia of the planetary gear         | $J_p$       | $5.6 \times 10^{-7}$ kg.m <sup>2</sup>  |
| Rotational inertia of the generator              | $J_g$       | $5.75 \times 10^{-6}$ kg.m <sup>2</sup> |
| Rotational inertia of the sun gear               | $J_s$       | $2.45 \times 10^{-7}$ kg.m <sup>2</sup> |
| Planetary gear radius                            | $r_p$       | 0.00925 m                               |
| Equivalent radius                                | $r_e$       | 0.033 m                                 |
| Generator rotor radius                           | $r_g$       | 0.01m                                   |
| Equivalent suspension damping                    | $c_L$       | 100 Ns/m                                |
| Efficiency of top plate                          | $\eta_{tp}$ | 92%                                     |
| Efficiency of planetary gear                     | $\eta_{pg}$ | 80%                                     |
| Efficiency of generator                          | $\eta_g$    | 65%                                     |
| Generator constant                               | $k_e$       | 0.065 Vs/rad                            |

#### 4.3.4 Performance analysis

The performance analysis of the direct-drive and indirect-drive regenerative shock absorbers is conducted based on the same quarter vehicle suspension system and the same generator configuration. The peak values of the frequency response amplitude curves coincide with those of the time domain response curves in terms of both the relative displacement and output voltage. The results of the output voltage, output power, electromagnetic damping, vehicle body acceleration and total conversion efficiency are compared for the quarter vehicle suspension system with both the direct-drive and indirect-drive regenerative shock absorbers and shown in Figure 4.33.

In Figures 4.33(a) and (b), the plots of the voltage ratios and power ratios in the frequency domain show that for both the direct-drive and indirect-drive systems, the maximum voltage and maximum power ratios occur at the second modal resonant frequencies due to the more aggressive shock hopping mode movement. The second resonant frequency of the indirect-drive is shifted slightly to a smaller value because of the added equivalent mass in the indirect-drive mechanism. The voltage output ratio amplitude of the indirect-drive regenerative shock absorber is 7 times larger than that of the direct-drive regenerative shock absorber. With the same road excitation displacement amplitude, the range of harvestable time domain power is 0-2500 W/m<sup>2</sup> for direct-drive system and 0-1.3×10<sup>5</sup> W/m<sup>2</sup> for indirect-drive system. The harvested power ratio increase brought by the indirect-drive regenerative shock absorber is more obvious than the harvested voltage ratio as a result of the square term in the relationship between the power and the voltage:  $P=V^2/R$ .



Shown in Figure 4.33(c) are the ratios of the electromagnetic damping force over the excitation displacement amplitude in the frequency domain. For both the systems, the damping force ratio has the same trend as the voltage output ratio in Figure 4.33(a), because the voltage output and the electromagnetic damping are both dependent on the shock absorber velocity. Due to the presence of the gearbox, the indirect-drive regenerative shock absorber has the electromagnetic damping ratio of 220 N/m, which is 7 times larger than that of the direct-drive regenerative shock absorber in the frequency range of 0 to 30 Hz.

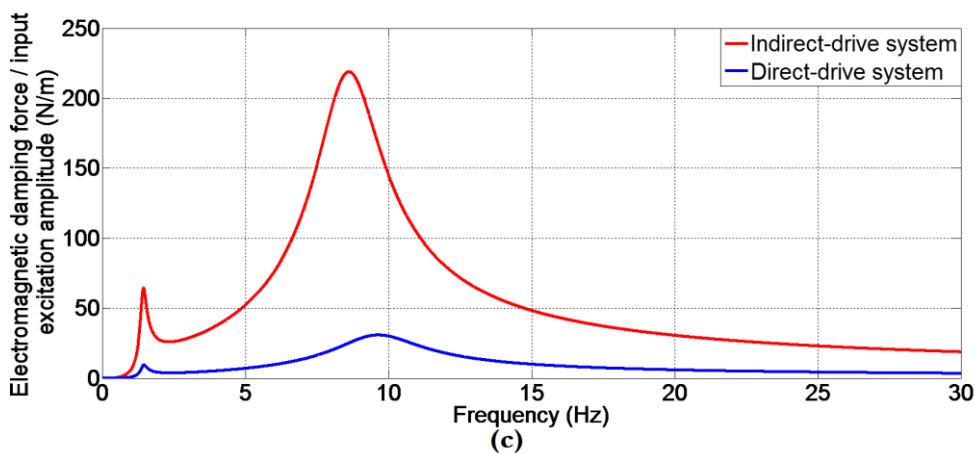
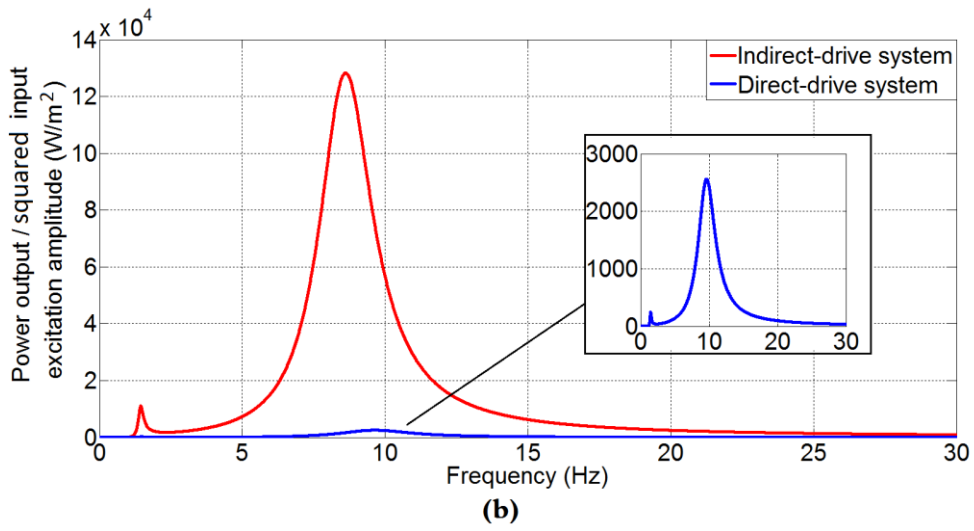
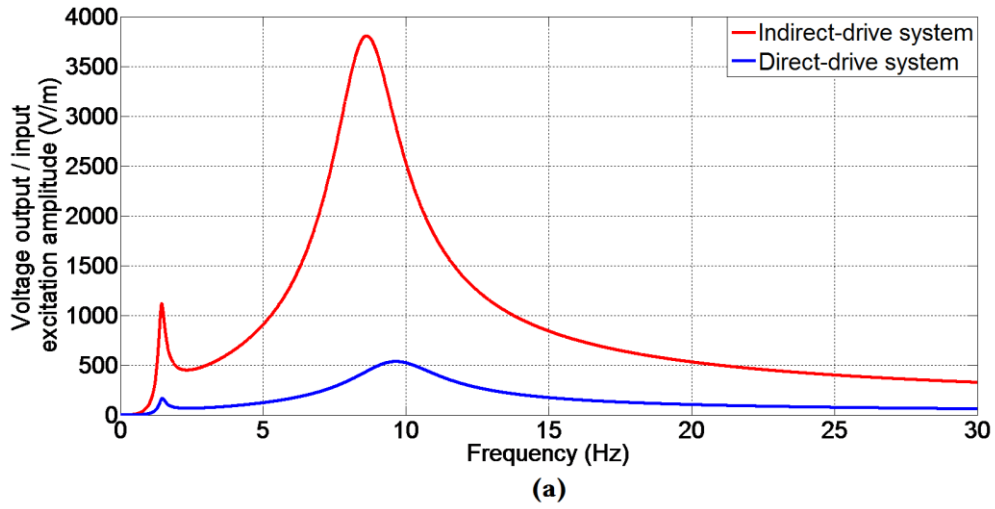
Figure 4.33(d) presents the frequency spectrum plots of the vehicle body acceleration amplitude divided by the road excitation displacement amplitude. The indirect-drive system provides better ride comfort than the direct-drive system when the excitation frequency is less than 13 Hz. This is because the extra damping brought by the indirect-drive regenerative shock absorber has positive effect on the ride comfort around the resonate frequencies. Since the comfort level of the vehicle largely depends on the vehicle body acceleration level, large vehicle body accelerations level should be avoided for a comfortable ride. For this purpose, the first resonant frequency where the least comfort situation occurs should be avoided. As mentioned previously, the power generated at the first modal resonant frequency is significantly lower than that at the second modal resonant frequency, as a result, the second resonant frequency should be focused for the purpose of both harvesting vibration energy and maintaining ride comfort. When the frequency is higher than the second resonant frequency and reaches the vibration isolation area, the effect of damping of the indirect-drive regenerative shock absorber on the vehicle suspension system vibration amplitude reduces,

resulting in the negative effects on the ride comfort. Therefore the indirect-drive system presents worse ride comfort after 13 Hz than the direct-drive system.

The total conversion efficiency is the ratio of the generated electrical power to the total heat power dissipated from the shock absorber, which can be calculated based on the Equation (4.7) and Equation (4.34). The results are shown in Equation (4.37) for direct-drive system and Equation (4.38) for indirect-drive system, where  $\omega$  is the excitation frequency. The total conversion efficiencies of both the direct-drive and indirect-drive systems are frequency dependent. However, the effect of frequency on the total energy conversion efficiency is trivial because the coil inductance coefficient  $L_e$  has an extremely small value of  $9.4 \times 10^{-5}$  H. The plot of total conversion efficiency in the frequency domain is shown in Figure 4.33(e). The efficiency of the indirect-drive systems is 0.87% which is 50 times more than 0.018% of the direct-drive system. The efficiency of both the systems can be improved by adopting powerful generators and matching the external resistance to the internal coil resistance.

$$\eta_{direct-drive} = \frac{Bl^2 \cdot R}{(L_e \cdot j\omega + R + R_e)^2 \cdot c_2} \quad (4.37)$$

$$\eta_{indirect-drive} = \frac{ke^2 \cdot i^2 \cdot R}{[L_e \cdot j\omega \cdot r_e + r_e \cdot (R + R_e)]^2 \cdot c_2} \quad (4.38)$$



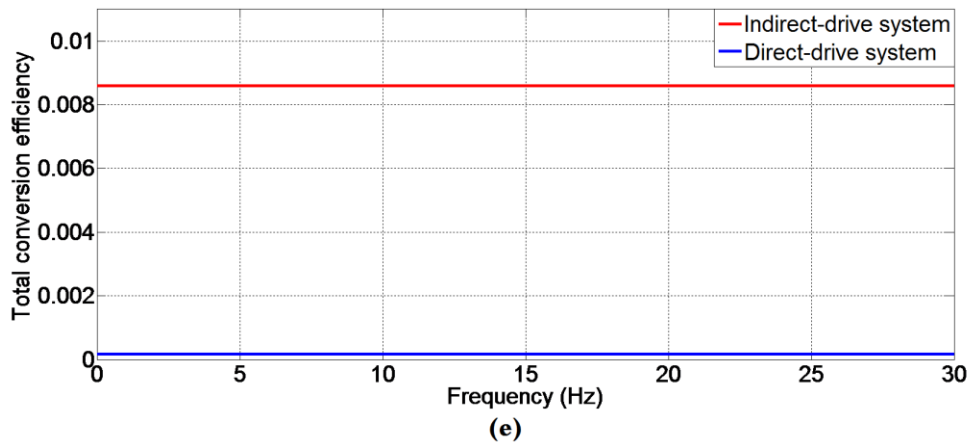
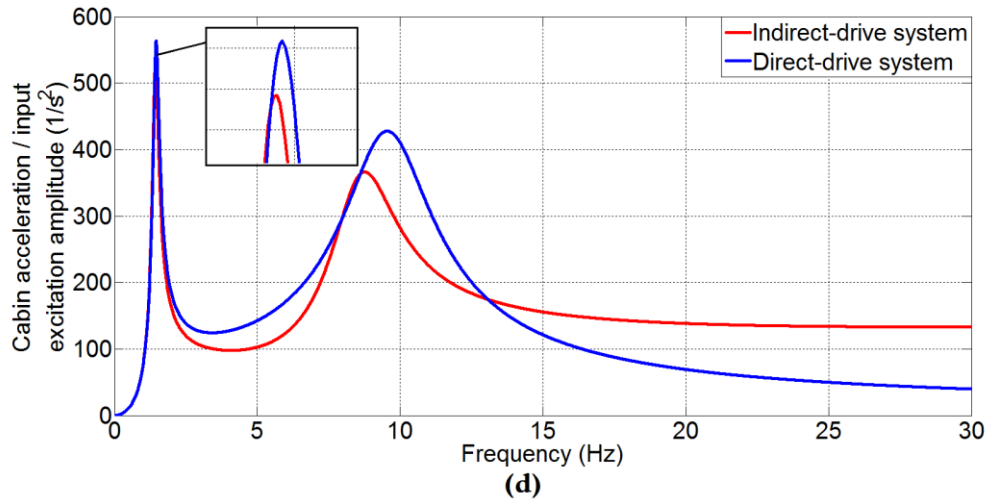


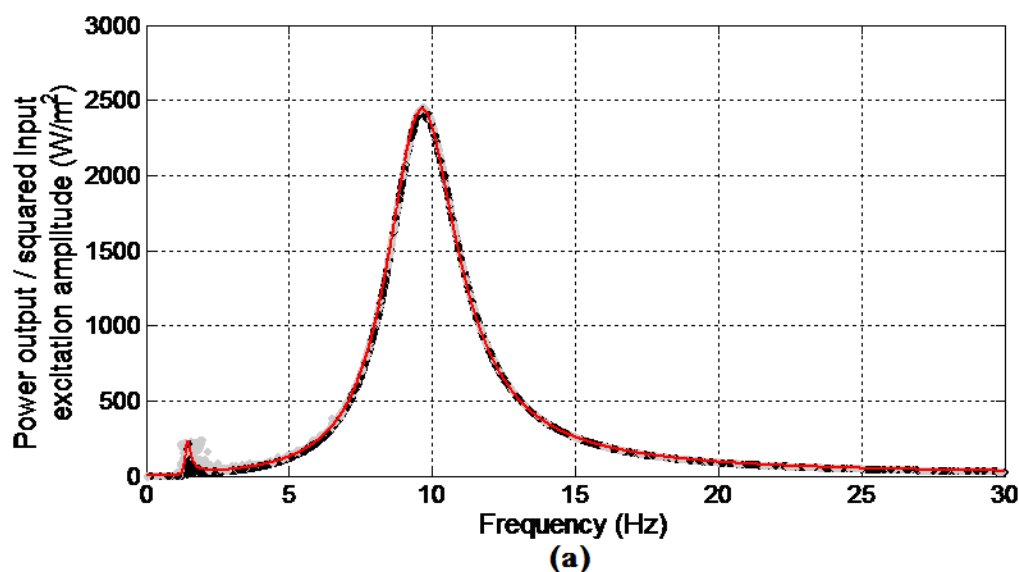
**Figure 4.33: The comparison of the quarter vehicle suspension system integrated with the direct-drive and the indirect-drive regenerative shock absorbers for (a) the ratio of the output voltage over excitation displacement amplitude, (b) the ratio of power over squared excitation displacement amplitude, (c) the ratio of the electromagnetic damping force over excitation displacement amplitude, (d) the ratio of the vehicle body acceleration over excitation displacement amplitude and (e) the total conversion efficiency of both the direct and indirect drive systems.**

#### 4.3.5 Parametrical Sensitivity Analysis using Monte Carlo simulation

Monte Carlo simulation investigates the uncertainties in a probabilistic way and can be utilized to compare the energy harvesting ability of the direct-drive and indirect-drive systems and their sensitivities to the parameter variation [150]. In the Monte Carlo simulation, the excitation frequency is uniformly distributed in the range of 0-30 Hz. It is assumed that the parameters such as quarter vehicle mass  $m_2$ , suspension stiffness  $k_2$ , tyre mass  $m_1$ , tyre stiffness  $k_1$ , suspension damping coefficient  $c_2$ , tyre damping coefficient  $c_1$ , electromechanical coupling constant  $Bl$ , internal coil resistance  $R_e$ , coil inductance  $L_e$  of both the direct-drive system and indirect-drive system and the gear ratio  $j$  of the indirect-drive system are normally distributed using their original values as the mean values and standard deviations of 20% of their mean values. The ratio of power output to the squared road excitation displacement amplitude is shown in Figures 4.34-4.44 where only one of the parameters is randomized each time in addition to the randomized excitation frequency. The parameter variations could be physically caused by the variations of materials, and manufacturing processes of the direct or indirect-drive system. The results can also reflect the sensitivity of the output power and energy harvesting bandwidth to the parameters of both the systems.

Based on the frequency response amplitude plot in Figure 4.33(b), 8000 sample points are taken for randomization of each parameter previously identified in Tables 4.2 and 4.3. The simulations show how sensitive the output power ratio values of the direct-drive system and indirect-drive system are with respect to their parameter variations. The red solid separating line between the black dots and grey dots in the Monte Carlo simulation plots represents the output power ratio when the parameter is taken as its original value or mean value. In Figures 4.34(a) and (b), it can be seen that for both the direct-drive and indirect-drive systems, the

variation of vehicle quarter mass  $m_2$  only affects the results in the first modal resonance frequency. For 20% variation of the vehicle quarter mass  $m_2$ , the range of the harvestable time domain power at the first modal resonance frequency is 0~200 W/m<sup>2</sup> for the direct drive system and 0~100000 W/m<sup>2</sup> for the indirect drive system. The range of the harvestable time domain power at the second modal resonance frequency is 0~0.02 W/m<sup>2</sup> for the direct drive system and 0~0.03 W/m<sup>2</sup> for the indirect drive system. Energy harvesting performance in the second modal resonance frequency is not changed much for both the systems. Similarly, for the variation of suspension stiffness  $k_2$  in Figures 4.35 (a) and (b), the change is very minor on the peak power output ratios and harvesting frequency bandwidths of both the systems. At the second resonant frequency, with 20%  $k_2$  variation, the ranges of the harvestable time domain power are 2150-2450 W/m<sup>2</sup> for the direct-drive system and  $1.2 \times 10^5$ - $1.3 \times 10^5$  W/m<sup>2</sup> for the indirect-drive system. Additionally, the change of quarter vehicle mass  $m_2$  and suspension stiffness  $k_2$  may largely affect the ride comfort of the vehicle, therefore it is not recommended to vary  $m_2$  or  $k_2$  due to their minor effects on the energy harvesting performance and the negative effects on the vehicle dynamics.



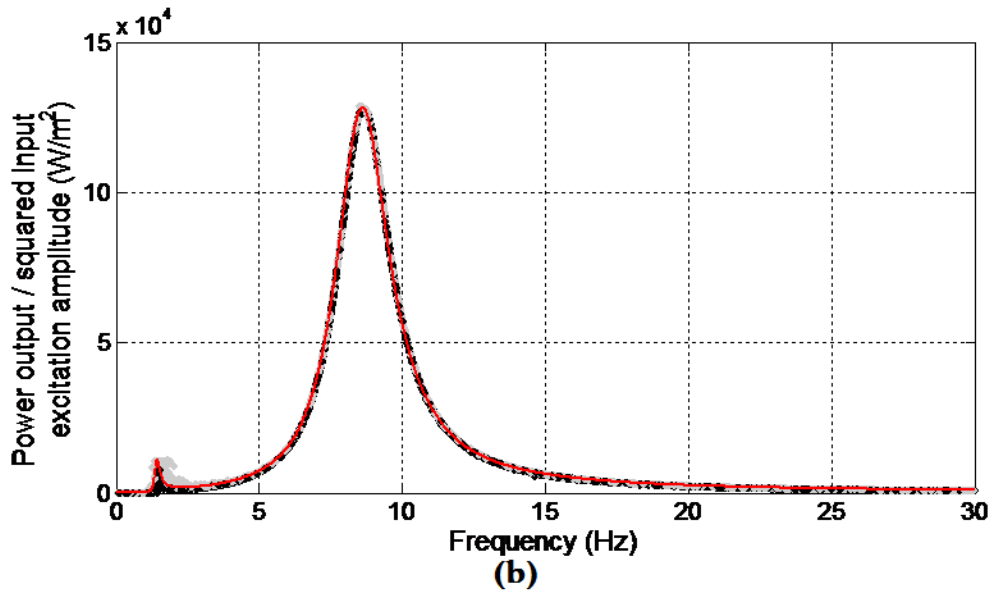
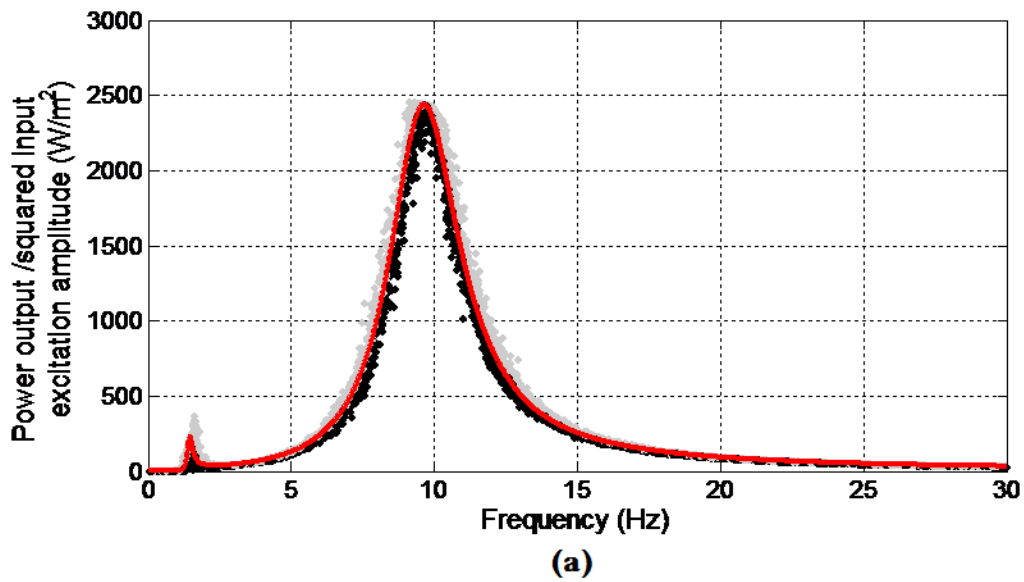


Figure 4.34: Ratio of the output power to squared excitation displacement amplitude for variation of  $m_2$  using its original value as the mean value and a standard deviation of 20% of the original value for (a) the direct-drive system and (b) the indirect-drive system.



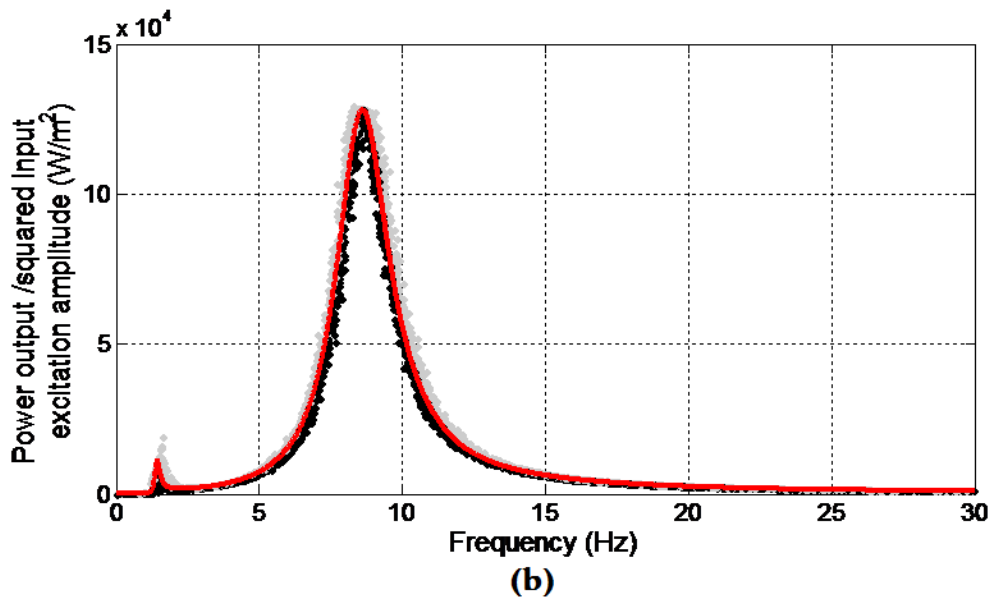
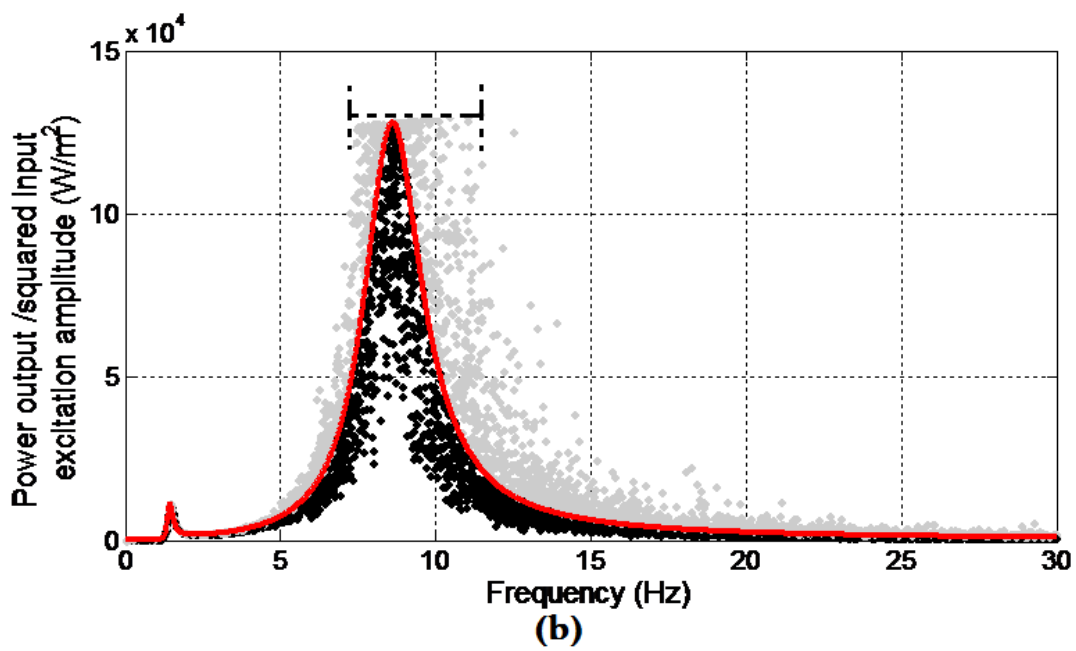
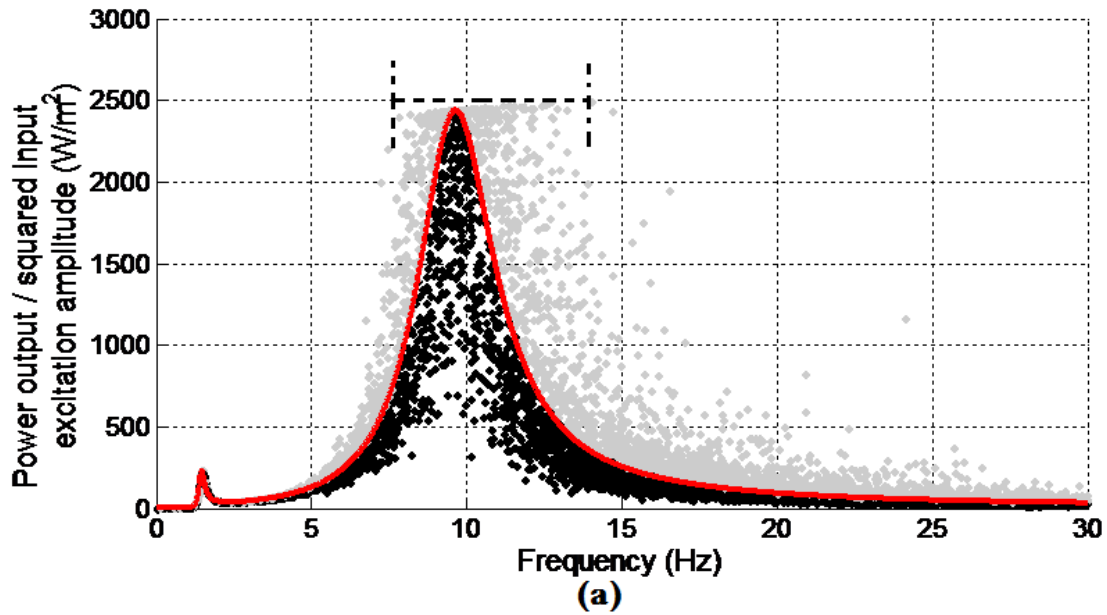


Figure 4.35: Ratio of the output power to squared excitation displacement amplitude for variation of  $k_2$  using its original value as the mean value and a standard deviation of 20% of the original value for (a) the direct-drive system and (b) the indirect-drive system.

In Figures 4.36(a) and (b), it can be seen that changing wheel assembly mass  $m_1$  does not increase the maximum power output ratio, however, the modal resonant frequencies can change over a wider frequency range. With a standard deviation of 20% of the mean value of the wheel assembly mass in the direct-drive system, the change range of the peak power ratio frequency (or modal resonant frequency) has been extended from 9.5Hz to 8Hz-13Hz. In the indirect-drive system, the change range of the peak power ratio frequency is extended from 8.6Hz to 7.5Hz-10Hz, as indicated by the dotted black line. The peak power output frequency of the direct-drive system is more sensitive to the wheel assembly mass  $m_1$  than that of the indirect-drive system. The maximum power output ratio of the indirect-drive system remains 50 times more than that of the direct-drive system. Since the excitation frequency range is based on the road on which the vehicle is likely to be driven, it is suggested that the mass of



the wheel assembly needs to be chosen to ensure the output power peak frequencies occur within the excitation frequency range.



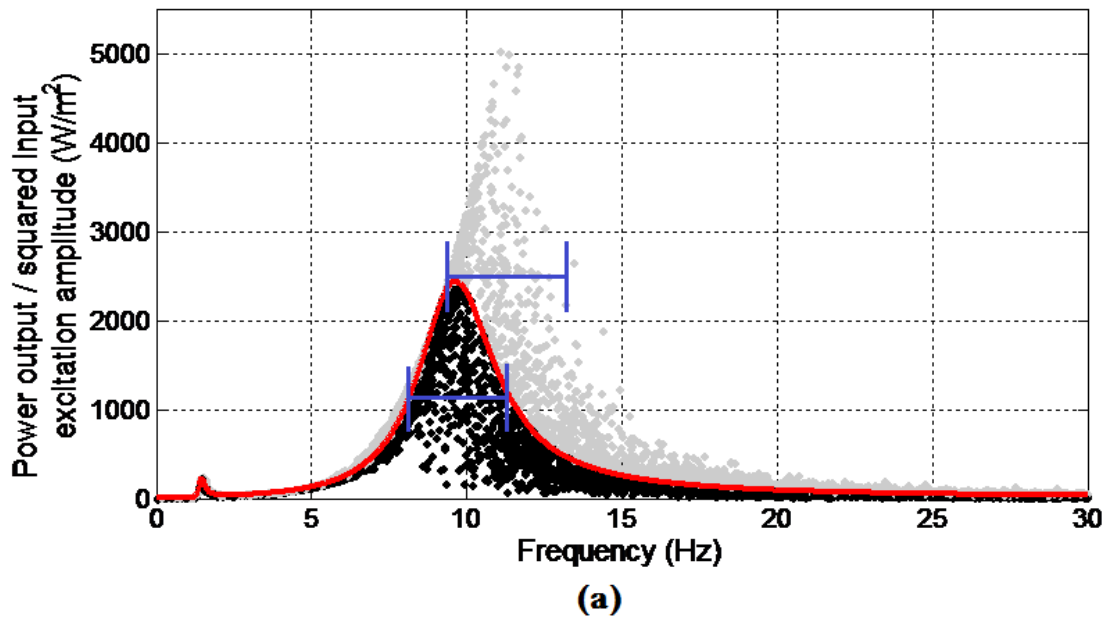
**Figure 4.36: Ratio of the output power to squared excitation displacement amplitude for variation of  $m_I$  using its original value as the mean value and a standard deviation of 20% of the original value for (a) the direct-drive system and (b) the indirect-drive system.**

In Figures 4.37(a) and (b), tyre stiffness  $k_I$  is randomized using its original value as the mean value and a standard deviation of 20% of the mean value. For both the direct-drive and indirect-drive systems, the variations of  $k_I$  show a broad peak (modal resonant) frequency range for the maximum power output ratio. With the variations of  $k_I$ , the direct-drive and indirect-drive systems have the maximum power output ratios of  $5000 \text{ W/m}^2$  and  $2.6 \times 10^5 \text{ W/m}^2$ , respectively, which is more than doubled original power output ratios. For 20% variation of  $k_I$ , the range of the mean harvestable time domain power is  $0\text{-}5000 \text{ W/m}^2$  for the direct-drive system and  $0\text{-}2.75 \times 10^5 \text{ W/m}^2$  for the indirect-drive system. Based on the half power bandwidth method where the harvesting bandwidth can be obtained as the frequency range when the power is half of the peak power, the range of the frequency bandwidth of the harvestable energy is 8 Hz to 11.5 Hz for the direct-drive and 7.5 Hz to 10 Hz for the indirect-drive, indicated by the blue solid line.

Assuming the road excitation displacement amplitude is 0.035m, the simulated peak output power after the randomization for the indirect-drive system reaches 8.7 kW at 10 Hz in Figure 4.37(b), which is significantly larger than 175 W of the direct-drive system in Figure 4.37(a). The bandwidth of the direct-drive system is 3.5 Hz, which is larger than 2.5 Hz of the indirect-drive system. The variation of  $k_I$  enables the harvesting bandwidth to be increased to 6 Hz for direct-drive system and to 5 Hz for indirect-drive system, resulting in more possibility of obtaining high power output. In addition,  $k_I$  should be properly chosen so that

the maximum power output significantly increases, while the modal resonant frequency stays within the range of the road excitation frequency similar to the chosen wheel assembly mass

$m_1$ .



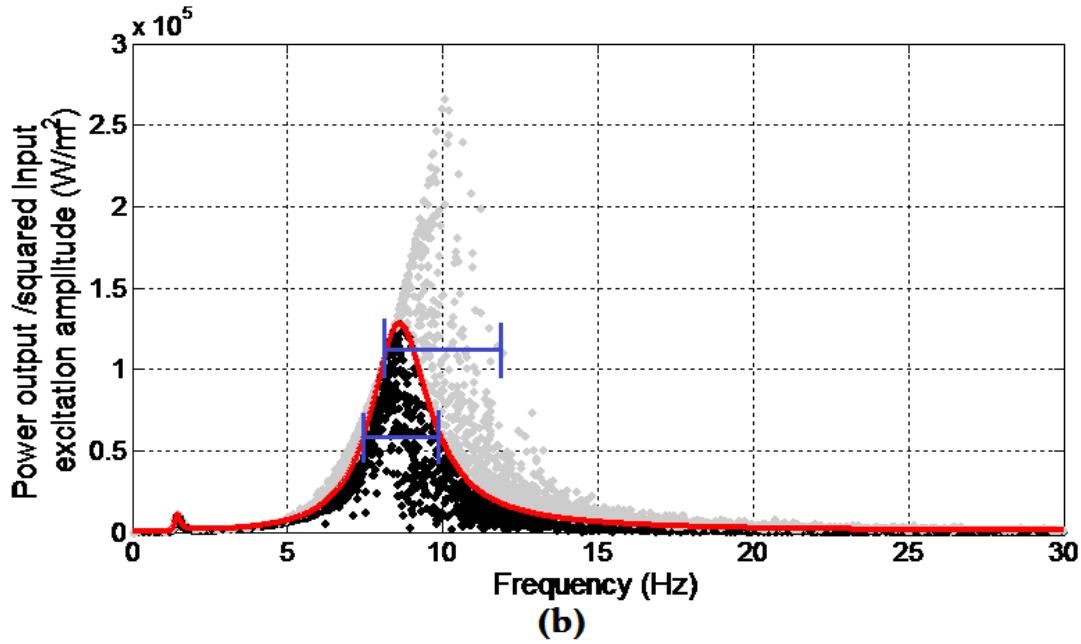


**Figure 4.37: Ratio of the output power to squared excitation displacement amplitude for variation of  $k_1$  using its original value as the mean value and a standard deviation of 20% of the mean value for (a) the direct-drive system and (b) the indirect-drive system.**

In Figures 4.38(a) and (b), the suspension damping coefficient  $c_2$  is randomized using its original value as the mean value and a standard deviation of 20% of the mean value. It is seen that varying  $c_2$  can also increase the maximum power output ratio from 2500 W/m<sup>2</sup> to 5300 W/m<sup>2</sup> for the direct-drive system and from  $1.3 \times 10^5$  W/m<sup>2</sup> to  $2.5 \times 10^5$  W/m<sup>2</sup> for the indirect-drive system without changing much the modal resonant frequencies. Varying tyre damping coefficient  $c_1$  can increase the maximum power output ratio in a similar way but not as large as varying  $c_2$ , as shown in Figures 4.39(a) and (b). Even though the maximum power output ratio can be increased by decreasing  $c_1$  and  $c_2$ , the energy harvesting bandwidth is noticeably smaller than by varying  $k_1$  and  $m_1$ . For both the systems, the probability of achieving high power output ratio at the non-resonant conditions through changing  $c_1$  or  $c_2$  is very low. It should also be noted that tuning suspension damping  $c_2$  can largely affect the vehicle

vibration isolation therefore it should be treated carefully to maintain an acceptable comfort level.

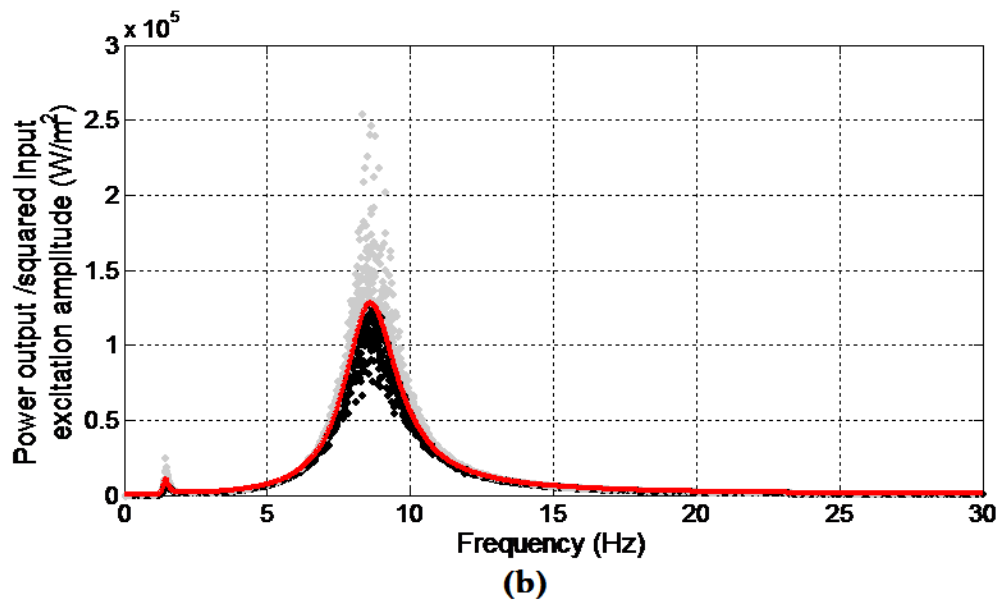
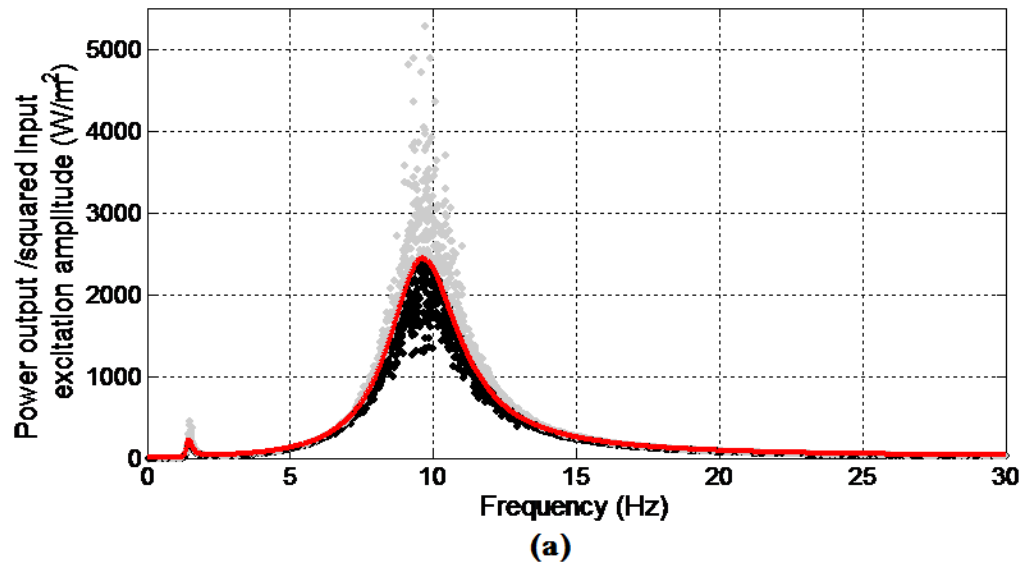


Figure 4.38: Ratio of the output power to squared excitation displacement amplitude for variation of  $c_2$  using its original value as the mean value and a standard deviation of 20% of the mean value for (a) the direct-drive system and (b) the indirect-drive system.

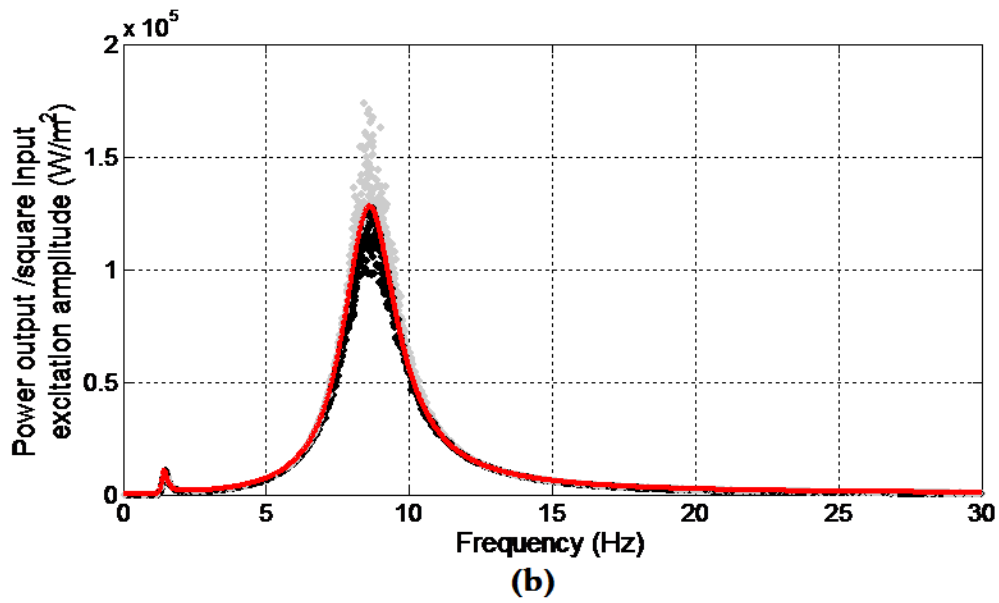
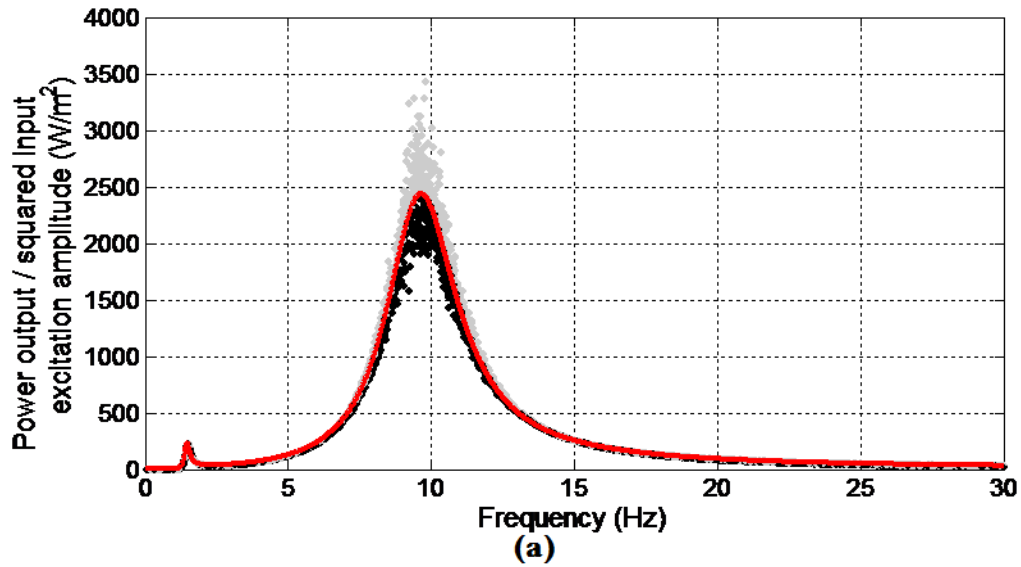


Figure 4.39: Ratio of the power output to squared excitation displacement amplitude for variation of  $c_1$  using its original value as the mean value and a standard deviation of 20% of the mean value for (a) the direct-drive system and (b) the indirect-drive system.

Figures 4.40, 4.41 and 4.43 present the ratio of the output power to the squared excitation displacement amplitude for variation of the electrical elements  $Bl$ ,  $L_e$  and  $R_e$  using their original values as the mean values and standard deviations of 20% of the mean values.

Figures 4.40(a) and (b) show the effect of the electromechanical coupling constant  $Bl$  on the power output ratio. The results are similar to those of the suspension damping  $c_2$  in Figures 4.38(a) and (b), because  $Bl$  is proportional to the electromagnetic damping, it can be treated as a coefficient of added equivalent damping. Variation of  $Bl$  in both the direct-drive and indirect-drive systems can achieve larger peak output power ratio and much broader harvesting bandwidth than the variation of the suspension damping  $c_2$ . With the variation of  $Bl$ , the peak power output ratio reaches  $5300 \text{ W/m}^2$  for the direct-drive system and  $3.1 \times 10^5 \text{ W/m}^2$  for the indirect-drive system.

For 20% variation of  $Bl$ , the range of the mean harvestable time domain power is 0-5000  $\text{W/m}^2$  for the direct-drive system and 0- $2.75 \times 10^5 \text{ W/m}^2$  for the indirect-drive system. The frequency bandwidth of the harvestable energy of both the direct-drive and the indirect-drive system do not change much. The peak output power ratio of the indirect-drive system remains 50 times more than that of the direct-drive system.

Figures 4.41(a) and (b) show that variation of the coil inductance  $L_e$  does not affect the maximum power output ratio of the direct-drive or indirect-drive systems.

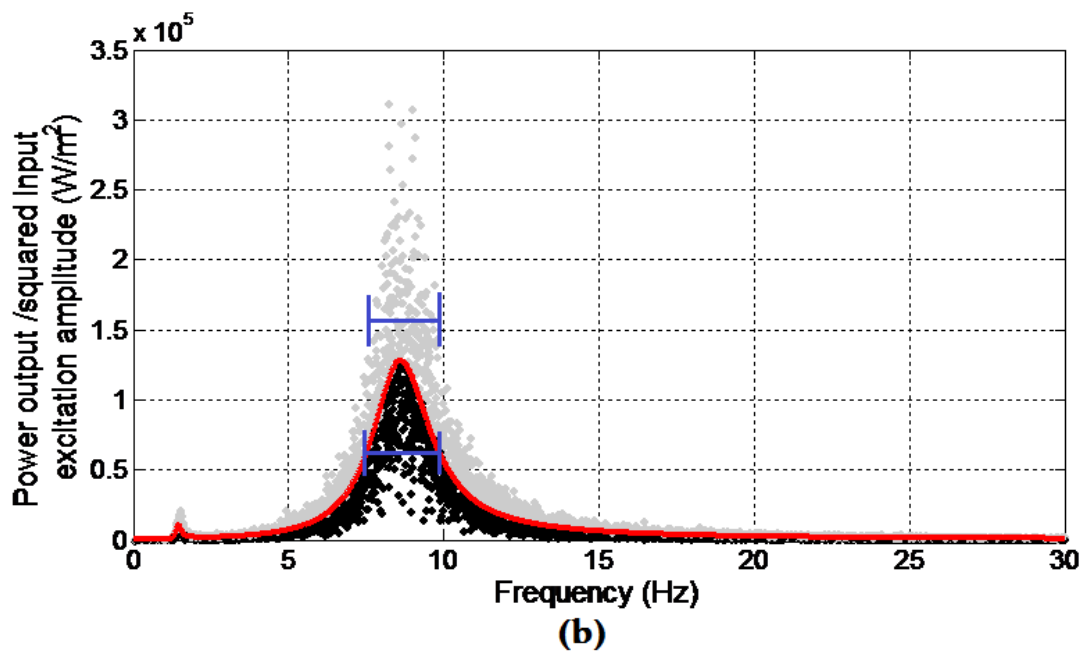
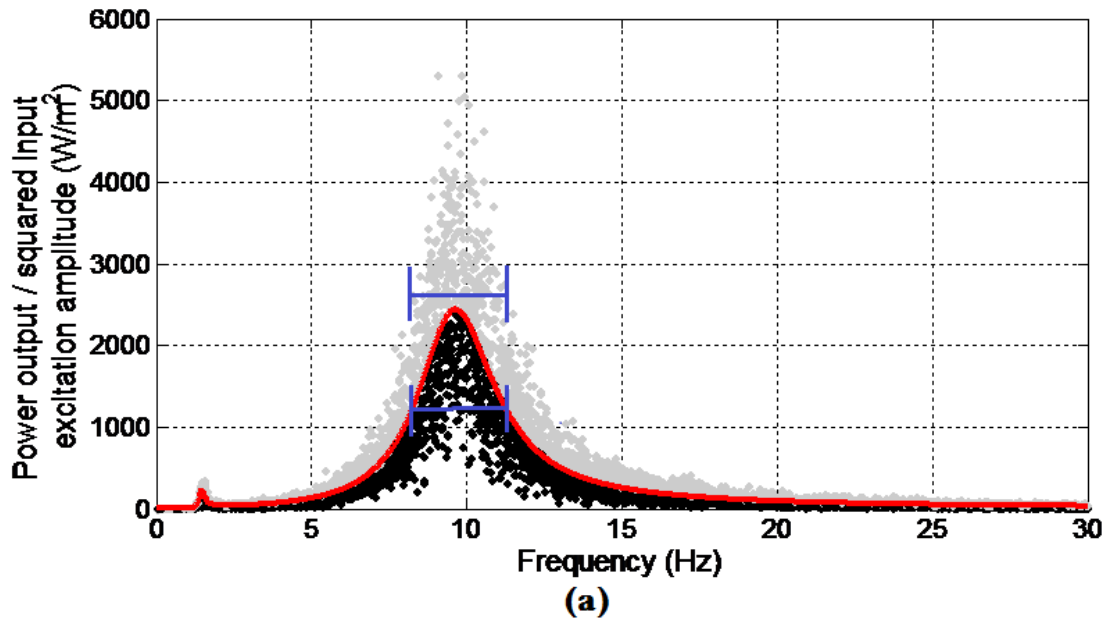




Figure 4.40: Ratio of the power output to squared excitation displacement amplitude for variation of  $Bl$  using its original value as the mean value and a standard deviation of 20% of the mean value for (a) the direct-drive system and (b) the indirect-drive system.

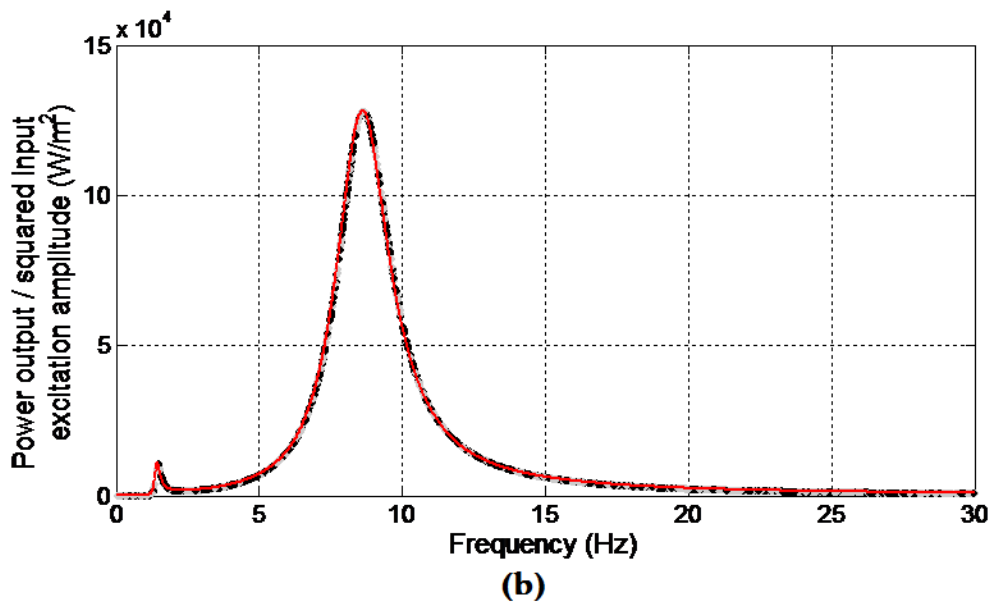
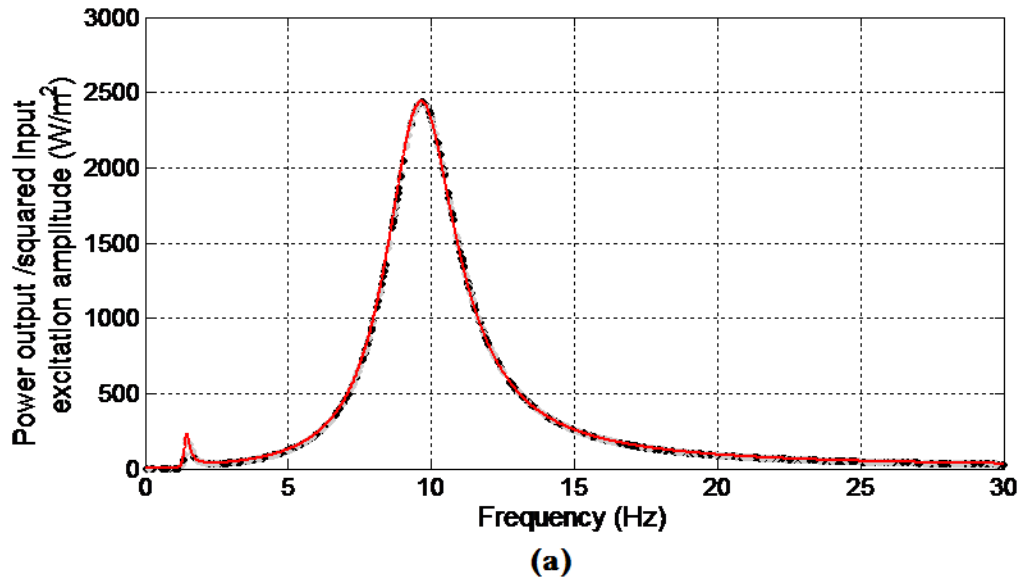
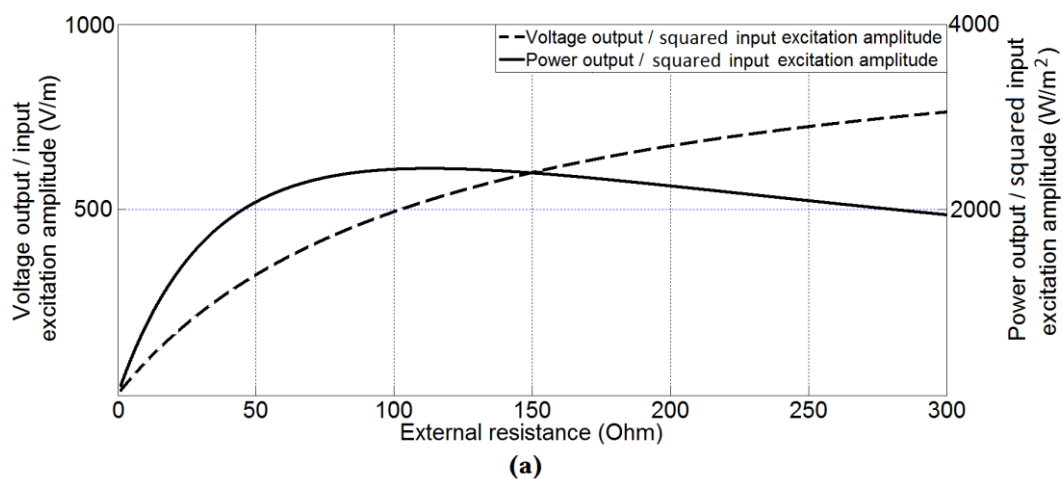
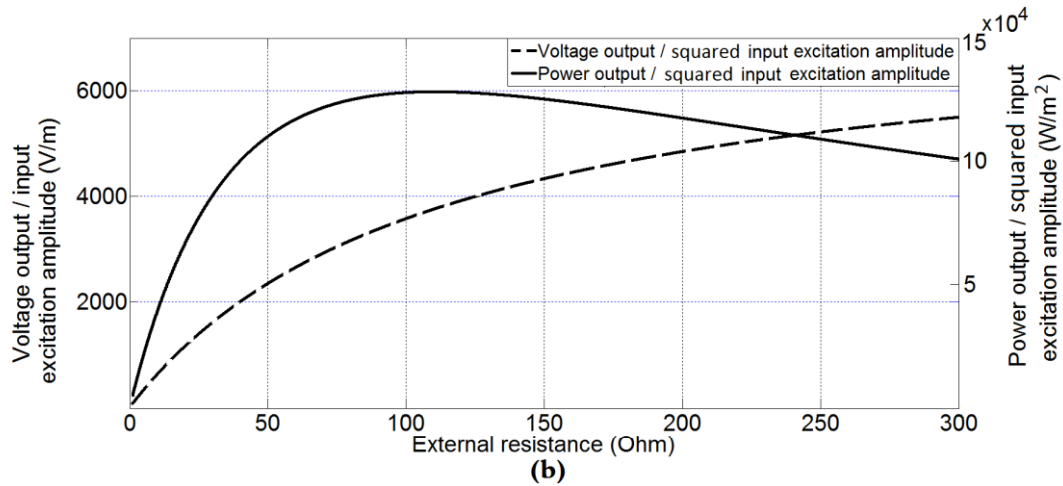


Figure 4.41: Ratio of the power output to squared excitation displacement amplitude for variation of  $L_e$  using its original value as the mean value and a standard deviation of 20% of the mean value for (a) the direct-drive system and (b) the indirect-drive system.

Figures 4.42 (a) and (b) show the effect of the external resistance on the voltage output ratio and power output ratio. For both the direct-drive and the indirect-drive systems, larger peak power output ratio can be identified at the modal resonant frequencies which are 9.67Hz for the direct-drive system and 8.6Hz for the indirect-drive system. At the modal resonant frequency, the power output ratio can be maximized when the external resistance is  $113\Omega$  which is same as the internal resistance of the generator. An increase in the external resistance can lead to the increase in the generated voltage, but at the same time, will reduce the current flowing through the circuit, resulting in the decrease in the output power ratio. Both the direct-drive and indirect-drive systems respond similarly to the change of the external resistance. The maximum peak output power ratio of the indirect-drive system always remains 50 times more than that of the direct-drive system regardless of the external resistances.





**Figure 4.42: Ratio of the output voltage to excitation displacement amplitude and ratio of power output to squared excitation displacement amplitude for increasing  $R$  in (a) the direct-drive system and (b) the indirect-drive system**

In Figures 4.43 (a) and (b), the coil resistance  $R_e$  is randomized using its original value as the mean value and a standard deviation of 20% of the mean value, the external resistance  $R$  is kept the same as  $R_e$  for the maximum power extraction based on Figure 4.42. The peak power output ratio can be identified at modal resonant frequency in Figures 4.43(a) and (b), it is seen that the change of  $R_e$  does not have a large effect on the modal resonant frequency. Also, the harvesting bandwidth does not change much with randomizing  $R_e$  for either of the direct-drive or indirect-drive systems.

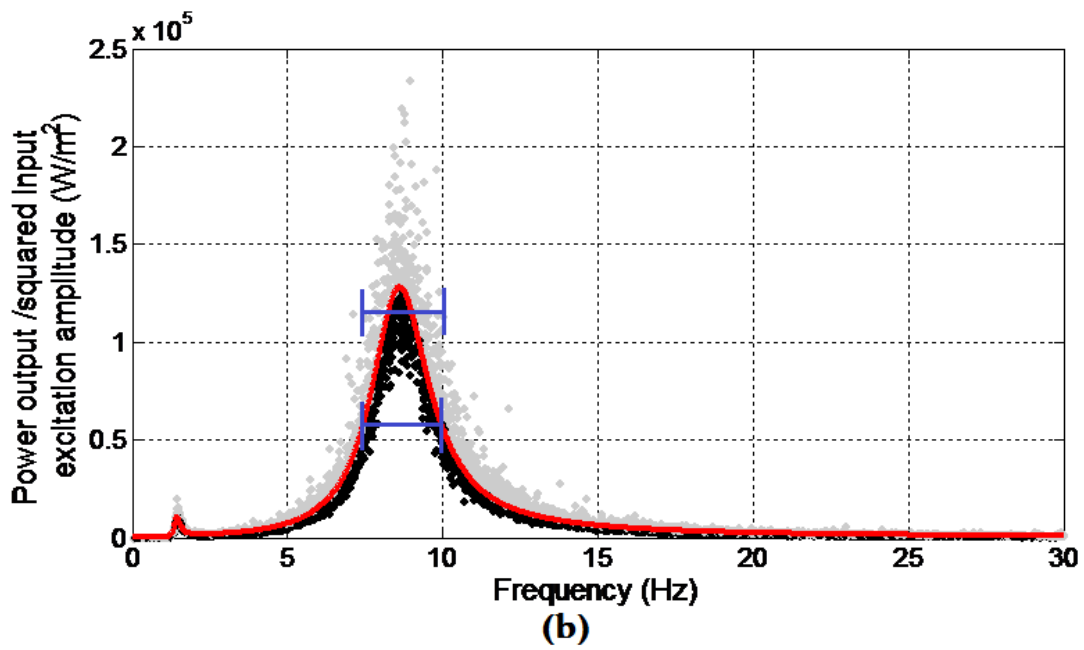
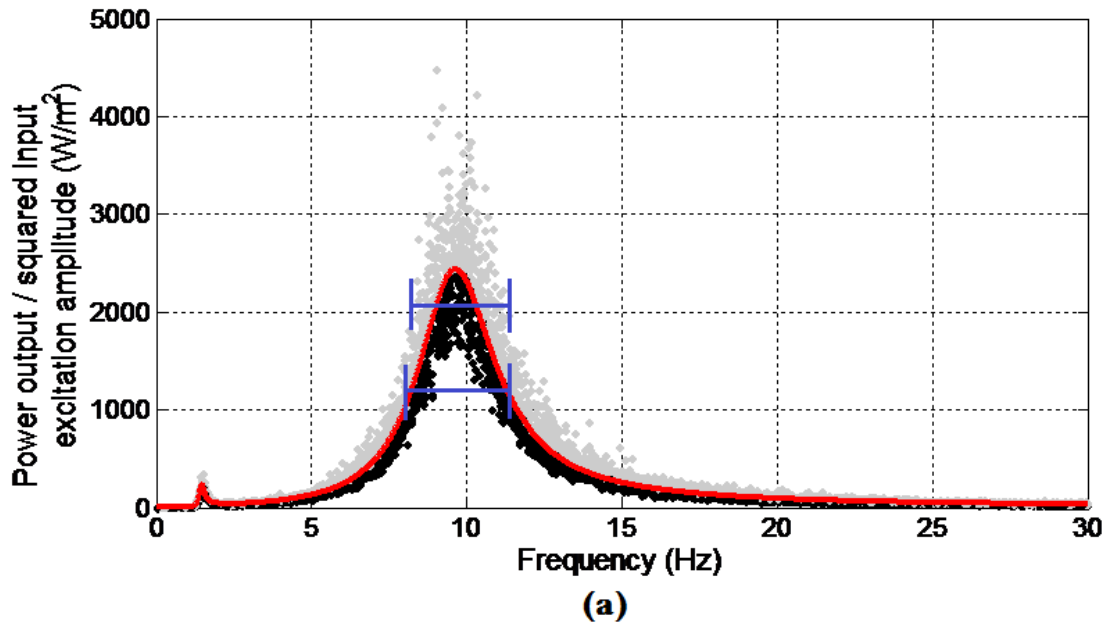
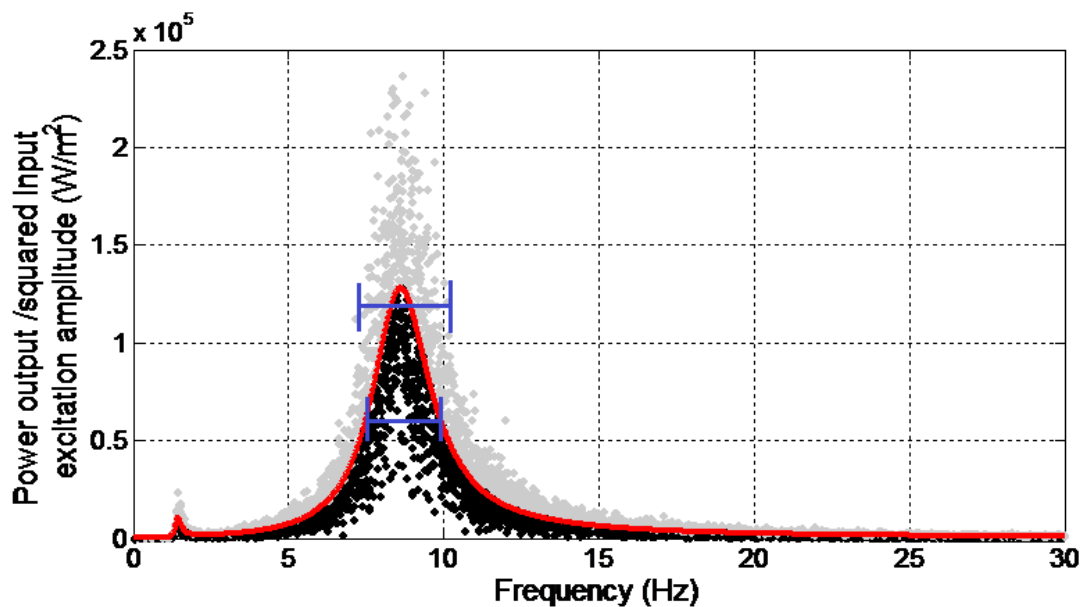


Figure 4.43: Ratio of the power output to squared excitation displacement amplitude for variation of  $R_e$  using its original value as the mean value and a standard deviation of 20% of the mean value for (a) the direct-drive system and (b) the indirect-drive system.

The results are similar to those of varying the suspension damping  $c_2$  in Figures 4.38(a) and (b), because  $R_e$  can be treated as the added equivalent electrical damping. However, the increase of the peak power output ratio through varying  $R_e$  is less significant than through varying other parameters, thus the variation of  $R_e$  on either of the systems does not guarantee a high peak power output ratio.

Variation of the gear ratio can only be applied to the indirect-drive system. When gear ratio  $j$  is randomized using its original value as the mean value and a standard deviation of 20% of the mean value, as shown in Figure 4.44, the maximum peak power output ratio at the modal resonant frequency reaches  $2.4 \times 10^5 \text{ W/m}^2$ , the bandwidth for achieving such power output ratio is 7.5-10 Hz.



**Figure 4.44: Ratio of the power output to squared excitation displacement amplitude for variation of the gear ratio  $j$  using its original value as the mean value and a standard deviation of 20% of the mean value in the indirect-drive system.**

#### 4.3.6 Results and discussion

The results of the Monte Carlo simulations reveal that among the parameters that have effects on the energy harvesting performance, a broad peak frequency variation range of the output power ratio can be achieved when the tyre mass  $m_l$  is varied. The maximum power output ratio will increase with broader peak frequency variation range when the tyre stiffness  $k_l$  is increased. Variation of tyre damping coefficient  $c_l$ , suspension damping coefficient  $c_2$  may result in an increased maximum power output ratio but with a very narrow harvesting frequency bandwidth. The variations of the electrical parameters do not affect the modal resonant frequencies of both the systems. The variation of the electromechanical coupling constant  $Bl$  can lead to the highest peak power output ratio with a broad peak frequency variation range in both the direct-drive and indirect systems. Assuming the external resistance  $R$  is kept the same as the internal coil resistance  $R_e$  due to power output maximization, the variation in internal resistance  $R_e$  (or external resistance  $R$ ) can result in an increase of the peak power output ratio similar to varying the suspension damping  $c_2$ .

Variation of the gear ratio which is the only unique parameter of the indirect-drive system presents the similar results to variation of the suspension damping  $c_2$  in terms of the peak power output of the indirect-drive system, but has a higher power output ratio at non-resonant conditions.

Regardless of the parameter variation, the power output ratio of the indirect-drive system always remain 50 times more than the direct-drive system. A well-tuned indirect-drive system is capable of harvesting more power without sacrificing the vehicle ride comfort. Compared with the direct-drive regenerative shock absorber, the main limitation of the indirect-drive regenerative shock absorber is its operation at high frequency. Its advances in power output over direct-drive regenerative shock absorber becomes less at higher frequency. The variation of the system parameter  $m_I$  and  $k_I$  can increase the power output of the indirect-drive regenerative shock absorber at non-resonant conditions. When subjected to the high frequency road excitation, the indirect-drive regenerative shock absorber may be more prone to failure due to the mechanical complication and excessive dynamic load applied on the shock absorber. A set of stronger driving arms or similar mechanisms are recommended for a better durability.

#### *4.3.7 Future perspective and recommendations*

The linear to rotary conversion of the indirect-drive regenerative shock absorber relies on the driving arms which forces the flywheel to rotate. When subjected to the higher frequency, the amount of dynamic force applied on the driving arms can be excessively large, causing the indirect-drive regenerative shock absorber to become vulnerable. The key to improve its reliability is to avoid the perpendicular position between the top plate and the driving arms. In that case, the aggressive dynamic force can be transferred to push the flywheel to rotate

instead of being applied vertically on the driving arms which may break under compression. For the practicality, it is recommended to constrain the driving arms so that it only rotates within the desired angle range. The driving arms can also be manufactured with strong material to withstand the large compression force.

In order to obtain a steady response, it is recommended for the indirect-drive regenerative shock absorber to have enough damping force during both compression phase and recoil phase. The flywheel should have teeth on both the top and bottom sides, with matching driving arms on the top and bottom sides as well, as shown in Figure 4.45. As a result when the shock absorber moves up and down, one set of the driving arms can always be engaged with the flywheel. The orientation direction of the teeth can ensure that the flywheel and the generator only rotate in one direction. The reliability and the efficiency of the optimized indirect-drive regenerative shock absorber will be investigated as the extension of the research.



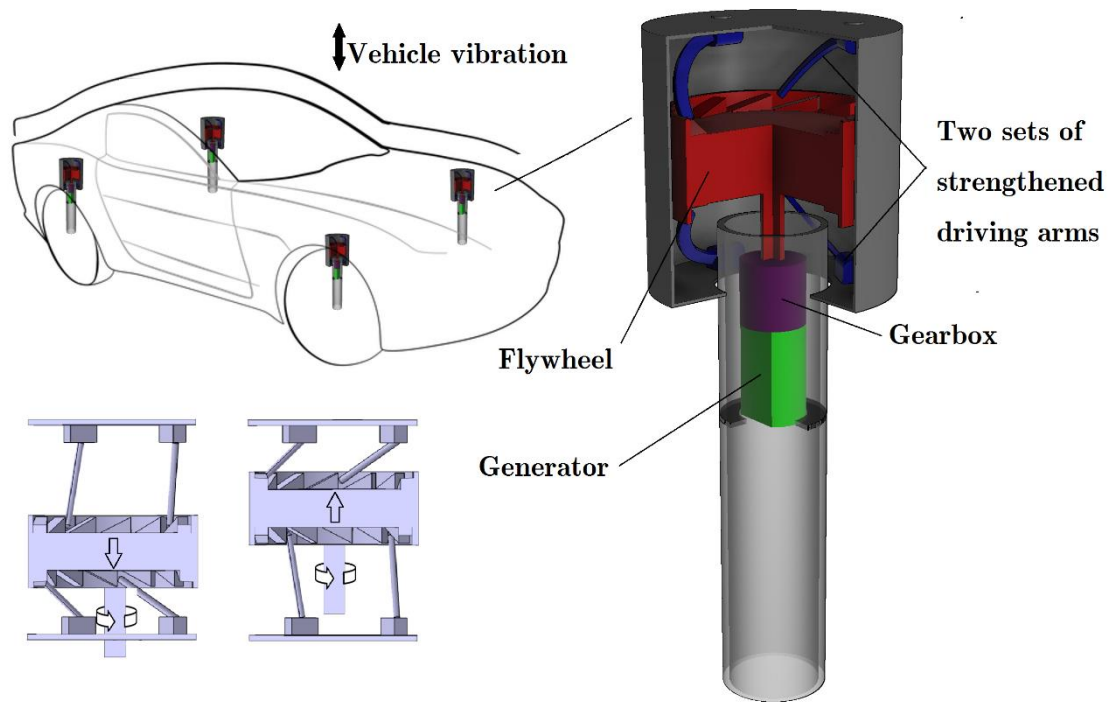


**Figure 4.45: The future design of the indirect-drive regenerative shock absorber.**

## 4.4 Conclusion:

In this chapter, two novel regenerative shock absorbers have been proposed aiming at harvesting more energy in comparison with the conventional regenerative shock absorber. For both designs, the prototypes have been built for the validation of the simulation models, which are established based on the quarter vehicle suspension system. For the double speed regenerative shock absorber (double speed RSA), the power generated is four times as large as that of the direct-drive regenerative shock absorber (direct drive RSA) under the same road profile displacement excitation, which includes the sinusoidal excitation and the random road profile displacement excitation. Based on the Monte Carlo simulation results, the double speed RSA can generate a higher voltage output peak than the direct drive RSA when subjected to the same random road profile displacement excitation. Comparing to the other

regenerative shock absorber designs, the proposed regenerative shock absorber is able to increase the power output and energy harvesting efficiency without increasing the complexity of the structure. An optimal regenerative shock absorber with a reciprocating coil mass and a speed amplifying mechanism has been proposed based on the double speed RSA. In order to improve the system power extraction, a best combination of the amplification factor and coil mass has been selected. It was found that in the regenerative shock absorber with the reciprocating coil mass, the output power can be sensitive to either the coil mass or amplification factor depending on the amount of the coil mass. A maximum of 54 W can be generated with the optimal selection of the coil mass  $m_c = 5$  kg and amplification factor  $n = 3$ .

In the second part of the chapter, based on the evaluation of the indirect-drive regenerative shock absorber (indirect-drive RSA), the results of the Monte Carlo simulation suggests that the indirect-drive regenerative shock absorber is capable of achieving higher peak power output ratio than the direct-drive RSA. In both the direct-drive and indirect-drive RSA systems, tyre stiffness  $k_t$ , electromechanical coupling  $Bl$  have significant effects on the vibration energy harvesting performance taking into account the peak power output ratio and the harvesting frequency bandwidth. The right choice of the gear ratio can further improve the peak power output ratio of the indirect-drive system. The direct-drive system and indirect-drive system perform similarly to the parameter variations. The peak power output ratio of the indirect-drive system always remains 50 times more than that of the direct-drive system. In terms of the bandwidth for achieving the maximum peak power output ratio, the direct-drive system is slightly better than the indirect-drive system.

## Chapter 5

*Parameter study and optimization of a half-vehicle suspension system model integrated with the indirect-drive regenerative shock absorber using Taguchi method*

*This chapter presents the optimization of a half-vehicle suspension system model integrated with the indirect-drive regenerative shock absorber through the Taguchi method. In this method, the ratio of the peak output power over the squared excitation displacement amplitude and the frequency bandwidth of the front and rear shock absorbers are set as targets and evaluated respectively. The effect of each parameter on the targets and the optimal parameter combination are identified through the Taguchi matrix calculations. The optimized system is evaluated at a vehicle speed of 20 km/h under the excitation of the road surface profiles of Class A, C and E of ISO 8606. It is proven that the optimized system is*

*able to harvest more energy than the original system at a certain speed for all three random road profile classifications.*

## 5.1 Introduction

In order to reveal the potential of the regenerative shock absorber in a realistic situation, harmonic displacement excitation signals of the road surface were widely applied [22, 23, 129, 151]. However, one common limitation of the above-mentioned research is that the road surface displacement profiles were mostly presented by a periodic sinusoidal signal, the randomness of the road surface displacement profile was ignored while it should not be. As a result, the operation of these systems on a vehicle driven on a random road surface displacement profile will be different from that of the systems subjected to a periodic harmonic displacement excitation due to the unpredicted change of the excitation displacement and frequency. Such the operation on the random road profile could lead to the undesired energy loss. Therefore, the kinetic energy storing element such as a flywheel is recommended.

Many attempts were made to optimize the system based on integration of the regenerative shock absorber into the quarter-vehicle suspension system [42, 71, 84, 95, 124]. In order to investigate the mutual interaction effects of the front and rear wheels, a half-vehicle suspension system model was proposed by many authors [70, 152]. The main limitation of the quarter vehicle suspension system is that simply adding the peak power output of the front and rear regenerative shock absorbers together does not yield the correct total power output. This is because the power outputs of the front and rear regenerative shock absorber do

not reach the peak values at the same time. Therefore, it is advisable to integrate the front and rear suspensions into the four degrees of freedom (DOF) half-vehicle suspension system model for a valid analysis.

Compared to all the methods of systematic evaluation and optimization, the Taguchi method has its own advantages in quantifying the effects of each parameter on the desired target [153, 154]. In addition, the coupling influence of the parameters can be evaluated in this method, which is important for a parameter study. In terms of the parameter optimization of the regenerative shock absorber, many have focused on improving the peak power output but not considering energy harvesting frequency bandwidth which is substantially important when dealing with the random road profile excitation. The Taguchi method allows for peak power output and energy-harvesting frequency bandwidth to be evaluated as targets for the parameter optimization under the random road profile excitations.

Therefore, in this chapter, the indirect-drive regenerative shock absorber is integrated into the half vehicle suspension system model, based on which the simulation model is developed to provide more reliable prediction. Taguchi method will be adopted for parameter optimization of the half vehicle suspension system model targeting at increasing the peak power output and broadening the energy harvesting frequency bandwidth. The energy harvesting performance of the optimized model will be evaluated according to the road classes defined by ISO 8606.

## 5.2 Half vehicle modelling with the integrated indirect-drive regenerative shock absorber.

The working principle of the indirect-drive regenerative shock absorber (or indirect-drive RSA) is shown in Figure 5.1. The proposed suspension system consists of the indirect-drive RSA and the spring installed on outside the indirect-drive RSA. When the shock absorber of the suspension system operates in the compression phase due to the uneven road surface excitation, the angled driving arms push the arm-teeth flywheel to rotate. When the shock absorber of the suspension system operates in the recoil phase, the driving arms and the arm-teeth flywheel becomes disengaged and flywheel continues to rotate in one direction as a result of inertia. The gear box connected to the generator amplifies the rotational speed of the flywheel, thus the power output can be greatly increased.

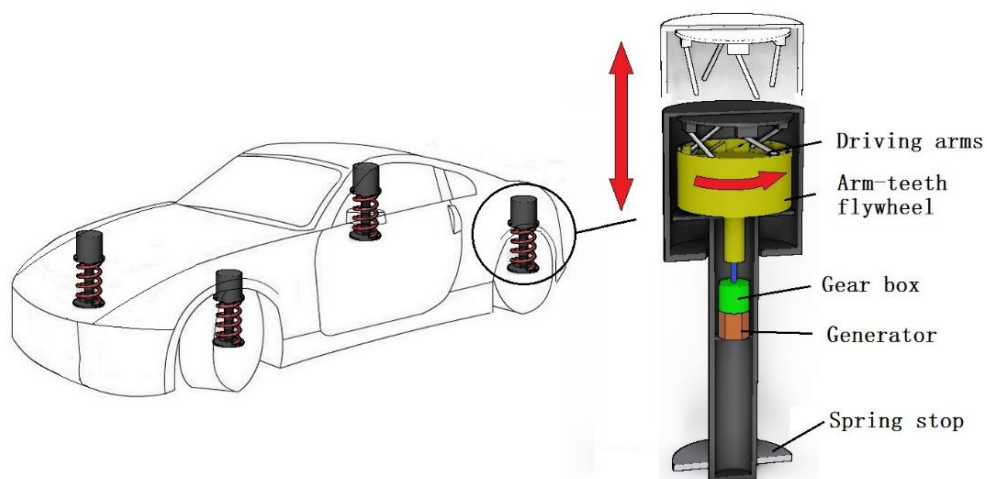


**Figure 5.1: The working principle of the indirect-drive RSA.**

Shown in Figure 5.2 is the half vehicle suspension system model of a passenger car integrated with two indirect-drive RSAs and its electrical circuit.  $m_2$  is the half vehicle mass,  $m_{1f}$  is front wheel assembly mass,  $m_{1r}$  is the rear wheel assembly mass;  $c_{2f}$  is the front suspension damping coefficient,  $c_{2r}$  is the rear suspension damping coefficient,  $c_{1f}$  is the front tyre damping coefficient,  $c_{1r}$  is the rear tyre damping coefficient;  $k_{2f}$  is the front suspension stiffness,  $k_{2r}$  is the rear suspension stiffness,  $k_{1f}$  is the front tyre stiffness,  $k_{1r}$  is the rear tyre stiffness;  $a$  is the distance between the centre of gravity of the vehicle to the front axial,  $b$  is the distance between the centre of gravity of the vehicle to the rear axial,  $J$  is the pitch rotational moment of inertia of the vehicle body about COG,  $\theta$  is the pitch angle of the vehicle body;  $x$  is the vertical displacement of the half vehicle body,  $x_f$  is the vertical displacement of the front wheel,  $x_r$  is the vertical displacement of the rear wheel,  $z_f$  is the road profile excitation displacement input on the front wheels,  $z_r$  is the road profile excitation displacement input on the rear wheels. The G in the circle represents the indirect-drive RSA generator, which has parameters of the coil resistance  $R_e$  and coil inductance  $L_e$ . The energy is harvested and converted into electricity and stored in an electric circuit with an external resistance  $R$ .

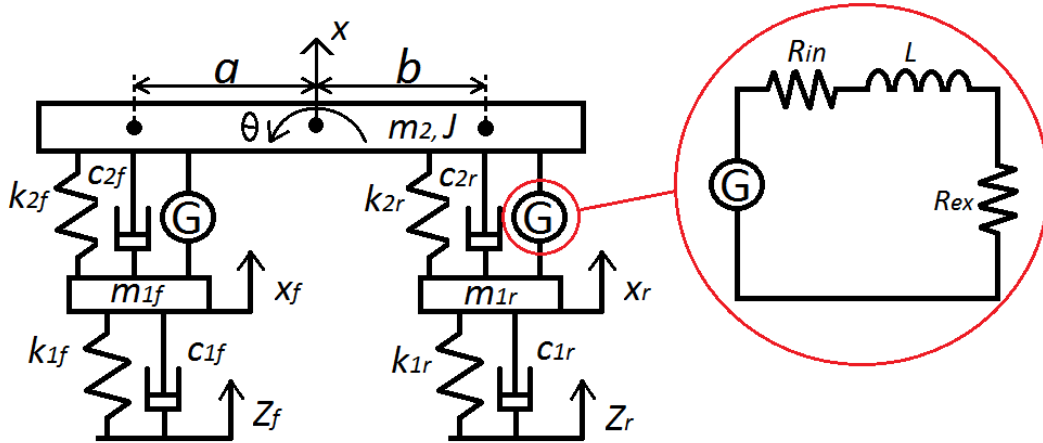


Figure 5.2: A half vehicle model with the indirect-drive RSAs and their electrical circuits.

Same as Equation (4.15), the force equilibrium equations of this 7 DOF oscillating system can be obtained by:

$$\begin{cases} F_{LR} = Bl \cdot \frac{U}{R} \\ F_{Gi} + F_{Wi} + F_{Ki} \pm n \cdot F_{LR} = 0 \end{cases} \quad (5.1)$$

where  $F_{LR}$  is the Lorenz force;  $F_{Gi}$  is the inertia force of the  $i^{\text{th}}$  degree of freedom oscillator ( $i=1,2,3,4$ );  $F_{Wi}$  is the damping force of the  $i^{\text{th}}$  degree of freedom oscillator;  $F_{Ki}$  is the spring restoring force of the  $i^{\text{th}}$  degree of freedom oscillator. The Lorenz force  $F_{LR}$  is amplified by the gearbox and this multiplication factor is denoted as  $n$ .

Based on the Lagrange's equation, individual forces of the system in Equation (5.1) can be expressed by:



$$\begin{cases} F_{Gi} = \frac{d}{dt} \frac{\partial T}{\partial \dot{x}_i} - \frac{\partial T}{\partial x_i} \\ F_{wi} = \frac{\partial W}{\partial \dot{x}_i} \\ F_{ki} = \frac{\partial V}{\partial x_i} \end{cases} \quad (5.2)$$

where  $\dot{x}_i$  and  $x_i$  are the velocity and displacement of the  $i^{\text{th}}$  degree of freedom oscillator;  $T$ ,  $W$  and  $V$  are the total kinetic energy, damping energy and spring potential energy, respectively, which are given by:

$$\begin{cases} T = \frac{1}{2} m_s (\dot{x}_f - \dot{x} + a\dot{\theta})^2 + \frac{1}{2} m_s (\dot{x}_r - \dot{x} - b\dot{\theta})^2 + \frac{1}{2} m_2 \dot{x}^2 + \frac{1}{2} m_{1f} \dot{x}_f^2 + \frac{1}{2} m_{1r} \dot{x}_r^2 + \frac{1}{2} J \dot{\theta}^2 \\ W = \frac{1}{2} c_{1f} (\dot{z}_f - \dot{x}_f)^2 + \frac{1}{2} c_{1r} (\dot{z}_r - \dot{x}_r)^2 + \frac{1}{2} c_{2f} (\dot{x}_f - \dot{x} + a\dot{\theta})^2 + \frac{1}{2} c_{2r} (\dot{x}_r - \dot{x} - b\dot{\theta})^2 + \frac{1}{2} c_L (\dot{x}_f - \dot{x} + a\dot{\theta})^2 + \frac{1}{2} c_L (\dot{x}_r - \dot{x} - b\dot{\theta})^2 \\ V = \frac{1}{2} k_{1f} (z_f - x_f)^2 + \frac{1}{2} k_{1r} (z_r - x_r)^2 + \frac{1}{2} k_{2f} (x_f - x + a\theta)^2 + \frac{1}{2} k_{2r} (x_r - x - b\theta)^2 \end{cases} \quad (5.3)$$

where  $m_s$  is the equivalent reciprocating mass of the combination of the top plate, arm-teeth mechanism, differential gear box and DC generator and  $c_L$  is the equivalent reciprocating damping of the combination of top plate, arm teeth mechanism, differential gear box and DC generator. It is assumed that the vertical stiffness of the regenerative shock absorber G is very small and ignored compared to those of the suspension and wheels. The equivalent reciprocating mass  $m_s$  includes the masses of the top plate, flywheel, driving arms, planetary gear carrier, 4 planetary gears and the combination of the sun gear and the generator after the gearbox, as shown in Figure 5.3. The top plate moves up and down with the vehicle body, the flywheel, driving arms, planetary gear carriers and 4 planetary gears rotate at the same angular velocity; the generator and the sun gear rotate faster due to the speed amplification of the attached gearbox.

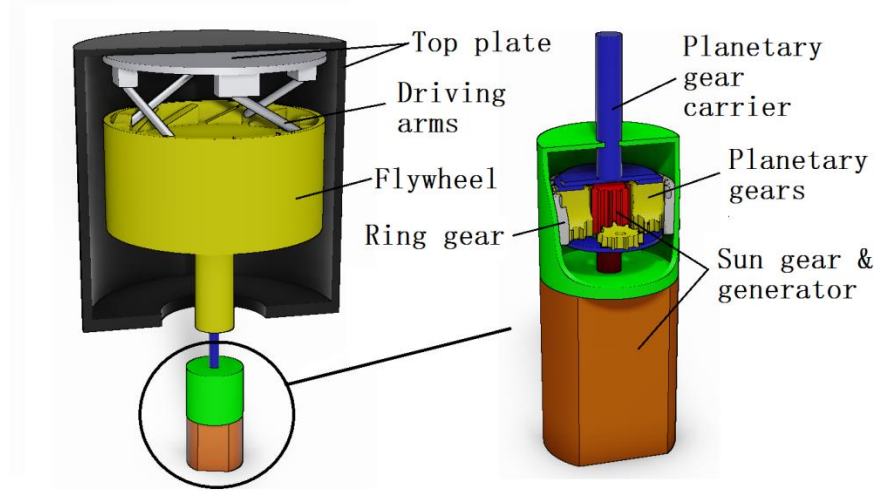


Figure 5.3: The composition of the equivalent reciprocating mass  $m_s$ .

Therefore,  $m_s$  can be given by

$$m_s = m_{tp} + \frac{J_{FW} + J_{am} + J_{pcr} + 4 \cdot (J_p + m_p \cdot r_p^2)}{r_e^2} + \frac{J_g + J_s}{r_e^2} \cdot j^2 \quad (5.4)$$

where  $m_{tp}$  is the equivalent reciprocating mass of the top plate;  $J_{FW}$ ,  $J_{am}$ ,  $J_{pcr}$ ,  $J_p$ ,  $J_s$  and  $J_g$  are the rotational inertia of the flywheel, arm teeth, planetary gear carrier, planetary gear, sun gear and generator;  $r_p$  is the distance from the centre of the sun gear to the centre of a planetary gear, which is equal to a sum of the sun gear pitch radius and planetary gear pitch radius;  $r_e$  is the equivalent rotational inertia radius of the flywheel, arm teeth, planetary gear carrier, planetary gear, sun gear and generator;  $m_p$  is the mass of the planetary gear;  $j$  is the gear ratio of the differential gear box.

Same as in the Equation (4.26), the damping coefficient of the differential gear box and DC generator  $c_L$  is given as:

$$c_L = \frac{k_e^2 \cdot j^2}{r_e^2 \cdot \eta_{tp} \cdot \eta_{pg} \cdot \eta_g \cdot (R + R_e)} \quad (5.5)$$

The governing equations of the front and rear regenerative shock absorbers in the electrical domain are given by Equation (5.6) and Equation (5.7).

$$L_e \cdot \frac{\dot{U}_f}{R} + \frac{U_f}{R} \cdot (R_e + R) = \frac{k_e \cdot j}{r_e} \cdot (\dot{x}_f - \dot{x} + a\dot{\theta}) \quad (5.6)$$

$$L_e \cdot \frac{\dot{U}_r}{R} + \frac{U_r}{R} \cdot (R_e + R) = \frac{k_e \cdot j}{r_e} \cdot (\dot{x}_r - \dot{x} - b\dot{\theta}) \quad (5.7)$$

Therefore, substitution of Equation (5.3), Equation (5.2) into Equation (5.1) and inclusion of Equation (5.6) Equation (5.7) give the dynamic equations of the half vehicle suspension system integrated with the indirect-drive RSAs.

$$\left\{ \begin{array}{l} m_s (\ddot{x}_f - \ddot{x} + a\ddot{\theta}) + m_{1f} \ddot{x}_f - c_{1f} (\dot{z}_f - \dot{x}_f) + c_{2f} (\dot{x}_f - \dot{x} + a\dot{\theta}) + c_L (\dot{x}_f - \dot{x} + a\dot{\theta}) - k_{1f} (z_f - x_f) + k_{2f} (x_f - x + a\theta) + Bl \cdot \frac{U_f}{R} \cdot \frac{j \cdot r_g}{r_e} = 0 \\ m_s (\ddot{x}_r - \ddot{x} - b\ddot{\theta}) + m_{1r} \ddot{x}_r - c_{1r} (\dot{z}_r - \dot{x}_r) + c_{2r} (\dot{x}_r - \dot{x} - b\dot{\theta}) + c_L (\dot{x}_r - \dot{x} - b\dot{\theta}) - k_{1r} (z_r - x_r) + k_{2r} (x_r - x - b\theta) + Bl \cdot \frac{U_r}{R} \cdot \frac{j \cdot r_g}{r_e} = 0 \\ -m_s (\ddot{x}_f - \ddot{x} + a\ddot{\theta}) - m_s (\ddot{x}_r - \ddot{x} - b\ddot{\theta}) + m_2 \ddot{x} - c_{2f} (\dot{x}_f - \dot{x} + a\dot{\theta}) - c_{2r} (\dot{x}_r - \dot{x} - b\dot{\theta}) - c_L (\dot{x}_f - \dot{x} + a\dot{\theta}) - c_L (\dot{x}_r - \dot{x} - b\dot{\theta}) - k_{2f} (x_f - x + a\theta) \\ - k_{2r} (x_r - x - b\theta) - Bl \cdot \frac{U_f}{R} \cdot \frac{j \cdot r_g}{r_e} - Bl \cdot \frac{U_r}{R} \cdot \frac{j \cdot r_g}{r_e} = 0 \\ a \cdot m_s (\ddot{x}_f - \ddot{x} + a\ddot{\theta}) - b \cdot m_s (\ddot{x}_r - \ddot{x} - b\ddot{\theta}) + J\ddot{\theta} + a \cdot c_{2f} (\dot{x}_f - \dot{x} + a\dot{\theta}) - b \cdot c_{2r} (\dot{x}_r - \dot{x} - b\dot{\theta}) + a \cdot c_L (\dot{x}_f - \dot{x} + a\dot{\theta}) - b \cdot c_L (\dot{x}_r - \dot{x} - b\dot{\theta}) \\ + a \cdot k_{2f} (x_f - x + a\theta) - b \cdot k_{2r} (x_r - x - b\theta) + a \cdot Bl \cdot \frac{U_f}{R} \cdot \frac{j \cdot r_g}{r_e} - b \cdot Bl \cdot \frac{U_r}{R} \cdot \frac{j \cdot r_g}{r_e} = 0 \\ L_e \cdot \frac{\dot{U}_f}{R} + \frac{U_f}{R} \cdot (R_e + R) = \frac{k_e \cdot j}{r_e} \cdot (\dot{x}_f - \dot{x} + a\dot{\theta}) \\ L_e \cdot \frac{\dot{U}_r}{R} + \frac{U_r}{R} \cdot (R_e + R) = \frac{k_e \cdot j}{r_e} \cdot (\dot{x}_r - \dot{x} - b\dot{\theta}) \end{array} \right. \quad (5.8)$$

where

$$\left\{ \begin{array}{l} m_s = m_{tp} + \frac{J_{FW} + J_{am} + J_{pcr} + 4 \cdot (J_p + m_p \cdot r_p^2)}{r^2} + \frac{J_g + J_s}{r^2} \cdot j^2 \\ c_L = \frac{k_e^2 \cdot j^2}{r^2 \cdot \eta_{tp} \cdot \eta_{pg} \cdot \eta_g \cdot (R_{in} + R_{ex})} \\ k_e = Bl \cdot r_g \end{array} \right. \quad (5.9)$$

Since the front wheel and rear wheel of the vehicle travel on the same road profile with a time delay depending on the vehicle speed, the sinusoidal wave road displacement excitations with the same amplitude are applied on both the wheels with a phase shift. It is assumed that the vehicle speed is 5.556 m/s (20 km/h). The ratio of the total power output over the squared input excitation displacement amplitude is shown in Figure 5.4 where the total power output accounts for the peak power output harvested in the same time from the front and rear indirect-drive RSAs. In Figure 5.4 where the frequency range is 0-30 Hz, it is shown that two total power output peaks occur at the first and second resonant frequencies. At the second resonant frequency the total power output ratio reaches  $2.25 \times 10^5$  W/m<sup>2</sup>, which is significantly higher than that at the first natural frequency, this is because the more aggressive shock absorber movement is shown to occur at the hopping mode.

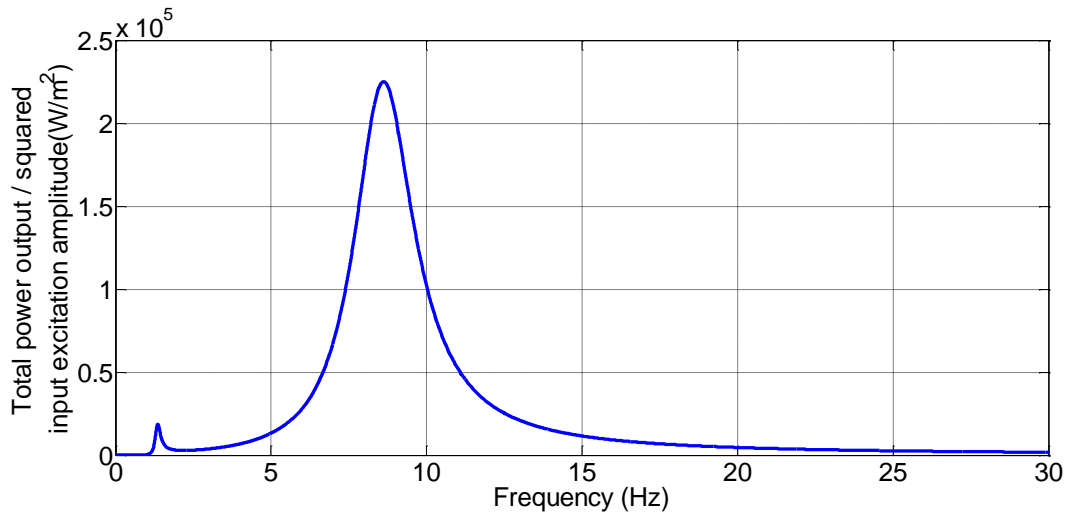


**Figure 5.4: The ratio of total power output to the squared input excitation displacement amplitude in the frequency range of 0-30 Hz.**

Time domain simulation allows for the response of the vehicle to the real road displacement profile input excitation to be evaluated for the system. Based on the Equation (5.8), five equations can be rearranged in the form shown in Equation (5.10). Each of the equations can be represented by the sum blocks in Figure 5.5, where all the branches can then be joined together to form a loop. The road profile excitation displacement inputs are then applied into two wheels where the rear wheel has a time delay in relation to the front wheel as the wheels travelling on the same road profile in different times. The road profile excitation displacement can be in forms of a sinusoidal wave signal, a step signal or random signals. Given the road profile excitation displacement input, the output voltage, harvested power and displacement of vehicle body and wheels can be simulated using Matlab Simulink code shown in Figure 5.5.

$$\left\{ \begin{aligned}
& \ddot{x}_f \cdot (-m_s - m_{1f}) = \dot{x}_f \cdot (c_{1f} + c_{2f} + c_L) + x_f \cdot (k_{1f} + k_{2f}) - m_s \cdot \ddot{x} + \dot{x} \cdot (-c_{2f} - c_L) + x \cdot (-k_{2f}) + a \cdot \ddot{\theta} \cdot m_s + \dot{\theta} \cdot (a \cdot c_{2f} + a \cdot c_L) \\
& + a \cdot k_{2f} \cdot \theta + U_f \cdot \left( \frac{Bl}{R_{ex}} \cdot \frac{j \cdot r_g}{r} \right) + \dot{z}_f \cdot (-c_{1f}) + z_f \cdot (-k_{1f}) \\
& \ddot{x}_r \cdot (-m_s - m_{1r}) = \dot{x}_r \cdot (c_{1r} + c_{2r} + c_L) + x_r \cdot (k_{1r} + k_{2r}) + \ddot{x} \cdot (-m_s) + \dot{x} \cdot (-c_{2r} - c_L) + x \cdot (-k_{2r}) + \ddot{\theta} \cdot (-b \cdot m_s) \\
& + \dot{\theta} \cdot (-b \cdot c_{2r} - b \cdot c_L) + \theta \cdot (-b \cdot k_{2r}) + U_r \cdot \left( \frac{Bl}{R_{ex}} \cdot \frac{j \cdot r_g}{r} \right) + \dot{z}_r \cdot (-c_{1r}) + z_r \cdot (-k_{1r}) \\
& \ddot{x} \cdot (-2m_s - m_2) = \dot{x} \cdot (c_{2f} + c_{2r} + 2c_L) + x \cdot (k_{2f} + k_{2r}) + \ddot{x}_f \cdot (-m_s) + \dot{x}_f \cdot (-c_{2f} - c_L) + x_f \cdot (-k_{2f}) + \ddot{x}_r \cdot (-m_s) \\
& + \dot{x}_r \cdot (-c_{2r} - c_L) + x_r \cdot (-k_{2r}) + \ddot{\theta} \cdot (-a \cdot m_s + b \cdot m_s) + \dot{\theta} \cdot (-a \cdot c_{2f} + b \cdot c_{2r} - a \cdot c_L + b \cdot c_L) + \theta \cdot (-a \cdot k_{2f} + b \cdot k_{2r}) \\
& + U_f \cdot \left( -\frac{Bl}{R_{ex}} \cdot \frac{j \cdot r_g}{r} \right) + U_r \cdot \left( -\frac{Bl}{R_{ex}} \cdot \frac{j \cdot r_g}{r} \right) \\
& \ddot{\theta} \cdot (-a^2 \cdot m_s - b^2 \cdot m_s - J) = \ddot{x}_f \cdot (a \cdot m_s) + \dot{x}_f \cdot (a \cdot c_{2f} + a \cdot c_L) + x_f \cdot (a \cdot k_{2f}) + \ddot{x}_r \cdot (-b \cdot m_s) + \dot{x}_r \cdot (-b \cdot c_{2r} - b \cdot c_L) \\
& + x_r \cdot (-b \cdot k_{2r}) + \ddot{x} \cdot (-a \cdot m_s + b \cdot m_s) + \dot{x} \cdot (-a \cdot c_{2f} + b \cdot c_{2r} - a \cdot c_L + b \cdot c_L) + x \cdot (-a \cdot k_{2f} + b \cdot k_{2r}) \\
& + \dot{\theta} \cdot (a^2 \cdot c_{2f} + b^2 \cdot c_{2r} + a^2 \cdot c_L + b^2 \cdot c_L) + \theta \cdot (a^2 \cdot k_{2f} + b^2 \cdot k_{2r}) + U_f \cdot \left( \frac{a \cdot Bl}{R_{ex}} \cdot \frac{j \cdot r_g}{r} \right) + U_r \cdot \left( -\frac{b \cdot Bl}{R_{ex}} \cdot \frac{j \cdot r_g}{r} \right) \\
& \dot{U}_f = \dot{x}_f \left( \frac{k_e \cdot j \cdot R_{ex}}{L \cdot r} \right) + \dot{x} \left( -\frac{k_e \cdot j \cdot R_{ex}}{L \cdot r} \right) + \dot{\theta} \left( \frac{a \cdot k_e \cdot j \cdot R_{ex}}{L \cdot r} \right) + U_f \left( -\frac{R_{in} + R_{ex}}{L} \right) \\
& \dot{U}_r = \dot{x}_r \left( \frac{k_e \cdot j \cdot R_{ex}}{L \cdot r} \right) + \dot{x} \left( -\frac{k_e \cdot j \cdot R_{ex}}{L \cdot r} \right) + \dot{\theta} \left( -\frac{b \cdot k_e \cdot j \cdot R_{ex}}{L \cdot r} \right) + U_r \left( -\frac{R_{in} + R_{ex}}{L} \right)
\end{aligned} \right. \tag{5.10}$$

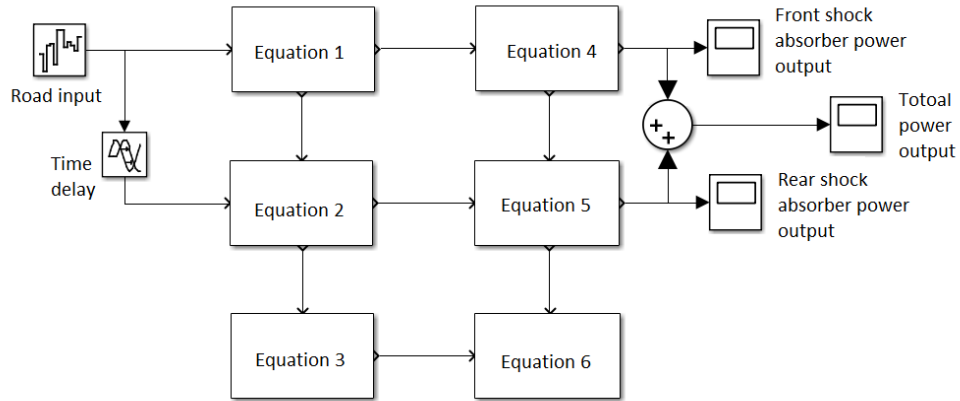


**Figure 5.5: Time domain simulation model of the half vehicle suspension system integrated with the indirect-drive RSA.**

## 5.3 Taguchi method

In order to conduct the evaluation in a systematic way, the Taguchi method is applied to analyse the performance sensitivity of the half vehicle suspension system integrated with the indirect-drive RSA to parameter variations. The Taguchi method aims at improving the performance of a product or a process in a systematic approach [153]. 7 controllable parameters have been chosen for the half vehicle suspension system model and each of the parameters has been set to have 2 levels of variations. By performing 8 system tests with the pre-set combinations of parameter levels, the effects of each parameter on the system target can be obtained and compared. For the half vehicle suspension system with the indirect-drive RSAs, the targets under evaluation are the peak output power ratio from the front and rear indirect-drive RSA and the energy harvesting bandwidth. The masses of the system are not selected as control variables for optimization because they have large influences on the other vehicle performance. Shown in Table 5.1 are the 7 controllable parameters with their minimum values and maximum values set as Level 1 and Level 2 values of their variations. It is assumed that the same regenerative shock absorbers are installed on the front and rear suspension systems. The suspension stiffness has two levels of 15000 N/m and 30000 N/m, the suspension damping has two levels of 500 Ns/m and 1500 Ns/m, tyre stiffness has two levels of 100000 N/m and 200000 N/m, tyre damping has two levels of 100 Ns/m and 300 Ns/m. The generator constant defines the energy generating ability of the generator and has two levels of 0.01 and 0.1, the coil resistance has two levels of 10  $\Omega$  and 200  $\Omega$  in correspondence with the generator constants. The gear ratio determines the rotational speed amplifying ability of the gear box and has two levels: 10 and 30. Taguchi matrix is shown in

Table 5.2. Based on the rules of the Taguchi method, the pre-defined combinations of parameters with different levels are presented to form 8 test run systems.

**Table 5.1: Parameters of Taguchi method in two levels.**

|                    |   |                      | <b>Level 1<br/>(min)</b> | <b>Level 2<br/>(max)</b> |
|--------------------|---|----------------------|--------------------------|--------------------------|
| <b>Parameter 1</b> | <b>Suspension stiffness(N/m)</b>              | $k_{2f}$<br>$k_{2r}$ | 15000                    | 30000                    |
| <b>Parameter 2</b> | <b>Suspension damping (Ns/m)</b>              | $c_{2f}$<br>$c_{2r}$ | 500                      | 1500                     |
| <b>Parameter 3</b> | <b>Tyre stiffness (N/m)</b>                   | $k_{1f}$<br>$k_{1r}$ | 100000                   | 200000                   |
| <b>Parameter 4</b> | <b>Generator constant<br/>(Dimensionless)</b> | $k_e$                | 0.01                     | 0.1                      |
| <b>Parameter 5</b> | <b>Tyre damping (Ns/m)</b>                    | $c_{1f}$<br>$c_{1r}$ | 100                      | 300                      |
| <b>Parameter 6</b> | <b>Coil resistance (<math>\Omega</math>)</b>  | $R_e$<br>$R$         | 10                       | 200                      |
| <b>Parameter 7</b> | <b>Gear ratio (Dimensionless)</b>             | $j$                  | 10                       | 30                       |



**Table 5.2: Taguchi matrix with 8 test run systems.**

|               | <b>Parameter 1</b>                | <b>Parameter 2</b>               | <b>Parameter 3</b>          | <b>Parameter 4</b>                        | <b>Parameter 5</b>         | <b>Parameter 6</b>                           | <b>Parameter 7</b>                |
|---------------|-----------------------------------|----------------------------------|-----------------------------|---|----------------------------|--|-----------------------------------|
| <b>System</b> | <b>Suspension stiffness (N/m)</b> | <b>Suspension damping (Ns/m)</b> | <b>Tyre stiffness (N/m)</b> | <b>Generator constant (Dimensionless)</b> | <b>Tyre damping (Ns/m)</b> | <b>Coil resistance (<math>\Omega</math>)</b> | <b>Gear ratio (Dimensionless)</b> |
| 1             | 15000                             | 500                              | 100000                      | 0.01                                      | 100                        | 10   | 10                                |
| 2             | 15000                             | 500                              | 100000                      | 0.1                                       | 300                        | 200  | 30                                |
| 3             | 15000                             | 1500                             | 200000                      | 0.01                                      | 100                        | 200  | 30                                |
| 4             | 15000                             | 1500                             | 200000                      | 0.1                                       | 300                        | 10   | 10                                |
| 5             | 30000                             | 500                              | 200000                      | 0.01                                      | 300                        | 10   | 30                                |
| 6             | 30000                             | 500                              | 200000                      | 0.1                                       | 100                        | 200  | 10                                |
| 7             | 30000                             | 1500                             | 100000                      | 0.01                                      | 300                        | 200  | 10                                |
| 8             | 30000                             | 1500                             | 100000                      | 0.1                                       | 100                        | 10   | 30                                |

Based on the 8 test run systems in Table 5.2, the ratio of the power output to the squared displacement input excitation amplitude can be calculated and then be plotted in the frequency range of 0 to 30 Hz for each test run system, as shown in Figure 5.6. It can be seen that different resonant frequencies are presented by different test run systems, which is mainly due to the variation of the tyre stiffness and the suspension stiffness. The results presented in Table 5.3 show the values of the peak power output ratio and energy harvesting bandwidth for all test run systems. It can be seen from Table 5.3 that System 8 presents that highest peak power output ratio of  $970000\text{W/m}^2$ , which is nearly 4 times larger than that of the original system or System 1. System 7 presents the widest bandwidth of 6.1Hz, however, the peak power output ratio is only  $67.8\text{W/m}^2$  ranked at the least. Even though System 8 does not provide the widest bandwidth, its bandwidth is only slightly narrower than that of System 7. Thus System 8 can be considered to give the best overall results. According to Table 5.2, System 8 has the suspension stiffness, suspension damping, tyre stiffness, generator constant, tyre damping, coil resistance and gear ratio of 30000 N/m, 1500 Ns/m, 100000 N/m, 0.1, 100 Ns/m,  $10\ \Omega$  and 30.

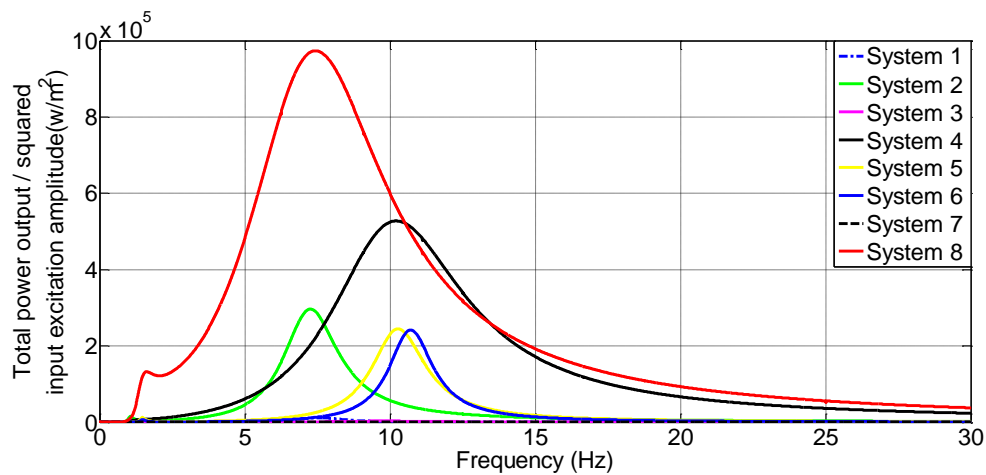


**Figure 5.6: The ratio of the total power output to the squared displacement input excitation amplitude for 8 systems.**

**Table 5.3: The results of the total power output ratio and energy harvesting bandwidth for the 8 test run systems.**

|               | <b>Peak power output ratio (Dimensionless)</b> | <b>Harvesting bandwidth (Hz)</b> |
|---------------|--|----------------------------------|
| <b>System</b> | <b>Nominal (TARGET)</b>                        | <b>Nominal (TARGET)</b>          |
| 1             | 12200  | 1.85                             |
| 2             | 296000   | 2.35                             |
| 3             | 3247   | 4.35                             |
| 4             | 527000   | 5.6                              |
| 5             | 244700   | 2.25                             |
| 6             | 241000   | 1.9                              |
| 7             | 67.8   | 6.1                              |
| 8             | 970000   | 5.6                              |

The total power output ratio and the bandwidth of System 8 are assessed separately to reveal the effect of each parameter at the peak frequencies. The calculation details are presented in Table 5.4. As shown in Table 5.4, for each parameter, the average value of the test results in Level 1 among the 8 tests are listed in the line “Average (1)”, the average value of the test results in Level 2 among the 8 tests are listed in the line “Average (2)”. The results in the line “Effect” are calculated by subtraction of the average values of the line “Average (2)” from those of the line “Average (1)”. The results in the line “Effect” reflect the changes of the target results due to the individual parameters switching from Level 1 to Level 2. A positive value of the effect indicates that the increase of the individual parameter from Level 1 to Level 2 yields the increase of the target results, and the negative value of the effect indicates that the target result decreases with the individual parameter increasing from Level 1 to Level

2. The effects of individual parameters are shown in Table 5.5 and Table 5.6 for the peak power output ratio and energy harvesting bandwidth, respectively.

**Table 5.4: The detailed Taguchi calculation**

| <b>INPUT PARAMETERS</b>                         |                 |                 |                 |                 |                 |                 |                 | <b>Total power output ratio</b> | <b>Energy harvesting bandwidth</b> |
|---|-----------------|-----------------|-----------------|-----------------|-----------------|-----------------|-----------------|---------------------------------|------------------------------------|
| <b>SYSTEM</b>                                   | <b>1-A</b>      | <b>2-B</b>      | <b>3-AxB</b>    | <b>4-C</b>      | <b>5-AxC</b>    | <b>6-BxC</b>    | <b>7-D</b>      | <b>Nominal (Dimensionless)</b>  | <b>Nominal (Hz)</b>                |
| <b>1</b>  | <b>1</b>        | <b>1</b>        | <b>1</b>        | <b>1</b>        | <b>1</b>        | <b>1</b>        | <b>1</b>        | <b>12200</b>                    | <b>1.85</b>                        |
| <b>2</b>  | <b>1</b>        | <b>1</b>        | <b>1</b>        | <b>2</b>        | <b>2</b>        | <b>2</b>        | <b>2</b>        | <b>296000</b>                   | <b>2.35</b>                        |
| <b>3</b>  | <b>1</b>        | <b>2</b>        | <b>2</b>        | <b>1</b>        | <b>1</b>        | <b>2</b>        | <b>2</b>        | <b>3247</b>                     | <b>4.35</b>                        |
| <b>4</b>  | <b>1</b>        | <b>2</b>        | <b>2</b>        | <b>2</b>        | <b>2</b>        | <b>1</b>        | <b>1</b>        | <b>527000</b>                   | <b>5.6</b>                         |
| <b>5</b>  | <b>2</b>        | <b>1</b>        | <b>2</b>        | <b>1</b>        | <b>2</b>        | <b>1</b>        | <b>2</b>        | <b>244700</b>                   | <b>2.25</b>                        |
| <b>6</b>  | <b>2</b>        | <b>1</b>        | <b>2</b>        | <b>2</b>        | <b>1</b>        | <b>2</b>        | <b>1</b>        | <b>241000</b>                   | <b>1.9</b>                         |
| <b>7</b>  | <b>2</b>        | <b>2</b>        | <b>1</b>        | <b>1</b>        | <b>2</b>        | <b>2</b>        | <b>1</b>        | <b>67.8</b>                     | <b>6.1</b>                         |
| <b>8</b>  | <b>2</b>        | <b>2</b>        | <b>1</b>        | <b>2</b>        | <b>1</b>        | <b>1</b>        | <b>2</b>        | <b>970000</b>                   | <b>5.6</b>                         |
| <b>AVERAGE (1)- Total power output ratio</b>    | <b>209611.8</b> | <b>198475</b>   | <b>319567</b>   | <b>65053.7</b>  | <b>306611.8</b> | <b>438475</b>   | <b>195067</b>   |                                 |                                    |
| <b>AVERAGE (2)- Total power output ratio</b>    | <b>363942</b>   | <b>375078.7</b> | <b>253986.8</b> | <b>508500</b>   | <b>266942</b>   | <b>135078.7</b> | <b>378486.8</b> |                                 |                                    |
| <b>EFFECT-Total power output ratio</b>          | <b>154330.2</b> | <b>176603.7</b> | <b>-65580.2</b> | <b>443446.3</b> | <b>-39669.8</b> | <b>-303396</b>  | <b>183419.8</b> |                                 |                                    |
|   |                 |                 |                 |                 |                 |                 |                 |                                 |                                    |
| <b>AVERAGE (1)- Energy harvesting bandwidth</b> | <b>3.5375</b>   | <b>2.0875</b>   | <b>3.975</b>    | <b>3.6375</b>   | <b>3.425</b>    | <b>3.825</b>    | <b>3.8625</b>   |                                 |                                    |
| <b>AVERAGE (2)-</b>                             | <b>3.9625</b>   | <b>5.4125</b>   | <b>3.525</b>    | <b>3.8625</b>   | <b>4.075</b>    | <b>3.675</b>    | <b>3.6375</b>   |                                 |                                    |

|   |              |              |              |              |             |              |               |  |  |
|---|--------------|--------------|--------------|--------------|-------------|--------------|---------------|--|--|
| <b>Energy harvesting bandwidth</b>        |              |              |              |              |             |              |               |  |  |
| <b>EFFECT-Energy harvesting bandwidth</b> | <b>0.425</b> | <b>3.325</b> | <b>-0.45</b> | <b>0.225</b> | <b>0.65</b> | <b>-0.15</b> | <b>-0.225</b> |  |  |

As shown in Table 5.5, the generator constant  $k_e$  has the largest effect on the power output ratio, which suggests that the powerful generators should be prioritized to improve the peak power output. Coil resistance has the second largest effect on the power output ratio. The matched coil resistance can increase the peak power output. Therefore, a generator with large generator constant and a matched coil resistance would lead to the significant improvement of the peak power output ratio. Parameter 5 – the tyre damping has the least effect on the peak power output ratio.

As shown in Table 5.6, compared with the other parameters, the vehicle front and rear suspension damping contribute to the largest improvement of the energy harvesting bandwidth.

The parameter effects are compared in Figure 5.7. It can be seen that changing tyre damping and gear ratio would have the opposite effect on total power output ratio and energy harvesting bandwidth. This means that for these two parameters, a compromise has to be reached to achieve a high peak power output ratio with a reasonably broad harvesting bandwidth.

Table 5.5: The effect of each parameter on the peak power output.

|             |                                    |                      | Total power output ratio |           |               |
|-------------|------------------------------------|----------------------|--------------------------|-----------|---------------|
|             |                                    |                      | Level 1                  | Level 2   | Effect        |
| Parameter 1 | Suspension stiffness (N/m)         | $k_{2f}$<br>$k_{2r}$ | 209611.75                | 363941.95 | 154330.2      |
| Parameter 2 | Suspension damping (Ns/m)          | $c_{2f}$<br>$c_{2r}$ | 198475                   | 375078.7  | 176603.7      |
| Parameter 3 | Tyre stiffness (N/m)               | $k_{1f}$<br>$k_{1r}$ | 319566.95                | 253986.75 | -65580.2      |
| Parameter 4 | Generator constant (Dimensionless) | $k_e$                | 65053.7                  | 508500    | 443446.3      |
| Parameter 5 | Tyre damping (Ns/m)                | $c_{1f}$<br>$c_{1r}$ | 306611.75                | 266941.95 | -39669.8      |
| Parameter 6 | Coil resistance ( $\Omega$ )       | $R_{in}$<br>$R_{ex}$ | 438475                   | 135078.7  | -<br>303396.3 |
| Parameter 7 | Gear ratio (Dimensionless)         | $j$                  | 195066.95                | 378486.75 | 183419.8      |

Table 5.6: The effect of each parameter on the energy harvesting bandwidth.

|             |                                    |                      | Bandwidth |         |            |
|-------------|------------------------------------|----------------------|-----------|---------|------------|
|             |                                    |                      | Level 1   | Level 2 | Effect     |
| Parameter 1 | Suspension stiffness (N/m)         | $k_{2f}$<br>$k_{2r}$ | 3.5375    | 3.9625  | 0.425      |
| Parameter 2 | Suspension damping (Ns/m)          | $c_{2f}$<br>$c_{2r}$ | 2.0875    | 5.4125  | 3.325      |
| Parameter 3 | Tyre stiffness (N/m)               | $k_{1f}$<br>$k_{1r}$ | 3.975     | 3.525   | -0.45      |
| Parameter 4 | Generator constant (Dimensionless) | $k_e$                | 3.6375    | 3.8625  | 0.225      |
| Parameter 5 | Tyre damping (Ns/m)                | $c_{1f}$<br>$c_{1r}$ | 3.425     | 4.075   | 0.65       |
| Parameter 6 | Coil resistance ( $\Omega$ )       | $R_{in}$<br>$R_{ex}$ | 3.825     | 3.675   | -0.15      |
| Parameter 7 | Gear ratio (Dimensionless)         | $j$                  | 3.8625    | 3.6375  | -<br>0.225 |



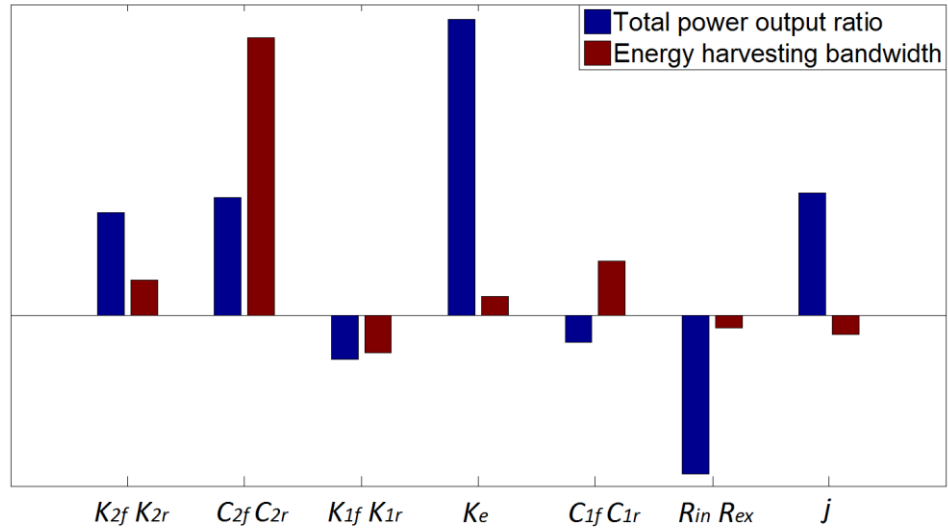


**Figure 5.7: The effect of each parameter on the total power output ratio and the energy harvesting bandwidth.**

## 5.4 Optimization

Even though System 8 has the best overall energy harvesting performance, its harvesting performance can be further enhanced by tuning some of the parameters. In order to develop a system where the energy can be efficiently harvested with relatively broad bandwidth, when a parameter is chosen to increase the energy harvesting bandwidth, its negative effect on the peak power output ratio needs to be minimized. It can be seen from Figure 5.8, suspension stiffness, suspension damping, tyre stiffness and generator constant have same effect trends on both the peak power output ratio and energy harvesting bandwidth. However, the tyre damping, coil and external resistance and gear ratio present the different effect trends. The decrease of the tyre damping and the increase of the generator constant have the same effects

on the peak power output ratio, which increase the peak power output ratio. The increases of the tyre damping and the generator constant have the same effects on the energy harvesting bandwidth, which increases the energy harvesting bandwidth. The greatest improvements of the peak power output ratio and harvesting bandwidth are brought by increasing the generator constant and suspension damping, which in addition, can also broaden the energy harvesting bandwidth. Therefore, tuning of the suspension damping and generator constant needs to be prioritized in the optimization. The increase of the tyre damping can also broaden the energy harvesting bandwidth however at the same time, it decreases the power output ratio. Since the energy harvesting bandwidth of System 8 still needs improvement, it is worthwhile sacrificing the peak power output ratio for a much broader bandwidth.

The optimization is based on System 8 which presents the highest power output ratio with the second broadest harvesting bandwidth amongst all the proposed test run systems. In Table 5.7, three parameters are to be optimized: suspension damping coefficients  $c_{2f}$  and  $c_{2r}$ , tyre damping  $c_{1f}$  and  $c_{1r}$  and generator constant  $k_e$ . The increase of the suspension damping from 1500 Ns/m to 2000 Ns/m and generator constant from 0.1 to 0.2 can result in the increase of both peak power output ratio and energy harvesting bandwidth. The increase of the tyre damping from 100 Ns/m to 120 Ns/m can increase the energy harvesting bandwidth with a minor drop on the peak power output ratio. The results in the frequency domain are shown in Figure 5.8. The energy harvesting bandwidth of the optimized System 8 nearly doubles that of the original System 8. It can be also seen that when the excitation frequency is larger than 1.5 Hz, the peak power output ratio of the optimized System 8 is higher than that of the original System 8 as well. The resonant natural frequency of the optimized System 8 is shifted to a slightly lower frequency.

**Table 5.7: The selected parameters in the original System 8 and the optimized System 8**

| Parameters                           | Effect trends on the peak output power ratio and energy harvesting bandwidth | System 8 | Optimized System 8 |
|--------------------------------------|--|----------|--------------------|
| Suspension damping<br>$c_{2f}c_{2r}$ | Same   | 1500     | 2000               |
| Tyre damping $c_{1f}, c_{1r}$        | Opposite   | 100      | 120                |
| Generator constant $k_e$             | Same   | 0.1      | 0.2                |

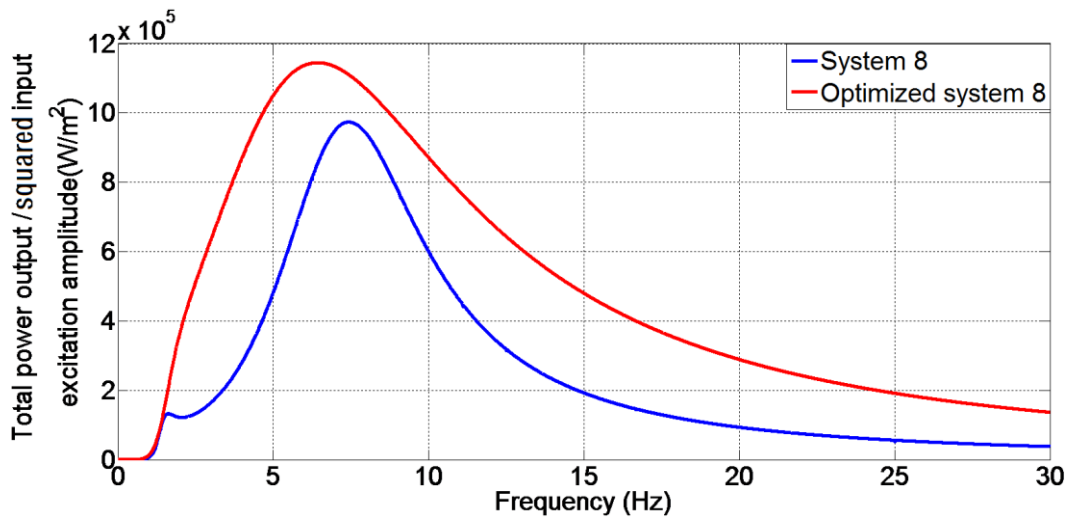


**Figure 5.8: The ratio of the total power output to the squared input displacement excitation amplitude for System 8 and the optimized System 8 in the frequency of 0-30 Hz.**

The application of the road displacement profile inputs from the road classification in the above simulation allows the real road conditions to be mimicked for the evaluation of the optimized System 8. The road profiles can be identified as Class A B C D and E in ISO 8606, representing the road conditions that are very good, good, average, poor and very poor. The

road profiles can then be modelled through the shaping filters based on the PSD of the road [155]. The vertical displacement of the road excitation  $z(t)$  can be expressed in Equation (5.11).

$$\frac{d}{dt} z(t) = -\alpha V z(t) + \omega(t) \quad (5.11)$$

where  $V$  is the vehicle travelling speed,  $\alpha$  is dependent on the road type and given in Table 5.8,  $\omega(t)$  is the white noise signal with the spectral density  $\Psi_\omega$ , which is given in Equation (5.12).

$$\Psi_\omega = 2\alpha V \sigma^2 \quad (5.12)$$

**Table 5.8: The road roughness of the different road class.**

| Road Class | $\sigma$             | $\alpha$ |
|------------|----------------------|----------|
| A          | $2 \times 10^{-3}$   | 0.127    |
| B          | $4 \times 10^{-3}$   | 0.127    |
| C          | $8 \times 10^{-3}$   | 0.127    |
| D          | $1.6 \times 10^{-2}$ | 0.127    |
| E          | $3.2 \times 10^{-2}$ | 0.127    |

It is assumed that the vehicle integrated with the indirect-drive RSA is travelling at 5.556 m/s (20 km/h) on a random road surface classified as Class A, C and E, whose time domain excitation displacement curves are plotted for 10 seconds in Figure 5.9. It can be seen that within the same time span, the road excitation displacement amplitude increases with the road class level.

The instantaneous power output of the indirect-drive RSAs of the front and rear suspensions are shown in Figure 5.10. It can be seen that the optimized System 8 presents higher peak power output than the original System 8 for the road profiles of Class A, C and E. The maximum displacement of the road excitation can be identified to occur at 10s in Figure 5.9. However, it can be seen in Figure 5.10, the highest road excitation displacement does not guarantee the highest power output. This is because there is a phase difference between the front and rear wheels and the power output performance of the shock absorbers is closely related to the resonant frequency and mode of the half vehicle suspension system, therefore a broader energy harvesting bandwidth can also improve its energy harvesting performance. In Figure 5.10, it also shows that at any arbitrary time, the optimized System 8 has higher power output than the original System 8 due to the broader energy harvesting bandwidth of the optimized System 8. The input road displacement profile is essentially based on the white noise random signal with varying frequencies. The broader harvesting bandwidth can result in the more possibility of achieving high power output.

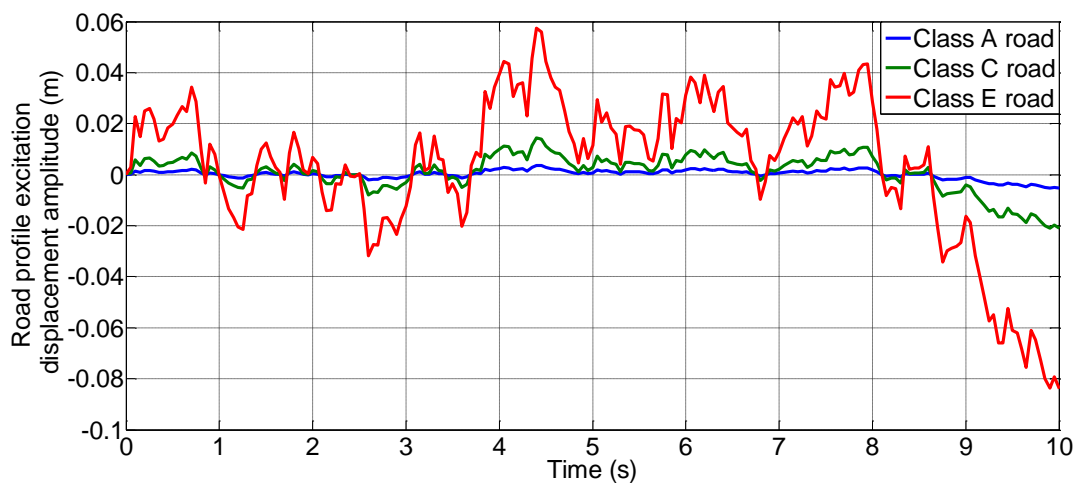


**Figure 5.9: The modelling of the road profiles of Classes A, C and E in the time domain when the vehicle is travelling at 5.556 m/s (20 km/h).**

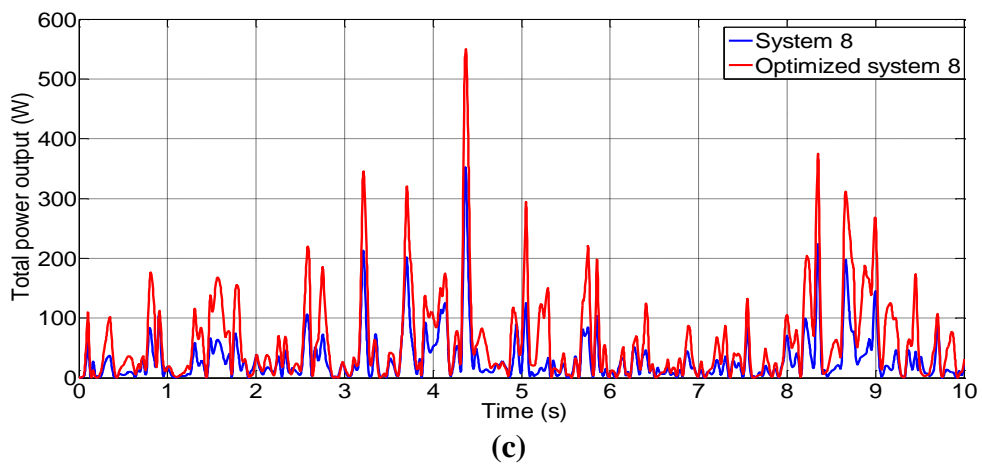
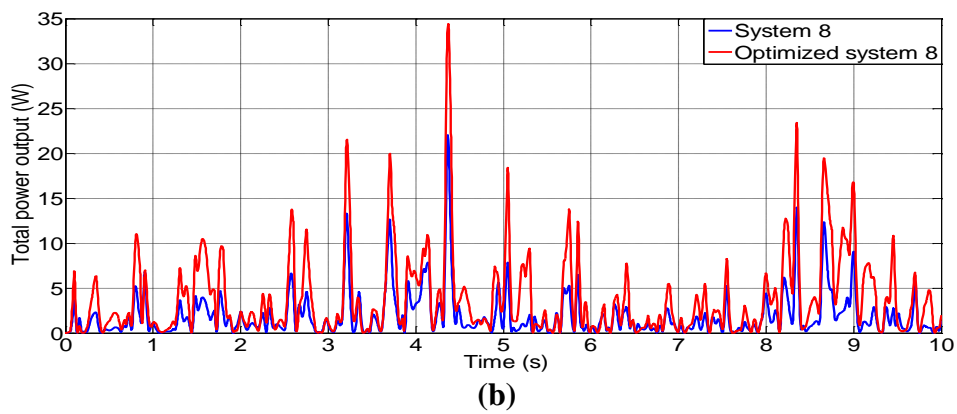
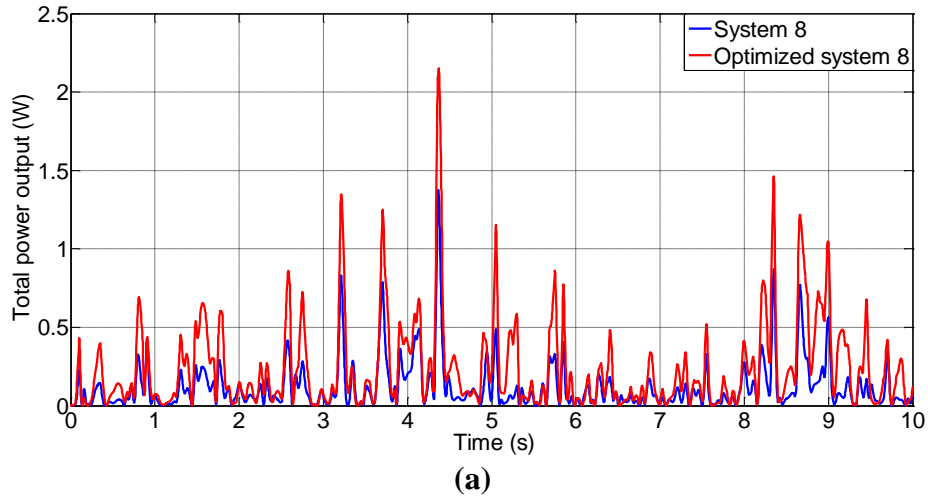


**Figure 5.10: The total power output of the original System 8 and the optimized System 8 at a vehicle speed of 20 km/h on the road profiles of (a) Class A, (b) Class C and (c) Class E.**

## 5.5 Conclusion

In this chapter, the mathematical model of the half vehicle suspension system installed with the two indirect-drive RSAs has been developed in both frequency domain and time domain. Taguchi method (L8) has been introduced for optimization of the system to enhance the energy harvesting ability, which involves increasing the peak power output ratio of the system and broadening the energy harvesting bandwidth. Totally 7 parameters are chosen from the half vehicle suspension system with the minimum value and maximum value representing Level 1 and Level 2. 8 combinations of these 7 parameters with different levels are developed to form 8 test run systems. It is found that System 8 has the best overall performance for its largest effect on the peak power output ratio and the second largest effect on the harvesting bandwidth.

Based on the results of the Taguchi method, the effects of each parameter on the peak power output ratio and energy harvesting bandwidth have been quantified and compared. Compromises have been reached to broaden the energy harvesting bandwidth of the original System 8 while minimizing the negative effects on decreasing the peak power output ratio. The suspension damping coefficients of  $c_{2f}$  and  $c_{2r}$ , tyre damping  $c_{1f}$  and  $c_{1r}$  and generator constant  $k_e$  have been prioritized to be changed for the optimization. It is found that in the

frequency range of 1-30Hz, the optimization of these three parameters can double the energy harvesting bandwidth and increase the peak power output ratio.

In order to evaluate the energy generating ability of the optimized half vehicle suspension system with the indirect-drive RSAs, different road displacement input profiles from the road classification have been developed using white noise signal. Road Class A C and E have been applied as the road displacement excitation input into the time domain simulation model. When the vehicle is travelling at 20 km/h, the results indicated that both the original System 8 and optimized System 8 can harvest more power as road roughness increases. It is also concluded the optimized System 8 has a better overall performance than the original System 8 on the road conditions of very good, average and very poor. The largest peak power output ratio does not necessarily occur at the largest road vertical displacement excitation, since the resonant frequency, mode and phase difference of the front and rear wheels can greatly affect the dynamic response of the half vehicle suspension system. Therefore, it is found the optimized System 8 is more advantageous in achieving high peak power output ratio and more suitable for energy harvesting even at off-resonant frequencies than the original System 8.



## Chapter 6

### *7 degrees of freedom full vehicle suspension system model*

*In this chapter, a 7 degrees of freedom full vehicle suspension system integrated with the indirect-drive regenerative shock absorber has been modeled based on the same conventional passenger vehicle from Chapter 4 and Chapter 5 for system comparison. In the simulation model, the indirect-drive regenerative shock absorbers are installed in parallel with the traditional vehicle suspension system. The ratio of the harvested power to the squared road excitation displacement amplitude are plotted in the frequency domain. The comparison of the results in terms of quarter vehicle, half vehicle and full vehicle suspension system are conducted to illustrate their advantages and disadvantages. The time domain simulation model has also been developed based on the governing equations, allowing for the real road profile data to be directly applied into each individual wheel in the simulation model.*

## 6.1 Introduction

The energy harvesting from the suspension system has attracted researcher's attentions for its potentials in achieving a greener transportation. Many off-road vehicles have potentials to be integrated with the regenerative shock absorber technologies onboard due to their large shock absorber displacement on the rough terrain. Most researches have investigated the energy harvesting performance of the shock absorber based on the quarter vehicle suspension system to evaluate its response under the single excitation on the wheel and half vehicle suspension system to consider its pitching motion due to the road elevation in the longitudinal direction. However, because of the randomness of the wheel displacement excitation especially on the off road, a full vehicle suspension system involving 7 degrees of freedom will need to be considered since the rolling motion of the vehicle body may also affects its energy harvesting performance and vehicle dynamics.

## 6.2 The modelling of the full vehicle suspension system integrated with the indirect-drive regenerative shock absorbers.

As shown in Figure 6.1, the full vehicle suspension system consists of 5 mass oscillators, namely the vehicle body and four-wheel assemblies. Damping and the stiffness coefficients of both the tyres and the suspensions are also included and applied in the full vehicle model. It is assumed that the vehicle has the same wheels and the suspension systems installed. The parameters of the full vehicle suspension system are shown in Table 6.1. The road excitation displacement amplitudes applied on the four wheels and tyres of the vehicle are denoted as  $y_{tfl}$ ,  $y_{tfr}$ ,  $y_{trr}$ ,  $y_{trl}$ ; the vertical displacement of the vehicle body is denoted as  $y_b$ ; the pitching angle and the rolling angle of the vehicle body are represented by  $\alpha$  and  $\beta$ , respectively.

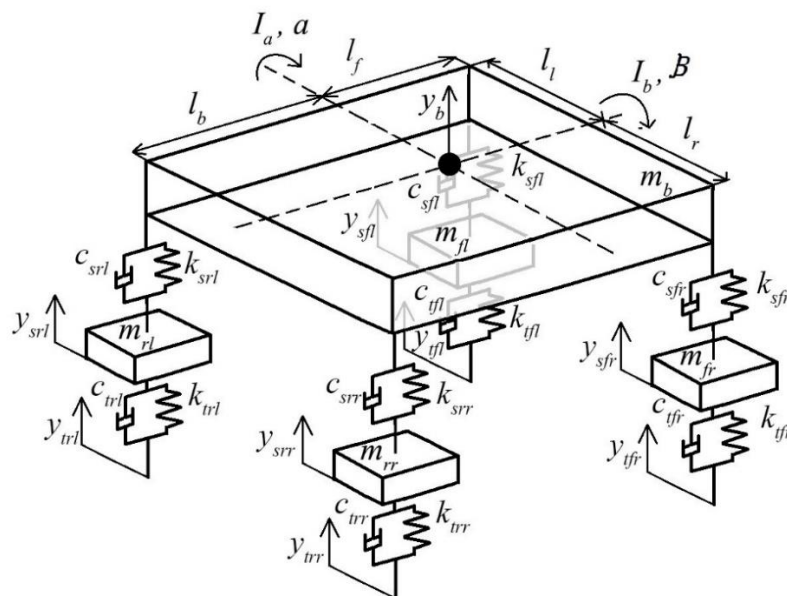


**Figure 6.1: The schematic of the 7 DOF full vehicle suspension system.**

**Table 6.1: The parameters of the 7 DOF full vehicle suspensions system.**

|   |          |      |
|---|----------|------|
| Vehicle body mass (kg)  | $m_b$    | 40   |
| Distance between the COG to the front axis (m)                                | $l_f$    | 1.6  |
| Distance between the COG to the rear axis (m)                                 | $l_b$    | 1.6  |
| Vertical distance between the COG to the centers of the left wheel-tyres (m)  | $l_l$    | 0.7  |
| Vertical distance between the COG to the centers of the right wheel-tyres (m) | $l_r$    | 0.7  |
| Pitching moment of inertia ( $\text{kg}\cdot\text{m}^2$ )                     | $I_a$    | 1500 |
| Rolling moment of inertia ( $\text{kg}\cdot\text{m}^2$ )                      | $I_b$    | 1500 |
| Mass of front right wheel assembly (kg)                                       | $m_{fr}$ | 40   |

|  |           |        |
|--|-----------|--------|
| Mass of front left wheel assembly (kg)     | $m_{fl}$  | 40     |
| Mass of the rear left wheel assembly (kg)  | $m_{rl}$  | 40     |
| Mass of the rear right wheel assembly (kg) | $m_{rr}$  | 40     |
| Front right wheel-tyre stiffness (N/m)     | $k_{tfr}$ | 130000 |
| Front left wheel-tyre stiffness (N/m)      | $k_{tfl}$ | 130000 |
| Rear left wheel tyre stiffness (N/m)       | $k_{trl}$ | 130000 |
| Rear right wheel tyre stiffness (N/m)      | $k_{trr}$ | 130000 |
| Front right suspension stiffness (N/m)     | $K_{sfr}$ | 26000  |
| Front left suspension stiffness (N/m)      | $K_{sfl}$ | 26000  |
| Rear left suspension stiffness (N/m)       | $K_{srl}$ | 26000  |
| Rear right suspension stiffness (N/m)      | $K_{srr}$ | 26000  |
| Front right wheel-tyre damping coefficient | $C_{tfr}$ | 264.7  |

|   |           |       |
|---|-----------|-------|
| (Ns/m)  |           |       |
| Front left wheel-tyre<br>damping coefficient<br>(Ns/m)  | $C_{flt}$ | 264.7 |
| Rear right wheel-tyre<br>damping coefficient<br>(Ns/m)  | $C_{trr}$ | 264.7 |
| Rear left wheel-tyre<br>damping coefficient<br>(Ns/m)   | $C_{trl}$ | 264.7 |
| Front right suspension<br>damping coefficient<br>(Ns/m) | $C_{sfr}$ | 520   |
| Front left suspension<br>damping coefficient<br>(Ns/m)  | $C_{sfl}$ | 520   |
| Rear right suspension<br>damping coefficient<br>(Ns/m)  | $C_{srr}$ | 520   |
| Rear left suspension<br>damping coefficient<br>(Ns/m)   | $C_{srl}$ | 520   |

The regenerative shock absorbers installed between the vehicle body and the wheel assembly are the indirect-drive arm teeth RSA, whose parameters are presented in Table 4.3. The same regenerative shock absorbers are integrated in the quarter vehicle, half vehicle and full vehicle suspension systems, respectively, therefore the difference in power output due to different platforms can be compared. Based on the Lagrange's equation, the individual forces can be expressed as:

$$\left\{ \begin{array}{l} F_{Gi} = \frac{d}{dt} \frac{\partial T}{\partial \dot{x}_i} - \frac{\partial T}{\partial x_i} \\ F_{Wi} = \frac{\partial W}{\partial \dot{x}_i} \\ F_{Ki} = \frac{\partial V}{\partial x_i} \end{array} \right. \quad (6.1)$$

where  $F_{Gi} + F_{Wi} + F_{Ki} = 0$ ;  $\dot{x}_i$  and  $x_i$  are the velocity and displacement of the  $i^{\text{th}}$  oscillator;  $T$ ,  $W$  and  $V$  are the total kinetic energy, damping energy and spring potential energy, respectively, which are given by:

$$\begin{aligned}
T &= \frac{1}{2} \cdot m_b \cdot \dot{y}_b^2 + \frac{1}{2} \cdot m_{fr} \cdot \dot{y}_{sfr}^2 + \frac{1}{2} \cdot m_{rr} \cdot \dot{y}_{srr}^2 + \frac{1}{2} \cdot m_{rl} \cdot \dot{y}_{srl}^2 + \frac{1}{2} \cdot m_{fl} \cdot \dot{y}_{sfl}^2 + \frac{1}{2} \cdot m_s \cdot (\dot{y}_{sfr} - \dot{y}_b + l_f \cdot \dot{\alpha} + l_r \cdot \dot{\beta})^2 \\
&+ \frac{1}{2} \cdot m_s \cdot (\dot{y}_{srr} - \dot{y}_b - l_b \cdot \dot{\alpha} + l_r \cdot \dot{\beta})^2 + \frac{1}{2} \cdot m_s \cdot (\dot{y}_{srl} - \dot{y}_b - l_b \cdot \dot{\alpha} - l_l \cdot \dot{\beta})^2 + \frac{1}{2} \cdot m_s \cdot (\dot{y}_{sfl} - \dot{y}_b + l_f \cdot \dot{\alpha} - l_l \cdot \dot{\beta})^2 + \frac{1}{2} \cdot I_a \dot{\alpha}^2 + \frac{1}{2} \cdot I_b \dot{\beta}^2 \\
W &= \frac{1}{2} \cdot c_{sfr} \cdot (\dot{y}_{sfr} - \dot{y}_b + l_f \cdot \dot{\alpha} + l_r \cdot \dot{\beta})^2 + \frac{1}{2} \cdot c_{srr} \cdot (\dot{y}_{srr} - \dot{y}_b - l_b \cdot \dot{\alpha} + l_r \cdot \dot{\beta})^2 + \frac{1}{2} \cdot c_{srl} \cdot (\dot{y}_{srl} - \dot{y}_b - l_b \cdot \dot{\alpha} - l_l \cdot \dot{\beta})^2 \\
&+ \frac{1}{2} \cdot c_{sfl} \cdot (\dot{y}_{sfl} - \dot{y}_b + l_f \cdot \dot{\alpha} - l_l \cdot \dot{\beta})^2 + \frac{1}{2} \cdot c_L \cdot (\dot{y}_{sfr} - \dot{y}_b + l_f \cdot \dot{\alpha} + l_r \cdot \dot{\beta})^2 + \frac{1}{2} \cdot c_L \cdot (\dot{y}_{srr} - \dot{y}_b - l_b \cdot \dot{\alpha} + l_r \cdot \dot{\beta})^2 \\
&+ \frac{1}{2} \cdot c_L \cdot (\dot{y}_{srl} - \dot{y}_b - l_b \cdot \dot{\alpha} - l_l \cdot \dot{\beta})^2 + \frac{1}{2} \cdot c_L \cdot (\dot{y}_{sfl} - \dot{y}_b + l_f \cdot \dot{\alpha} - l_l \cdot \dot{\beta})^2 + \frac{1}{2} \cdot c_{tfr} \cdot (\dot{y}_{tfr} - \dot{y}_{sfr})^2 + \frac{1}{2} \cdot c_{trr} \cdot (\dot{y}_{trr} - \dot{y}_{srr})^2 \\
&+ \frac{1}{2} \cdot c_{trl} \cdot (\dot{y}_{trl} - \dot{y}_{srl})^2 + \frac{1}{2} \cdot c_{tfl} \cdot (\dot{y}_{tfl} - \dot{y}_{sfl})^2 \\
V &= \frac{1}{2} \cdot k_{sfr} \cdot (y_{sfr} - y_b + l_f \cdot \alpha + l_r \cdot \beta)^2 + \frac{1}{2} \cdot k_{srr} \cdot (y_{srr} - y_b - l_b \cdot \alpha + l_r \cdot \beta)^2 + \frac{1}{2} \cdot k_{srl} \cdot (y_{srl} - y_b - l_b \cdot \alpha - l_l \cdot \beta)^2 \\
&+ \frac{1}{2} \cdot k_{sfl} \cdot (y_{sfl} - y_b + l_f \cdot \alpha - l_l \cdot \beta)^2 + \frac{1}{2} \cdot k_{tfr} \cdot (y_{tfr} - y_{sfr})^2 + \frac{1}{2} \cdot k_{trr} \cdot (y_{trr} - y_{srr})^2 + \frac{1}{2} \cdot k_{trl} \cdot (y_{trl} - y_{srl})^2 + \frac{1}{2} \cdot k_{tfl} \cdot (y_{tfl} - y_{sfl})^2 \quad (6.2)
\end{aligned}$$

where  $m_s$  is the equivalent mass of the indirect-drive RSA, which is given in Equation (5.4);  $c_L$  is the equivalent damping coefficient of the indirect-drive RSA, which is given in Equation (5.5). Therefore, the governing equation of the full vehicle suspension system integrated with the indirect-drive RSAs are given in Equation (6.3) by substituting Equation (6.2) into Equation (6.1) and applying the force balance relationship:





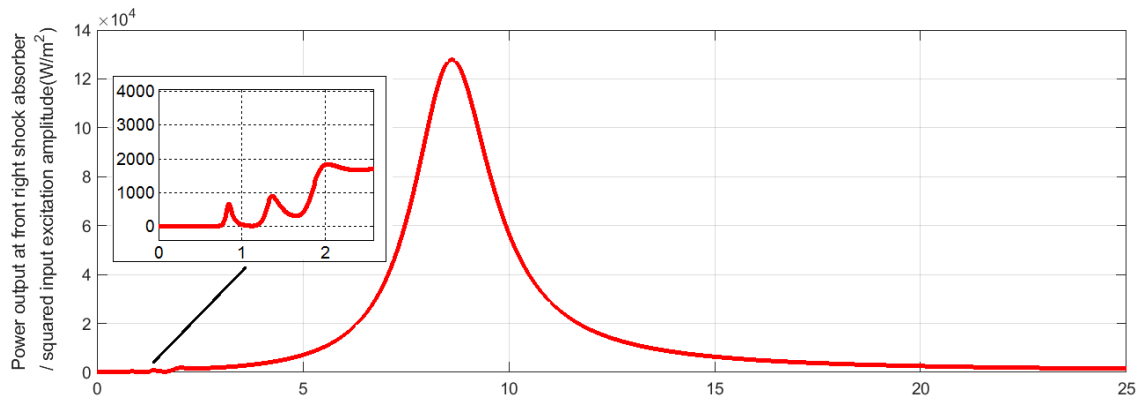
## 6.3 Results and discussions

Based on Equation (6.3), the power output of each RSA can be calculated from the Fourier transforms of the equation and plotted in frequency domain. The road excitation displacement excitation signal is applied on the front right wheel, the power output values of the front right, rear left, front left and rear right RSAs are calculated and shown in Figure 6.2. It can be observed from Figure 6.2 that the highest power output can be obtained at the front right shock absorber which are directly attached to the wheel under the road excitation. The peak power output ratio of the front right RSA reaches  $130000 \text{ W/m}^2$  at the natural frequency of 8.6 Hz, the other lower power output ratio peaks occur at 0.8 Hz, 1.3 Hz and 1.8 Hz. In Figure 6.2 (b) (c) (d), for the rear left, front left and rear right RSA, the power output ratios are in the similar range of  $600\text{-}900 \text{ W/m}^2$  which is much lower than that of the front right RSA, and the peak power output ratio occurs at 0.8 Hz, 1.3 Hz and 1.8 Hz. The resonant frequencies of the 7 DOF full vehicle suspension system are listed in Table 6.2 below.

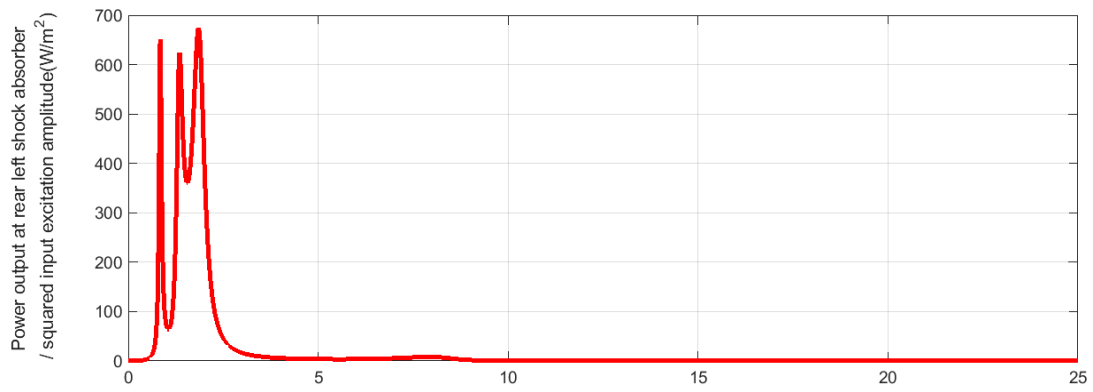
**Table 6.2: Natural frequencies of the 7 DOF vehicle suspension system.**

|        |        |        |        |        |        |       |
|--------|--------|--------|--------|--------|--------|-------|
| 1.3 Hz | 8.6 Hz | 8.6 Hz | 8.6 Hz | 8.6 Hz | 1.8 Hz | 0.8Hz |
|--------|--------|--------|--------|--------|--------|-------|

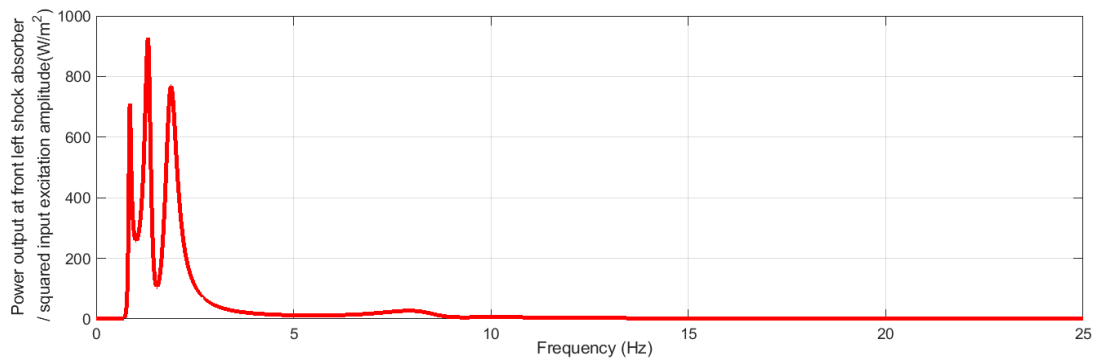
where according to the mode shape values from eigen value analysis, 0.8 Hz is the vehicle rolling mode frequency, 1.3 Hz is the bouncing mode frequency; 1.8 Hz is the pitching mode frequency; 8.6 Hz is the hopping mode frequency.



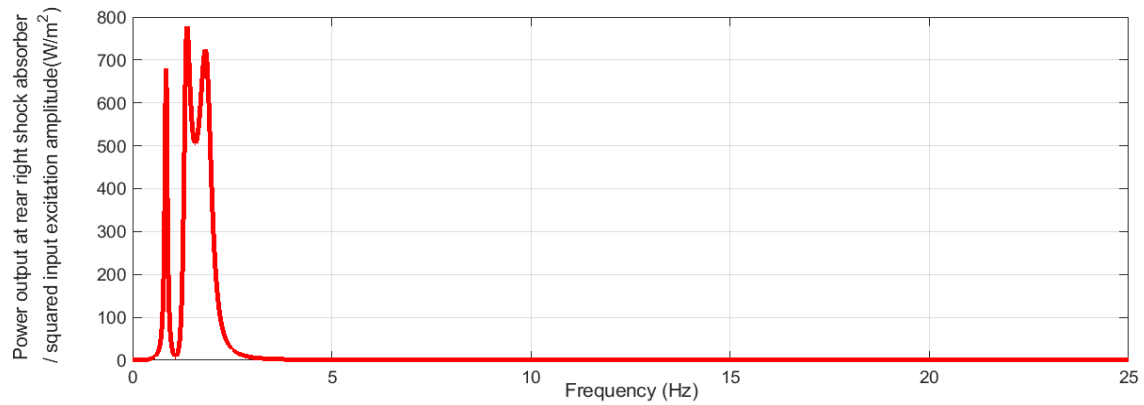
(a)



(b)



(c)

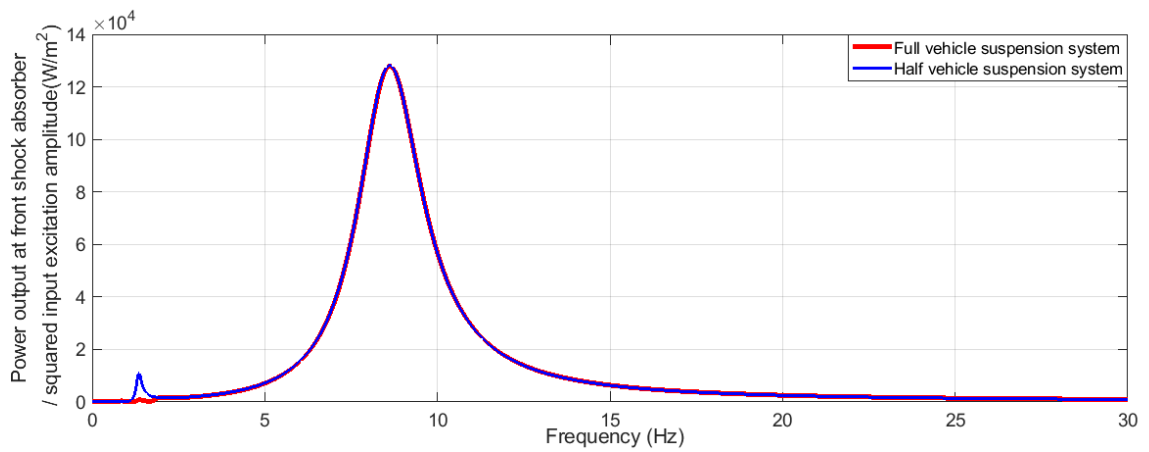


(d)

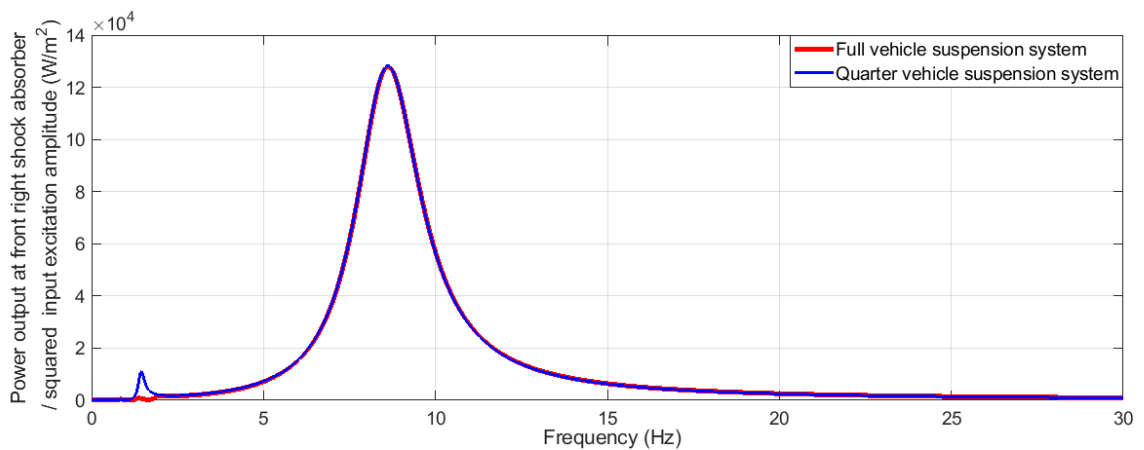
**Figure 6.2: The ratios of power output to the squared input excitation displacement amplitude of the (a) front right RSA, (b) the rear left RSA, (c) front left RSA and (d) rear right RSA.**

Figure 6.3 compares the difference of the full vehicle, half vehicle and quarter vehicle suspension system under the same road excitation applied on the front right wheel. For both the half vehicle and quarter vehicle suspension systems, the peak power output ratios are the same at the natural frequency of 8.6 Hz. The main difference occurs at the natural frequency of 1.3 Hz, where the power output ratios of the full vehicle suspension system model are lower than that of the half vehicle and the quarter vehicle suspension system. This is because the changes of the mass and stiffness coefficients from 2DOF to 4DOF and 7DOF vehicle systems are proportional so that the first and second modal resonant frequencies are maintained to be same, the changes of the wheel-tyre damping coefficients from the 2DOF to 4DOF and 7DOF vehicle systems are not proportional. The vehicle system model of more degrees of freedom would tend to have more equivalent bouncing mode damping which results in smaller resonant power output peak value at the bouncing modal resonant frequency. The 7DOF vehicle system model has four wheel-tyres contributing to the bouncing mode damping, the 4DOF vehicle system model has two wheel-tyres contributing

to the bouncing mode damping and the 2DOF vehicle system model has one wheel-tyre contributing to the bouncing mode damping. The power output peak values at the hopping mode frequency of the 7DOF, 4DOF and 2DOF vehicle system models are close to one other, which means that the contribution of the electromechanical and suspension damping to the hopping mode is same for all the 2DOF to 4DOF and 7DOF vehicle system models. The 7DOF vehicle system model has four indirect-drive regenerative shock absorbers, the 4DOF vehicle system model has two indirect-drive regenerative shock absorbers and the 2DOF vehicle system model has one indirect-drive regenerative shock absorber.



(a)



(b)

**Figure 6.3: The comparison of the power output ratios between (a) front shock absorber in half vehicle suspension system and front right shock absorber in full vehicle suspension system and (b) shock absorber in quarter vehicle suspension system and front right shock absorber in full vehicle suspension system.**

Based on Equation 6.3, the time domain simulation model can be established using MATLAB Simulink and is presented in Figure 6.4. The road excitation displacement signals applied on each wheel-tyre can be set as input signals, the corresponding power output from each RSA are set as output signals, allowing for the real road profile to be directly implemented in the simulation model. Shown in Figure 6.5 is the power output ratio from the front right RSA obtained in the frequency domain and its comparison with result obtained in the time domain. It can be seen that results simulated in the time domain (blue triangle marks) are very close to the results in the frequency domain (red solid line), which validates the frequency response model of Equation (6.3).

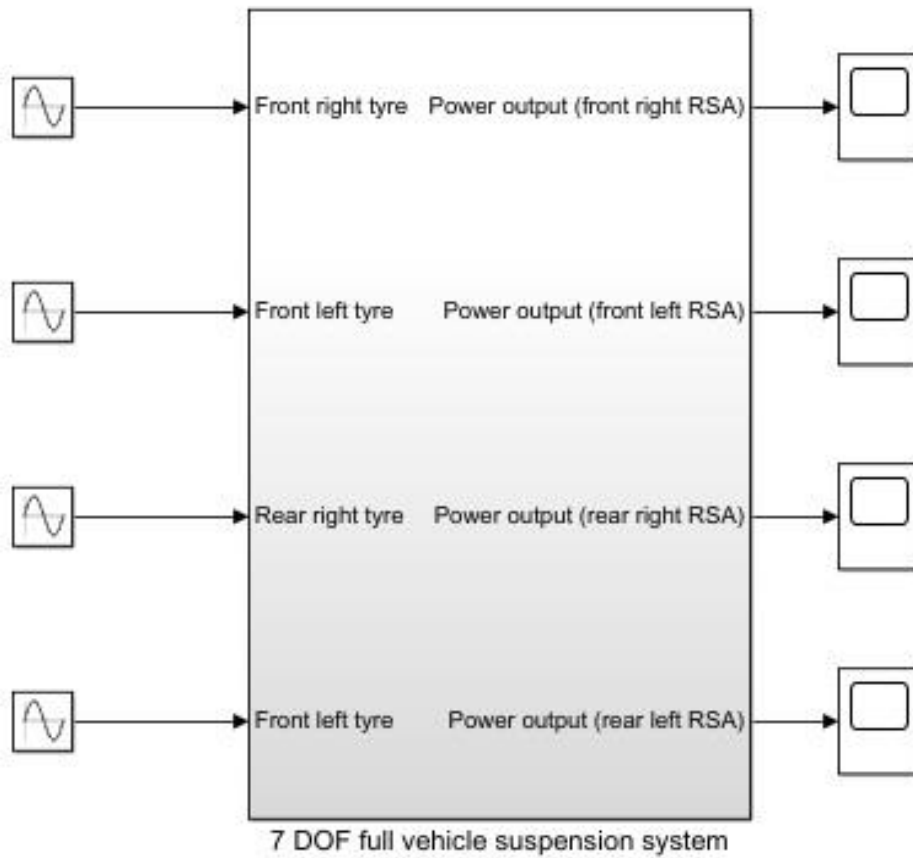
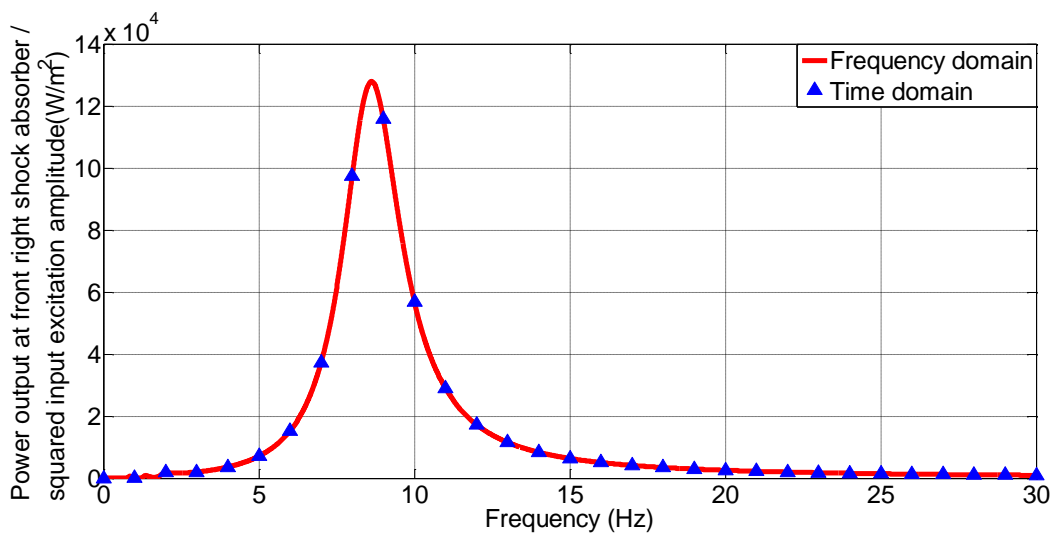


Figure 6.4: The modelling of 7 DOF full vehicle suspension system in time domain.



**Figure 6.5: The comparison of the power output ratios of the front right shock absorber simulated in the frequency domain and the time domain.**

## 6.4 Conclusion

In this chapter, a 7 degrees of freedom full vehicle suspension system has been modelled in both the frequency domain and time domain. 7 resonant frequencies of the system have been identified corresponding to the modes of rolling, bouncing, pitching and hopping. The power output of each regenerative shock absorber has been obtained given the road excitation displacement input. It is found that the regenerative shock absorber connected with the wheel where the road excitation is directly applied harvests the most power among all the four regenerative shock absorbers. The highest power output can be harvested at the hopping mode frequency of 8.6 Hz. In addition, the advantage of the full vehicle suspension system model over the half and quarter vehicle suspension system models is that it presents more accurate results in the low frequency range. However, at the hopping mode frequency where the highest power outputs ratio is obtained, the peak output power result of the full vehicle suspension system model is same as that of the half and quarter vehicle suspension system models. Therefore, the full vehicle suspension system model is more suitable for predicting the energy harvesting performance at the lower frequency range or in the situation where the difference of the road profiles in the transverse direction cannot be neglected and induces the vehicle rolling mode vibration, such as an off-road condition.



# Chapter 7

## *Conclusion*

### 7.1 Research contribution

In order to summarise the key contributions of the research, all the research questions have been individually addressed.

Firstly, the research question 1 “How can the performance of the electromagnetic energy harvester in 2DOF system be improved?” is answered in Chapter 3. The key contribution is to identify the premium profile for the coil and magnets.

Secondly, the research question 2 “For the direct drive and indirect drive regenerative shock absorbers, which one has better performance?” is discussed in Chapter 4. The results indicate that the indirect drive regenerative shock absorber has higher power output and energy

harvesting efficiency than direct drive regenerative shock absorber when considering the same generator configuration.

Finally, the research question 3 “How can the half vehicle model with regenerative shock absorbers be modelled for the premium energy harvesting performance?” is answered in Chapter 5. Different random road profile has been applied to a 7 DOF half vehicle suspension system which is integrated with the four regenerative shock absorbers. The total power output of the system can be substantially increased through tuning certain parameters.

## 7.2 Future work

The energy harvesting ability of the regenerative shock absorber has been the focus of the research for its potential of improving fuel efficiency and even replacing alternator. It has been approved that it can be achieved through advance design of the electromechanical mechanism and optimized vehicle system. However, its ability as the shock absorber to attenuate the vibrations induced by the road roughness has not been addressed enough especially when it is integrated with the concept of energy harvesting.

Due to the bidirectional nature of the electrical motor, it can be utilized as both generator to harvest kinetic energy and actuator for the active control. Even though the technologies of energy harvesting shock absorber and active control suspension have been developed for years, the intelligent suspension system combining these two technologies has not attracted much attentions which, if fully developed, will allow for the driver to select between the “eco-mode” and “comfort-mode” manually or through the help of the control system.

# Reference

1. Poulin, G., E. Sarraute, and F. Costa, *Generation of electrical energy for portable devices: Comparative study of an electromagnetic and a piezoelectric system*. Sensors and Actuators A: physical, 2004. **116**(3): p. 461-471.
2. Zhang, P.S., *Design of Electromagnetic Shock Absorbers for Energy Harvesting From Vehicle Suspensions*. 2010, MS thesis, Stony Brook University, Stony Brook, NY.
3. Zhang, R., X. Wang, and Z. Liu, *A novel regenerative shock absorber with a speed doubling mechanism and its Monte Carlo simulation*. Journal of Sound and Vibration, 2018. **417**: p. 260-276.
4. Zhang, R., X. Wang, and S. John, *A comprehensive review of the techniques on regenerative shock absorber systems*. Energies, 2018. **11**(5): p. 1167.
5. Al Shami, E., X. Wang, R. Zhang, and L. Zuo, *A parameter study and optimization of two body wave energy converters*. Renewable Energy, 2019. **131**: p. 1-13.
6. Liu, Z., X. Wang, R. Zhang, and L. Wang, *A dimensionless parameter analysis of a cylindrical tube electromagnetic vibration energy harvester and its oscillator nonlinearity effect*. Energies, 2018. **11**(7): p. 1653.
7. Al Shami, E., R. Zhang, and X. Wang, *Point Absorber Wave Energy Harvesters: A Review of Recent Developments*. Energies, 2019. **12**(1): p. 47.
8. Zhang, R., X. Wang, H. Shu, and S. John, *The effects of the electro-mechanical coupling and Halbach magnet pattern on energy harvesting performance of a two degree of freedom electromagnetic vibration energy harvester*. International Journal of Vehicle Noise and Vibration, 2018. **14**(2): p. 124-146.
9. Zhang, R., X. Wang, E. Al Shami, S. John, L. Zuo, and C.H. Wang, *A novel indirect-drive regenerative shock absorber for energy harvesting and comparison with a conventional direct-drive regenerative shock absorber*. Applied Energy, 2018. **229**: p. 111-127.
10. Zhang, R. and X. Wang, *Parameter study and optimization of a half-vehicle suspension system model integrated with an arm-teeth regenerative shock absorber using Taguchi method*. Mechanical Systems and Signal Processing, 2019. **126**: p. 65-81.
11. Liu, Z., X. Wang, S. Ding, R. Zhang, and L. McNabb, *A new concept of speed amplified nonlinear electromagnetic vibration energy harvester through fixed pulley wheel mechanisms and magnetic springs*. Mechanical Systems and Signal Processing, 2019. **126**: p. 305-325.
12. Choi, J.-S. and J. Yoo, *Design of a Halbach magnet array based on optimization techniques*. IEEE Transactions on Magnetics, 2008. **44**(10): p. 2361-2366.
13. Jang, S.-M., S.-S. Jeong, D.-W. Ryu, and S.-K. Choi, *Comparison of three types of PM brushless machines for an electro-mechanical battery*. IEEE transactions on magnetics, 2000. **36**(5): p. 3540-3543.
14. Cheng, S. and D.P. Arnold, *A study of a multi-pole magnetic generator for low-frequency vibrational energy harvesting*. Journal of Micromechanics and Microengineering, 2009. **20**(2): p. 025015.
15. Kulkarni, S., E. Koukharenko, R. Torah, J. Tudor, S. Beeby, T. O'Donnell, and S. Roy, *Design, fabrication and test of integrated micro-scale vibration-based electromagnetic generator*. Sensors and Actuators A: Physical, 2008. **145**: p. 336-342.
16. Harne, R.L., *Theoretical investigations of energy harvesting efficiency from structural vibrations using piezoelectric and electromagnetic oscillators*. The Journal of the Acoustical Society of America, 2012. **132**(1): p. 162-172.
17. Chen, C. and W.-H. Liao, *A self-sensing magnetorheological damper with power generation*. Smart Materials and Structures, 2012. **21**(2): p. 025014.
18. Ebrahimi, B., M.B. Khamesee, and M.F. Golnaraghi, *Design and modeling of a magnetic shock absorber based on eddy current damping effect*. Journal of Sound and Vibration, 2008. **315**(4): p. 875-889.
19. Aldraihem, O. and A. Baz, *Energy harvester with a dynamic magnifier*. Journal of Intelligent Material Systems and Structures, 2011: p. 1045389X11402706.

20. Lin, X. and G. Xuexun. *Hydraulic transmission electromagnetic energy-regenerative active suspension and its working principle*. in *2010 2nd International Workshop on Intelligent Systems and Applications*. 2010.
21. Noritsugu, T., *Energy saving of a pneumatic system (2). Energy regenerative control of a pneumatic drive system. Application to active air suspension*. Hydraulics & Pneumatics, 1999. **38**(4): p. 1-4.
22. Zuo, L., B. Scully, J. Shestani, and Y. Zhou, *Design and characterization of an electromagnetic energy harvester for vehicle suspensions*. Smart Materials and Structures, 2010. **19**(4): p. 045003.
23. Gupta, A., J. Jendrzeczyk, T. Mulcahy, and J. Hull, *Design of electromagnetic shock absorbers*. International Journal of Mechanics and Materials in Design, 2006. **3**(3): p. 285-291.
24. Ebrahimi, B., H. Bolandhemmat, M.B. Khamesee, and F. Golnaraghi, *A hybrid electromagnetic shock absorber for active vehicle suspension systems*. Vehicle System Dynamics, 2011. **49**(1-2): p. 311-332.
25. Tang, X., T. Lin, and L. Zuo, *Design and optimization of a tubular linear electromagnetic vibration energy harvester*. Mechatronics, IEEE/ASME Transactions on, 2014. **19**(2): p. 615-622.
26. Cheung, J.T., *Frictionless Linear Electrical Generator for Harvesting Motion Energy*. 2004, DTIC Document.
27. Jang, S.-M., J.-Y. Choi, S.-H. Lee, H.-W. Cho, and W.-B. Jang, *Analysis and experimental verification of moving-magnet linear actuator with cylindrical Halbach array*. IEEE transactions on magnetics, 2004. **40**(4): p. 2068-2070.
28. Zhu, D., S. Beeby, J. Tudor, and N. Harris, *Vibration energy harvesting using the Halbach array*. Smart Materials and Structures, 2012. **21**(7): p. 075020.
29. Long, Z., G. He, and S. Xue, *Study of EDS & EMS hybrid suspension system with permanent-magnet halbach array*. IEEE transactions on magnetics, 2011. **47**(12): p. 4717-4724.
30. Yan, L., L. Zhang, T. Wang, Z. Jiao, C.-Y. Chen, and I. Chen, *Magnetic field of tubular linear machines with dual Halbach array*. Progress In Electromagnetics Research, 2013. **136**: p. 283-299.
31. Salauddin, M. and J.Y. Park, *Design and experiment of human hand motion driven electromagnetic energy harvester using dual Halbach magnet array*. Smart Materials and Structures, 2017.
32. Zhu, D., S. Beeby, M. Tudor, and N. Harris, *Electromagnetic vibration energy harvesting using an improved Halbach array*. 2012.
33. Zhu, D., S. Beeby, J. Tudor, and N. Harris, *Increasing output power of electromagnetic vibration energy harvesters using improved Halbach arrays*. Sensors and Actuators A: Physical, 2013. **203**: p. 11-19.
34. Elvin, N.G. and A.A. Elvin, *An experimentally validated electromagnetic energy harvester*. Journal of Sound and Vibration, 2011. **330**(10): p. 2314-2324.
35. Goldner, R., P. Zerigian, and J. Hull, *A preliminary study of energy recovery in vehicles by using regenerative magnetic shock absorbers*. 2001, SAE Technical Paper.
36. Xie, X. and Q. Wang, *Energy harvesting from a vehicle suspension system*. Energy, 2015. **86**: p. 385-392.
37. Sapiński, B., M. Rosół, and M. Węgrzynowski, *Evaluation of an energy harvesting mr damper-based Vibration reduction systemstem*. Journal of Theoretical and Applied Mechanics, 2016. **54**(2): p. 333-344.
38. Tang, X., T. Lin, and L. Zuo, *Design and optimization of a tubular linear electromagnetic vibration energy harvester*. IEEE/ASME Transactions on Mechatronics, 2014. **19**(2): p. 615-622.
39. Wang, R., R. Ding, and L. Chen, *Application of hybrid electromagnetic suspension in vibration energy regeneration and active control*. Journal of Vibration and Control, 2016: p. 1077546316637726.
40. Asadi, E., R. Ribeiro, M.B. Khamesee, and A. Khajepour, *Analysis, Prototyping and Experimental Characterization of an Adaptive Hybrid-Electromagnetic Damper for Automotive Suspension Systems*. IEEE Transactions on Vehicular Technology, 2016.
41. Li, Z., L. Zuo, J. Kuang, and G. Luhrs. *A motion rectifier based energy harvesting shock absorbers*. in *2012 ASME Design Engineering Conference, Chicago, Aug12-15*. 2012.
42. Li, P. and L. Zuo, *Assessment of vehicle performances with energy-harvesting shock absorbers*. SAE International Journal of Passenger Cars-Mechanical Systems, 2013. **6**(2013-01-0170): p. 18-27.
43. Zhang, Z., X. Zhang, W. Chen, Y. Rasim, W. Salman, H. Pan, Y. Yuan, and C. Wang, *A high-efficiency energy regenerative shock absorber using supercapacitors for renewable energy applications in range extended electric vehicle*. Applied Energy, 2016. **178**: p. 177-188.
44. Guo, S., Y. Liu, L. Xu, X. Guo, and L. Zuo, *Performance evaluation and parameter sensitivity of energy-harvesting shock absorbers on different vehicles*. Vehicle System Dynamics, 2016. **54**(7): p. 918-942.

45. Xie, L., J. Li, and M. Cai, *Design of a Hybrid Energy-Harvesting Shock Absorber*. 2015.
46. Fukumori, Y., R. Hayashi, R. Matsumi, Y. Suda, and K. Nakano, *Study on Independent Tuning Damping Characteristic by Coupling of Electromagnetic Dampers for Automobiles*. 2015, SAE Technical Paper.
47. Zheng, X.-c., F. Yu, and Y.-c. Zhang, *A novel energy-regenerative active suspension for vehicles*. Journal of Shanghai Jiaotong University (Science), 2008. **13**: p. 184-188.
48. Kawamoto, Y., Y. Suda, H. Inoue, and T. Kondo, *Modeling of electromagnetic damper for automobile suspension*. Journal of System Design and Dynamics, 2007. **1**(3): p. 524-535.
49. Kawamoto, Y., Y. Suda, H. Inoue, and T. Kondo, *Electro-mechanical suspension system considering energy consumption and vehicle manoeuvre*. Vehicle System Dynamics, 2008. **46**(S1): p. 1053-1063.
50. Ebrahimi, B., M.B. Khamesee, and M.F. Golnaraghi. *Feasibility study of an electromagnetic shock absorber with position sensing capability*. in *Industrial Electronics, 2008. IECON 2008. 34th Annual Conference of IEEE*. 2008. IEEE.
51. Zhang, Y., K. Huang, F. Yu, Y. Gu, and D. Li. *Experimental verification of energy-regenerative feasibility for an automotive electrical suspension system*. in *Vehicular Electronics and Safety, 2007. ICVES. IEEE International Conference on*. 2007. IEEE.
52. Cheng, S., N. Wang, and D.P. Arnold, *Modeling of magnetic vibrational energy harvesters using equivalent circuit representations*. Journal of Micromechanics and Microengineering, 2007. **17**(11): p. 2328.
53. Liu, Y., L. Xu, and L. Zuo, *Design, Modeling, Lab and Field Tests of a Mechanical-motion-rectifier-based Energy Harvester Using a Ball-screw Mechanism*. IEEE/ASME Transactions on Mechatronics, 2017.
54. Cargo, C.J., A.R. Plummer, A.J. Hillis, and M. Schlotter, *Determination of optimal parameters for a hydraulic power take-off unit of a wave energy converter in regular waves*. Proceedings of the Institution of Mechanical Engineers, Part A: Journal of Power and Energy, 2011: p. 0957650911407818.
55. Lin, X., Y. Bo, G. Xuexun, and Y. Jun. *Simulation and performance evaluation of hydraulic transmission electromagnetic energy-regenerative active suspension*. in *2010 Second WRI Global Congress on Intelligent Systems*. 2010. IEEE.
56. Avadhany, S., P. Abel, V. Tarasov, and Z. Anderson, *Regenerative shock absorber*. 2013, Google Patents.
57. Henderson, R., *Design, simulation, and testing of a novel hydraulic power take-off system for the Pelamis wave energy converter*. Renewable energy, 2006. **31**(2): p. 271-283.
58. Antaki, J.F., G.E. Bertocci, E.C. Green, A. Nadeem, T. Rintoul, R.L. Kormos, and B.P. Griffith, *A gait-powered autologous battery charging system for artificial organs*. ASAIO journal, 1995. **41**(3): p. M588-M595.
59. Chandler, D., *More power from bumps in the road-MIT students develop energy-harvesting shock absorbers*. MIT News, 2009.
60. Liang, X.-C. and J.-S. Zhao, *Research on recycling vibration energy of shock absorber*. International Journal of Vehicle Design, 2015. **68**(1-3): p. 201-220.
61. Fang, Z., X. Guo, L. Xu, and H. Zhang, *Experimental study of damping and energy regeneration characteristics of a hydraulic electromagnetic shock absorber*. Advances in Mechanical Engineering, 2013. **5**: p. 943528.
62. Wang, R., F. Gu, R. Cattley, and A.D. Ball, *Modelling, testing and analysis of a regenerative hydraulic shock absorber system*. Energies, 2016. **9**(5): p. 386.
63. Galluzzi, R., A. Tonoli, N. Amati, G. Curcuruto, P. Conti, G. Greco, and A. Nepote, *Regenerative Shock Absorbers and the Role of the Motion Rectifier*. 2016, SAE Technical Paper.
64. van der Westhuizen, S.F. and P.S. Els, *Comparison of different gas models to calculate the spring force of a hydropneumatic suspension*. Journal of Terramechanics, 2015. **57**: p. 41-59.
65. Tao, S., Y. Fan, and Z. You, *Investigation on Non-linear Characteristics of Hydropneumatic Suspension Modeling and Simulation for Engineering Vehicles [J]*. Acta Simulata Systematica Sinica, 2005. **1**: p. 055.
66. Longxin, Z. and W. Xiaogang, *Structure and performance analysis of regenerative electromagnetic shock absorber*. Journal of networks, 2010. **5**(12): p. 1467-1474.
67. Crolla, D., *Off-road vehicle dynamics*. Vehicle System Dynamics, 1981. **10**(4-5): p. 253-266.
68. Shaiju, M. and M. Mitra, *Energy Generating Suspension System for Commercial Vehicles*. SAE International Journal of Commercial Vehicles, 2008. **1**(2008-01-2605): p. 248-253.

69. Jin-qiu, Z., P. Zhi-zhao, Z. Lei, and Z. Yu. *A review on energy-regenerative suspension systems for vehicles*. in *Proceedings of the World Congress on Engineering*. 2013.
70. Nakano, K., *Combined type self-powered active vibration control of truck cabins*. *Vehicle System Dynamics*, 2004. **41**(6): p. 449-473.
71. Choi, S., M. Seong, and K. Kim, *Vibration control of an electrorheological fluid-based suspension system with an energy regenerative mechanism*. *Proceedings of the Institution of Mechanical Engineers, Part D: Journal of Automobile Engineering*, 2009. **223**(4): p. 459-469.
72. Chu, K.S., L. Zou, and W.-H. Liao. *A mechanical energy harvested magnetorheological damper with linear-rotary motion converter*. in *SPIE Smart Structures and Materials+ Nondestructive Evaluation and Health Monitoring*. 2016. International Society for Optics and Photonics.
73. Sabzehgar, R., A. Maravandi, and M. Moallem, *Energy regenerative suspension using an algebraic screw linkage mechanism*. *IEEE/ASME Transactions on Mechatronics*, 2014. **19**(4): p. 1251-1259.
74. Zhang, Y., X. Zhang, M. Zhan, K. Guo, F. Zhao, and Z. Liu, *Study on a novel hydraulic pumping regenerative suspension for vehicles*. *Journal of the Franklin Institute*, 2015. **352**(2): p. 485-499.
75. Singh, S. and N.V. Satpute, *Design and analysis of energy-harvesting shock absorber with electromagnetic and fluid damping*. *Journal of Mechanical Science and Technology*, 2015. **29**(4): p. 1591.
76. Satpute, N.V., S.N. Satpute, and L.M. Jugulkar, *Hybrid electromagnetic shock absorber for energy harvesting in a vehicle suspension*. *Proceedings of the Institution of Mechanical Engineers, Part C: Journal of Mechanical Engineering Science*, 2016: p. 0954406216663577.
77. Demetgul, M. and I. Guney, *Design of the Hybrid Regenerative Shock Absorber and Energy Harvesting from Linear Movement*. *Journal of Clean Energy Technologies*, 2017. **5**(1).
78. Liu, Y. and L. Zuo, *Mixed skyhook and power-driven-damper: a new low-jerk semi-active suspension control based on power flow analysis*. *Journal of Dynamic Systems, Measurement, and Control*, 2016. **138**(8): p. 081009.
79. Cole, D. and D. Cebon, *Truck suspension design to minimize road damage*. *Proceedings of the Institution of Mechanical Engineers, Part D: Journal of Automobile Engineering*, 1996. **210**(2): p. 95-107.
80. Yan, S. and W. Sun. *Energy regeneration scheme and self-powered criterion of motor-driven active suspension*. in *Control Conference (CCC), 2016 35th Chinese*. 2016. IEEE.
81. Sapiński, B., M. Rosół, and M. Węgrzynowski, *Investigation of an energy harvesting MR damper in a vibration control system*. *Smart Materials and Structures*, 2016. **25**(12): p. 125017.
82. Shi, D., P. Pisu, L. Chen, S. Wang, and R. Wang, *Control design and fuel economy investigation of power split HEV with energy regeneration of suspension*. *Applied Energy*, 2016. **182**: p. 576-589.
83. Ottman, G.K., H.F. Hofmann, A.C. Bhatt, and G.A. Lesieutre, *Adaptive piezoelectric energy harvesting circuit for wireless remote power supply*. *IEEE Transactions on power electronics*, 2002. **17**(5): p. 669-676.
84. Ding, R., R. Wang, X. Meng, and L. Chen, *Study on coordinated control of the energy regeneration and the vibration isolation in a hybrid electromagnetic suspension*. *Proceedings of the Institution of Mechanical Engineers, Part D: Journal of Automobile Engineering*, 2016: p. 0954407016675812.
85. Arroyo, E., A. Badel, and F. Formosa. *Synchronized switch harvesting technique applied to electromagnetic vibrations harvester*. in *Proc. 10th Int. Workshop on Micro and Nanotechnology for Power Generation and Energy Conversion Applications (Power MEMS 2010), Tech. Dig.-Poster Sessions, Leuven, Belgium*. 2010.
86. Arroyo, E., A. Badel, and F. Formosa. *Synchronized switch harvesting technique applied to electromagnetic vibrations harvester*. in *Proc. 10th Int. Workshop on Micro and Nanotechnology for Power Generation and Energy Conversion Applications (Power MEMS 2010), Tech. Dig.-Poster Sessions, Leuven, Belgium*. 2010.
87. Sanchez, D., E. Jodka, D. Hoffmann, and Y. Manoli. *Interface circuit using SMFE technique for an inductive kinetic generator operating as a frequency-up converter*. in *Journal of Physics: Conference Series*. 2013. IOP Publishing.
88. Arroyo, E., A. Badel, and F. Formosa, *Energy harvesting from ambient vibrations: Electromagnetic device and synchronous extraction circuit*. *Journal of Intelligent Material Systems and Structures*, 2013. **24**(16): p. 2023-2035.

89. Dwari, S. and L. Parsa, *An efficient AC–DC step-up converter for low-voltage energy harvesting*. IEEE Transactions on Power Electronics, 2010. **25**(8): p. 2188-2199.
90. Liu, Y., W. Chen, Z. Zhang, and G. Hua, *Energy-Regenerative Shock Absorber for Transportation Vehicles Based on Dual Overrunning Clutches: Design, Modeling, and Simulation*. Transportation Research Record: Journal of the Transportation Research Board, 2016(2551): p. 126-136.
91. Han, S. and D. Divan. *Bi-directional DC/DC converters for plug-in hybrid electric vehicle (PHEV) applications*. in *Applied Power Electronics Conference and Exposition, 2008. APEC 2008. Twenty-Third Annual IEEE*. 2008. IEEE.
92. Cao, X., W.-J. Chiang, Y.-C. King, and Y.-K. Lee, *Electromagnetic energy harvesting circuit with feedforward and feedback DC–DC PWM boost converter for vibration power generator system*. IEEE Transactions on Power Electronics, 2007. **22**(2): p. 679-685.
93. Kazimierczuk, M.K. and A. Massarini, *Feedforward control of DC-DC PWM boost converter*. IEEE Transactions on Circuits and Systems I: Fundamental Theory and Applications, 1997. **44**(2): p. 143-148.
94. Liu, J., X. Li, Z. Wang, and Y. Zhang, *Modelling and Experimental Study on Active Energy-Regenerative Suspension Structure with Variable Universe Fuzzy PD Control*. Shock and Vibration, 2016. **2016**.
95. Fayyad, S.M., *Constructing control system for active suspension system*. Contemporary Engineering Sciences, 2012. **5**(4): p. 189-200.
96. Tiwari, A., M.K. Siddique, and M. Naseem, *Controlling the Vibration of Bus Suspension System using PID Controller*.
97. Mouleeswaran, S., *Design and development of PID controller-based active suspension system for automobiles*. 2012: INTECH Open Access Publisher.
98. Gururaj, M.S. and A. Selvakumar, *Fuzzy Logic Control for Half Car Suspension System Using Matlab*. 2014.
99. Rao, K.D., *Modeling, Simulation and Control of Semi Active Suspension System for Automobiles under MATLAB Simulink using PID Controller*. IFAC Proceedings Volumes, 2014. **47**(1): p. 827-831.
100. Kuber, C., *Modelling Simulation And Control of an Active Suspension System*. International Journal of Mechanical Engineering & Technology (IJMET), 2014. **5**(11): p. 66-75.
101. Ahmed, A.E.-N.S., A.S. Ali, N.M. Ghazaly, and G.A. El-Jaber, *PID CONTROLLER OF ACTIVE SUSPENSION SYSTEM FOR A QUARTER CAR MODEL*. International Journal of Advances in Engineering & Technology, 2015. **8**(6): p. 899.
102. Zhou, Q., *Research and Simulation on New Active Suspension Control System*. 2013.
103. Gaur, S., *Vibration Control of Bus Suspension System using PI and PID Controller*. International Journal of Advances in Engineering Sciences, 2013. **3**(3): p. 94-99.
104. Fukumori, Y., R. Hayashi, H. Okano, Y. Suda, and K. Nakano. *Study on coupled shock absorber system using four electromagnetic dampers*. in *Journal of Physics: Conference Series*. 2016. IOP Publishing.
105. Zhang, H., G. Li, Y. Wang, Y. Gu, X. Wang, and X. Guo, *Simulation Analysis on Controllability of Hydraulic Electrical Energy Regenerative Semi-Active Suspension*. 2016, SAE Technical Paper.
106. Hsieh, C.-Y., B. Huang, F. Golnaraghi, and M. Moallem, *Regenerative Skyhook Control for an Electromechanical Suspension System Using a Switch-Mode Rectifier*. IEEE Transactions on Vehicular Technology, 2016. **65**(12): p. 9642-9650.
107. Hsieh, C.-Y., M. Moallem, and F. Golnaraghi, *A Bidirectional Boost Converter With Application to a Regenerative Suspension System*. IEEE Transactions on Vehicular Technology, 2016. **65**(6): p. 4301-4311.
108. Ataei, M., E. Asadi, A. Goodarzi, A. Khajepour, and M.B. Khamesee, *Multi-objective optimization of a hybrid electromagnetic suspension system for ride comfort, road holding and regenerated power*. Journal of Vibration and Control, 2017. **23**(5): p. 782-793.
109. Clemen, L., O.M. Anubi, and D. Margolis, *On the Regenerative Capabilities of Electrodynamic Dampers Using Bond Graphs and Model Predictive Control*. Journal of Dynamic Systems, Measurement, and Control, 2016. **138**(5): p. 051006.
110. Casavola, A., F. Di Iorio, and F. Tedesco, *A multiobjective  $H^\infty$  control strategy for energy harvesting in regenerative vehicle suspension systems*. International Journal of Control, 2017: p. 1-14.
111. Zuo, L. and X. Tang, *Large-scale vibration energy harvesting*. Journal of intelligent material systems and structures, 2013. **24**(11): p. 1405-1430.

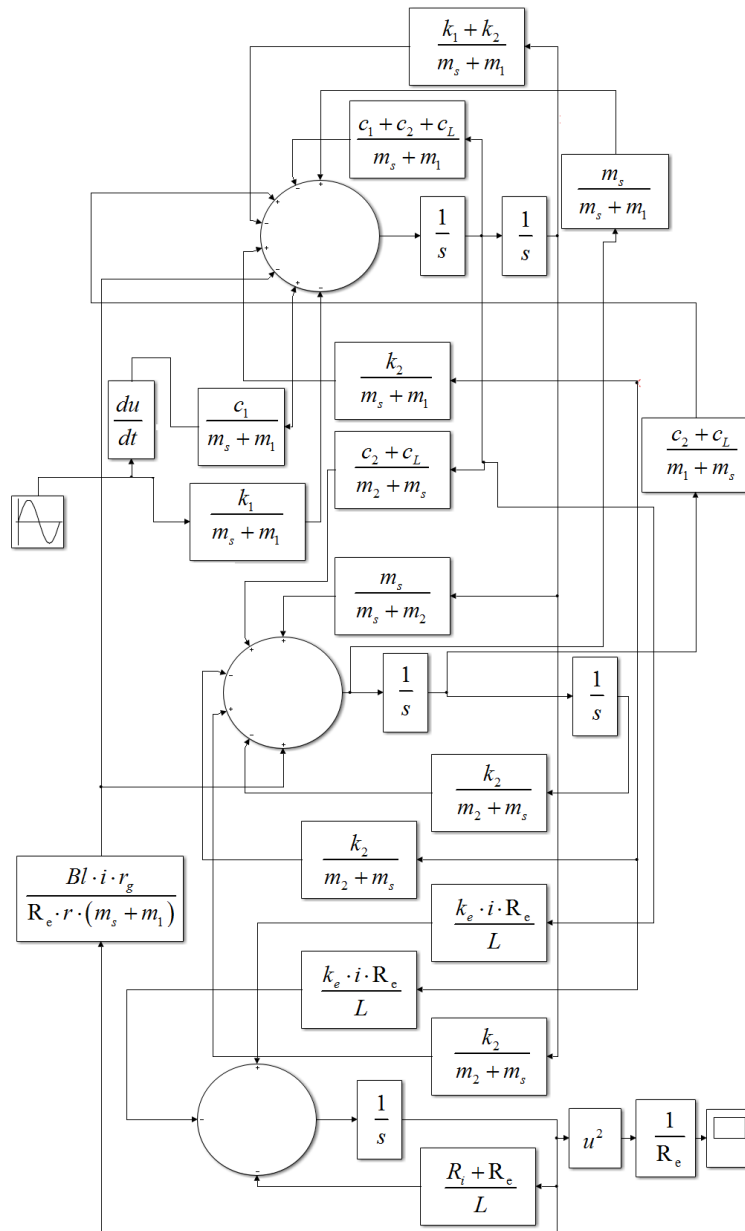
112. Nakano, K., Y. Suda, and S. Nakadai, *Self-powered active vibration control using a single electric actuator*. Journal of Sound and Vibration, 2003. **260**(2): p. 213-235.
113. Scruggs, J. and W. Iwan, *Control of a civil structure using an electric machine with semiactive capability*. Journal of Structural Engineering, 2003. **129**(7): p. 951-959.
114. Scruggs, J., *Active, regenerative control of civil structures*. 1999, Virginia Polytechnic Institute and State University.
115. Scruggs, J.T. and W. Iwan, *Structural control with regenerative force actuation networks*. Structural Control and Health Monitoring, 2005. **12**(1): p. 25-45.
116. Okada, Y., *Variable resistance type energy regenerative damper using pulse width modulated step-up chopper*. Journal of Vibration and Acoustics, 2002. **14**: p. 110-115.
117. Tang, X. and L. Zuo. *Simulation and experiment validation of simultaneous vibration control and energy harvesting from buildings using tuned mass dampers*. in *American Control Conference (ACC), 2011*. 2011. IEEE.
118. Wang, Z., Z. Chen, and B.F. Spencer Jr. *Self-powered and sensing control system based on MR damper: presentation and application*. in *SPIE Smart Structures and Materials+ Nondestructive Evaluation and Health Monitoring*. 2009. International Society for Optics and Photonics.
119. Choi, Y.-T. and N.M. Wereley, *Self-powered magnetorheological dampers*. Journal of Vibration and Acoustics, 2009. **131**(4): p. 044501.
120. Yu, L., S. Huo, W. Xuan, and L. Zuo, *Assessment of Ride Comfort and Braking Performance Using Energy-Harvesting Shock Absorber*. SAE International Journal of Passenger Cars-Mechanical Systems, 2015. **8**(2015-01-0649): p. 482-491.
121. Zheng, X.-c., F. Yu, and Y.-c. Zhang, *A novel energy-regenerative active suspension for vehicles*. Journal of Shanghai Jiaotong University (Science), 2008. **13**(2): p. 184-188.
122. Huang, B., C.-Y. Hsieh, F. Golnaraghi, and M. Moallem, *Development and optimization of an energy-regenerative suspension system under stochastic road excitation*. Journal of Sound and Vibration, 2015. **357**: p. 16-34.
123. Wang, X., X. Liang, and H. Wei, *A study of electromagnetic vibration energy harvesters with different interface circuits*. Mechanical Systems and Signal Processing, 2015. **58**: p. 376-398.
124. Li, P. and L. Zuo, *Influences of the electromagnetic regenerative dampers on the vehicle suspension performance*. Proceedings of the Institution of Mechanical Engineers, Part D: Journal of Automobile Engineering, 2017. **231**(3): p. 383-394.
125. Perret, A.H., O. Curea, S. Cagin, and A.G. Ortega, *From functional analysis to energy harvesting system design: application to car suspension*.
126. ISO-, *Mechanical vibration-Road surface profiles-Reporting of measured data*. 1995, International Organization for Standardization (ISO) Geneva.
127. Agostinacchio, M., D. Ciampa, and S. Olita, *The vibrations induced by surface irregularities in road pavements—a Matlab® approach*. European Transport Research Review, 2014. **6**(3): p. 267-275.
128. Zhang, Y., K. Guo, D. Wang, C. Chen, and X. Li, *Energy conversion mechanism and regenerative potential of vehicle suspensions*. Energy, 2016.
129. Li, Z., L. Zuo, J. Kuang, and G. Luhrs, *Energy-harvesting shock absorber with a mechanical motion rectifier*. Smart Materials and Structures, 2012. **22**(2): p. 025008.
130. Barton, D.A., S.G. Burrow, and L.R. Clare, *Energy harvesting from vibrations with a nonlinear oscillator*. Journal of Vibration and Acoustics, 2010. **132**(2): p. 021009.
131. Soliman, M., E. Abdel-Rahman, E. El-Saadany, and R. Mansour, *A wideband vibration-based energy harvester*. Journal of Micromechanics and Microengineering, 2008. **18**(11): p. 115021.
132. Yang, W. and S. Towfighian, *A hybrid nonlinear vibration energy harvester*. Mechanical Systems and Signal Processing, 2017. **90**: p. 317-333.
133. Erturk, A., J. Hoffmann, and D. Inman, *A piezomagnetoelastic structure for broadband vibration energy harvesting*. Applied Physics Letters, 2009. **94**(25): p. 254102.
134. Ferrari, M., V. Ferrari, M. Guizzetti, B. Andò, S. Baglio, and C. Trigona, *Improved energy harvesting from wideband vibrations by nonlinear piezoelectric converters*. Sensors and Actuators A: Physical, 2010. **162**(2): p. 425-431.
135. Stanton, S.C., C.C. McGehee, and B.P. Mann, *Reversible hysteresis for broadband magnetopiezoelectric energy harvesting*. Applied Physics Letters, 2009. **95**(17): p. 174103.



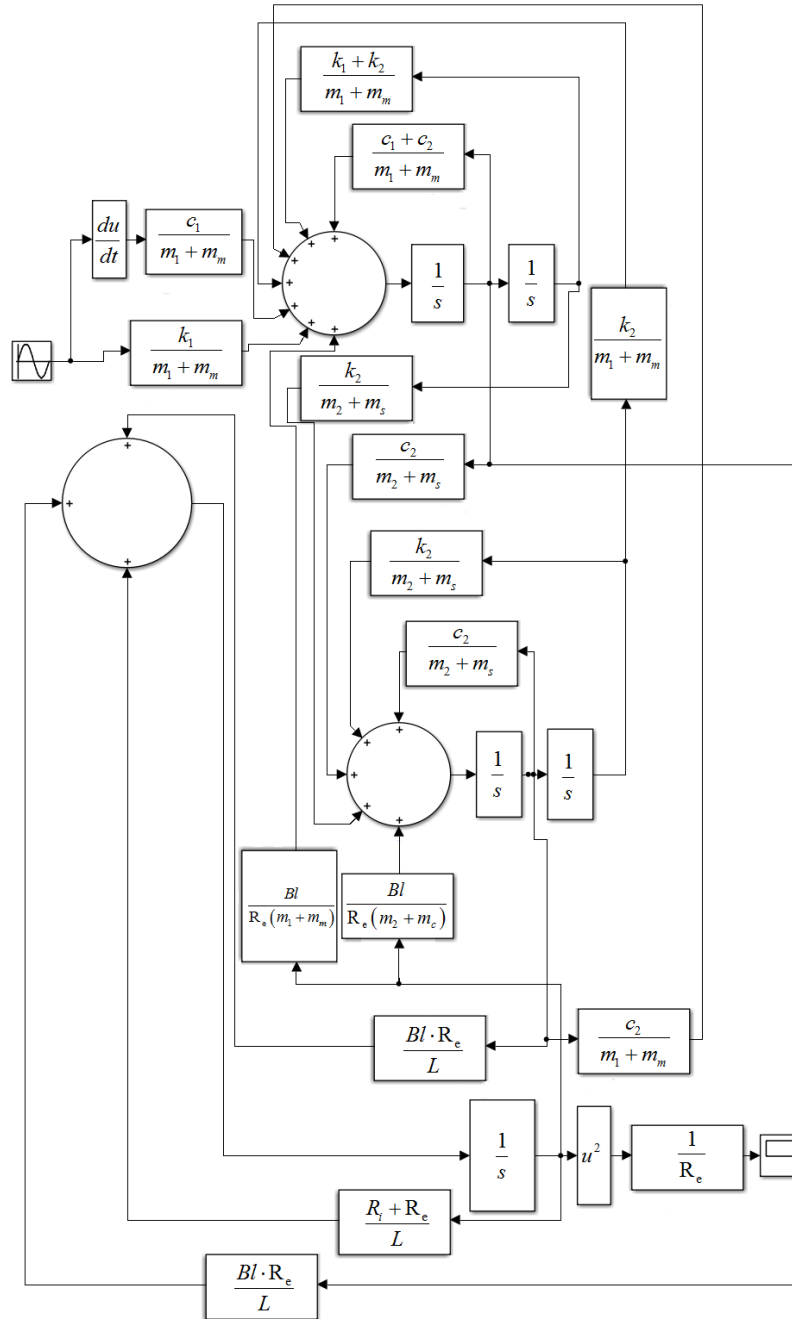
136. Mann, B. and N. Sims, *Energy harvesting from the nonlinear oscillations of magnetic levitation*. Journal of Sound and Vibration, 2009. **319**(1): p. 515-530.
137. Nguyen, D., E. Halvorsen, G. Jensen, and A. Vogl, *Fabrication and characterization of a wideband MEMS energy harvester utilizing nonlinear springs*. Journal of Micromechanics and Microengineering, 2010. **20**(12): p. 125009.
138. Özcan, D., Ü. Sönmez, and L. Güvenç, *Optimisation of the nonlinear suspension characteristics of a light commercial vehicle*. International Journal of Vehicular Technology, 2013. **2013**.
139. Cui, Y., T.R. Kurfess, and M. Messman. *Testing and modeling of nonlinear properties of shock absorbers for vehicle dynamics studies*. in *Proceedings of the World Congress on Engineering and Computer Science*. 2010.
140. Zhang, J., B. Ma, and M. Zehn, *Study on clutch engagement judder during launch process for dual clutch transmissions*. International Journal of Vehicle Noise and Vibration, 2010. **6**(2-4): p. 176-199.
141. Häfele, J. and F. Küçükay, *Multi-body dynamics analysis of power train judder oscillations considering aggregate dynamics*. International Journal of Vehicle Noise and Vibration, 2014. **10**(1-2): p. 64-76.
142. Qatu, M.S., *Recent research on vehicle noise and vibration*. International Journal of Vehicle Noise and Vibration, 2012. **8**(4): p. 289-301.
143. Qatu, M.S., M.K. Abdelhamid, J. Pang, and G. Sheng, *Overview of automotive noise and vibration*. International Journal of Vehicle Noise and Vibration, 2009. **5**(1-2): p. 1-35.
144. Wang, X., F. Bi, and H. Du, *Reduction of low frequency vibration of truck driver and seating system through system parameter identification, sensitivity analysis and active control*. Mechanical Systems and Signal Processing, 2018. **105**: p. 16-35.
145. Ung, C., S.D. Moss, and W.K. Chiu, *Vibration energy harvesting from heavy haul railcar vibrations using a two-degree-of-freedom coupled oscillating system*. Proceedings of the Institution of Mechanical Engineers, Part F: Journal of Rail and Rapid Transit, 2015: p. 0954409715569861.
146. Kawamoto, Y., S. Yoshihiro, H. Inoue, and T. Kondo, *Modeling of electromagnetic damper for automobile suspension*. Journal of System Design and Dynamics, 2007. **1**(3): p. 524-535.
147. Tang, X. and L. Zuo, *Enhanced vibration energy harvesting using dual-mass systems*. Journal of sound and vibration, 2011. **330**(21): p. 5199-5209.
148. Yang, B., C. Lee, W. Xiang, J. Xie, J.H. He, R.K. Kotlanka, S.P. Low, and H. Feng, *Electromagnetic energy harvesting from vibrations of multiple frequencies*. Journal of Micromechanics and Microengineering, 2009. **19**(3): p. 035001.
149. Smith, M.C. and S.J. Swift, *Power dissipation in automotive suspensions*. Vehicle System Dynamics, 2011. **49**(1-2): p. 59-74.
150. Jeon, C. and J. Shin, *Long-term renewable energy technology valuation using system dynamics and Monte Carlo simulation: Photovoltaic technology case*. Energy, 2014. **66**: p. 447-457.
151. Zhang, H., X. Guo, L. Xu, S. Hu, and Z. Fang, *Parameters analysis of hydraulic-electrical energy regenerative absorber on suspension performance*. Advances in Mechanical Engineering, 2014. **6**: p. 836502.
152. Wei, C. and H. Taghavifar, *A novel approach to energy harvesting from vehicle suspension system: Half-vehicle model*. Energy, 2017. **134**: p. 279-288.
153. Yang, W.p. and Y. Tarnq, *Design optimization of cutting parameters for turning operations based on the Taguchi method*. Journal of materials processing technology, 1998. **84**(1-3): p. 122-129.
154. Wang, X., F. Gauterin, and E.-U. Saemann, *Tire Acoustic Optimization Using Point Damping Method*. Tire Science and Technology, 2004. **32**(2): p. 81-115.
155. Tyan, F., Y.-F. Hong, S.-H. Tu, and W.S. Jeng, *Generation of random road profiles*. Journal of Advanced Engineering, 2009. **4**(2): p. 1373-1378.

# Appendix:

## Appendix 1: The time domain simulation model of the indirect-drive system using Matlab SIMULINK.



**Appendix 2: The time domain simulation model of the direct-drive system using Matlab SIMULINK.**



---

**The effects of the electro-mechanical coupling and Halbach magnet pattern on energy harvesting performance of a two degree of freedom electromagnetic vibration energy harvester**

---

Ran Zhang and Xu Wang\*

School of Engineering,  
RMIT University, Australia  
Fax: +03-9925-6108  
Email: s3253199@student.rmit.edu.au  
Email: xu.wang@rmit.edu.au  
\*Corresponding author

Hongli Shu

Jiangxi Professional Institute of Mechatronics Technology,  
Nanchang North Development District,  
ICP 05001964, Fenglin Road,  
Jiangxi 330013, China  
Email: shltj@126.com

Sabu John

School of Engineering,  
RMIT University, Australia  
Fax: +03-9925-6108  
Email: sabu@rmit.edu.au



**Abstract:** This paper studies a two degree of freedom electromagnetic vibration energy harvesting system with a magnet arrangement of the Halbach array. A theoretical analysis and computational simulation of the system were established through frequency response analysis and time domain integration of the system motion equations using the Matlab Simulink software. The results of the theoretical analysis and simulation models were compared with the results of a series of experiments, verifying the analysis approach.

**Keywords:** electromagnetic; Halbach array; two degrees of freedom; 2DOF; vibration energy harvesting; coil profile; magnetic field intensity; electro-mechanical coupling; power output.

**Reference to this paper should be made as follows:** Zhang, R., Wang, X., Shu, H. and John, S. (2018) 'The effects of the electro-mechanical coupling and Halbach magnet pattern on energy harvesting performance of a two degree of freedom electromagnetic vibration energy harvester', *Int. J. Vehicle Noise and Vibration*, Vol. 14, No. 2, pp.124–146.

Review

# A Comprehensive Review of the Techniques on Regenerative Shock Absorber Systems

Ran Zhang, Xu Wang\*  and Sabu John 

School of Engineering, RMIT University, Bundoora Campus, East, Corner Plenty Rd and McKimies Rd, Bundoora, VIC 3083, Australia; s3253199@student.rmit.edu.au (R.Z.); sabu@rmit.edu.au (S.J.)

\* Correspondence: xu.wang@rmit.edu.au; Tel.: +61-3-9925-6028; Fax: +61-3-9925-6108

Received: 28 March 2018; Accepted: 3 May 2018; Published: 7 May 2018



**Abstract:** In this paper, the current technologies of the regenerative shock absorber systems have been categorized and evaluated. Three drive modes of the regenerative shock absorber systems, namely the direct drive mode, the indirect drive mode and hybrid drive mode are reviewed for their readiness to be implemented. The damping performances of the three different modes are listed and compared. Electrical circuit and control algorithms have also been evaluated to maximize the power output and to deliver the premium ride comfort and handling performance. Different types of parameterized road excitations have been applied to vehicle suspension systems to investigate the performance of the regenerative shock absorbers. The potential of incorporating nonlinearity into the regenerative shock absorber design analysis is discussed. The research gaps for the comparison of the different drive modes and the nonlinearity analysis of the regenerative shock absorbers are identified and, the corresponding research questions have been proposed for future work.

**Keywords:** regenerative; shock absorber; drive mode; vehicle dynamics; output power; nonlinearity

## 1. Introduction

Due to the growing number of vehicles over recent decades and the increase of clean energy demand, the energy dissipation of a vehicle on different parts has been investigated. Recently, regenerative shock absorber systems caught the attention of many researchers because of the capability to harvest dissipated energy, due to its feasibility and accessibility. The fuel energy consumption of a car was analysed by Lafarge, Cagin [1] who stated that the fuel energy dissipated to drive the wheels accounts for up to 22.5% of the total fuel energy consumed, which ranks it the second following engine heat losses of 75.2%. In reality, the percentage of the dissipated fuel energy on driving the wheels is expected to increase as a result of the uneven or rough road surfaces.

Unlike the conventional shock absorber which reduces the vibration through viscous damping and converts the kinetic energy into heat energy dissipated, the regenerative shock absorber converts the kinetic energy mainly into electrical energy. This harvested electrical energy can be stored in the battery for later use. According to Zuo, Scully [2], automobiles contribute 70% of the carbon monoxide, 45% of the nitrogen oxide and 34% of the hydrocarbon pollution throughout the United States. One of the benefits brought by the regenerative shock absorber is that it can extend the mileage of the vehicle by saving petroleum fuel or electrical energy to achieve a reduction in the greenhouse gas emission.

In addition, the regenerative shock absorber can operate as a part of the active suspension system in order to improve the ride and comfort performance [3–7]. Proportional–integral–derivative control is commonly used in these applications for obtaining stable output power or reducing vibrations [8,9]. Based on the conservation of energy principle, better ride and comfort performance resulting from less kinetic energy or less vibration energy of the suspension system yields less amount of harvested energy. This contradiction can be overcome by adopting the control system which can make a compromise for



Contents lists available at ScienceDirect

Journal of Sound and Vibration

journal homepage: [www.elsevier.com/locate/jsvi](http://www.elsevier.com/locate/jsvi)



## A novel regenerative shock absorber with a speed doubling mechanism and its Monte Carlo simulation



Ran Zhang, Xu Wang\*, Zhenwei Liu

School of Aerospace, Mechanical and Manufacturing Engineering, RMIT University, Australia

### ARTICLE INFO

#### Article history:

Received 11 July 2017

Received in revised form 1 December 2017

Accepted 8 December 2017

Available online 27 December 2017

#### Keywords:

regenerative

Shock absorber

Double speed

Power

Efficiency

Random excitation

Monte carlo simulation

Coil mass

Amplification factor

### ABSTRACT

A novel regenerative shock absorber has been designed and fabricated. The novelty of the presented work is the application of the double speed regenerative shock absorber that utilizes the rack and pinion mechanism to increase the magnet speed with respect to the coils for higher power output. The simulation models with parameters identified from finite element analysis and the experiments are developed. The proposed regenerative shock absorber is compared with the regenerative shock absorber without the rack and pinion mechanism, when they are integrated into the same quarter vehicle suspension system. The sinusoidal wave road profile displacement excitation and the random road profile displacement excitation with peak amplitude of 0.035 m are applied as the inputs in the frequency range of 0–25 Hz. It is found that with the sinusoidal and random road profile displacement input, the proposed innovative design can increase the output power by 4 times comparing to the baseline design. The proposed double speed regenerative shock absorber also presents to be more sensitive to the road profile irregularity than the single speed regenerative shock absorber as suggested by Monte Carlo simulation. Lastly the coil mass and amplification factor are studied for sensitivity analysis and performance optimization, which provides a general design method of the regenerative shock absorbers. It shows that for the system power output, the proposed design becomes more sensitive to either the coil mass or amplification factor depending on the amount of the coil mass. With the specifically selected combination of the coil mass and amplification factor, the optimized energy harvesting performance can be achieved.

© 2017 Elsevier Ltd. All rights reserved.

### 1. Introduction

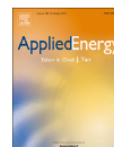
Since the fossil fuel has been largely consumed worldwide and caused a large amount of green-house gas emissions, it is necessary to replace the fossil fuel energy with renewable clean energy to protect the environment. Reducing the use of fossil fuel can greatly lower energy costs and reduce air pollution and climate change. In United States, 70% of the carbon monoxide, 45% of the nitrogen oxide and 34% of the hydrocarbon pollution are contributed by automobiles which are most powered by the fossil fuel [1]. Many studies have been conducted on reducing the fuel consumption of the vehicle by harvesting the energy that otherwise would have been wasted and dissipated as heat energy into the ambient. If this wasted thermal energy or vibration energy can be harvested and converted into the electric energy, not only will the travelling distance be extended,

\* Corresponding author.

E-mail address: [xu.wang@rmit.edu.au](mailto:xu.wang@rmit.edu.au) (X. Wang).

<https://doi.org/10.1016/j.jsv.2017.12.017>

0022-460X/© 2017 Elsevier Ltd. All rights reserved.



## A novel indirect-drive regenerative shock absorber for energy harvesting and comparison with a conventional direct-drive regenerative shock absorber



Ran Zhang<sup>a,b</sup>, Xu Wang<sup>a,\*</sup>, Elie Al Shami<sup>a</sup>, Sabu John<sup>a</sup>, Lei Zuo<sup>c</sup>, Chun H. Wang<sup>d</sup>

<sup>a</sup> School of Engineering, RMIT University, Australia

<sup>b</sup> Defence Materials Technology Centre, 24 Wakefield Street, Hawthorn, VIC 3122, Australia

<sup>c</sup> Department of Mechanical Engineering, Virginia Polytechnic Institute and State University, USA

<sup>d</sup> School of Mechanical and Manufacturing Engineering, University of New South Wales, Sydney, NSW 2052, Australia

### HIGHLIGHTS

- A novel regenerative shock absorber for motion conversion and energy harvesting.
- Simultaneous motion conversion, speed amplification and fluctuation elimination.
- An indirect and direct-drive system comparison for the same generator configuration.
- Parameter sensitivity analysis of the direct and indirect-drive systems via Monte-Carlo simulation.

### ARTICLE INFO

**Keywords:**  
Regenerative shock absorber  
Direct-drive  
Indirect-drive  
Monte Carlo simulation

### ABSTRACT

Energy harvesting from the shock absorbers is now becoming an important technology in developing the electrical vehicles. Compared with other kinetic energy sources such as engine and brake systems which are continuous or periodic, the shock absorber is subjected to the fluctuated linear motion with relatively small displacement. This paper presents a novel indirect-drive regenerative shock absorber system that utilizes an arm-teeth mechanism to achieve linear to rotary motion conversion and to amplify its input speed for increasing energy harvesting output. The fluctuation of road randomness can be smoothed out through the flywheel. The proposed design has the advantage of achieving all the targets with less number of components. Two prototypes of the direct-drive and indirect-drive regenerative shock absorbers have been built. The simulation models have been developed and validated by experimental results. The performance of this new indirect-drive system has been compared, through experimental testing and analytical modeling, with that of a conventional direct-drive system of the same generator configuration. The results show that this indirect-drive system can achieve greater peak power output and broader frequency bandwidth than the conventional direct-drive system. The indirect-drive system also presents a better ride comfort up to 13 Hz. Using Monte Carlo simulation, a parameter sensitivity analysis of both the indirect-drive and direct-drive systems has been carried out to compare their energy harvesting performances in terms of increasing the peak power output and broadening the energy harvesting frequency bandwidth. In both the systems, choosing the right tyre stiffness and electromechanical coupling constant is beneficial to increasing the peak power output ratio and the harvesting frequency bandwidth. The right choice of the gear ratio can further improve the peak power output ratio of the indirect-drive system. The variation of these parameters will allow for possibility of achieving higher power output when vehicle is driven on random road surfaces.

### 1. Introduction

Improving energy efficiency of transport vehicles has attracted great

interests in the past few decades due to the need to reduce consumption of the fossil fuel worldwide. Regenerative shock absorber is one of the promising technologies for reducing fuel consumptions that have been

\* Corresponding author.

E-mail address: [xu.wang@rmit.edu.au](mailto:xu.wang@rmit.edu.au) (X. Wang).

<https://doi.org/10.1016/j.apenergy.2018.07.096>

Received 14 April 2018; Received in revised form 16 July 2018; Accepted 20 July 2018  
0306-2619/ © 2018 Elsevier Ltd. All rights reserved.





## Parameter study and optimization of a half-vehicle suspension system model integrated with an arm-teeth regenerative shock absorber using Taguchi method



Ran Zhang<sup>a,b</sup>, Xu Wang<sup>a,b,\*</sup>

<sup>a</sup>School of Engineering, RMIT University, Australia

<sup>b</sup>Defence Materials Technology Centre, 24 Wakefield Street, Hawthorn, VIC 3122, Australia

### ARTICLE INFO

#### Article history:

Received 1 June 2018

Received in revised form 23 January 2019

Accepted 10 February 2019

#### Keywords:

Regenerative shock absorber

Arm-teeth mechanism

Random road profile

Taguchi method

Frequency bandwidth

### ABSTRACT

This paper presents a novel regenerative shock absorber that utilizes an arm-teeth mechanism to convert linear to rotational motion and to amplify the generator input speed. The flywheel of the arm-teeth mechanism also acts as an energy-storing element, allowing for smooth operation especially on a rough and uneven road surface. The critical parameters are identified through experiments and the simulation model is established based on a half-vehicle suspension system model. The novelty of this work is the proposed arm-teeth mechanism and the optimization of the half-vehicle suspension system through the Taguchi method. In this method, the ratio of the peak output power over the squared excitation displacement amplitude and the frequency bandwidth of the front and rear shock absorbers are set as targets and evaluated respectively. The effects of each parameter on the targets and the optimal parameter combinations are identified through the Taguchi matrix calculations. The optimized system is evaluated under the excitation of the road surface profiles of Class A, C and E of ISO 8606. It is found that the optimized system is able to harvest more energy with a broader frequency bandwidth than the original system at a certain speed for all three random road profile classifications.

© 2019 Elsevier Ltd. All rights reserved.

### 1. Introduction

Energy harvesting from the vehicle suspension system has recently drawn great amount of interests since suspension system was meant to be one of the main sources of energy loss. Only 21.5% of the fuel energy can be used eventually to move the vehicle [1]. The power dissipation due to the suspension shock absorbers, rolling resistance and the aerodynamic drag force of the vehicle accounts for 37% of the total power loss [2] where one shock absorber alone can consume 3–57 W of power [3]. The energy harvested by the regenerative shock absorber can be used to recover a part of the energy and to convert it into electricity which will charge the batteries or power the active suspension system.

Different types of transducers have been used to convert kinetic energy of shock absorbers into electrical energy, and the electromagnetic generator is the most suitable one considering the large displacement of the shock absorber and low modal resonant frequency of the vehicle suspension [4]. Many studies have attempted to increase the input speed of the generator because it is proportional to the power output of the generator [5]. For a vehicle travelling at a certain speed, the vertical

\* Corresponding author.

E-mail address: [xu.wang@rmit.edu.au](mailto:xu.wang@rmit.edu.au) (X. Wang).

<https://doi.org/10.1016/j.ymssp.2019.02.020>

0888-3270/© 2019 Elsevier Ltd. All rights reserved.